



Chalcogenide of type I-V-VI for thermoelectric applications

Sunanda Mitra

► To cite this version:

Sunanda Mitra. Chalcogenide of type I-V-VI for thermoelectric applications. Material chemistry. Université Paris Saclay (COMUE), 2016. English. NNT : 2016SACLS562 . tel-01552309v2

HAL Id: tel-01552309

<https://theses.hal.science/tel-01552309v2>

Submitted on 7 Jul 2017

HAL is a multi-disciplinary open access archive for the deposit and dissemination of scientific research documents, whether they are published or not. The documents may come from teaching and research institutions in France or abroad, or from public or private research centers.

L'archive ouverte pluridisciplinaire **HAL**, est destinée au dépôt et à la diffusion de documents scientifiques de niveau recherche, publiés ou non, émanant des établissements d'enseignement et de recherche français ou étrangers, des laboratoires publics ou privés.

NNT : 2016SACLS562

**THESE DE DOCTORAT
DE
L'UNIVERSITE PARIS-SACLAY
PREPAREE A
L'UNIVERSITE PARIS SUD**

ECOLE DOCTORALE N° 571
Sciences chimiques : molécules, matériaux, instrumentation et biosystèmes

Spécialité de doctorat : Chimie

Par

Mlle Sunanda MITRA

Chalcogenide of type I-V-VI₂ for thermoelectric applications

Thèse présentée et soutenue à Orsay, le 15 décembre 2016 :

Composition du Jury :

Pr. Franger Sylvain	Professeur, Université Paris-Sud	Président
Pr. Lenoir Bertrand	Professeur, Ecole des Mines de Nancy	Rapporteur
Dr. Alleno Eric	CR, ICMPE	Rapporteur
Dr. Beaudhuin Mickaël	MCF, Université de Montpellier	Examineur
Pr. Foury Pascale	Professeur, Université Paris-Sud	Examinatrice
Dr. Bérardan David	MCF, Université Paris-Sud	Directeur de thèse

Acknowledgements

First and foremost, I would like to express my sincere gratitude to my supervisor Dr. David Berardan for the continuous support of my PhD study, for his patience, motivation and immense knowledge. I must admit that his innovative ideas and the willingness to look at the positive side of the results had kept me motivated.

I would like to express my appreciation to the people who helped me in various ways during my PhD period. I would like to thank Dr. Celine Barreteau for her guidance and helping me to understand the basic steps of experiments, Dr. Romuald Saint-Martin for assisting in XRD analysis, Dr. Celine Byl for helping in the measurements and Dr. Cataline Alexandru Popescu for performing the pressure work. I would like to thank Dr. Lin Pan for giving me opportunity to work in his project. I would also like to thank Mr. Jeremy Forte for his guidance in XRD analysis. Besides, I must confess that outside my PhD work, I managed bureaucracy troubles because of him. Thank you Jeremy, I am grateful for your help and friendship towards me. Many thanks go to my colleagues, their encouragements and friendships are invaluable and unforgettable.

I am deeply grateful to my parents and my sister for their support, understanding and love.

I would like to thank all my friends whom I met during my stay in Paris. I would specially like to acknowledge the name of the person whose guidance and friendship help me to achieve this doctoral thesis. Words can't describe how thankful I am. Thank you so much Prabal, I will forever remember your precious support towards me.

Finally, all I can say, this three years of the doctoral thesis was a wonderful experience.

Table of Contents

General Introduction.....	5
<i>Chapter 1</i>	8
Thermoelectric and thermoelectric materials.....	8
1.1 Motivation behind this chapter	9
1.2 Context, history and background of thermoelectric.....	9
1.3 Fundamental of thermoelectric effects	10
1.3.1 Seebeck effect (Thomas Johann Seebeck, 1770-1831).....	11
1.3.2 Peltier Effect (Jean Peltier-1834)	12
1.3.3 Thompson Effect (Lord Kelvin-1851)	14
1.4 Thermoelectric application in General	15
1.5 Thermoelectric modules	17
1.5.1 Mathematical Modelling.....	19
1.5.1.1 Coefficient of performance of Peltier device (COP).....	19
1.5.1.2 Efficiency of a power generator (η)	20
1.5.1.3 Figure of merit	21
1.6 Challenges in enhancing ZT.....	22
1.6.1 Seebeck coefficient and electrical conductivity.....	24
1.6.2 Thermal conductivity	26
1.7 Thermoelectric materials	27
1.7.1 Historical background	27
1.7.2 State-of –the-art TE materials and their Figure- of –merit value	29
1.7.2.1 Conventional materials	29
1.7.2.2 Search for new TE materials: Novel approaches to enhance ZT.....	32
1.8 Advanced Chalcogenide Compounds	44
1.8.1 Chalcogenide of Type I-V-VI ₂	47
1.8.1.1 Introduction	47
1.8.1.2 Structural background	47
1.8.1.3 Paradigm of materials under this category of I-V-VI ₂	48
1.9 Conclusion.....	58

<i>Chapter 2</i>	59
Experimental methods.....	59
2.1 Motivation and organization of this chapter	60
2.2 Synthesis of composition (solid solution $\text{AgBiSe}_2\text{-AgBiS}_2$)	60
2.2.1 Method, instruments and raw materials used for synthesis.....	60
2.2.2 Densification of material: Spark plasma sintering	63
2.2.2.1 Sample preparation and geometry of sintered material	65
2.3 Structural characterization of material.....	67
2.3.1 X-ray powder diffraction (PXRD).....	67
2.3.2 High pressure measurement.....	70
2.3.3 Refinement Method.....	72
2.3.3.1 Rietveld Refinement	73
2.3.3.2 Le Bail Refinement	74
2.3.4 Thermal analysis by Differential Scanning Calorimeter (DSC)	75
2.4 Transport property measurement techniques/ Electrical characterization	78
2.4.1 Seebeck coefficient measurement	78
2.4.2 Seebeck and Resistivity measurement at high temperature.....	81
2.4.3 Hall Effect measurement	82
2.4.4 Specific heat measurement	84
2.4.5 Thermal diffusivity measurement (LASER FLASH method).....	86
<i>Chapter 3</i>	90
Experimental Results on solid solution $\text{AgBiSe}_2\text{-AgBiS}_2$	90
3.1 Motivation behind this chapter	91
3.2 Results of synthesis.....	91
3.2.1 Raw materials and Calculation of compositions.....	91
3.2.2 Heat treatment and water quenching	95
3.3 Result of structural and thermal analysis	100
3.3.1 Powder X-ray diffraction (PXRD).....	100
3.3.1.1 Determination of lattice parameters	104
3.3.2 DSC (Differential Scanning calorimetry).....	108
3.3.2.1 Comparative study (DSC and HT-XRD)	111
3.3.3 High pressure measurements	118

3.4 Conclusion	121
<i>Chapter 4</i>	122
Suppression of phase transition through substitution	122
4.1 Motivation and organization of the chapter	123
4.2 Synthesis and structural characterization of substituted solid solutions	123
4.2.1 Introduction	123
4.2.2 Method of synthesis	124
4.2.3 Substitution with antimony (Sb)	124
4.2.3.1 Heat treatment	124
4.2.3.2 PXRD (Powder X-ray diffraction)	125
4.2.3.3 Thermal analysis (DSC)	127
4.2.4 Substitution on solid solution AgBiSe_2 - AgBiS_2	128
4.2.4.1 Introductions	128
4.2.4.2 Heat treatment	129
4.2.4.3 PXRD (Powder X-ray diffraction)	131
4.2.4.4. Determination of lattice parameters	132
4.2.4.5 DSC (Differential scanning calorimeter)	134
4.3 Conclusion	135
<i>Chapter 5</i>	137
Influence of doping on solid solution (AgBiSe_2 - AgBiS_2)	137
5.1 Motivation and organization of the chapter	138
5.2 Synthesis of solid solutions with Niobium (Nb) doping on Silver (Ag) site	138
5.2.1 Introduction	138
5.2.2 Method of synthesis	138
5.2.3 Raw materials and calculation of compositions	139
5.2.4 Heat treatment	139
5.3 Result of Structural and thermal analysis	140
5.3.1 PXRD (Powder X-ray diffraction)	140
5.3.2 Determination of lattice parameters	142
5.3.3 DSC (Differential scanning calorimeter)	143
5.4 Densification of samples	145
5.5 Transport properties measurements	145

5.6 Conclusion and future work.....	148
<i>Chapter 6</i>	150
The effect of ionized impurity scattering on the TE performances of rock salt $\text{AgPb}_m\text{SnSe}_{2+m}$	150
6.1 Organization of the chapter	151
6.2 Introduction	151
6.3 Synthesis of solid solution.....	152
6.4 Methods and devices used for characterization.....	153
6.5 Results and discussion	153
6.5.1 Structural characterization results.....	153
6.5.2 Results of electrical and thermal property measurements	154
6.5.2.1 Seebeck and Resistivity measurements.....	154
6.5.2.2 Hall Effect measurements.....	156
6.5.2.3 Specific heat measurements.....	158
6.5.2.4 Thermal conductivity measurements	159
6.5.2.5 Figure of merit value	160
6.6 Conclusion	161
Conclusion and perspectives	162
Annex	165
Bibliography.....	169
List of Figures	187
List of Tables	192
Résumé en français	

General Introduction

The increased world-wide demand for electric power fueled the challenging task to find alternative, renewable and sustainable power sources. The development of alternative power sources will accelerate the transition from the use of fossil fuel to sustainable energy production along with a reduced emissions of carbon dioxide. The most recent energy flow chart (Figure A), developed at Lawrence Livermore National Laboratory (LLNL), illustrates the constituents of energy sources in the U.S. in the year 2015 is shown below. At present, the most striking fact is that a considerable amount of the energy produced is lost as heat and only less than half satisfy the needs of human society. In this respect, as the existing energy sources have been depleting at a fast pace, thermoelectric materials have received significant attention in recent years due to its role in conversion of waste heat into electricity.

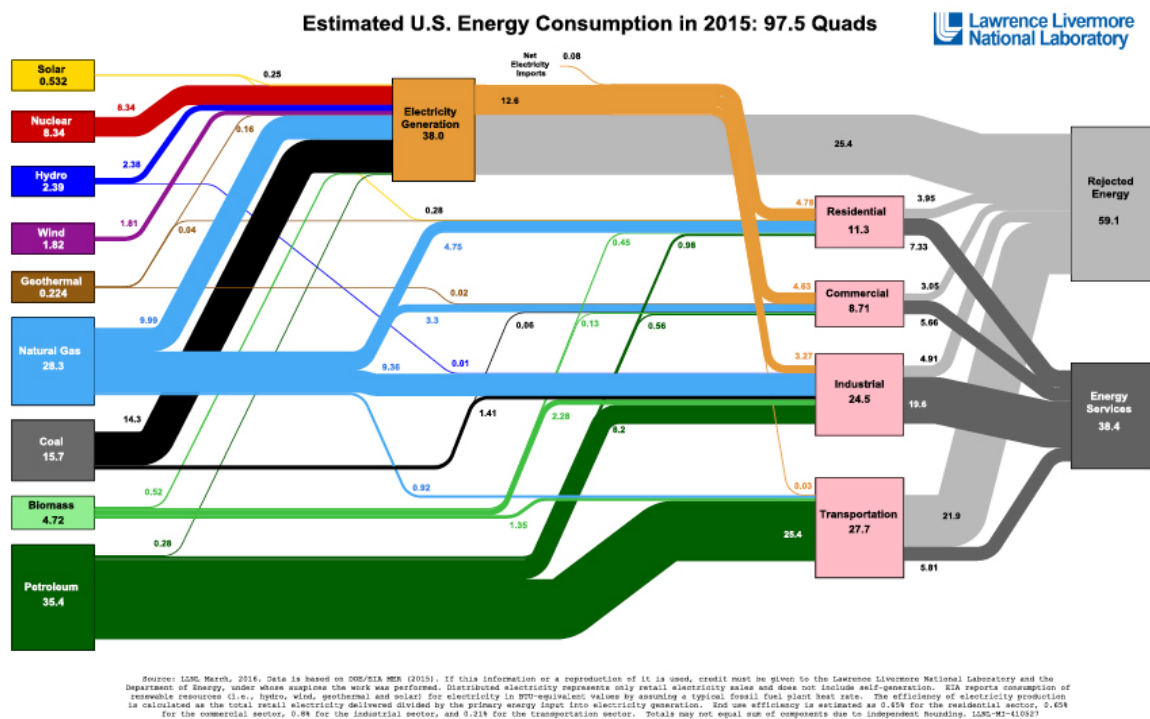


Figure A: The estimated energy consumption in US in 2015 and different sources of energy [https://flowcharts.llnl.gov/].

Thermoelectrics were studied since early stage of 19th century. The most recognizable discovery in thermoelectric was made between 1821 and 1850 which included the discovery of three thermoelectric effects, namely, Seebeck, Peltier and Thomson. Based on such effects, potential applications of thermoelectric devices were recognized by the researchers from refrigeration to power generation. The thermoelectric (TE) devices have triggered great attention in viable technologies including automotive, military equipment, aerospace, medical and industries. Unlike other devices, they have many advantages, such as, long life, usage without any vibrations or noisy sound as they have no mechanical moving parts. Additionally they are compact, possess a high level of scalability/reliability and require less maintenance. However, one of the major challenges in thermoelectric is to develop material systems that have high thermoelectric figures of merit, ZT , in the temperature ranges of interest. However, despite such benefits, their applications are restricted to specific zones due to their low efficiency and high manufacturing cost. Currently, the material cost of thermoelectrics is around \$ 1-2 per Watt, but it is possible to bring down to \$0.05-0.1 per Watt to make it more competitive by exploration of more efficient and high ZT materials. To date, the conventional TE materials have shown limited energy conversion efficiency. Therefore, the idea is to develop new materials and to optimize the existing ones in order to improve their yields. In this respect, the concept of nanostructuring (such as nanowires, nanorods, superlattices,...) and development of novel TE materials with complex structures (such as clathrates, skutterudites,...) have opened new avenues to improve significantly the ZT values.

The thesis is structured into six chapters and a brief description of chapters is given below.

The first chapter describes a brief summary of thermoelectricity which enables the reader to understand the requirement of thermoelectric materials in a better way. Furthermore, we discuss about the various thermoelectric materials and the class of material used in the context of thesis.

The second chapter presents the synthesis method and the useful experimental techniques used for structural characterization and transport property measurement.

The third chapter presents a detailed investigation on the synthesis and the structural characterization of solid solution $\text{AgBiSe}_2\text{-AgBiS}_2$ by X-ray diffraction and by thermal analysis using DSC (Differential scanning calorimeter). Moreover, the experimental results obtained under high temperature and high pressure XRD study will be presented in this chapter.

The fourth chapter describes the influence of substitution on the Bi site on solid solution in order to suppress the phase transition by using chemical pressure. A detailed description of synthesis steps and structural analysis performed on the samples will be presented.

The fifth chapter describes the influence of doping on the substituted solid solutions. The synthesis method, structural analysis and transport property measurements conducted on few samples will be presented.

The sixth chapter is a supplementary chapter based on the rock salt material $\text{AgPb}_m\text{SnSe}_{2+m}$. This chapter will present the details of synthesis process and the results of thermoelectric performance of $\text{AgPb}_m\text{SnSe}_{2+m}$ samples.

Finally, some general conclusions and perspectives within the context of the work in the thesis will be given.

Chapter 1

Thermoelectric and thermoelectric materials

1.1 Motivation behind this chapter

This theses work deals with the synthesis and characterisation of thermoelectric material. So, for the better understanding of the reader; the following chapter aims to present relevant background information about thermoelectricity, a short review on the current status of thermoelectric materials and their applications. The interested reader can find more detailed explanation in the references mentioned in the section bibliography.

1.2 Context, history and background of thermoelectric

Over decades, a continuous depletion of existing energy sources due to the huge consumption rate becomes a serious problem. In addition, major threats to our climatic situation come from the emission of carbon dioxide. Moreover, scientific evidence has supported the long-term argument that there is an urgent need to establish some useful measures to get rid of from these catastrophic situations. So, the biggest challenge for the mankind is to find the alternate sources of energy. For several years, researchers and industries are putting much effort to overcome such issues. The best possible way is the development of new technologies which can increase the output power of the existing fuels, the use of alternative energy sources (renewable sources; wind, solar, biomass and others) and improvement of the thermal management. On the other side, in everyday life, the enormous amount of unused waste heat is generated from various sources; home heating, automotive exhaust, industrial processes, chemical reactions, combustion, nuclear decay, etc. So, it would be advantageous to develop some techniques which can directly harvest this waste heat into the useful forms of energy, most favorable would be electricity. Nowadays, electricity becomes an indispensable component of human life. In this context, thermoelectric emerged as an advanced way to fulfill such need.

Thermoelectric was studied since the early stage of 19th century. In the early 1800's, the main physical principles were studied upon which the modern thermoelectric coolers are based on. The most recognizable discovery in this field occurred in 1821 due to a German Scientist, Thomas Seebeck [1]. He observed that a magnetic compass needle was deflected when placed in the vicinity

of a closed loop formed by two dissimilar metals, with a temperature difference applied between the junctions. But he was unable to comprehend the scientific reason behind his discovery. He thought the magnetism (thermo-magnetic effect) was responsible for this kind of phenomena. Later, Danish physicist Hans Christian Orsted realized that the deflection occurred due to the induced electric current. In 1834, French watchmakers, Jean Peltier [2], investigated the Seebeck Effect and discovered the phenomenon opposite to it; heat is absorbed or rejected at the junction of two dissimilar materials when an electrical current passes through it in a closed circuit. But, he failed to demonstrate the full implications of his findings. Later, the more clear explanation was obtained when in 1838, Heinrich Lenz experimentally showed that a water droplet freeze when placed at the soldered joint of bismuth and antimony wires on application of electric current and melts with the reversal of polarity. After few years, in 1851, William Thomson (later Lord Kelvin) established the interdependency of Seebeck and Peltier effects with the thermodynamic relations. Thompson also discovered that in the presence of a temperature gradient, the cooling or heating of a uniform conductor can be obtained with the onset of current flow. This is known as the Thomson effect [3,4].

1.3 Fundamental of thermoelectric effects

Thermoelectric effect is defined as the direct conversion of temperature difference into electrical energy (or vice-versa). This effect arises because the charge carriers (electrons or holes) in metals and semiconductors are free to move much like gas molecules, while carrying the charge as well as heat. So, in the presence of a temperature gradient, the mobile charge carriers can diffuse and results in a build-up of net charge carriers, thereby producing a voltage and an electric current in a closed loop. This implies a coupling between the thermal and electrical phenomena. The most prominent three fundamental effects which are involved in thermoelectric phenomena were discovered by Seebeck, Peltier and Thomson in the early 1800s. These three effects are classified as Seebeck effect, Peltier effect and Thomson effect. Apart from such effects, there is another heat release phenomenon known as joule heating or resistive heating. Here, in this process, heat is also generated though it is not considered as TE effects. The three TE effects are basically reversible thermodynamic processes whereas the joule heating is not. Entropy is produced by the irreversible processes in the thermoelectric devices. If such processes could be eliminated, then entropy production would be reduced to zero, allowing the TE device efficiency to approach to the Carnot efficiency.

1.3.1 Seebeck effect (Thomas Johann Seebeck, 1770-1831)

Seebeck effect is a phenomenon in which a temperature difference between two dissimilar electrical conductors or semiconductors produces a voltage difference between the two substances schematically shown in Figure 1-1. The Seebeck effect is the principle behind thermoelectric power generation. The voltage difference produced is proportional to the thermal gradient, and the proportionality constant is known as Seebeck coefficient or the thermopower, denoted by S (volts/Kelvin). The thermopower also measures the entropy per charge carrier in the material. A detail explanation of Seebeck effect is mentioned below.

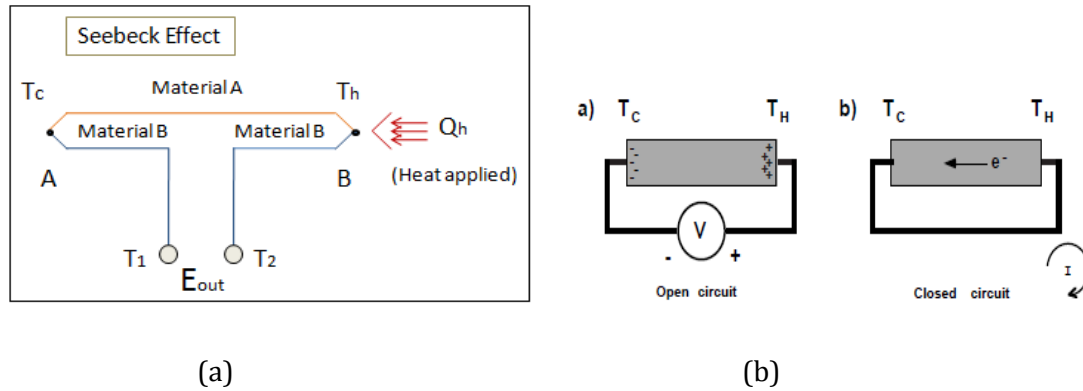


Figure 1-1: A schematic diagram illustrating the Seebeck effect of two dissimilar material A & B.

Figure 1-1a denotes the two dissimilar materials named as A and B. The junction temperature at A is used as a reference and is maintained at a relatively cold temperature (T_c). And the junction temperature T_h at B is used as temperature higher than T_c . Now, with the heat applied Q_h to junction B, an output voltage (V_1 and V_2) will appear across terminals T_1 and T_2 respectively and hence an electric current would flow continuously in this closed circuit shown in Figure 1-1b. Therefore, the mathematical relation defines the Seebeck effect expressed as:

$$S_{AB} = S_A - S_B = \frac{\Delta V}{\Delta T} \quad \text{..... 1.1}$$

Where, S_A and S_B , denotes the thermopower of material A and material B respectively, ΔV is the voltage difference and ΔT is the temperature differences between the hot and cold side of the junctions. The sign of the thermopower can determine which charge carriers dominate the electric transport in both metals and semiconductors. In semiconducting material, Seebeck coefficient

varies with doping. The value of S is negative for n-type semiconductors, when the electrons diffuses from the hot end to the cold end; and S is positive for p-type semiconductors, when the holes diffuses from the hot end to the cold end i.e., electrons moves in the opposite direction. The voltages produced by Seebeck effect is very small only a few to some hundreds microvolt per kelvin of temperature difference at the junction. If the temperature difference is large enough, then Seebeck-effect devices can produce a few millivolts.

1.3.2 Peltier Effect (Jean Peltier-1834)

The Peltier effect is the inverse to the Seebeck effect. This effect has been defined as a heat absorption or rejection when an electric current passes through a junction of two dissimilar materials A and B shown in Figure 1-2. The absorption of this heat or its evolution depends on the direction of the electric current. It is used for thermoelectric devices in cooling applications, as p and n type materials can be made to exhibit the Peltier effect in very small packages. The detailed description of this effect is mentioned below.

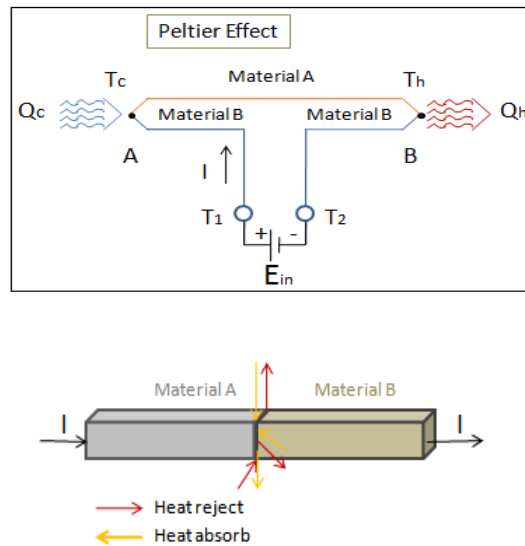


Figure 1-2: Schematic diagram of Peltier effect between two dissimilar materials A and B.

If a voltage (E_{in}) is applied to the terminals T_1 and T_2 then an electrical current (I) will flow in the circuit. As a result of the current flow, a slight cooling effect (Q_c) will occur at thermocouple junction A where heat is absorbed, and a heating effect (Q_h) will occur at junction B where heat is released. This effect can be reversed, whereby a change in the direction of electric current flow will

reverse the direction of heat flow. The Peltier heat absorbed or rejected at the junction is mathematically expressed as:

$$Q = \Pi I \quad \text{..... (1.2a)}$$

and
$$Q = \Pi_{AB} I = (\Pi_A - \Pi_B) I \quad \text{.....(1.2b)}$$

Where, Q is the cooling or heating rate in watts, I is the electric current in amperes, Π is the proportionality constant known as Peltier coefficient, Π_A and Π_B are the Peltier coefficients of material A and B respectively. Peltier coefficient depends on the temperature and materials of a junction. The value of this coefficient can be positive or negative as shown in Figure 1-3.

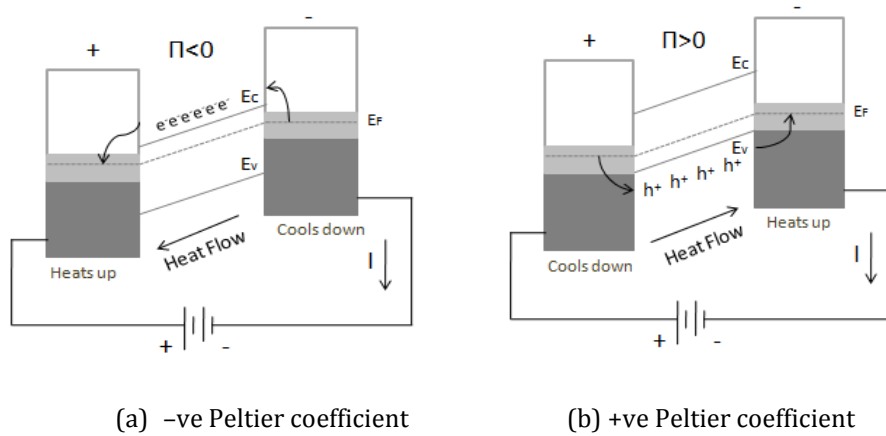


Figure 1-3: Schematic diagram of n and p-type semiconductor showing the Peltier effect.

Figure 1-3 describes the Peltier effect for a semiconductor between two pieces of metal. The Figure 1-3(a) shows an n-type semiconductor in which conduction band electrons are the predominant charge carriers. This semiconductor is connected to a voltage source by metallic conductors on its both sides. In this case, electrons flow from right to left in the semiconductor, carrying heat as well, which results in a flow of electric current in opposite direction. The electrons from the metal enters the semiconductor after overcoming the energy barrier, which is the difference in energy between the conduction band edge (E_c) and the Fermi level, (E_f), to enter the conduction band. Finally, the highest-energy or the hottest electrons from the metal were able to cross to the other metal-semiconductor interface. As a result, the right side is depleted of high energy electrons as shown in the Figure 1-3a. Now, these electrons can travel through the semiconductor and face no energy barrier as they enter the metal on the left side and achieve a net gain of high-energy electrons. Hence, the heat is transported from right to left i.e. an electrical current is accompanied by a

thermal current. One side heats up above the ambient temperature and the other side cools down below the ambient temperature. In this case the value of Π is negative. Now secondly we consider a p-type semiconductor connected to a voltage source to describe the Peltier effect which is shown in Figure 1-3b. Here, in this case, holes are the majority carriers flowing from left to right in the semiconductor, carrying heat from the left to the right side of the semiconductor which is in the same direction as the electric current. The electric current is carried by positive holes travelling from left to right in the semiconductor valence band. These holes must overcome the energy barrier between the Fermi level and the valence band edge, E_v , to enter the semiconductor. The left side is depleted of the highest energy holes resulting in a thermal current from left to right. Hence, the Peltier coefficient Π is positive. In Figure 1-3, E_c , E_v , and E_F denote the energies of the conduction band edge, the valence band edge, and the Fermi energy respectively.

1.3.3 Thomson Effect (Lord Kelvin-1851)

The Thomson effect [3,4] describes either the heating or cooling of a current-carrying conductor within a temperature gradient. It has a connection with the temperature dependence of Seebeck coefficient. When an electric current is passed through a conductor having a temperature gradient over its length, heat will be either absorbed by or expelled from the conductor shown schematically in Figure 1-4. The absorption or rejection depends on the direction of both the electric current and the temperature gradient. This phenomenon is known as the Thomson effect. The Thomson coefficient, τ is given as:

$$\frac{dQ}{dx} = \tau I \frac{dT}{dx} \quad \dots\dots\dots (1.3)$$

Where, $\frac{dQ}{dx}$ is the Thomson heat transfer per unit length, $\frac{dT}{dx}$ is the thermal gradient over the length of the material and I is the applied current. This effect is a reversible thermoelectric phenomenon. The Thomson effect does not occur in a current-carrying conductor which is initially at uniform temperature. Thomson coefficient can be positive, negative or zero.

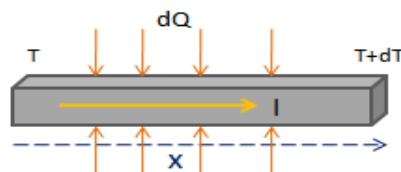


Figure 1-4: Schematic diagram of Thompson effect in a single material.

1.3.4 Kelvin relations

All the three coefficients stated earlier are related to each other by Kelvin relations [9,10]. Thomson (Lord Kelvin) found the relations between the three coefficients in 1854. The first Kelvin relation connects the temperature derivative of Seebeck coefficient and the Thompson coefficient which is mathematically defined as,

$$\tau = T \frac{dS}{dT} \quad \text{..... (1.4a)}$$

Where, T is the absolute temperature in Kelvin. The second Kelvin relation connects the Seebeck coefficient and the Peltier coefficient by the expression:

$$\Pi = ST \quad \text{..... (1.4b)}$$

1.4 Thermoelectric application in General

Thermoelectric devices have been used in different fields for long time. Such devices are based on thermoelectric effects and due to this unique feature thermoelectric materials cover a vast area of application in the field of; medical, defence, scientific laboratories, and industries, in aerospace and also in thermal management applications. It has been reported that 66% of primary energy is wasted as heat as shown in Figure 1-5. So, the development of such devices is essential to utilize this waste heat and convert it into useful electric power. More specifically, the two main applications are thermoelectric generator and cooling system based on Seebeck and Peltier effects.

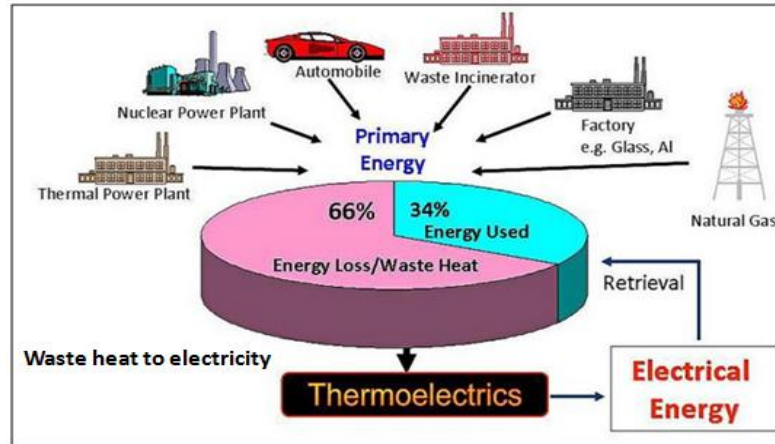


Figure 1-5: Waste heat recovery

In everyday life, enormous amounts of waste heat are generated from various sources and can be categorised into micro-scale and macro-scale waste heat applications. For e.g., in power plants and factories as thermoelectric power generator to recover the waste heat, in cars and other automobiles as automotive thermoelectric generators (ATGs) for increasing fuel efficiency and also to recover the waste heat originating from the domestic appliances. In addition, micro-scale power generators made by integrated circuit (IC) technology are used for energy conversion in micro-systems and wearable electronics. In addition, in space exploration, TE generators acquire a great attention; RTG (radioisotope thermoelectric generator) have been used by NASA to provide power to the space probes, where radioisotopes are used as a heat source. RTG (radioisotope thermoelectric generator) uses the radioactive materials (such as plutonium oxide) which generate heat as they decay into non-radioactive materials. This heat is converted into electricity to produce power for the spacecraft. It also supplies energy to remote areas, such as a series of lighthouses along the coasts. The main advantage of using RTG is that it works as a long-lived power system without any requirement of fuel. It has been successful to power a number of space missions. NASA has developed a new generation of such power system called MMRTG (Multimission radioisotope thermoelectric generator). Another advantage of TE generator is that they operate without any vibration and noisy sound as they have no mechanical moving parts. They are compact and bear a high level of scalability and reliability, and require less maintenance. [22-30]

Thermoelectric cooling devices are well-known as the Peltier device, Peltier heat pump, solid state refrigerator, or thermoelectric cooler (TEC). They can be used either for heating or for cooling. TE coolers are solid state heat pumps used in applications where temperature stabilization, temperature cycling, or cooling below ambient are required. The basic applications area of TE

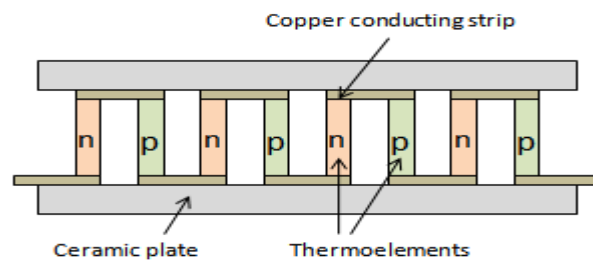
coolers are in electronics, medicine, scientific and laboratory equipment, temperature controller in missiles and space systems, telecommunication instruments, consumer goods, in air-conditioning systems. The use of TE coolers in electrical instrumentation are quite common due to its various advantages such as; TE module function without any moving parts(no electrical noise and works silently), they are small in size and lighter in weight. They are also used where a stable operation temperature is required such as laser diodes and provide small area cooling for infrared detectors, and computer processor. Moreover, in automobile industry, recently developed cooling system are considered as a green energy application in heating or cooling of car seats; for e.g., CCS (climate control seat developed by Gentherm Company). Apart from this, in consumer goods like portable refrigerators, water coolers, etc., TEC occupy less space compare to vapour compressive refrigerators and work without any use of harmful refrigerants such as CFCs or HFC. [31-37]

Both of these TE generators and cooling devices provide an environmentally friendly green technology as there is no outcome of any kind of toxic, gaseous, chemical waste during operation. Even though, they possess many advantages, their applications are restricted to specific zones due to their low efficiency and high manufacturing costs. The market in TE generators has been expanded in recent years but one of the key factors is the cost of thermoelectric module. Yazawa & Shakouri estimated the cost of materials (in dollars per watt) as a function of heat source power density for different material properties (ZT) and also as a function of module design [38]. Their report showed that the design of the module also plays an important role in determining the cost of waste-heat- recovery thermoelectric devices. The materials cost is around \$ 1-2 per watt but through exploration of more efficient and high ZT materials; it could be possible to bring down to \$0.05-0.1 per watt to make it more competitive with the other current technologies in the market.

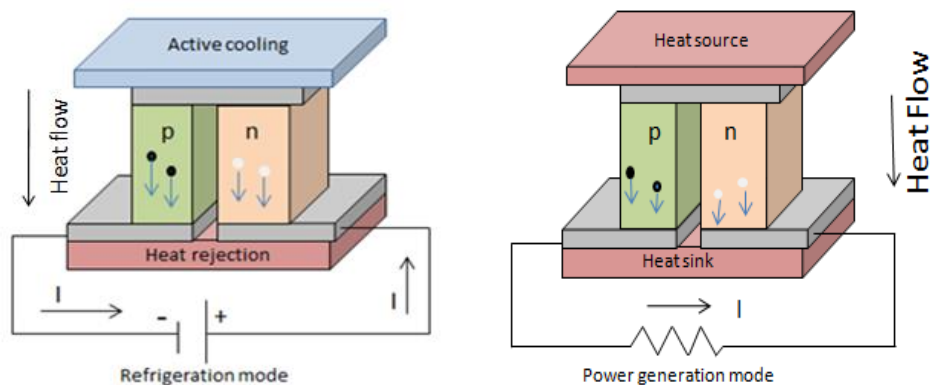
1.5 Thermoelectric modules

The Peltier effect is the basis for many modern day TE refrigeration devices and the Seebeck effect is the basis for TE power generation devices. Both of these devices can be accomplished with a basic unit known as thermoelectric module. Basically, a thermoelectric module consists of several n and p type legs connected through the electrical contact pads, sandwiched between two ceramic plates shown in Figure 1-6(a). The two ceramic plates are used to provide electrical insulation for n-type and p-type semiconductor thermo-elements as well as mechanical resistance. One pair of n-type and p-type semiconductors forms a thermocouple. The multiple thermocouples in the resultant structure are connected in such a way that the electric current flows in series and heat flows in

parallel. The reason for use of both p and n branches is because their Seebeck and Peltier coefficients are of opposite sign, such that both branches can contribute to desired thermoelectric effects. When heat is applied to one surface of the thermoelectric generator, the electrons in the n-type semiconductor and the holes in the p-type semiconductor will move away from the heat source. And this movement of electrons and holes gives rise to an electrical current. Thus, by creating the appropriate electrical connections, current in the generator flows in a closed loop through the p-type and n-type semiconductors and an external load. Electrical power is obtained due to the movement of electrical carriers brought on by the flow of heat through the thermoelectric pellets. When the thermoelectric module is operating as a refrigerator, the bottom plate is connected to a heat sink. With the application of DC current of proper polarity; heat is pumped from the top plate to the bottom plate and into the heat sink, where it is dissipated. The resultant is that the top surface becomes cold. Reversal of the current direction leads to the warming up of the top plate. Like-wise, both refrigeration and power generation may be accomplished using the same module shown in Figure 1-6(b).



(a)



(b)

Figure 1-6:(a) Schematic diagram of thermoelectric module and (b) diagram illustrates both power generation (Seebeck effect) and electronic refrigeration (Peltier effect).

1.5.1 Mathematical Modelling

In this section, basically, the fundamental equations are derived which helps in determining the value of coefficient of performance of a Peltier device and efficiency of a thermoelectric generator.

1.5.1.1 Coefficient of performance of Peltier device (COP)

The performance of a cooling device (Peltier device) can be evaluated with the following parameters; the coefficient of performance, COP (ϕ), the heat pumping rate (Q_c) from the cold side and the maximum temperature difference (ΔT_{\max}) that the device will produce. The COP is defined by the relation,

$$\phi = \frac{Q_c}{P} \quad \text{..... (1.5a)}$$

Where, P is the input electrical power. The cooling effect is given by sum of the three terms: the Joule heat of each side per unit time, the heat transfer rate when current is equal to zero between the two sides and the Peltier heat rate of each side. Here, it is usual to assume that one half of the Joule heat is transferred to each junction. So, the Q_c is:

$$Q_c = S \cdot T_c \cdot I - \frac{1}{2} I^2 R - K \Delta T \quad \text{..... (1.5b)}$$

Where, $S = (S_n + S_p)$, S_n and S_p are the Seebeck coefficients of the semiconductor materials, I is the current, R is the electric resistance (Ω) and K is the thermal conductance (W/K) of the thermoelectric cooling module. Now, the second thing is the input power given as:

$$P = V \cdot I = S \cdot I \cdot \Delta T + I^2 R = \frac{V(V - S \cdot \Delta T)}{R} \quad \text{..... (1.5c)}$$

Where, $\Delta T = (T_h - T_c)$, T_h and T_c are the temperatures of hot and cold sides respectively. V is the applied voltage. Therefore, the coefficient of performance is expressed as:

$$\phi = [m T_c - \frac{1}{2} m^2 - (\frac{\Delta T}{Z})] / (m \Delta T + m^2) \quad \text{..... (1.5d)}$$

Where, $m = \frac{IR}{s}$ and Z will be defined later.

The current value that maximizes the COP is obtained by taking the derivative of the COP with respect to m equal to zero and is given by,

$$I = \frac{S\Delta T}{R(\omega - 1)} \quad \text{..... (1.5e)}$$

Hence, the maximum COP expressed as,

$$\Phi_{\max} = \frac{T_c}{\Delta T} \left[\frac{\omega - \left(\frac{T_h}{T_c}\right)}{\omega + 1} \right] \quad \text{..... (1.5f)}$$

where, $\omega = (1 + ZT_{\text{avg}})^{1/2}$, $T_{\text{avg}} = \frac{T_h + T_c}{2}$ and Z is the figure of merit of the material (mention in section 1.5.1.3).

For a completely reversible thermoelectric system (with $R=0$), the COP reaches the Carnot cycle value.

1.5.1.2 Efficiency of a power generator (η)

The efficiency of a power generator, η is defined as the ratio of the electrical power output P_o to the thermal power input Q_h to the hot junction given as:

$$\eta = \frac{P_o}{Q_h} \quad \text{..... (1.6a)}$$

The thermal power input is given by sum of the three terms: the Joule heat of each side per unit time, the heat transfer rate when current is equal to zero between the two sides and the Peltier heat rate of each side. It is assumed that one half of the Joule heat is transferred to each junction.

$$Q_h = ST_h I + \frac{1}{2} I^2 R + K\Delta T \quad \text{..... (1.6b)}$$

Where, S is the Seebeck coefficient, T_h is the temperature at the hot end, I is the current, R is the electric resistance, K is the total thermal conductance of the thermoelectric module and ΔT is the temperature difference between the hot and cold sides. And, the electric output power is

$$P_o = I^2 R_L = VI \quad \text{..... (1.6c)}$$

Where, R_L is the load resistance. The maximum efficiency value can be expressed as:

$$\eta = \frac{\left(\frac{\Delta T}{T_h}\right)(\omega + 1)}{\left[\omega + \left(\frac{T_c}{T_h}\right)\right]} \quad \text{..... (1.6d)}$$

1.5.1.3 Figure of merit

The material's potential depends on the factor called figure of merit, Z . It has the unit of inverse Kelvin. But generally, the quality and performance of a TE material is determined by the dimensionless figure of merit (ZT), which was first introduced by Edmund Altenkirch in the early 1900's [14,15]. This factor ZT is incorporated with physical transport properties and is formulated as:

$$ZT = \frac{S^2 \sigma T}{k} = \frac{S^2 T}{\rho k} \quad \text{..... (1.7a)}$$

Where, S is the Seebeck coefficient, σ is the electrical conductivity, ρ is the electrical resistivity, and k is the total thermal conductivity and T is the absolute temperature. The maximum power is proportional to $S^2 \sigma$ (or S^2 / ρ) known as power factor. For a TE couple consisting of both n-type and p-type material, the figure of merit value is given by the relation:

$$Z_{pn} = \frac{(s_p - s_n)^2 T}{(\rho_n k_n)^{1/2} + (\rho_p k_p)^{1/2}} \quad \text{..... (1.7b)}$$

Equations 1.5(f) and 1.6(d) shows that the COP of a Peltier device and the efficiency of a TE power generator strongly depend on ZT of the materials used in the thermoelements and the dependency is shown in

Figure 1-7.

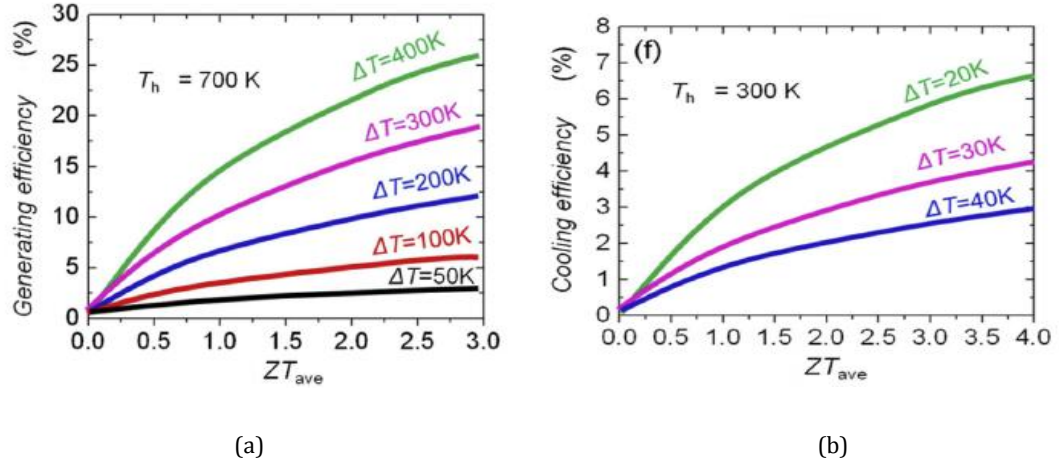


Figure 1-7: Dependence of efficiency with ZT. [17]

This plot clearly shows that the largest value of ZT is required to obtain the maximum device efficiency. The absence of thermal conductivity causes the ZT value to reach infinity and the TE devices approach the Carnot cycle efficiency. And moreover, it designates two important factors towards achieving the maximum efficiency: proper selection of materials with high figure of merit value and appropriate choice of significant temperature difference to design an effective system. Hence, for the thermoelectric to be more applicable compare to the current technologies, ZT values are expected to rise above 1.5 for power generation and 2-4 for cooling application respectively [16,17].

1.6 Challenges in enhancing ZT

Over decades, the primary aim of thermoelectric is to attain improved value of ZT and overcome the upper limit $ZT \approx 1$. The value of ZT is related to Seebeck coefficient (S), electrical conductivity (σ) and thermal conductivity (κ) as given in equation 1.7(a). In order to obtain high ZT value, S and σ should be high while κ should be reduced. But, this is not an easy task, as S , σ and κ are interconnected with each other in such a way that each of them cannot be optimized independently[16]. It's important to create materials which possess the combination of the good electronic properties of a crystal and the low thermal conductivity of a glass leading to outstanding TE performances. And moreover, all depend strongly on the material's crystal structure, electronic structure and carrier concentration. Their interdependency become an obstacle in the development and limits the selection of materials for TE applications. The properties dependency is shown schematically in Figure 1-8.

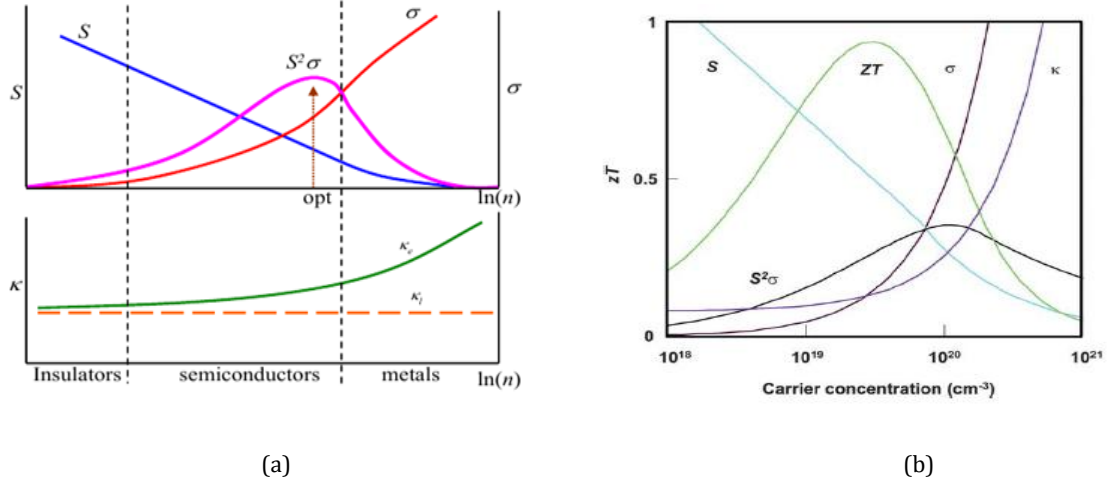


Figure 1-8: (a) The dependence and variation of s , k , σ and $s^2\sigma$ as a function of carrier concentration n [16] and (b) also ZT variation with carrier concentration [127].

From Figure 1-8, it is clear that, with increase in carrier concentration, thermal conductivity (κ) increases with respect to electrical conductivity (σ) due to its electronic part (κ_e) while the Seebeck coefficient (S) is decreasing. Therefore, the increased κ value lowers the figure of merit and on the other hand σ increases it. So, a compromise must be found between these two situations through optimisation of figure of merit. The optimisation can be accomplished by either increasing the power factor ($S^2\sigma$) or reducing the thermal conductivity. To do so, some strategies are adapted towards increasing ZT such as; solid solution alloying, nanostructuring and development of new materials which can operate over a wide temperature range.

Another important part in thermoelectric is the material selection. Materials can be classified as metals, semiconductors and insulators depending on the carrier concentration and electronic structure. They can be distinguished according to their TE properties at 300K which is tabulated Table 1. Also, the variation of various physical properties as a function of carrier concentration for this materials is clearly visible in Figure 1-8(a). It shows that insulators are poor thermal and electrical conductors whereas metals exhibit high value of σ and κ along with small value of $S^2\sigma$. However, in comparison with this two, semiconductors possess large thermopower, relatively high σ , and lower value of κ which may lead to an optimum ZT value. The optimum value lies in the narrow band gap semiconductor region. Till now, semiconductors are proved to be the best candidate for a good TE material. [16,17]

Table 1: Comparison of TE properties of metals and semiconductors and insulators at 300K [16].

Property	Metals	Semiconductors	Insulators
S (μVK^{-1})	~ 5	~ 200	~ 1000
σ ($\Omega^{-1}\text{cm}^{-1}$)	$\sim 10^6$	$\sim 10^3$	$\sim 10^{-12}$
Z (K^{-1})	$\sim 3 \times 10^{-6}$	$\sim 2 \times 10^{-3}$	$\sim 5 \times 10^{-17}$

So far, we have seen the dependency of S, σ and κ with the carrier concentration n graphically, the mathematical interrelationship between these parameters can be summarised as follows:

1.6.1 Seebeck coefficient and electrical conductivity

The Seebeck coefficient can be defined as entropy per carrier given by the relation $S \approx \frac{C}{q}$, where C is the specific heat and q is the carrier charge. For metals and semiconductors, this S value is related to a quantity $\frac{K_B}{e}$ given approximately in the two equations 1.8(a) and 1.8(b) respectively [5]. These relations are rough approximations. The quantity ($\frac{K_B}{e} \approx 87 \mu\text{V}\text{K}^{-1}$) is a constant and originates from the energy relation of a classical gas particle as $\frac{3}{2K_B T}$, where K_B is the Boltzmann constant and e is the electron charge.

$$S \approx \frac{C}{q} \approx \left(\frac{K_B}{e}\right) \frac{K_B T}{E_F} \quad \dots\dots\dots (1.8a)$$

and
$$S \approx \frac{C}{q} \approx \left(\frac{K_B}{e}\right) \frac{E_G}{K_B T} \quad \dots\dots\dots (1.8b)$$

Where, E_F and E_G is the Fermi energy and the energy gap of the material respectively. Now, coming to the conflicting part in determining ZT is the carrier concentration (n), as the Seebeck coefficient(S) and electrical conductivity (σ) are related to n in a reverse way. For metals and highly degenerate semiconductors, the relationship between S and n is represented by a simple electron transport models defined by Mott-Jones relation [22] as:

$$S = \frac{8\pi^2 K_B^2}{3eh^2} m^* T \left(\frac{\pi}{3n}\right)^{2/3} \quad \dots\dots\dots (1.8c)$$

Where, m^* is the effective mass of the carrier and h is the Planck's constant. This relation indicates that the S value decreases with increase in n . On the other hand, the interrelationship between electrical conductivity (σ) and carrier concentration (n) shows the increase in σ with n determined as:

$$\sigma = \frac{1}{\rho} = ne\mu = \frac{ne^2}{m^*}\tau \quad \text{..... (1.8d)}$$

Where, $\mu = \frac{e\tau}{m^*}$, is the mobility of charge carrier, ρ is the resistivity and τ is the scattering rate.

Moreover, the effective mass m^* also appears as a second contradictory part due to its reverse relation with s and σ as mentioned in equation (1.8c) and (1.8d). These equations gives a clear image that larger effective mass will produce high thermopower whereas electrical conductivity become lower as heavy carriers will move with lower velocities, which in turn reduce the mobility of the charge carrier. This fact is satisfied by the relation given in (1.8d). So, the only possibility is to find a compromise between higher value of effective mass and high mobility. Generally, materials containing elements with small electronegativity differences possess low effective mass and high mobility, whereas the opposite characteristic is shown by the narrow band gap materials. A way to satisfy this compromise is by creating materials with multiple band or multivalleys. Such structures have the effect of producing large m^* without explicitly reducing μ . For materials with multiple electronic bands, the band offset E (i.e., the energy difference between the bands) between the bands at the top of valence bands (p-type semiconductors) or the bands at the bottom of conduction bands (n-type semiconductors) should be within few $\pm k_B T$ (k_B is the Boltzmann constant) which means the energy separation is small; this leads to an effective increase in density of states, thereby increasing the effective mass. This is possible when electronic bands are effectively converged, named as band convergence, and it is an effective route to improve the power factor.

Apart from this, for semiconductors, another important relation which combines electrical conductivity (σ) with the band gap energy can be approximated as:

$$\sigma = \sigma_0 \exp \left(-\frac{E_G}{kT} \right) \quad \text{..... (1.8e)}$$

Considering the above equation, the best choice of E_G is preferable depending on the range of temperature for the applications. It is generally considered that the band gap should be of the order

of $10 k_B T$ with T being the temperature of the applications. For applications in the range 400-600°C, the optimum band gap is 0.6-0.8 eV from this estimation.

1.6.2 Thermal conductivity

Another essential factor which plays an important role in determining ZT is the thermal conductivity (κ). It has three contributing parts; the heat transport through electrons (κ_E) and the heat transport by lattice vibrations called phonons (κ_L), and the contribution by the bipolar effect (κ_{bi}), normally expressed as:

$$\kappa = \kappa_L + \kappa_E + \kappa_{bi} \quad \text{..... (1.9a)}$$

Moreover, the relation which combines the thermal conductivity originated from electrons (κ_E) with the electrical conductivity (σ) can be expressed through Wiedemann-Franz law [13], as:

$$\kappa_E = L_0 \sigma T = ne\mu L_0 T \quad \text{..... (1.9b)}$$

Where, $L_0 = \frac{\pi^2}{3} \left(\frac{k_B}{e} \right)^2$, known as Lorentz number and its value typically taken as $2.4 \times 10^{-8} \text{ J}^2 \text{K}^{-2} \text{C}^{-2}$.

Following this, by considering the presence of both κ_L and κ_E in κ , a new way to express the figure of merit value is given by:

$$ZT = \frac{S^2 / L}{1 + \frac{\kappa_L}{\kappa_E}} \quad \text{..... (1.9c)}$$

Equation (1.9b) shows that reduction in the κ_E value will further reduce the σ . So, the idea to decouple σ and κ in order to obtain maximum ZT value can come through the minimization of the lattice part of thermal conductivity (κ_L). However, the ideal situation occurs when the materials reach the condition $\frac{\kappa_L}{\kappa_E} \ll 1$ and the Seebeck coefficient alone determines the value of figure of merit.

Secondly, the bipolar effects arise due to the presence of two types of carriers and this makes hard to achieve effective thermoelectric material. It's originated from the conduction of heat from hot end to cold end even during the absence of the net current. This bipolar nature also suppresses the Seebeck coefficient by the presence of both carriers with the opposite signs of electronics charge. The bipolar thermal conductivity in semiconductors can be expressed as,

$$\kappa_{bi} = \frac{\sigma_n \sigma_p}{\sigma_n + \sigma_p} (S_p - S_n)^2 T \quad \text{..... (1.9d)}$$

Where, (σ_n, σ_p) and (S_n, S_p) are the electrical conductivities and Seebeck coefficients for electrons and holes respectively.

Thirdly, the reduction of the lattice thermal conductivity can maximize the ZT value, which is the only parameter not determined by the electronic structure. The lattice thermal conductivity based on the classical kinetic theory for any heat transport can be expressed as:

$$\kappa_{\text{lattice}} = \kappa_L = \frac{1}{3}(C_v v_s L_{\text{ph}}) \quad \text{..... (1.9e)}$$

Where, C_v is the specific heat at constant volume, v_s is the velocity of sound, L_{ph} is the mean free path of the phonons. Typically in most of the materials, at high temperatures ($T > \approx 300\text{K}$), the sound velocity and the specific heat are basically independent of temperature. Thus, the magnitude and temperature dependence of κ_L is completely determined by the mean free path of phonons. However, at very low temperature (below 40K), κ_L is determined by Debye T^3 law for C_v as ($C_v \sim T^3$) and therefore it increases with temperature. But the phonon scattering is insignificant in this temperature range because of very less excitation of number of phonons and of their long wavelengths. However, at high temperatures, i.e., above Debye temperature, ($C_v \sim \text{constant}$), so κ_L is determined by only phonon mean free path. In addition, at high temperature, κ_L has inverse dependency with temperature. Slack defined the minimum thermal conductivity (κ_{min}) as the thermal conductivity when the phonon mean free path (mfp) is limited by the interatomic distance between the atoms within the crystals. Typically, the value of κ_{min} is $\approx 0.25\text{-}0.5 \text{ Wm}^{-1}\text{K}^{-1}$ estimated by Slack, depending on the crystal structure.

1.7 Thermoelectric materials

Here, in the following sections, we mainly focus on the history and development in thermoelectric materials. In addition, we mention the strategies which can tune the ZT value towards maximum efficiency.

1.7.1 Historical background

The preliminary ideas (mentioned in section 1.2) developed by Seebeck, Peltier and Thompson become an essence concern for the upbringing of the TE materials [1-4]. At the beginning of research, the theoretical investigation for TE devices done by Edmund Altenkrich shows that metals are inefficient for thermoelectric applications [14,15]. He was the first who derive the maximum

efficiency of a thermoelectric generator in 1909 as well as the performance of a cooler by using a constant property model. Later, the actual relationship was developed into the figure of merit ZT. In 1904, several attempts were carried out to study the change of quality of thermoelectric power by magnetization with iron, cobalt, and nickel. During this period, measurement made by A Eucken gave a new strategy of reduction of thermal conductivity due to the presence of defects. However, in 1930, research interest turned towards the semiconductor based TE materials. The frontiersman behind the development of the modern theory of thermoelectricity based on semiconductors was Abram Ioffe [12]. According to his analysis, narrow gap semiconductors of post transition elements of the 5th and 6th period should be efficient for TE applications. Also, in 1954, Goldsmid and Wright find one of the best semiconductors such as Bi₂Te₃ for TE devices and identified as first generation TEs [11]. Along with these inventions, several ideas were proposed by the researchers to attain peak value of efficiency. In 1956, Ioffe [12] and his co-workers demonstrated that the ratio of thermal conductivity to the electrical conductivity could be decreased by alloying the material. Further, in 1980, Rowe and his co-workers proposed that phonon scattering at the grain boundary may improve the device efficiency [7]. In 1990's, two leading ideas emerged for increasing the ZT of TE material: PGEC concept proposed by Slack [18] and the idea of quantum confinement through nanostructuring by Dresselhaus and Hicks [136-142]. This discovery gave birth to second generation TEs in the form of complex (such as clathrates, half-Heuslers, LAST, and skutterudite compounds) and low dimension TE materials (such as, super lattices, quantum dot super-lattices, nanocomposites, and others). An overview of the whole illustration of the TE materials is shown in Figure 1-9. Now, at present, the prime idea is to develop third generation materials of higher ZT value with efficiency above 3 compare to the current value 1.5 to 2 [17,23].

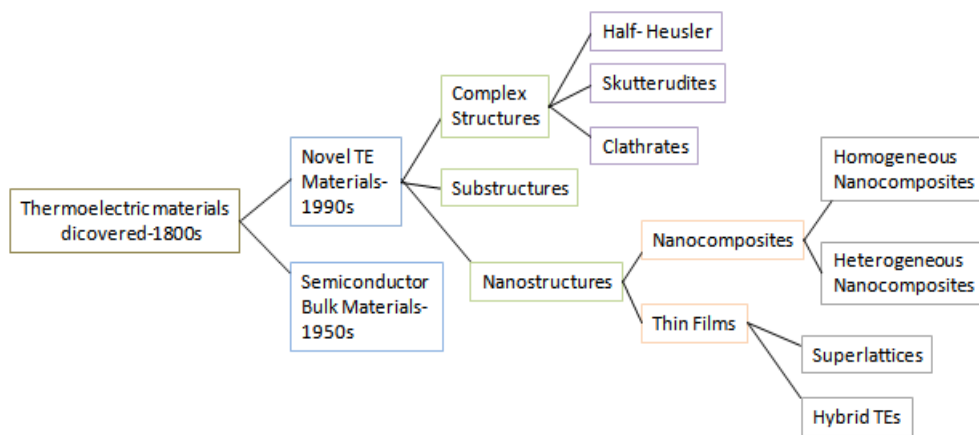


Figure 1-9: Schematic illustration of the current state of the TE materials.

1.7.2 State-of -the-art TE materials and their Figure- of -merit value

To understand the current progress in TE materials, a clear knowledge of the established state-of-the-art materials should be considered first.

1.7.2.1 Conventional materials

The traditional materials found its novel application in power generation and refrigeration over decades. But, in spite of their potential application, such contemporary TE materials exhibit rather low efficiency. So, for researchers, the key factor is to develop high performance TE materials, either by making completely new materials or through improving the properties of the existing one. Normally, TE materials are categorized on the basis of their application temperature range. A limited number of TE materials operate at low temperatures while other materials function at intermediate and high temperatures. The materials which are suitable at low temperature range can be classified as cryogenic temperature range materials. Figure 1-10 displays the ZT values of different class of TE materials with respect to their suitable temperature range for TE applications.

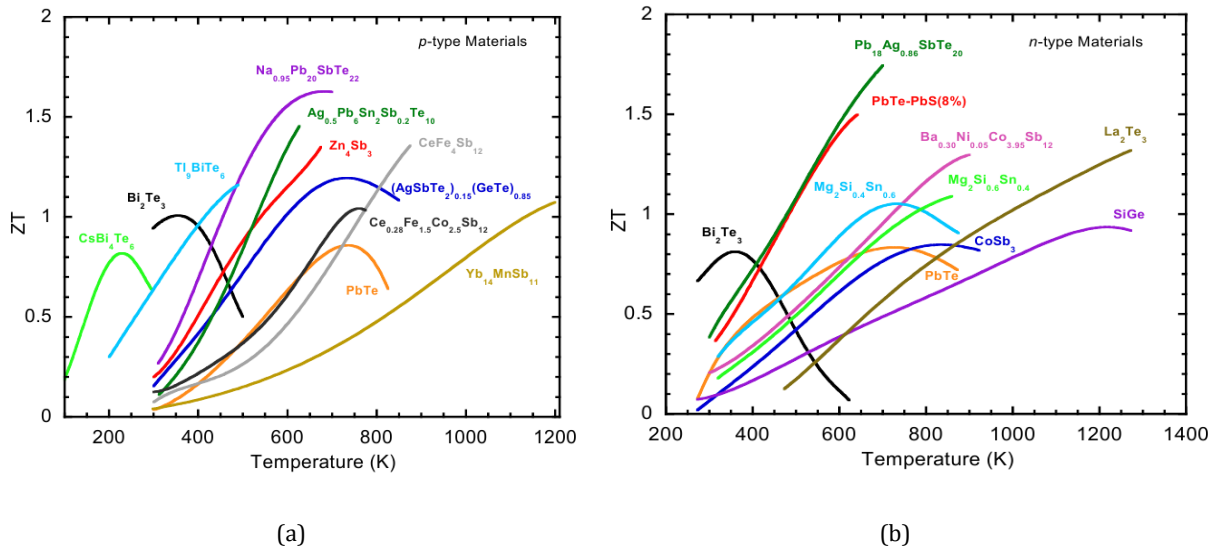


Figure 1-10: Plot of ZT versus temperature for TE materials (a) p-type and (b) n-type [17].

Most of the early TE works were based on semiconductors. The first well known paradigms that provided the basis for TE materials were Bismuth telluride (Bi_2Te_3) and lead telluride (PbTe) [39]. The compound Bi_2Te_3 has a considerable range of homogeneity, and possesses different types of conduction, namely, p or n types. It is a narrow band gap semiconductor with indirect gap of energy 0.15eV, suitable for room temperature applications. It crystallizes in a layer structure with rhombohedral-hexagonal symmetry. The maximum ZT of p-type and n-type Bi_2Te_3 crystalline materials at room temperature are about 0.75 and 0.86 and the thermal conductivity is $\sim 1.9 \text{ Wm}^{-1}\text{K}^{-1}$ [40-43]. Further investigation by Ioffe suggested that alloying allows fine tuning of the carrier concentration along with reduction of thermal conductivity. First realization of this fact was done by alloying Bi_2Te_3 with Sb_2Te_3 . The ultimate compositions obtained by taking the solid solution of Bi_2Te_3 and Sb_2Te_3 are $\text{Bi}_2\text{Te}_{2.7}\text{Se}_{0.3}$ (n-type) and $\text{Bi}_{0.5}\text{Sb}_{1.5}\text{Te}_3$ (p-type) with $\text{ZT} \approx 1$ near room temperature and they possess low value of k. All this quality makes this Bi_2Te_3 alloy suitable for TE application near room temperature such as refrigeration and waste recovery up to 200°C . Also, in the low temperature range up to 300K, Bi_2Te_3 and Sb_2Te_3 alloys have shown very descent performances [43-46]. On the other hand, for the temperature above 450K, one issue which limits the use of Bi_2Te_3 originates from its chemical instability in this temperature range.[39]

The group IV tellurides such as PbTe , GeTe , SnTe are the premiere TE materials used at mid temperature range applications (600 – 800K)[39,40,52,47]. They crystallize in a cubic rock-salt type structure. The PbTe contains lead which is one of the most useful elements in good TE materials, due to its great abundance in the Earth's crust and can be easily processed. This material has played a dominating role in TE power generation for more than 50 years. The TE properties of PbTe are of no special interest, while doping with either n- and p-type dopants can improve the TE properties. The ZT of bulk PbTe were underestimated for long time due to difficulty of measuring precisely its thermal conductivity at high temperature. After, Synder and co-workers [48] performed the measurements using advanced laser flash technique and corrected the ZT of p-type Na-doped PbTe and n-type I-doped PbTe from 0.8 and 0.7 to 1.5 and 1.4 at 750K respectively [48-50]. The solid solution was also considered as a way to obtain lower value of thermal conductivity. For instance, the formation of solid solution compositions (PbTe-SnTe) resulted in a decrease in thermal conductivity and reached the maximum ZT of 0.75 at 700K, which in turn makes PbTe a promising candidate for power generation in this temperature range [41]. Moreover, when Tl was substituted in PbTe , the large ZT value of 1.5 at 773K was obtained and increase in Seebeck coefficient compared to that of PbTe [41]. Another way of enhancement of Seebeck coefficient was obtained by tuning the energy offsets between the light and heavy valence bands in PbTe . The

valence band structure of PbTe consists of a second valence band (Σ) which lies energetically below the upper light hole band (L)[50-52], shown in Figure 1-11. The energy offset between L and Σ band is about 0.15 eV in PbTe system. If the L and Σ band edges move closer in energy, then there is a redistribution of carriers between these two bands with different effective masses. The overall effective mass can be enhanced by the carrier injections from Σ band to L band. It has been studied that the compositional alloying in the matrix could reduce the energy offsets between the L and Σ bands. Two such examples are Mn and Mg alloyed PbTe, where with increasing the solute fraction of M (i.e., Mn, Mg), both L and Σ bands lower their energies, but the L band decreases faster than the Σ band, thus the two bands get closer shown in Figure 1-11. This type of M solid solution alloying helps to raise the Seebeck coefficients value. By this alloying, high ZT of 1.6 at 700K and 2.0 at 873K was achieved for Mn and Mg alloying PbTe respectively [53,54]. Further research work has focused on improving the TE properties of PbTe by nanostructuring. At first, the formation of superlattices of alternating materials acquires interest to obtain high ZT value with reduction in phonon thermal conductivity. Harman et al. reported ZT value of 3.0 at 550K for PbTe/PbTeSe quantum dot superlattices [122], but this value has never been reproduced. Another advance work was made on PbTe through nano-inclusions to reduce the thermal conductivity [59-61]. The nano-inclusions are of two types; coherent precipitates which are slightly mismatched with the matrix and the incoherent precipitates that show a clear boundary with the host. Both of them help to reduce thermal conductivity in PbTe-based materials but they follow different mechanisms. The coherent nano-inclusions act as point defects and scatter short wavelength phonons due to their slight mismatch with the matrix. While the incoherent ones act as nanoparticles and shows a large mismatch with the matrix, results in scattering of mid to long wavelength phonons. A ZT of 1.7-1.8 for both n-type and p-type PbTe was obtained with the use of coherent nano-inclusions of AgSbTe₂ [62], NaSbTe₂ [63], and SrTe [64]. On the other hand, with incoherent nano inclusions of Sb and Ag₂Te, ZT value of 1.4-1.5 has been achieved in n-type PbTe [60,61]. Biswas et al. [65] reported the ZT of 2.2 at 915K in p-type PbTe doped with 4% SrTe. They achieved the maximum reduction in lattice thermal conductivity by improving the phonon scattering on all relevant length in a hierarchical system. Besides all this work, another route was applied in order to get low thermal conductivity, i.e., chemical doping. By doping Se into PbTe, Biswas et al. [64] found ZT of 1.8 in Na_{0.02}Pb_{0.98}Te_{0.85}Se_{0.15}. This doping helps in increasing the carrier mobility without lowering the carrier concentration due to convergence of electronic bands. Further, interesting result for PbTe nanocomposites were observed by applying wet chemical synthesis approach. For example, a synthesized core-shell [66] PbTe@PbS nanoparticle in organic solvent shows ZT value of 1.07 at

700K. But there are other chalcogenides apart from PbTe such as PbSe and PbS which possess the similar structure as PbTe. As Se and S is not very expensive in comparison to Te, so there are more opportunities to work with such materials. It was considered that the p-type PbSe would be a good TE material [67]. Some reports are there which shows ZT of 1.2 at 850 K obtained by Na doping in PbSe [58] and also with Al doping in n-type PbSe [68], ZT reached 1.3 at 850K. However, the toxicity of lead (Pb), presence of scarce and expensive elements such as tellurium, leads to the development of new materials [55].

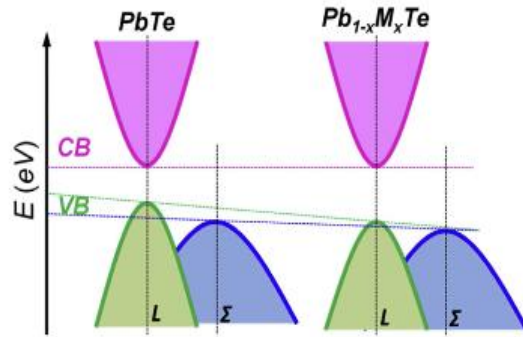


Figure 1-11: Schematic diagram showing the relative energy of the valence bands in PbTe system, with rising solid solution fraction M.[17]

The next material of interest is Si-Ge alloy. Individually, Si and Ge are not favourable as a good TE material, as they possess very high lattice thermal conductivity values; ($150 \text{ Wm}^{-1}\text{K}^{-1}$) for Si and ($63 \text{ Wm}^{-1}\text{K}^{-1}$) for Ge. The only way to overcome this barrier is by forming a solid solution of $\text{Si}_x\text{Ge}_{1-x}$. The best alloy composition is $\text{Si}_{0.7}\text{Ge}_{0.3}$ as its thermal conductivity is about $10 \text{ Wm}^{-1}\text{K}^{-1}$. Such a large reduction provides $\text{ZT} \approx 0.6-0.7$ at the elevated temperature [71,73]. Moreover, high temperature TE generators ($>900\text{K}$) use Si-Ge alloys for both n- and p-type legs. But, the ZT value of these materials is generally low, particularly for p-type. However, this alloy occupies a special place of interest to NASA for use in RTGs in deep -space probes due to its extraordinary characteristic of chemical stability at high temperature ($\sim 1200\text{K}$).

However, in the conventional materials, the cost of Germanium, toxicity of lead (Pb), presence of scarce elements such as tellurium is a limiting factor for the application. Such drawbacks put much emphasis on development of new material to solve such issues. [39]

1.7.2.2 Search for new TE materials: Novel approaches to enhance ZT

The idea behind the improvement of ZT along with the invention of new materials is described in the following paragraphs. One of the most outstanding ideas to achieve high ZT value was suggested by Slack in 1995[18]. According to him, candidates must be narrow band gap semiconductors with high mobility carriers. Slack suggested that the best TE material is the one which possesses high electronic conductivity due to its highly periodic crystal structure but low thermal conductivity which appears from the complex structural features of the crystal lattice. This approach is known as phonon-glass/electron-crystal (PGEC), more clearly as electrical properties of crystalline material and thermal properties of a glass like material. So, outstanding thermoelectric performances could be achieved by creating material using PGEC concept. The main attempts are made to reduce the thermal conductivity value to its minimum. Based on this concept, materials which are developed are explained briefly in the section below.

The novel material which is interesting to work with is clathrates. They exhibit cage like structure, thus allowing for a rattling mechanism which can reduce the thermal conductivity. This generally forms an open framework composed of tetrahedrally coordinated atoms (Al, Ga, Si, Ge, Sn) forming cages that enclose relatively large metal atoms [82]. The special features of clathrates crystal structures are their low thermal conductivity comparable with that of glasses. Here, the guest atoms trapped in the large cavities are capable of rattling and scatter the lattice phonons thus suppressing the lattice thermal conductivity. There are two main types of structures; Type I (shown in Figure 1-12) and Type II. Several compositions with these two structures are possible. They are of fundamental interest from the perspective of bonding and their physical properties. The Type I structure is represented by the general formula $X_2Y_6E_{46}$, where X and Y are alkali metal or rare earth metal often known as guest atoms that are encapsulated in two different polyhedral cages and E represents the group 14 elements such as Si, Ge or Sn [40,75,81]. On the other hand, the Type II structure is represented by the formula $X_8Y_{16}E_{136}$. It is composed of E_{20} and E_{28} cages. At the beginning of the research with this class of material, ZT values for the Type I clathrates were predicted based on DFT calculation. It has been reported that ZT values of optimised compositions $Sr_8Ga_{16}Ge_{30}$ and $Ba_8In_{16}Sn_{30}$ reach 0.5 at room temperature and 1.7 at 800K [76,80]. Further study of Type I clathrates resulted in ZT =0.7 at 700K for $Ba_8Ga_{16}Ge_{30}$ and ZT=0.87 at 870K for $Ba_8Ga_{16}Si_{30}$ respectively [78,79,80,83]. Recently, optimizing the TE properties of Type I clathrates above room temperature yielded promising results. By Czochralski methods, $Ba_8Ga_{16}Ge_{30}$ clathrates showed larger electrical conductivity 1500 to 1600S/cm at 300 to 900K and in addition thermopower of -45 to -150 μ VK⁻¹. The decrease in thermal conductivity from 1.8Wm⁻¹K⁻¹ at 300K to 1.25Wm⁻¹K⁻¹ at

900K gives ZT of 1.35 at 900K. Moreover, repeated experiments show a maximum of $ZT \approx 0.9$ at 1000K and make these clathrates promising candidates for high temperature TE applications. Only Type I clathrates were extensively studied while Type II clathrates are generally of less interest due to the difficulty to synthesize it as pure phase with defined components and in a reproducible manner. However, Type I clathrates sound more interesting compared to Type II clathrates in terms of thermal conductivity especially. But, the high cost of gallium and germanium puts a limitation for commercial application of this material.[40]

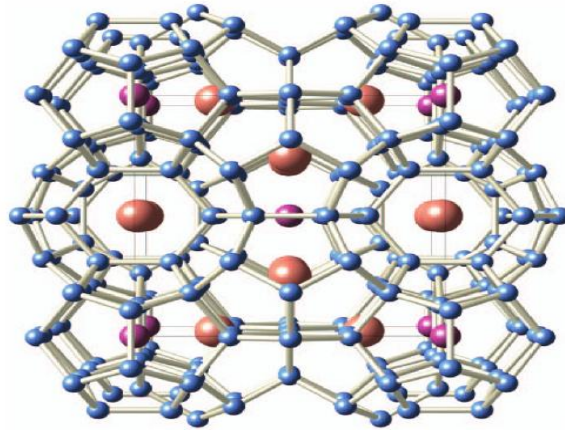


Figure 1-12: Crystal structure of the Type I clathrate. Framework atoms are shown in blue, guest atoms inside the tetrakaidecahedra are orange, and guest atoms inside the pentagonal dodecahedra are in purple [5].

The second class of compounds which are highly promising is Skutterudites. They are mainly useful for the medium temperature applications (600K-900K). Skutterudites family is composed of binary semiconducting compounds with general formula XY_3 , where X is a transition metal element Ir, Co or Rh, and Y is pnictogen element such as P, As and Sb. This family of compounds is designated with the chemical composition $CoAs_3$. The skutterudite $CoSb_3$ has a very high power factor but its lattice thermal conductivity is too high. Skutterudites can also be represented as $A_xT_4E_{12}$, where A is an alkali, alkaline-earth or rare earth metal, T is a transition metal and E is P, As or Sb. They are traditionally called filled skutterudites. In the context of doping, the general crystal structure of these materials can be best described by the formula $\square_2Co_8Sb_{24}/\square_2X_8Y_{24}$. The open square \square indicates the presence of two voids in the structure which can be filled by the rare earth atoms to help in the reduction of thermal conductivity. The other metal and pnictide sites are doped to charge compensate for the additional electrons contributed by the rare earth doping and to enhance the electronic properties. The main idea of introducing guest's atoms into the voids is to

act as strong phonon scattering centres, thus reducing the lattice thermal conductivity of these compounds, hence leading to the improvement in TE properties of skutterudites. For e.g., skutterudite antimonides possess the largest voids and are of great interest for TE application. Here are some examples of compounds which shows good value of ZT. Two compounds such as $\text{LaFe}_3\text{CoSb}_{12}$ and $\text{CeFe}_3\text{CoSb}_{12}$ which shows ZT value 1.4 above 900K, indicate successful optimization for TE power conversion applications [84,87,89]. Another e.g., is Yb partially filled skutterudites has ZT value >1 at 600K [85,91]. Recently, higher ZT values of partially filled skutterudites with small amount of Ni doping for Co such as $\text{Ba}_{0.30}\text{Ni}_{0.05}\text{Co}_{3.95}\text{Sb}_{12}$ ($\text{ZT} \approx 1.25$ at 900K) and $\text{Ca}_{0.18}\text{Ni}_{0.03}\text{Co}_{3.97}\text{Sb}_{12.4}$ ($\text{ZT} \approx 1$ at 800K) were reported [86,87,89]. All these observations motivate to do much work with this system. [39]

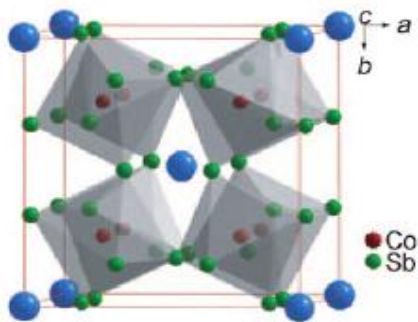


Figure 1-13: The unit cell skutterudite structure of CoSb_3 ; the transition metals (Co) are at the centre of octahedral formed by pnictogen atoms (Sb), the void cages are filled with blue spheres for clarity [41].

Apart from the materials mentioned above, other emerging materials are mentioned in the following paragraphs. Half-Heusler (HH) intermetallic alloys become profound as potential TE materials for high temperature applications owing to their high temperature stability. They can be formulated as MNiSn ($\text{M}=\text{Ti}, \text{Zr}, \text{Hf}$). They possess the MgAgAs type crystal structure which consists of three interpenetrating fcc sublattices and one vacant sub-lattice [92]. One of the structural examples of half-Heusler material is shown Figure 1-14. The general formula of HH alloys is denoted by XYZ, where X and Y are transition metals and Z is a main group element. The rock salt structure is formed by X and Z and filled with element Y at one of the two body diagonal positions, leaving the other one unoccupied. The absence of part Y provides the semiconducting properties. Heusler alloys differ from HH alloys and exhibit interesting magnetic properties and behave as metallic or half-metallic. On the other hand, HH alloys are small band gap semiconductors with a gap of ($E_g \approx 0.1\text{-}0.5\text{eV}$). The narrow band gap leads to high thermopower $\sim 100\mu\text{VK}^{-1}$ at room temperature and moderate electrical resistivities of $\sim 1\text{-}10\mu\Omega\text{m}$. They also exhibit both positive and negative thermopower value depending on doping which are necessary for potential thermoelectric

materials [40]. For e.g., Sb doped on Sn site leads to large power factor of $70\mu\text{Wm}^{-1}\text{K}^{-1}$ at 650K [99]. But unfortunately, the thermal conductivity is relatively high on the order of $10\text{-}20\text{Wm}^{-1}\text{K}^{-1}$ and results ZT of only 0.45 at 650K. The advantage of HH alloy is that they exhibit high melting points of $1100\text{-}1300^\circ\text{C}$ and zero sublimation at temperatures near 1000°C . According to the present reports, $ZT \approx 0.7$ at $T=700\text{-}800\text{K}$ is achieved in n-type Sb-doped ZrNiSn alloys [92]. However, the considerable number of substitutions and / or possible doping to improve TE properties has been studied in several HH alloys [94,95,96].

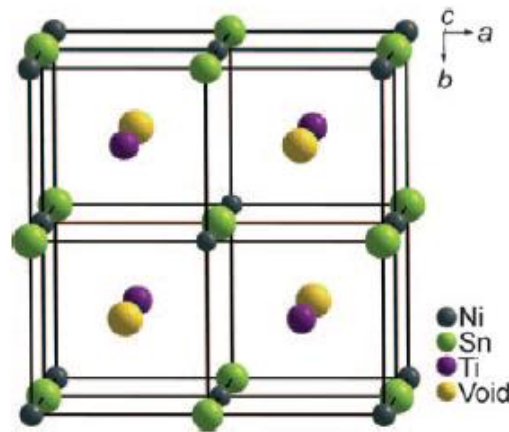


Figure 1-14: Crystal structure of Half-Heusler , TiNiSn, in a unit cell of cubic structure [41].

The next promising TE material that emerged recently for very high temperature operations is an intermetallic compound $\text{Yb}_{14}\text{MnSb}_{11}$, the structure is shown in Figure 1-15. It is characterised by its high chemical stability. This compound belongs to the Zintl family, $\text{A}_{14}\text{MPn}_{11}$, where A is an alkaline earth or rare earth metal, M is a transition or main group metal, and Pn is a pnictogen. A Zintl phase compounds contains a valence-balanced combination of both ionically and covalently bonded atoms, $\text{Yb}_{14}\text{MnSb}_{11}$ is one such example. The Yb analogue proves to be an excellent p-type TE material [100,101,102,104,105]. It crystallizes in a complex structure which in results gives low thermal conductivity and also there is flexibility in the chemical composition. Generally, this material exhibits weakly metallic or semi-metallic behaviour as a function of temperature. However, this material possesses low power factor value, but on the other hand the low thermal conductivity ($0.7\text{-}0.9\text{Wm}^{-1}\text{K}^{-1}$) in the temperature between 200-1275K gives the remarkable ZT. The ZT value increased from 0.2 at room temperature to the maximum $ZT \approx 1.3$ at 1223K [103]. To the present date, $\text{Yb}_{14}\text{MnSb}_{11}$ has the highest figure of merit value at high temperature (above 900K). In comparison with p-type Si-Ge based material whose ($ZT \approx 0.6$ at 873K), $\text{Yb}_{14}\text{MnSb}_{11}$ has

nearly twice ZT value at much higher temperature (975-1275K). So, in future, $\text{Yb}_{14}\text{MnSb}_{11}$ and its alloys will be a good replacement for Si-Ge alloy in RTG for deep space probes [41]. But, again a question of limitation comes due to the high cost of the raw materials (ytterbium).

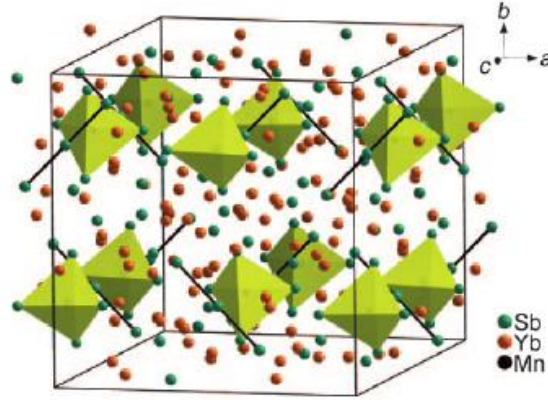


Figure 1-15: The cubic crystal structure of $\text{Yb}_{14}\text{MnSb}_{11}$ consists of one $[\text{MnSb}_4]^{9-}$ tetrahedral unit (yellow), one $[\text{Sb}_3]^{7-}$ ion (centres linked by black lines), four Sb^{3-} ions situated between the $[\text{MnSb}_4]^{9-}$ and $[\text{Sb}_3]^{7-}$ units, and 14 Yb^{2-} ions per formula [41].

Apart from this, a new class of compounds in the field of thermoelectric is the class of metal oxides. The prime advantage of these oxides is their high thermal and chemical stability in air; making them a potential candidate for the thermoelectric power generation at elevated temperature over the existing ones. Another advantage is that they are easy to synthesize compared to the conventional materials. Despite of all these positive sides, oxides acquire very little attention due to their strong ionic character, and low carrier mobility due to narrow conduction band width. Moreover, their development was limited in a long run because of their very low power factor. However, this situation changed with the introduction of new concept of nanoblock assembling of crystalline structures, capable of transforming mixed oxides into potential TEs. According to this concept, blocks responsible for either high electrical conductivity or the low thermal conductivity alternate along one of the lattice directions. This approach was first demonstrated in a strongly correlated layered oxide NaCo_2O_4 (type of metal cobaltites) [106,107,108], the crystal structure is shown in Figure 1-16. The layered NaCo_2O_4 has large thermo-power and low thermal conductivity. The thermopower and conductivity of NaCo_2O_4 single crystals reach the value $100\mu\text{VK}^{-1}$ and 5000Scm^{-1} at 300K, so in results power factor is $50\mu\text{Wcm}^{-1}\text{K}^{-2}$. Further, it has been reported that thermoelectric performances of polycrystalline sample is lower compare to the single crystal, for e.g., $\text{ZT} \approx 0.8$ at 1000K [108] for polycrystalline sample and $\text{ZT} > 1$ at 800K for single crystal. However, the limiting factor comes from its instability in air. Further study of mixed cobalt oxides

gives promising compounds including $\text{Ca}_3\text{Co}_4\text{O}_9$ [109] and $\text{Bi}_2\text{Sr}_2\text{CaCo}_2\text{O}_8$ [113] which crystallize in misfit layered structures. There are other several derivatives including the bismuth doped $\text{Ca}_3\text{Co}_4\text{O}_9$ which shows good p-type TE performance [110]. Efforts have been made to discover oxides with good n-type TE properties. Some of the n-type oxides to date are SrTiO_3 [111,112,113], doped with Nb and La shows $ZT \approx 0.3$ and 0.26 at 1000K , Al-doped ZnO [114,115,116], shows ZT value 0.3 at 1000K , n-type composite phase, Ca doped $(\text{ZnO})_3(\text{In}_2\text{O}_3)$ [117] shows the $ZT \approx 0.31$ at 1053K . But currently, the major disadvantages of using oxide materials in constructing modules are the high contact resistance at the junction of oxide/metal electrode and cracking/exfoliation during operation cycles.[41,119,120]

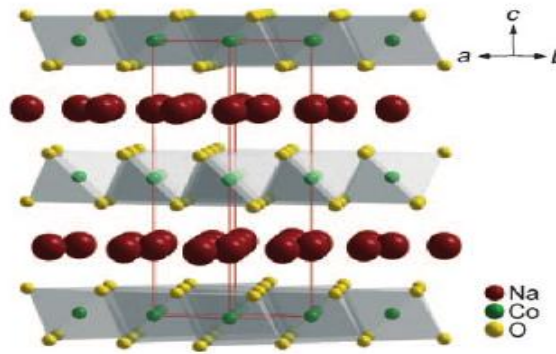


Figure 1-16: The crystal structure of NaCo_2O_4 is composed of $[\text{CoO}_2]^-$ ionic layers and Na^+ ions which occupy half of the interlayer atomic sites. The Co ions $[\text{CoO}_2]^-$ in the layers have an octahedral coordination environment and adopt the CdI_2 structure type [41].

1.7.2.3 Nanostructure materials

Introduction

So far, we have seen that due to strong interdependence of materials properties, it is hard to engineer bulk materials with high figure of merit value. Therefore, the nanostructures were developed in order to improve the overall efficiency of TE materials; due to their ability to tune material properties by reducing their size and dimensionality. The idea of selectively improving the materials properties using lower dimensional structures was pioneered by Hicks and Dresselhaus in 1993[122]. There are two prime ideas lying behind this low dimension approach. Firstly, the introduction of nanoscale constituents would further introduce the quantum confinement effects to increase the power factor, and secondly, building up of many internal interfaces which enhance the phonon scattering would be designed to reduce the thermal conductivity. Moreover, the reduction in size could introduce new physical phenomena which help the S , σ and κ to vary independently

and lead to the development of nanostructured materials with enhanced ZT. Indeed, it is believed that, if dimensionality of the material is decreased and approaches to nanometer length, then this new variable of length scale will come forward to control the material properties and thus, it is possible to cause dramatic differences in the density of electronic states as shown in Figure 1-17. [123,125].

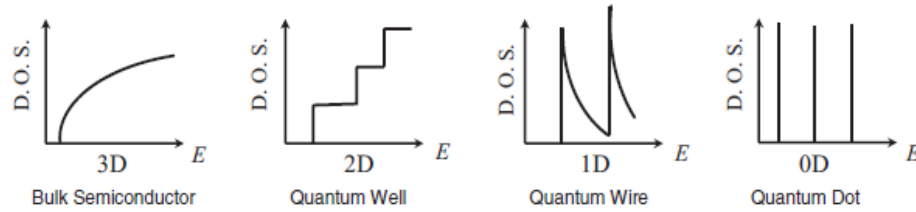


Figure 1-17: Electron density of states of a bulk semiconductor (3D), a quantum well (2D), a quantum wire (1D) and a quantum dot (0D). [125]

Earlier, Hicks and Dresselhaus theoretically showed that by using two, one or even zero-dimensional structures, one could achieve significant increase in electronic properties, in comparison to what obtained for the bulk materials [122]. Motivated by these prediction, researchers fabricated nanostructures such as 2D structures (superlattices), 1D structures (nanowires), 0D structures (quantum dots), thin film and nanocomposites materials for which the TE properties could be measured.

2D Nanostructuring: Quantum well and superlattices

The development of superlattices based on known TE materials is a promising trend in a search for the new TE materials. The formation of superlattices of alternating materials is rather simple and the impact of such structure on TE properties have been studied in various systems including $\text{Bi}_2\text{Te}_3/\text{Sb}_2\text{Te}_3$ [130], $\text{PbTe}/\text{PbSeTe}_{1-x}$ [131], $\text{Si}/\text{Si}_{1-x-y}\text{Ge}_x\text{C}_y$ [132,133], $\text{GaAs}/\text{Al}_x\text{Ga}_{1-x}\text{As}$ [134], $\text{InGa}_{1-x}\text{As}/\text{Al}_y\text{In}_x\text{Ga}_{1-y-z}\text{As}$ [135], and layered WSe_2 crystals [136]. At first, Hicks and Dresselhaus pioneered the idea that in 2D Bi_2Te_3 quantum well structures, ZT could be increased due to confinement of electronic wave function, thereby enhancing the thermopower through an increase in DOS (density of electronic states) near the Fermi level. And further, they showed that ZT in the 2D system could be tuned by varying the Bi_2Te_3 layer thickness as shown in Figure 1-18 [122]. Here, the interfaces between layers would effectively scatter phonons if the Bi_2Te_3 layer thickness was less than the phonon mfp (mean free path), which results in reduction of thermal conductivity [122,128].

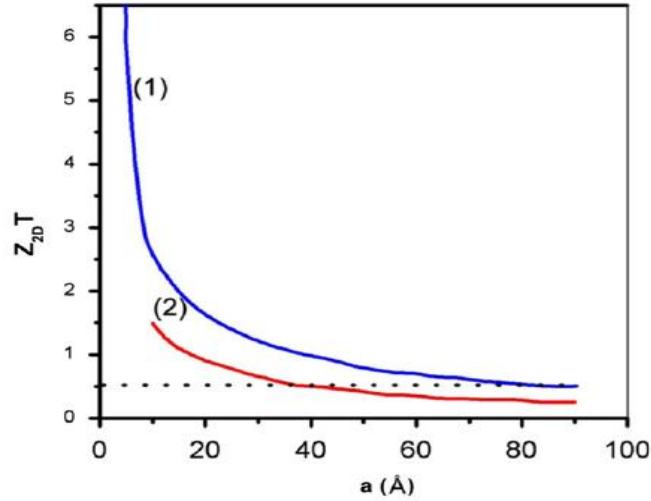


Figure 1-18: Calculated ZT as a function of layer thickness (a) in a quantum well structure for layers parallel to the a - b plane (1) and layers parallel to the a - c plane (2). The dashed line corresponds to the ZT for bulk Bi_2Te_3 . [122]

Venkatasubramanian *et al.* obtained the highest ZT of 2.4 for the Bi_2Te_3 - Sb_2Te_3 quantum well superlattices with a periodicity of 6nm [130]. Also, the lattice thermal conductivity value has been believed to be well below the alloy limit, for example a remarkably low value of $0.22 \text{ Wm}^{-1}\text{K}^{-1}$ was estimated for the Bi_2Te_3 - Sb_2Te_3 system. This was observed by using 3ω method. Another example of high ZT was reported by Harman *et al.* by producing a quantum dot superlattice structure (QDSL), namely PbTe - PbSeTe system [129,137]. Using Bi as an n-type dopant for this QDSL, ZT of 1.6 and 3.5 were obtained at 300K and 570K, respectively [138]. This large value of ZT shows that in QDSL, it is possible to have the increase thermopower and lower thermal conductivity at the same time. Moreover, enhanced TE performances were reported in 2D thin films, multiple quantum well $\text{PbTe}/\text{Pb}_{1-x}\text{Eu}_x\text{Te}$ [139], and $n\text{-PbTe}/p\text{-SnTe}/n\text{-PbTe}$ quantum well [140], AlAs/GaAs superlattice structures [134]. Earlier, these investigation were stimulated by the idea that the quantum confinement of in-plane transport could eventually enhanced the thermo power over that of the homogeneous materials, and thus leading to ten-fold increases in ZT [122]. According to Shakouri, this enhancement occurred due to the sharp characteristic observed in the DOS of quantum confined structures enabling a doping-level-tunable increase in the asymmetry between the hot and cold electron transport [141]. This results in high value of seebeck coefficient and electrical conductivity. These two dimensional TE materials could be used in small scale applications, and for electrical and optical devices [142]. But, the high cost and low scalability of thin films limits their use in large-scale power generation and heating/cooling applications. Some additional challenge may come due to parasitic heat loss from thermal conduction in the electrically

insulating layers, which may affect the efficiency of the whole quantum well devices. Also, these structures could not be used in medium or high temperature applications due to poor stability. Last, most of the highest ZT values have never been reproduced.

1D Nanostructuring: Nanowires

The second research towards low dimensionality begins with the study of quantum wires. So far, theoretical studies predict that the large ZT inside quantum wires appeared due to an additional electron confinement. Also, it is believed that an enhanced TE performance could be attained in 1D-systems due to strong confinement and phonon scattering [124]. However, some of the nanowire materials showed TE properties lower than the corresponding bulk materials. The exact reason is not well understood, but it may probably due to the limited inability to control dopant and impurity concentrations in nanowires. Further, it has also been proposed that nanotubes may possess thermal conductivity lower than nanowires due to additional phonon scattering on the inner and outer surfaces. Till date, there are many reports based on 1D material. Hochbaum *et al.*[143] showed ZT value of 0.60 at room temperature for 50 nm diameter rough silicon nanowires which represents a 60 fold increase in ZT compare to the bulk. Such enhancement in ZT value comes from the effective phonon scattering on the surface of nanowires. Boukai *et al.*[144] also reported a large ZT value of 1 at 200K for silicon nanowires with 20nm diameter due to reduction in thermal conductivity and further contribution of phonon drag to the power factor. At present, development of low cost techniques to easily integrate the nanowire arrays into TE devices is required. In these studies, the TE measurements were done using a suspended microheater platform which overcomes the difficulties in property measurement of single nanowires, nanoribbons, nanotubes and other nano-structures. In many practical applications however, arrays of nanowires are required to build up and embedded in a matrix but to have good electrical contact to all wires in the array is quite hard, having high packing densities and minimum matrix heat leakage have prevented measuring any significant enhancement in nanowire composites[145].

0D Nanostructuring : Nanodots

The next approach towards low dimension nanostructure materials is nanodots. The main idea which supports all the nanodots systems in the enhancement of TE performance is the strong decrease in lattice thermal conductivity, rather than increase in electrical power factor. Up to date, there have been many reports on nanodots including PbTe/PbSe nanodots superlattices (NDSLs), LAST-m, NaPb_mSbTe_{2+m} (SALT-m), ErAs:InGaAs, PbSnTe-PdS and Si/Ge [41]. Almost, in all of them,

the values of lattice thermal conductivity are below the alloy limit. It is interesting to note that the LAST-m system form spontaneous nanostructures from the melt during cooling. Indeed, the formation of nanoscale inclusions of minor phases was observed for the LAST system through TEM image. Similar response was shown by SALT-m system by creating Na-Sb rich clusters in the lattice. High ZT value of 1.6 at 675 K was obtained for SALT-20 system with p-type behavior [25,41]. The InGaAs:ErAs system shows a reduction in thermal conductivity value by a factor of 3 as compared to the bulk alloy. This can be clearly understood on the basis of Rayleigh scattering (d^6/λ^4), where d is the nanodot diameter and λ is the phonon wavelength. Hence, the short wavelength phonons are scattered effectively in alloys but the mid- and long- wavelength phonons travels without much scattering and while propagating they carry heat as well. But, by inclusion of nanoparticles, there is an additional scattering of mid- and long- wavelength phonons by the nanoparticles, which further helps to reduce the thermal conductivity. A schematic diagram of phonon scattering is shown in Figure 1-19 [145].

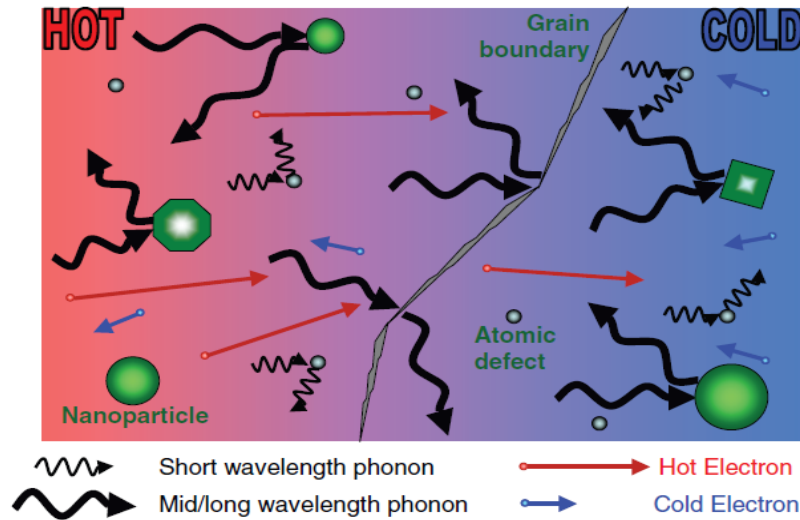


Figure 1-19: Schematic diagram illustrating various phonon scattering mechanisms within a TE material, along with electronic transport of hot and cold electrons. Atomic defects are effective at scattering the short wavelength phonons, but larger embedded nanoparticles are required to scatter mid- and long-wavelength phonons effectively. Grain boundaries can also play an effective role in scattering longer wavelength phonons.[145]

Nanocomposite Materials

The development of nanocomposites [153] is one of the potential cheap alternatives to the expensive superlattices. Nanostructured composites have been proposed to enhance ZT, by phonon scattering. Here, preferential scattering is possible, because the phonons mfps typically ranges from the single nanometers up to several micrometers, whereas the value is just a few nanometers for the carrier mfp [126]. Therefore, it is believed that the lifetime of a wide distribution of phonons could be reduced by incorporating the nanostructures covering a variety of length scales while keeping the charge transport unchanged. In this approach, nanostructuring has been made through the formation of nanometer sized polycrystalline samples, by using the various techniques such as hot pressing or spark plasma sintering of fine powders formed by grinding and milling or wet chemistry processing. Also, here the material is prepared into nanosized particles and then further hot pressed into monoliths. The main goal of designing such materials is to introduce many interfaces which will reduce the thermal conductivity. Also, they possess some advantages over other techniques which create very large grain or single crystal material, such as increased power factor due to electron filtering at grain boundaries, lower value of thermal conductivity, better mechanical properties and improved isotropy [145]. Moreover, the nanocomposites materials can easily be handled from the view point of property measurements and they can be made into desired shapes and scaled up for commercial purpose. In this system, the bulk materials acting as a host material and the nanomaterials are assembled together as nanocomposites containing assembly of nanoclusters as shown in Figure 1-20. Some examples of nanocomposite materials which have been reported with enhanced ZT are Bi_2Te_3 -based nanocomposites, PbTe -based nanocomposites and SiGe nanocomposites. Bi_2Te_3 and their nanocomposites are the best TE material at room temperature and suitable for thermo-cooling applications. A noticeable enhanced value of ZT was observed in a polycrystalline p-type $\text{Bi}_{0.5}\text{Sb}_{1.5}\text{Te}_3$ bulk alloy fabricated by hot pressing of ball-milled nanopowders. It exhibit ZT of 1.2 at room temperature and ZT of 1.4 at 373K with low value of thermal conductivity $1.0 \text{ Wm}^{-1}\text{K}^{-1}$ [147]. Further research made on p-type Bi_2Te_3 based composites shows ZT about 1.3 between 75 and 375K [154] and for n-type, the value reaches 1.04 at 398K [156]. Another report on p-type $(\text{Bi,Sb})_2\text{Te}_3$ nanocomposite fabricated by melt spinning method shows ZT of 1.56 at 300K [157]. Cao *et al.* [158] obtained a high ZT of 1.47 at 438K by applying hydrothermal synthesis process. Biswas *et al.* [159] has reported a high record value of ZT 2.2 at 915K obtained for p-type PbTe-SrTe system by nanostructuring via grain boundary phonon scattering. A significant increase in ZT was obtained in p-type SiGe nanocomposites with a peak value of 0.95 at 1173-1223K through a ball milling and hot pressing method [160]. Further, a peak ZT of 1.3 at 1173K was achieved for n-type SiGe nanocomposites [161].

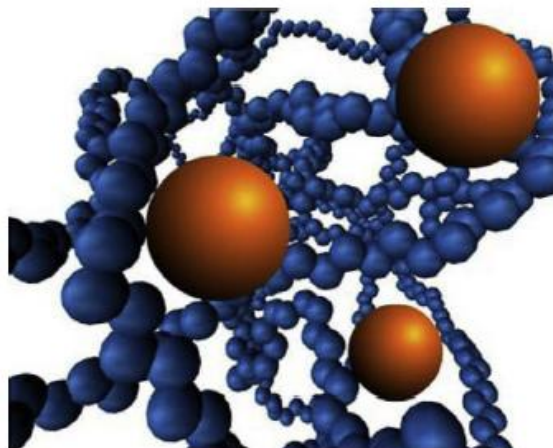


Figure 1-20: Nanocomposite thermoelectric material.[39]

It is interesting to note that the lowest thermal conductivity occurs for an amorphous material with lattice constant of the order of 0.2-0.5nm. So, far we have seen that through nanostructuring, the lowest thermal conductivity was estimated as low as $0.25 \text{ Wm}^{-1}\text{K}^{-1}$. Also, a recent report in superlattices of WSe_2/W layers shows cross plane lattice thermal conductivity values as low as $0.02 \text{ Wm}^{-1}\text{K}^{-1}$. [162,163] But the exact reason behind this is not well understood. Moreover, till date, it seems difficult to achieve ZT values of 3 or greater, as it needs a dramatic enhancement in power factor and huge reduction in thermal conductivity. So, a new physical understanding needs to be urgently developed to attain lower value of thermal conductivity. This opens a new area to do thorough investigation of TE materials. One should finally note some important points regarding the nanostructure TE materials: 1) it should be scalable, less expensive and high quality, 2) high thermal stability over an extended period of time at the temperature of the desired applications, 3) must be able to form dense compacts for device integration, 4) and finally should demonstrate enhanced ZT value in comparison to the bulk material.

1.8 Advanced Chalcogenide Compounds

Since the early stage of thermoelectric research, the materials which occupy a prominent place in the TE field are Chalcogenides. A large class of compounds categorised predominantly as semiconductors comprises of chalcogenide compounds. Some of the compounds are not ionic, but the bonding is largely covalent, an important characteristic of high mobility semiconductors.

Usually, they are air stable, melt congruently and possess high melting points. These compounds do have many promising characteristics suitable for thermoelectric applications. They show good versatility in combination with other elements. Moreover, the small variation in electronegativity between sulphur, selenium, and tellurium results in semiconductors with tunable energy gap (e.g. 0.1-0.8eV) required for thermoelectric applications over a wide range of temperature (typically 100-1400K). This gap can be tuneable by alloying.

Recent research interests to obtain high performance bulk TE materials mainly focus on ternary and quaternary chalcogenides containing heavy atoms with low dimensional or isotropic complex structure to take advantage of large carrier effective masses and low lattice thermal conductivity associated with such systems. The attractive materials of this group which become a milestone for TE applications are Bi_2Te_3 and PbTe . Today's thermoelectric cooling technology uses for e.g., Bi_2Te_3 and its solid solutions both p-type and n-type, and PbTe for power generation at intermediate temperature. In the following, we give a short overview of the properties of ternary and quaternary chalcogenides with good TE properties.

Thallium compounds: These compounds possess low thermal conductivity and high Seebeck coefficient but relatively low electrical conductivity. Since thallium (Tl) is a heavy metal, introduction of Tl into the semiconductors like Bi_2Te_3 and PbTe , decreases the thermal conductivity [165]. The promising TE materials of this group are Tl_9BiTe_6 , Tl_2SnTe_5 , and Ag_9TlTe_5 [164,165,166,167]. Such compounds belong to large group of ternary compounds. The crystal structure of compounds Tl_9BiTe_6 and Tl_2SnTe_5 belonging to this group is shown in Figure 1-21. Tl_9BiTe_6 exhibit $ZT \approx 1.2$ at 500°C with κ_L value of $\sim 0.39\text{Wm}^{-1}\text{K}^{-1}$ at 300K. And, Tl_2SnTe_5 can be optimized to get $ZT \approx 1$ at 500K, with $\kappa_L \sim 0.5\text{Wm}^{-1}\text{K}^{-1}$, whereas Ag_9TlTe_5 possess κ_L value ($\sim 0.22\text{Wm}^{-1}\text{K}^{-1}$) even lower than Tl_2SnTe_5 and have very low value of electrical resistivity too, which gives $ZT = 1.23$ at 700K. Despite of having interesting TE properties due to very low thermal conductivity, Tl-containing compounds are not well accepted for practical use. The main reason behind this rejection is because of its toxic nature and environmental issues. But they acquire a point of interest from a scientific background, to give better understanding of how to reduce thermal conductivity and optimize the ZT value.

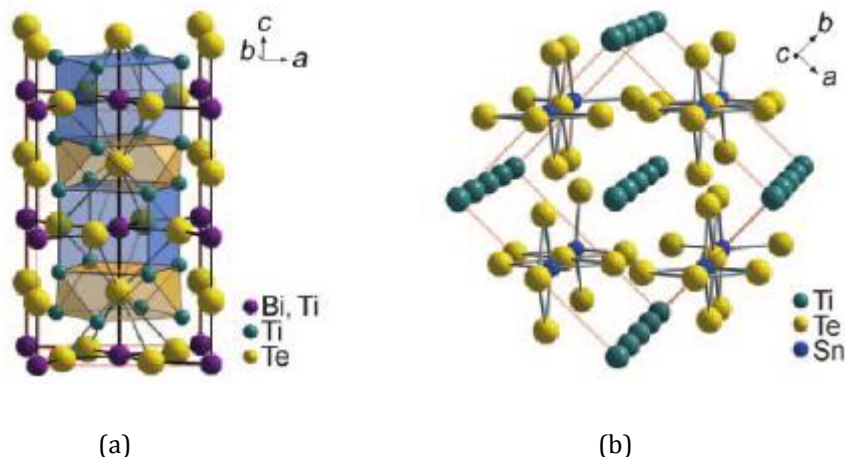


Figure 1-21: The crystal structure of Tl_9BiTe_6 ; the heavy-atom site disordered being occupied by Bi and Tl. There are two alternating cages of Tl atoms (yellow and blue). (b) The crystal structure of Tl_2SnTe_5 is composed of tetrahedral $[\text{SnTe}_4]$ units bridged by Te atoms in square-planar geometry. [41].

Alkali metal bismuth chalcogenides: Bismuth chalcogenides acquire much attention over last decades due to their potential properties in TE. In addition, there is a possible place to discover new compounds in this area. Some of the new compounds are CsBi_4Te_6 , $\text{K}_2\text{Bi}_8\text{S}_{13}$, BaBiTe_3 , $\text{Cd}_2\text{Bi}_2\text{S}_4$ and many others [41]. This type of compounds shows low thermal conductivity, high thermopower, and high electrical conductivity. The common feature of these materials is their high structural anisotropy. They possess characteristic features which can generate chemical and structural complexity, diversity and disorder, mostly desirable for good TE materials. Among this class of compounds, $\beta\text{-K}_2\text{Bi}_8\text{S}_{13}$ (structure shown in Figure 1-22a) is a promising one and shows low thermal conductivity ($\sim 1.3 \text{ Wm}^{-1}\text{K}^{-1}$) and relatively high power factor ($\approx 10 \mu\text{Wcm}^{-1}\text{K}^{-2}$) at room temperature, giving $\text{ZT} = 0.22$. CsBi_4Te_6 is another good TE material for low temperature TE applications. The crystal structure is shown in Figure 1-22 b. It can be obtained as both n-type and p-type with appropriate doping. It is sensitive to the type and level of doping element. The narrower band gap and large anisotropy in the effective mass is the main factor for the maximum ZT of this compound. For e.g., ZT value of 0.8 at 225K was reported for p-type doping of CsBi_4Te_6 with SbI_3 or Sb, this is the highest value ever seen below room temperature. But, there is no report about the reproducibility of this value. [168,169]

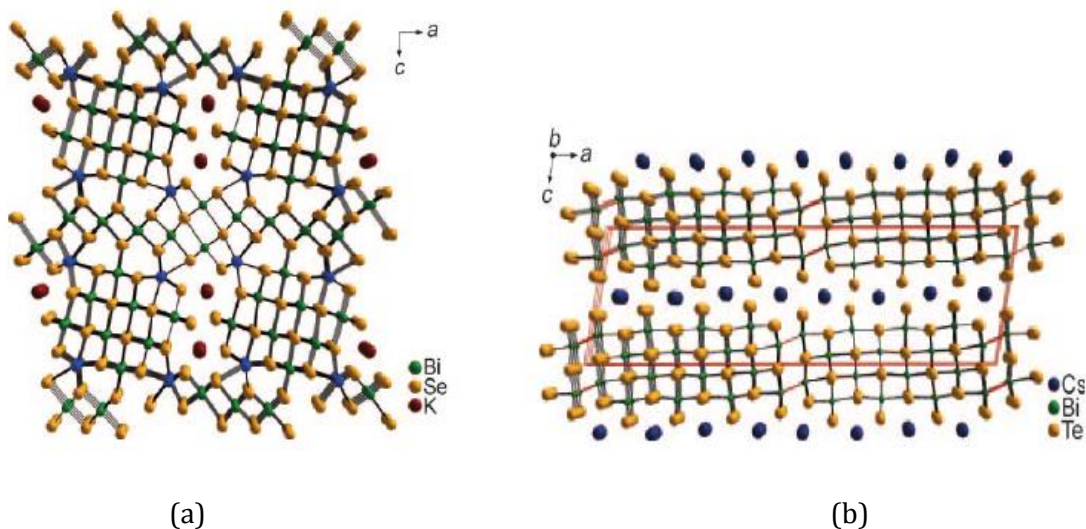


Figure 1-22: (a) Crystal structure of $\beta\text{-K}_2\text{Bi}_8\text{S}_{13}$ viewed down to the b-axis. It consists of two Bi/Se building blocks connected at the K/Bi mixed site (blue), the K atoms are in the channels and (b) crystal structure of CsBi_4Te_6 viewed down to b-axis. Cs atoms are located between NaCl-type Bi/Te layers which are composed of $[\text{Bi}_4\text{Te}_6]$ building units interconnected by Bi-Bi bonds (red) [41].

TAGS and LAST are other promising TE materials are described in the following section.

1.8.1 Chalcogenide of Type I-V-VI₂

1.8.1.1 Introduction

Ternary chalcogenide materials have drawn tremendous attention in recent years because of potential applications in photovoltaic, TE and photo-thermal areas. They have been studied in a large scale due to their optical phase-change and photovoltaic applications [170,171,172]. My Phd work is based on the solid solution of $\text{AgBiSe}_2\text{-AgBiS}_2$ belonging to this class of ternary chalcogenide materials.

1.8.1.2 Structural background

The Ternary Chalcogenide materials of type (I-V-VI₂) are based on the Ternary semiconducting compounds with general formula ABX_2 . A denotes the group I element which can be Cu, Ag or Au or alternatively an alkali metal, B denotes the group V element can be P, As, Sb or Bi, and the X represents the group VI element can be S, Se, or Te. They derive from PbX by replacing Pb^{2+} by

equal amounts of A^+ and B^+ leading to ABX_2 . They exhibit sodium chloride or rocksalt type structure. The most common examples belonging to this class of compounds are $AgSbSe_2$, $AgSbTe_2$, $AgSbS_2$, $AgBiS_2$, $AgBiSe_2$ [173,174,175,176].

1.8.1.3 Paradigm of materials under this category of I-V-VI₂

Firstly, this paragraph focuses on commonly known Ag-Sb based materials namely $AgSbTe_2$ [178,180,183,184] and $AgSbSe_2$ [191,192]. Both $AgSbTe_2$ and $AgSbSe_2$ were synthesized in the late 1950s and believed to have a rocksalt NaCl type (Fm-3m) structure shown in Figure 1-23 with random distribution of Ag and Sb cations occupying the Na site whereas Te or Se is located at the Cl position [177,189,190]. They are isostructural compounds and known as a narrow-gap semiconductor. Alloys of both compounds received interest due to their TE, optical and electronic properties. In addition, they are phase change materials, so can be used as a switching medium in rewritable optical memories.

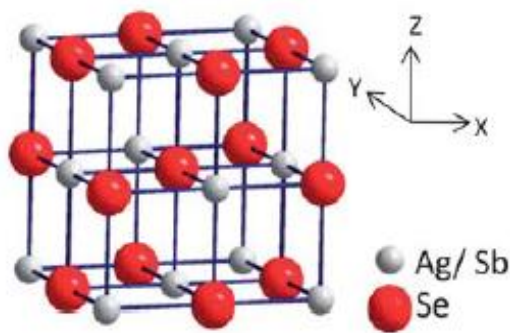


Figure 1-23: Crystal structure of 1-V-VI₂ compound $AgSbSe_2$ [174].

$AgSbTe_2$ is a good TE material and constituent for a number of high-temperature high-performance thermoelectric. The cubic $AgSbTe_2$ is a very promising p-type TE material for the thermal energy conversion at the 500-800K temperature range. This compound is meta-stable at low temperatures; but due to the thermodynamic instability below 360°C, it slowly decomposes into secondary phases Ag_2Te and Sb_2Te_3 , and this issues limits its application area. So, most of the samples of $AgSbTe_2$ may contains three-phase mixtures. So, to stabilize the NaCl structure, alloying of $AgSbTe_2$ with other compounds (for ex., TAGS alloys) is considered. This class of compounds are well-known owing to their very low lattice thermal conductivity $<1W/mK$. For ex., $AgSbTe_2$ has a

value of the order of $\kappa \sim 0.63 \text{ W/mK}$ and similarly low values were measured on other I-V-VI₂ compounds. The low κ value leads to high ZT values of 1.6 and 0.4 at 700K for AgSbTe₂ and AgSbSe₂ respectively. In the rocksalt I-V-VI₂ semiconductors, the external *s* electrons and part of the *p* electrons are non-bonding and are believed to form a shell of relatively large radius. This is the fundamental reason for the large anharmonicity of the bonds in this group of materials and that leads to low lattice thermal conductivity. For example, the valence electronic configuration of Sb in AgSbSe₂ is 5s²5p³, where only 5p³ electrons take part in bond formation with the Se valence electrons while the 5s² electrons of Sb form a lone pair. The origin of anharmonicity in Sb-Se bond is the electrostatic repulsion between the stereochemically active lone pair of Sb and the valence bonding charge of Se. The schematic representation of harmonicity and anharmonicity is shown in Figure 1-24. At first, the perfect harmonic bonds in one-dimension are shown in Figure 1-24a. In this case, the force to which the atom is subjected is proportional to its displacement from equilibrium position, and the proportionality constant is the spring constant or stiffness. While in Figure 1-24b, for the anharmonic system, the spring constant does not remain constant with increasing atom displacements, which has a strong effect when two phonons run into each other. The first phonon changes the value of spring constant seen by the second one. Thus, the second one runs into a medium with modified elastic properties. The anharmonicity results in enhanced phonon-phonon scattering which reduces the κ_{lat} value. The strength of anharmonicity is measured by the factor known as Gruneisen parameter γ expressed as $\gamma = 3\beta B V_m / C_v$, where β is the volume thermal expansion coefficient, *B* is the isothermal bulk modulus, *C_v* is the isochoric specific heat per mole, and *V_m* is the molar volume. The larger the value of γ , the stronger is the phonon scattering. The low thermal conductivity value of AgSbTe₂ and AgSbSe₂ are expected to originate from strong anharmonicity of their chemical bonds express by large Gruneisen parameters (2.05 and 3.5) for AgSbTe₂ and AgSbSe₂ respectively.

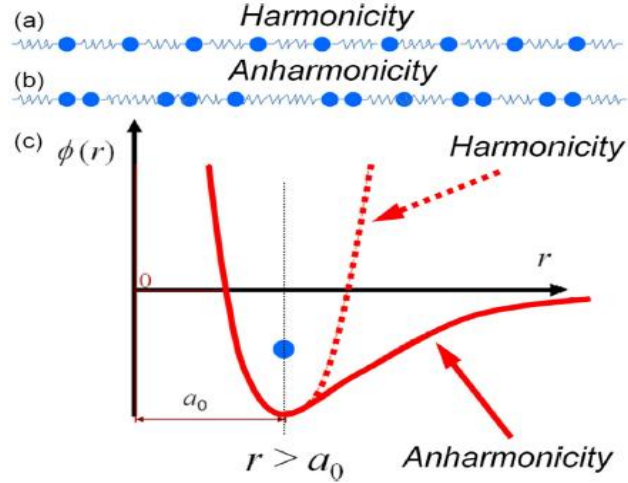


Figure 1-24: The schematic representation of (a) harmonicity, (b) anharmonicity and (c) shows the balance phonon transport in harmonicity and an imbalance phonon transport in anharmonicity [17].

Recent studies have been made to enhance the thermoelectric performance of AgSbTe_2 and AgSbSe_2 materials by tuning their electrical and thermal properties through doping or substitution [193]. Some of the examples are given here: For AgSbTe_2 , the TE performance is greatly improved by Na doping on p-type AgSbTe_2 , ZT of 1.50 is reached at 570K for $\text{Ag}_{0.99}\text{Na}_{0.01}\text{SbTe}_{2.02}$ sample [194]; the effect of Bi (bismuth) doping on p-type AgSbTe_2 leads to ZT value ~ 1.0 at 570K and low $\kappa \sim 0.48 \text{ W/mK}$ is obtained for $\text{AgBi}_{0.05}\text{Sb}_{0.95}\text{Te}_2$ material, suitable for mid-temperature range TE applications [195]; Se (selenium) doping on p-type AgSbTe_2 with large electrical conductivity and low value of κ give ZT of 1.37 at 565K [196]; with Mn-doped p-type AgSbTe_2 compounds, ZT of 1.2 at 573K is attained for the sample $\text{Ag}_{0.9}\text{SbMn}_{0.1}\text{Te}_{2.05}$ [197]; Sn doped AgSbTe_2 , was reported to achieved high ZT ~ 1.1 at 600K ; In p-type doping results in enhanced power factor and highest ZT=1.35 is obtained for $\text{Ag}(\text{Sb}_{0.97}\text{In}_{0.03})\text{Te}_2$ compound at 650K, good for the applications in the intermediate temperature range[199]. The best bulk nanocomposite material based on p-type AgSbTe_2 is one of the TE materials which form spontaneously nanostructures without the need for artificial nanostructuring [186,187]. Moreover, there are reports on effect of natural formation of nanoscale impurities on matrix, and their influence on the improvement of ZT in bulk nanostructured AgSbTe_2 come from the very large reduction in thermal conductivity. In addition, here are some examples of doping for AgSbSe_2 . Na doping in AgSbSe_2 improves the power factor and decreases the thermal conductivity to a lower value. The ZT of 0.92 is achieved for $\text{AgSb}_{0.99}\text{Na}_{0.01}\text{Se}_2$ composition [203]. Recently, a small amount of metal ion doping (Pb^{2+} , Cd^{2+} , Zn^{2+} or Bi^{3+}) in single phase p-type AgSbSe_2 enhanced the electrical transport properties, leading to a ZT

value above unity [204,205,206]. Even with Tin doping, highest ZT value of 1.21 at 660K is obtained for $\text{AgSb}_{0.99}\text{Sn}_{0.01}\text{Se}_2$ material [207]. Moreover, (Mg^{2+} and Ba^{2+}) doping on p-type AgSbSe_2 leads $\text{ZT} \sim 1$ at 673K for $\text{AgSb}_{0.98}\text{Mg}_{0.02}\text{Se}_2$ and $\text{AgSb}_{0.98}\text{Ba}_{0.02}\text{Se}_2$ samples, making the AgSbSe_2 suitable for medium-temperature power generation applications [208]. Further, with carrier engineering and nanostructuring in AgSbSe_2 , maximum ZT of ~ 1.1 at 635K is obtained in $\text{AgSbSe}_2\text{-ZnSe}$, higher than the value obtained for the pristine AgSbSe_2 [205]. Moreover, the nanostructure of the composites SnTe-AgSbTe_2 prepared by the zone melting method also give relatively high value ZT of 0.92 at 820K with low lattice thermal conductivity ~ 0.6 W/mK at 820K due to the intense scattering of phonon [201]. Here, most of the results are based on p-type compounds and the n-type ones are rather scarce in this family.

Secondly, here in we describe about the alloying approach which is expected as one of the way to achieve high thermoelectric performance. Two such pseudo-binary alloys LAST and TAGS are described here. AgSbTe_2 is the main constituent of this two high-performance class of TE materials known as $(\text{AgSbTe}_2)_{1-x}(\text{GeTe})_x$ (TAGS) and $(\text{AgSbTe}_2)_{1-x}(\text{PbTe})_x$ (LAST). The ZT value can be controlled by changing the x (concentration of GeTe or PbTe). They have been studied since 1950s.

The solid solutions of GeTe with AgSbTe_2 give alloys of the form $(\text{AgSbTe}_2)_{1-x}(\text{GeTe})_x$ known as TAGS. The TAGS system undergoes a polymorphic transformation in the structure from low-temperature rhombohedral to a high temperature NaCl-type cubic structure (Fm-3m) [210,211,212]. The transport properties vary smoothly, with the variation in composition from AgSbTe_2 to GeTe in the solid solution. This material system possess combination of high electrical conductivity, Seebeck coefficient and extremely low lattice thermal conductivity ($\kappa \sim 0.3$ W/mK) on GeTe-rich side, especially for TAGS-80 and TAGS-85; this contributes to high thermoelectric performance. Before, lattice strain was considered to be the only reason of low κ value but recent work suggests that the presence of twin-boundary defects could be the reason for this minimum value. TAGS is one of the first TE material which possesses $\text{ZT} > 1$ at high temperature. Only the p-type alloy $(\text{GeTe})_{0.85}(\text{AgSbTe}_2)_{0.15}$, commonly referred as TAGS-m, (m represents the mole percent of GeTe), has ZT greater than 1.2 around 400K; and it has been successfully used in long -life TEG. Further, optimization resulted in high ZT value of approximately 1.4 and 1.5 at 750K for m=80 and m=85 respectively, which further triggered the studies on GeTe-rich compositions. Even though, TAGS-80 compositions [213, 214] possess high ZT value 1.7, but due to its stability problem TAGS-85 was preferred for space applications. Since 1970s, TAGS-85 has been used in NASA missions. However, again due to high temperature stability issues, these compositions are not currently

favoured in TE devices. Also, its application areas are limited due to their high sublimation rate, high cost of germanium and the presence of a low temperature phase transition; this is an issue in case of thermal cycling but not a problem for space applications.

LAST is a solid solution between NaCl based isostructural compounds PbTe and AgSbTe₂. This alloy AgPb_mSbTe_{m+2} or LAST-m material is the first system which achieve ZT>1 from the combination of PbTe and AgSbTe₂ with p-type properties [217]. A large number of possible compositions can be developed by changing m. It exhibits a very low thermal conductivity leading to high ZT value. The LAST-m system; (LAST-10) gives ZT~1.2 and (m≈18-22) system shows high power factor with ZT≈1.7 at approximately 700K. At present, the highest reported ZT_{max} is 2.2 at 800K. Interesting feature of this material is that they are thermally stable up to their melting point >1200K. The LAST-m system is an interesting bulk-grown material that spontaneously forms nanostructures during cooling from the melt. Moreover, recent studies shows the presence of nanoclusions in LAST material which lead to the net enhancement of ZT. But, due to the complex nature of phase diagram, TE properties of these materials are highly sensitive to the synthesis conditions and small changes in chemical compositions. Moreover, applications are limited due to the inhomogeneity and thermodynamic instability; as a result they lose excellent TE properties at high temperatures.

To summarise, only p-type compounds are found in these two families, and severe issues limit their potential for wide scale applications [217,218,219].

Thirdly, we describe about the research works on Ag-Bi based materials such as AgBiSe₂, AgBiS₂. In the early 1960s, the phase diagram of AgBiSe₂/AgBiS₂ [230] was first mentioned by Wernick shown in Figure 1-25. But the published results were not very precise and also contained made with very few data sets.

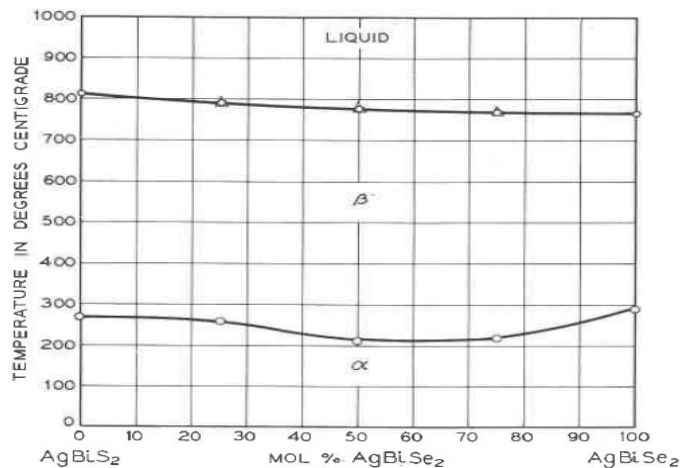


Figure 1-25: The AgBiSe_2 - AgBiSe_2 system [230].

Later, in 1965, Geller and Wernick showed that AgBiSe_2 undergoes a transformation from hexagonal to rhombohedral upon heating and again further heating transforms into the NaCl structure. In addition, they also proved that the high temperature state of AgBiSe_2 and AgBiSe_2 forms a disordered NaCl type structure in which Ag and Bi atoms are randomly distributed on Na sites and the Se or S atoms are present on Cl sites. The temperature dependent structural evolution of AgBiSe_2 is shown in Figure 1-26; at room temperature, it crystallizes in the hexagonal phase, then to rhombohedral phase around 460K and finally to cubic phase at 580K. The similar phase changing behaviour of AgBiSe_2 was also reported by other research groups which are in agreement with previously reported structural phase transition. Previous work made on AgBiSe_2 nanoplatelet prepared by chemical synthesis shows that it exhibits very low lattice thermal conductivity with p-type semiconducting behavior.

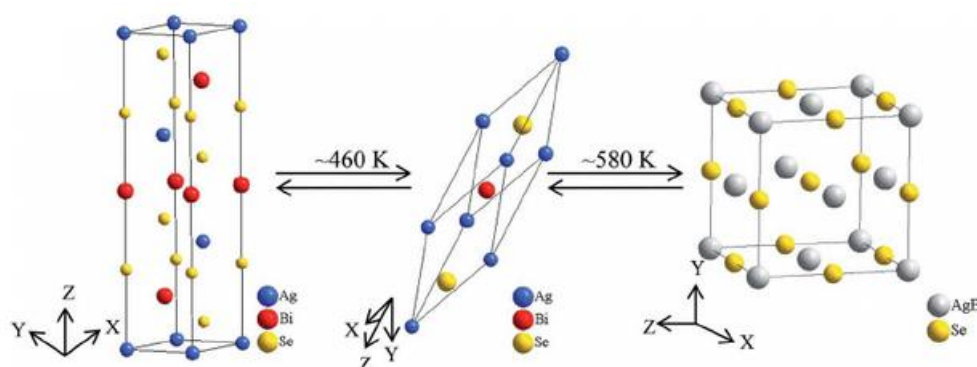


Figure 1-26: Temperature dependent crystal structure evolution of AgBiSe_2 . [220]

Moreover, very high ZT value 1.5 at 700K and reversible p-n-p semiconducting switching were achieved in chalcogenide AgBiSe_2 , during the continuous phase transition [223]. Here, in this report, unexpected properties were obtained due to the potential bimetal atoms exchange during the phase transition. The high ZT value was reached due to the full disordering of Ag/Bi atoms in high temperature cubic lattice; as it was supposed to cause a strong anharmonicity of chemical bond which results in low lattice thermal conductivity, and simultaneous rise in electrical conductivity. The Ag-Bi atoms exchange during the phase transition allowed AgBiSe_2 to switch reversibly between p- and n- type conduction. At first, the AgBiSe_2 nanocrystals were synthesized through colloidal method and structural characterization was done using XRD, Raman spectroscopy, TGA and DSC. The structural study obeys the continuous phase transition property of

this compound. The thermoelectric properties of AgBiSe₂ nanocrystals samples were measured, shown in Figure 1-27. In this figure, a profound peak in the seebeck coefficient with two changes in the sign of the value was observed, indicating both p- and n-type conduction. Moreover, the increase in σ value and decrease in κ value with increasing temperature around 583K clearly reflect the phase transition behavior and increases the ZT value.

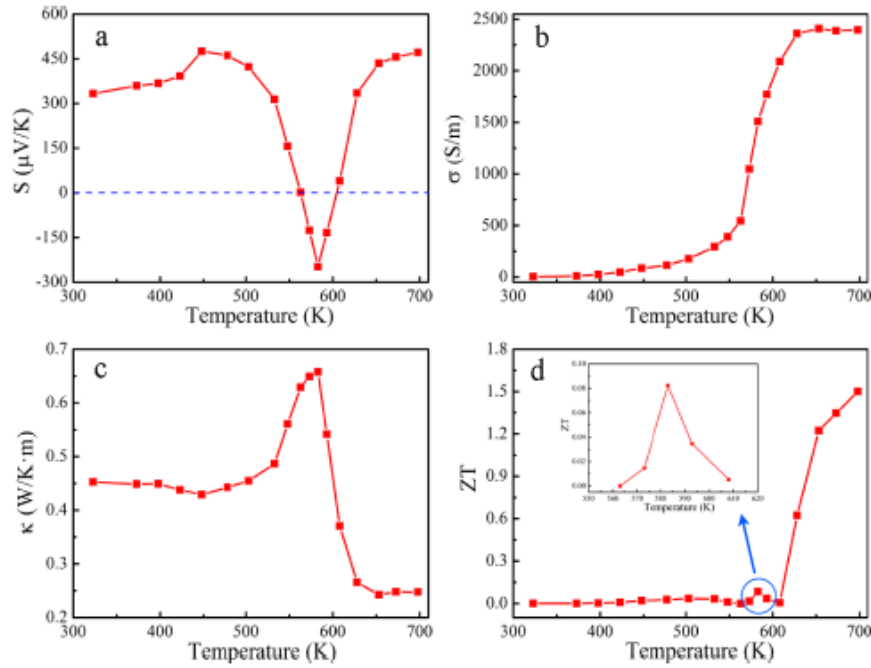


Figure 1-27: Temperature dependence of S , σ , κ , and ZT [223].

However, the results obtained in the laboratory before the beginning of this thesis were not consistent with these reports, as pristine AgBiSe₂ prepared by solid-state synthesis was found to be n-type. Also, it was shown that the type of carriers can be tuned from intrinsic n-type to p-type by Pb doping and the TE properties of n-type AgBiSe₂ were improved by Nb doping due to increased carrier concentration [222]. Here, in this report, all the samples were synthesized using solid state method and were characterized using XRD and DSC. The PXRD results obtained is shown in Figure 1-28, is in agreement with the results obtained in earlier reports.

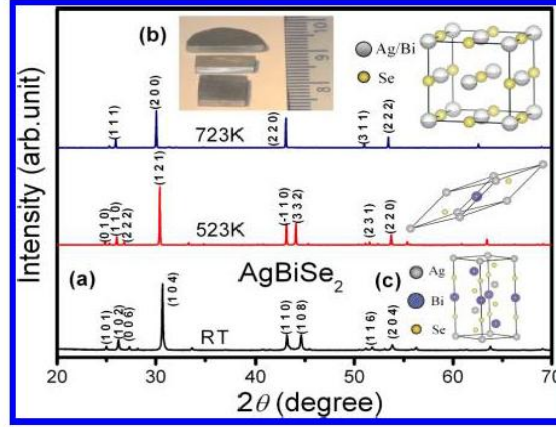


Figure 1-28: PXRD patterns of pristine AgBiSe_2 ; showing the structural phase transition from hexagonal to rhombohedral to cubic [222].

The temperature dependence of ρ and S for the Pb-doped and Nb-doped AgBiSe_2 samples and finally the λ and ZT for Nb doped sample are shown in Figure 1-29. This figure firstly shows that Pb^{2+} doping at Bi^{3+} sites in n-type pristine AgBiSe_2 results in decrease in electron concentration and increase in both ρ and $|S|$. Further, when Pb^{2+} concentration increased above the intrinsic electron concentration, the compounds switch from n-type to p-type. And, further increase in Pb^{2+} results in increasing hole concentration, thereby decreasing the ρ and S value. So, this shows a clear switching from n-type to p-type conduction of AgBiSe_2 through Pb doping. This switching of carrier type was also verified with Hall effect measurements. Secondly, in regards to the Nb fraction dependence of the transport properties, ρ and $|S|$ both decreases monotonically with increasing Nb concentration for the entire temperature range. And the value of thermal conductivity also increases with increasing Nb percentage due to the increase in electronic contribution. This properties leads to a very low thermal conductivity (0.7W/mK) and peak ZT value 1 at 773 K for the composition $\text{Ag}_{0.96}\text{Nb}_{0.04}\text{BiSe}_2$, makes it a promising n-type TE material for mid-temperature applications.

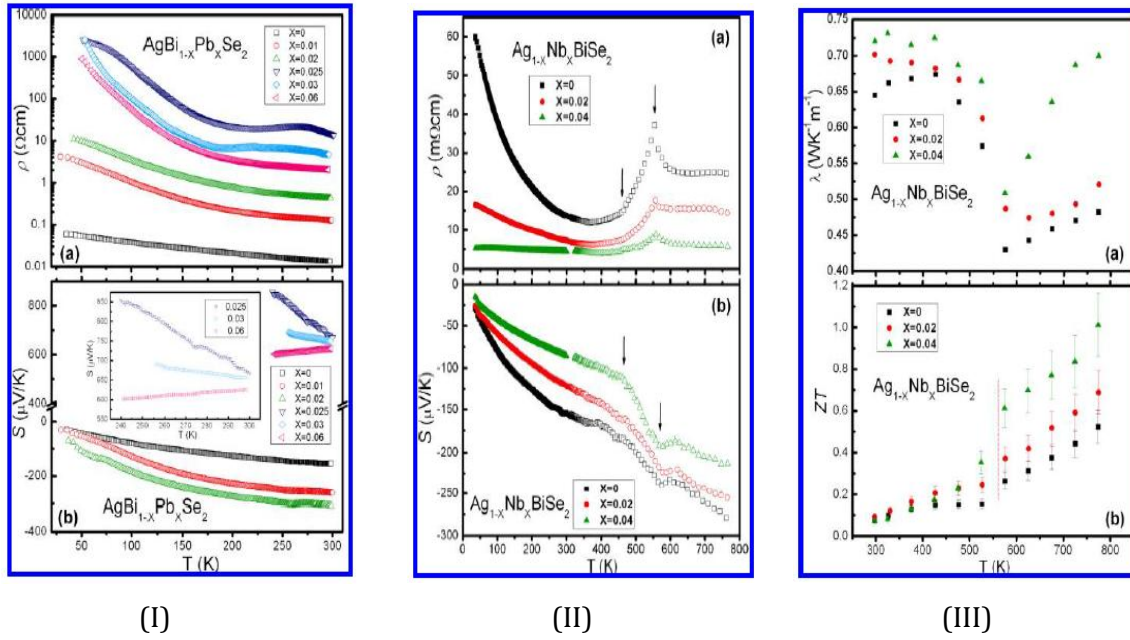


Figure 1-29: Temperature dependence of ρ and S for (I) $\text{AgBi}_{1-x}\text{Pb}_x\text{Se}_2$ from 20-300K, (II) $\text{Ag}_{1-x}\text{Nb}_x\text{BiSe}_2$ from 20-773K, and (III) λ and ZT for $\text{Ag}_{1-x}\text{Nb}_x\text{BiSe}_2$ from 300-773K [222].

Further research was carried out on improving the TE performance of AgBiSe_2 through doping. The aliovalent halide ion doping (Cl/Br/I) on n-type bulk AgBiSe_2 prove to be beneficial [220]; as the bond anharmonicity and effective phonon scattering results in low value of lattice thermal conductivity $\sim 0.27 \text{ W/mK}$ at 810 K and a high ZT value of ~ 0.9 at $\sim 810 \text{ K}$ was obtained for the $\text{AgBiSe}_{1.98}\text{Cl}_{0.02}$ sample. Here, the materials were synthesized using simple solid state method and were characterized using PXRD. This also shows the similar structural phase transition of AgBiSe_2 as mentioned earlier, and n-type behavior in pristine AgBiSe_2 . Temperature dependent thermoelectric properties of pristine AgBiSe_2 and doped samples were shown in Figure 1-30. From this Figure 1-30, it is evidenced that metal to semiconductor type transition occurred during rhombohedral to cubic phase transformation in halogen doped AgBiSe_2 . The halogen dopants effectively enhanced the electrical conductivity of AgBiSe_2 by doping electrons in the conduction band. Moreover, the combination of high value of S and σ results in increase in power factor at high temperature 810K, as shown in the figure. All such factors along with low κ_{lat} value obtained for the sample $\text{AgBiSe}_{1.98}\text{Cl}_{0.02}$ make it a promising n-type TE material suitable for mid-temperature applications.

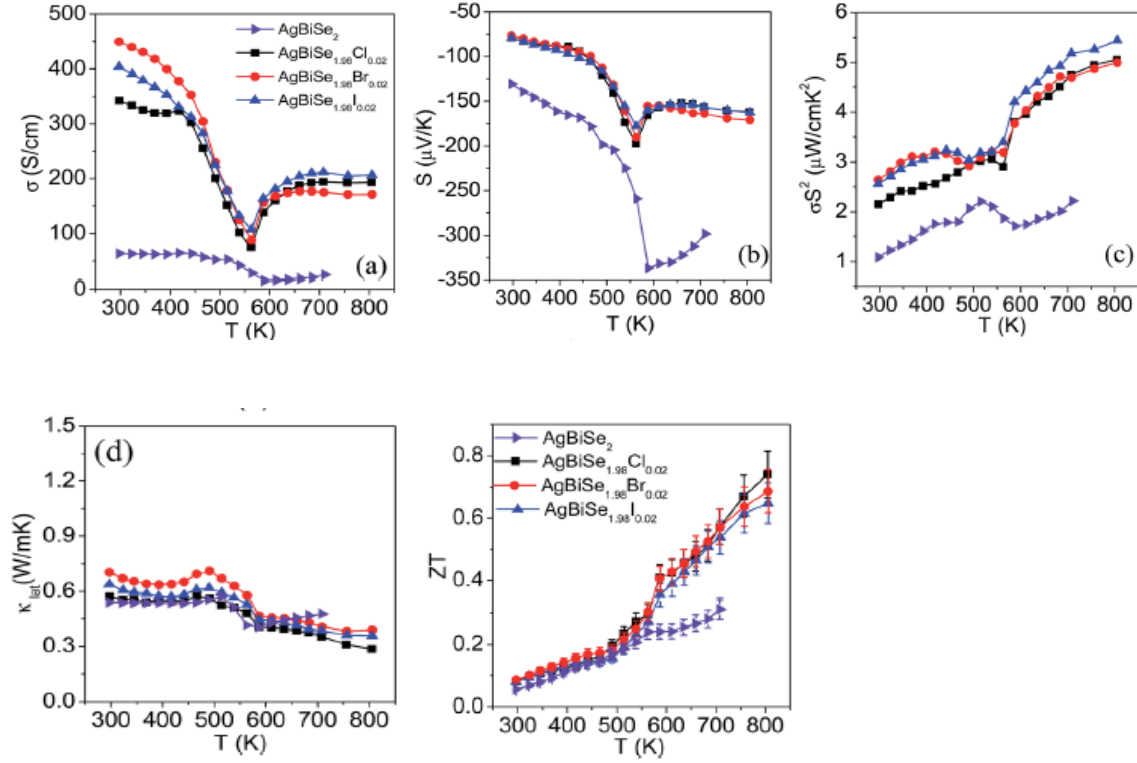


Figure 1-30: Temperature dependent (a) electrical conductivity (σ), (b) Seebeck coefficient (S), and (c) Power factor (σS^2), (d) lattice thermal conductivity (κ_{lat}) and finally ZT of AgBiSe_2 and doped samples [220].

AgBiSe_2 is one of the less explored member of the I-V-VI₂ family, but it acquires important applications in the field of non-linear optoelectronic, TE and in optical media. So far, there were few reports on AgBiSe_2 based on different synthesis techniques, whereas, the structural characteristic was given by Wernick in 1960s. At room temperature, AgBiSe_2 crystallizes in hexagonal phase and with increase in temperature, it transforms to the cubic rocksalt structure (shown in Figure 1-31) but no other attempt was made to prove the existence of intermediate phase similarly to AgBiSe_2 . Recently made study on AgBiSe_2 nanocrystal shows a extremely low value of $\kappa \sim 0.4\text{-}0.5 \text{ W/mK}$ in 300-850K range and ZT value of ~ 0.2 at 810K. The low κ value occurs due to strong anharmonicity of Bi-S bonds and effective phonon scattering. Till date, no doping study was made on this compound [224]

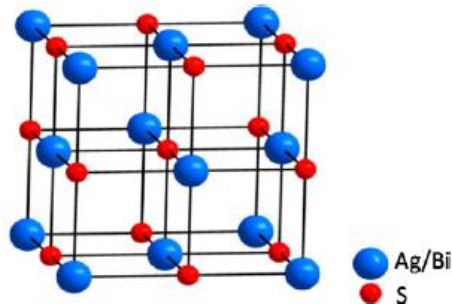


Figure 1-31: Crystal structure of high temperature cubic phase of AgBiS_2 [224]

Other I-V-VI₂ compounds were also synthesized and investigated, but there are not many reports till date. For example, AgSbS_2 is used for technical and device applications. It is considered to be an excellent candidate for photovoltaic, solar cells and optical frequency converters in solid-state laser systems. A detailed study of electronic and optical properties of this material was reported recently. Alloy with AgBiTe_2 and SnTe attained a low k value of $\sim 0.7 \text{ W/mK}$ at $\sim 750 \text{ K}$. Consequently, a high ZT value of ~ 1.1 at 775 K is achieved for $\text{AgSn}_x\text{BiTe}_{x+2}$ ($x=15$), which makes it a Pb-free material for TE power generation.[225,226]

1.9 Conclusion

So far, we have seen a strong literature background indicating the I-V-VI₂ family of compounds could be a good candidate for TE applications. Researchers put much emphasis on Ag-Sb based I-V-VI₂ materials in comparison to Ag-Bi based compounds but there are some good results reported on AgBiSe_2 materials till date. It can show both n and p type semiconducting behavior which is valuable for TE leg. Such remarks suggest that it is noteworthy to do more investigation on this compound. The specific objectives of this thesis are mainly focused on analyzing the structure and the phase transition of the solid solution of AgBiSe_2 - AgBiS_2 . According to the literature, the cubic I-V-VI₂ compounds exhibit very low thermal conductivity due to strong anharmonicity. So, the idea of obtaining the cubic phase is of prime interest. The solid solution or substitution or doping may be a potential route to suppress the phase transition, which is also an important factor to count for TE application. Indeed, the phase transition in material is detrimental for application purpose, as thermal cycling of the modules would damage the TE legs. So a better understanding and a proper idea is required to suppress it.

Chapter 2

Experimental methods

2.1 Motivation and organization of this chapter

This chapter contains the relevant information about the synthesis methods and the useful experimental techniques for the characterizations. The whole chapter is separated into two parts, to give a clear overview to the readers. The first half mainly depicts the details of the synthesis steps and the second half portrays the techniques that are adapted for both the structural and transport property measurement.

2.2 Synthesis of composition (solid solution $\text{AgBiSe}_2\text{-AgBiS}_2$)

The synthesis of the samples of the solid solution corresponding to the compositions $\text{AgBiSe}_{2-x}\text{S}_x$ is one of the tasks of our project. Here, we present the technique and the instruments used for our purpose.

2.2.1 Method, instruments and raw materials used for synthesis

In the thermoelectric field, researchers use different techniques to produce thermoelectric materials. The final products of different systems are composed of different elements, which further vary in their melting points. So, by taking into account such consideration, various methods are applicable for synthesis purpose. From technological point of view, thermoelectric materials can be classified into three groups: low temperature with melting point $500\text{-}700^\circ\text{C}$; mid-range with melting point $700\text{-}1000^\circ\text{C}$; and high melting point temperature greater than 1350°C . So, the right selection of temperature is one of crucial part of synthesis. In our case also, temperature and time of annealing is a major factor, as it will be seen in chapter 3.

To begin with, our synthesis route follows the idea of conventional solid state chemistry techniques. The whole synthesis process was carried out by considering the melting point of Ag (961.8°C), Bi (271.4°C), Se (220.8°C) and S (115.2°C), which are our prime raw materials. In brief, the synthesis process combines the preparation of compounds belonging to the solid solution of $\text{AgBiSe}_2\text{-AgBiS}_2$ using glove box, further sealing of samples inside silica tubes using blow torch and finally the heat treatments inside the furnace. Each of these synthesis steps will be described in details in the following paragraphs.

Initially, the starting materials (listed in Table 2) were collected and the whole preparation was done inside glove box. The basic precursors used were Silver (Ag), Bismuth (Bi), Selenium (Se) and Sulfur (S). At first, the appropriate stoichiometric amounts of highly pure Ag (99.9%), Bi (99.99%),

Se (99.99%) and S (99.98%) in the form of powder or granules are accurately weighed using weighing machine. The appropriate ratios of weighed powders were then mixed and grinded uniformly to obtain the desired compositions $\text{AgBiSe}_{2-x}\text{S}_x$ by using agate mortar. Thus, the well grinded mixture will enhance the diffusion into the grains during the annealing. However, during grinding we lost a little bit of Ag in our compounds and Se, S during the heat treatment, so less Bi has been used to compensate such losses. The idea of working inside glove box is to protect the user from any kind of hazardous, toxic or reactive precursors. Moreover, it allows processing of substances which required a high purity inert atmosphere, such as argon or nitrogen. To maintain such conditions, various synthetic steps (weighing, mixing and grinding) were performed inside glove box under an argon atmosphere (percentage of Oxygen (O_2) and water (H_2O) were maintained at 0.5ppm). Further, for our convenience, we turned the grinded powder mixture into the form of bar shape pellet of size $3*3*12\text{mm}^3$, thus provides better reactivity for solid state reactions due to better density as compared to powders. To obtain the bar shape, the powders were first put into the system shown in Table 4 (chapter 3) and then pressed using a uniaxial press ($P=250\text{MPa}$).





The second step of the synthesis deals with the sealing of above obtained bars of particular compositions inside silica tubes. For this part of the experiment, two silica (SiO_2) glass tubes of varying diameter were used; the bigger and the smaller one with diameter of 15mm and 12mm respectively. We first closed the one end of larger radius glass tubes by using a blow torch with a flame of fuel source (oxygen and acetylene). In the same time, several small crucibles were prepared out of the smaller radius glass tubes. The small crucibles were then filled up with the mixtures (bar shape pellets) prepared inside glove box and placed inside the bigger diameter glass tubes. The silica glass tubes containing the precursor's mixtures were then evacuated to different pressure and sealed off circumferentially under argon atmosphere. The sealing was done at a position away from the top of the small crucible, thus providing sufficient space for the material inside to avoid volatilization of the precursors. The choice of using SiO_2 glass tube in our experiment comes from its quality of having high working and melting temperatures. It possess extremely low coefficient of thermal expansion which further increase its ability to withstand large, rapid temperature ranges without cracking. Moreover, the excellence of using silica tubes for high temperature thermal processes lies in its strong resistive behavior to thermal shock and due to its nature to remain chemically inert to most of the elements. All such qualities of silica glass tube are of great importance in the synthesis process, as we did water quenching at high temperature.

After sealing the material inside silica tube, we placed the tube vertically inside the furnace for the heat treatment. The temperature of the furnace is accurate at the mid-position, so considering that three tubes undergoes heat treatment at the same time. During the synthesis of the same series of sample, it is also possible to place several crucibles within the same glass tube (maximum three to keep the temperature uniformity in the furnace).

Table 2: Specifications of raw materials.

Silver (Ag)	Alfa Aesar Silver powder, spherical, APS 0.6-2 micron, 99.9% (metals basis) S.A. 0.4-1.5 m/g 41598 LOT:C02X008, CAS:7440-22-4, EINECS 231-131-3
Bismuth (Bi)	SIGMA- ALDRICH Granular, 99.99% trace metals basis LOT: BGBN0187V, CAS: 7440-69-9
Selenium (Se)	Alfa Aesar Selenium powder, -200 mesh, 99.99% (metals basis) LOT: 61200473, CAS: 7782-49-2
Sulfur (S)	SIGMA- ALDRICH Powder, 99.98% trace metals basis LOT: 11325MIV, CAS: 7704-34-9
Antimony (Sb)	SIGMA-ALDRICH Antimony , Shot,1-2mm, 99.999% CAS 7440-36-0, Sb
Niobium (Nb)	Merck, 99.99%

Table 3: Picture of instruments used for the synthesis in our laboratory.

 <p>Glove Box → Used for weighing, mixing and grinding precursors</p>	 <p>Blow torch (Oxy-acetylene flame) set up→ Used for making crucibles and sealing of material inside silica glass tube</p>	 <p>Furnace for heat treatment → Temperature range 30-3000°C</p>	 <p>Cylindrical furnace for heat treatment → Temperature range : front one goes till 600°C and other two on back side goes till 1000°C</p>
--	--	--	---

2.2.2 Densification of material: Spark plasma sintering

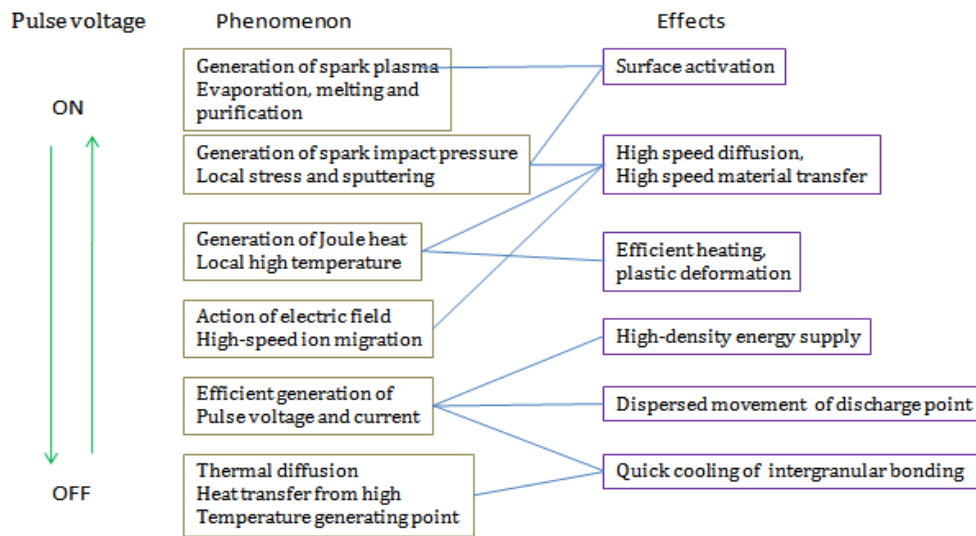
Spark plasma sintering (SPS) is a high speed powder consolidation technique which utilizes uni-axial force and ON-OFF DC pulse energizing under low atmospheric pressure. This DC pulse creates spark discharges which momentarily appear in the gaps between powder materials. The SPS system comprises of a pressurization system, punch electrodes, a water cooling unit, a DC pulse power generator, a vacuum chamber, a position, temperature and pressure measuring unit and various interlock safety units. The sintering process is carried out by following three steps: Plasma heating, Joule heating and plastic deformation. The ON-OFF pulse energizing method generates: spark plasma, spark impact pressure, joule heating and an electrical field diffusion effect.

Plasma heating: At first, the spark discharge between powder particles creates a local heating of up to several thousand°C. The high temperature sputtering phenomena generated by spark plasma and spark impact pressure causes vaporization of the impurities and purification of the surface of

particles. Immediately after, the purified surface of particles melt and fuse together forming a neck between the particles.

Joule heating: At this stage, the DC pulse current flows from one particle to another via the neck. The joule heat generated by the electrical current increases the diffusion process due to high speed migration of ions, which results in enhancement of neck size and helps them to gradually develop.

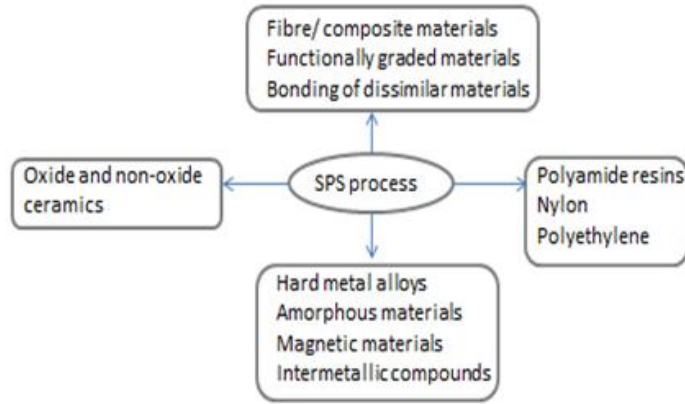
Plastic deformation: The radiant heat also generates plastic deformation under uniaxial force on the surface of particles. This stage determines the densification of the powder compact. During the whole process, heat is maintained uniformly throughout the surfaces of particles. And the sintered material obtained is highly uniform and without any noticeable change in the particles characteristics. The whole effect of application of DC voltage is summarized in the flowchart 2.1.[231]



Flowchart 2.1: Effect of ON-OFF DC pulse voltage

The advantages of using SPS system is that it provides fast and uniform sintering with low grain growth. It can sinter materials without the use of binders. Moreover, compared to conventional systems; it can control sintering energy and operation speed accurately. Also, it provides ease operation, high reproducibility, safety and reliability. Apart from the positive sides, limitation comes with the formation of only simple symmetrical shapes of sintered material and the

requirement of expensive pulsed DC generator. The SPS processing covers a wide range of materials shown in flowchart 2.2.



Flowchart 2.2: Examples of materials covered by SPS

2.2.2.1 Sample preparation and geometry of sintered material

In order to carry out the transport property measurement, powder samples need to be consolidated into dense pellets. So, for this, powder samples are required before being subjected to sintering process. The material obtained after synthesis were crushed and grinded into powder form manually using an agate mortar. The powder samples were sintered using SPS technique. The SPS used is a Syntec-SPS-511S. The mechanical scheme of this process is similar to the uni-axial die pressing. A schematic drawing of SPS comprises of a die set-up, the pressing unit and the electric current applied via electrodes is shown in Figure 2-32.

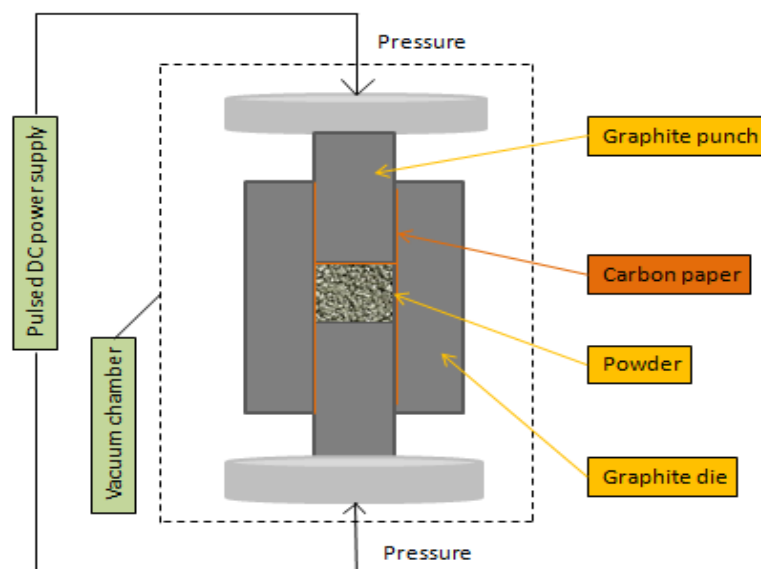


Figure 2-32: Schematic drawing of SPS comprises of a die set-up, the pressing unit and the electric current applied via electrodes.

The powder was first loaded into the graphite die with diameter ($\varnothing=10$ and 15mm) and fixed in a vertical position with two graphite rod on top and bottom. The graphite die was covered with a graphite sheet from inside before the powder being placed. The graphite sheet is use as a separation medium between the powder and the die. Moreover, the graphite has characteristic of heat resistance, chemical resistance, and can be compress easily. The die with the powder was mounted on the sintering system. Once the die set-up is loaded, the powder was pressed with the application of high DC voltage across the sample through the graphite plunger. At the same time, the temperature feedback system, the pressure unit, the atmosphere (vacuum and/or inert gas), the electrical settings are all programmed manually. The sample was heated according to Joule's heating to a temperature below the melting point of the material. When the temperature reached the set value, it was held for few minutes under respective pressure, in order to obtain uniformly dense pellets. The disc shape pellets obtained after sintering were then cut into desired shapes required for transport property measurement. The various shapes are shown below in Figure 2-33.

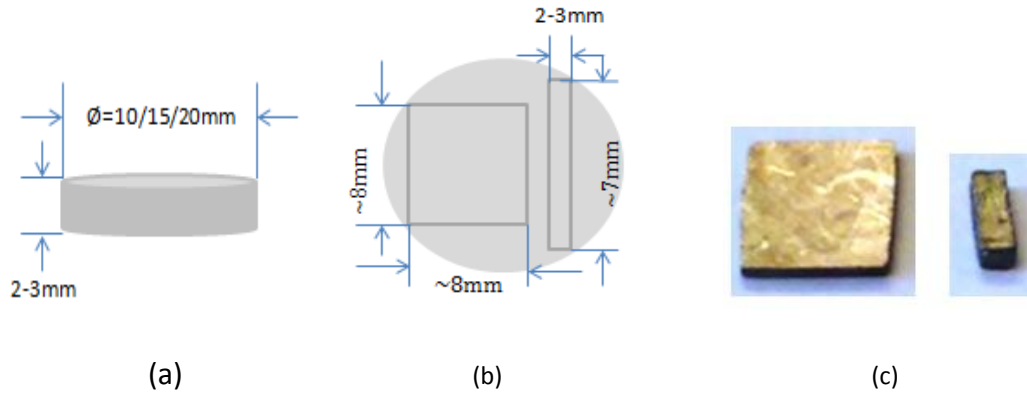


Figure 2-33: A schematic drawing of (a) sintered disc shape pellet, (b) top view of disc, and (c) square and bar shape pellet obtained after cutting.

2.3 Structural characterization of material

After synthesis, phase identification and structural analysis of the materials is the most important part of characterization. The various techniques applied are mentioned in the following sections.

2.3.1 X-ray powder diffraction (PXRD)

The principle of X-ray powder diffraction is very simple and straightforward. It is mainly based on the Bragg's law. The schematic drawing is shown in Figure 2-34. Atoms in a crystal are arranged in a periodic array in three dimensions. According to Brag law, a monochromatic X-ray beam incident upon the crystal is diffracted when reflected on the crystal planes and undergo a constructive interference. This situation occurs when the path difference between the rays reflected from successive planes differs by an integral multiple of wavelength of X-ray beam; which can be expressed as:

$$n\lambda = 2d_{hkl} \sin\theta \quad \dots\dots\dots (2.1)$$

Where, n is an integer, λ is the wavelength of X-ray, d_{hkl} is the spacing between the crystal planes and θ is the angle between the incident ray and the scattering planes.

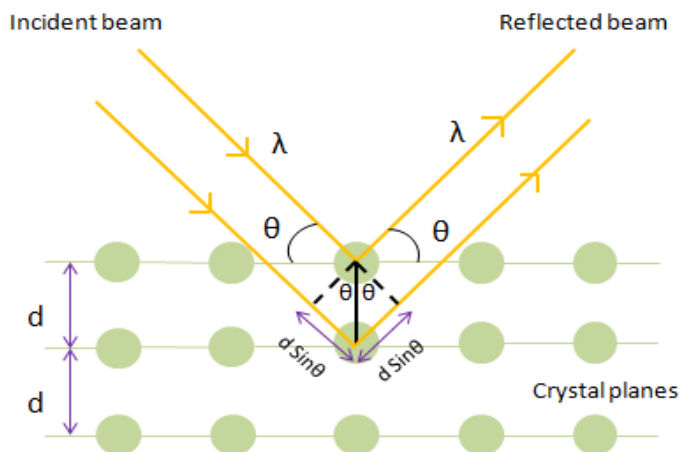
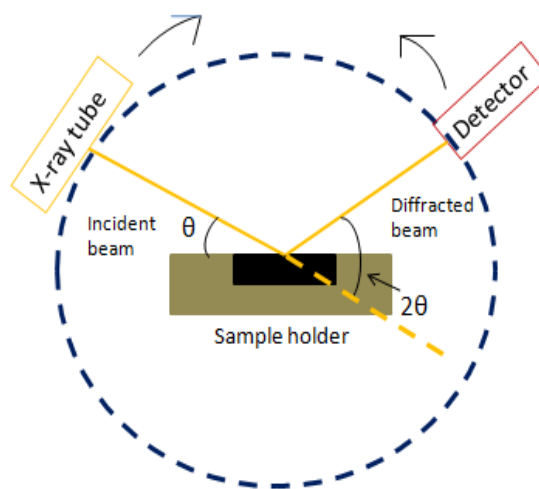


Figure 2-34: Schematic diagram of Bragg diffraction.

The structural characterization of all samples in our study was done by using powder X-ray diffraction technique with PANalytical Xpert Pro diffractometer shown in Figure 2-35(a).



(a)



(b)

Figure 2-35: (a) PANalytical Xpert Pro Diffractometer and (b) Bragg Brentano geometry.

The main three elements with which the diffractometer comprises of an X-ray tube, a sample holder and an X-ray detector. Here, the X-rays are collimated and directed towards the sample. As, the sample and detector are rotated, the intensity of the reflected X-rays is recorded. The detector

processes the X-ray signal and converts this signal into a count rate which is then transferred as an output (diffractogram) to a computer monitor. The whole assembly of this diffractometer also consists of a monochromator, and an X'Celerator. The powder was prepared on glass slide over a tape. This diffractometer is based on Bragg-Brentano geometry (Figure 2-35(b)), equipped with a Copper (Cu)- $k_{\alpha 1}$ anode source of wavelength $\lambda=1.540560\text{\AA}$. In this geometry, the sample moves by the angle θ and the detector simultaneously moves by the angle 2θ . The XRD measurement was operated at 40kv and 40mA. The phase and peaks identification was done by using software X'Pert High Score Plus which is supported with multiple reference databases.

Apart from this, we performed XRD analysis of our samples at high temperature (HTK). In this study, powder on a sample holder was heated from room temperature to the desired temperature with a predetermined rate under argon atmosphere. Here, we have adjusted the temperatures manually. One of the examples of High temperature XRD measurement is shown in Figure 2-36.

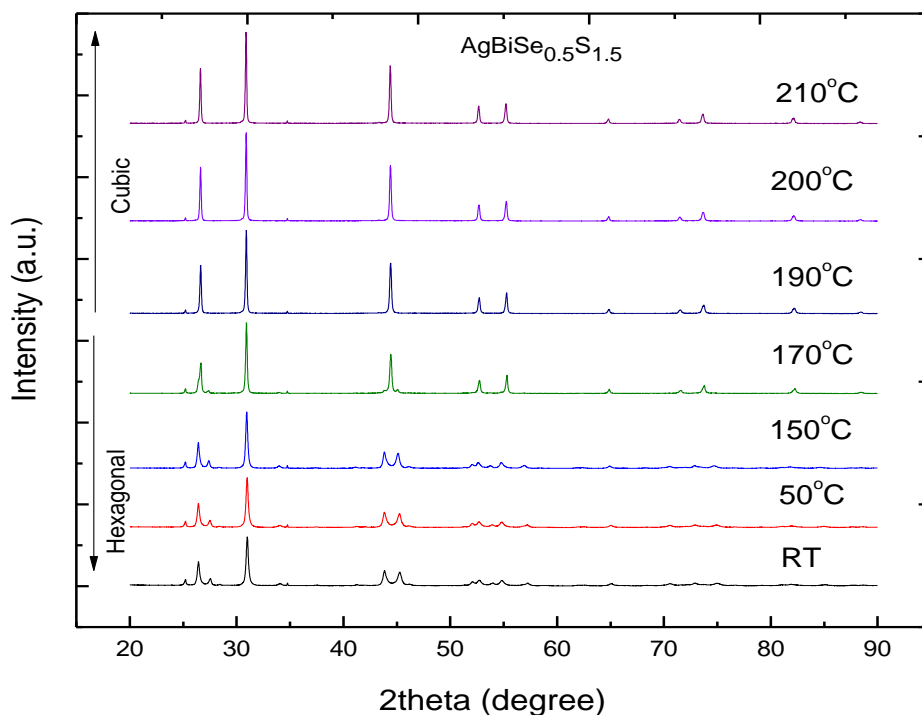


Figure 2-36: High temperature XRD analysis of $\text{AgBiSe}_{0.5}\text{S}_{1.5}$.

Figure 2-36 shows the XRD patterns collected at different temperatures. The choice of temperature range came from DSC result, in order to notice the phase change at the particular temperature as obtained in the DSC study. At the beginning, the data were collected at RT and then the temperature was increased slowly at the rate of $1^{\circ}\text{C}/1\text{min}$. Following this rate, we adjusted the required temperature, and waited for few minutes to get the steady state. We left the specimen at the required temperature for at least five minutes before recording the diffraction patterns. After this step, we took powder diffraction pattern at another temperature just by changing the temperature manually as mentioned above. Here, in this plot, we observed phase change from hexagonal to cubic, which is in accordance with the DSC result mentioned later in chapter 3.

2.3.2 High pressure measurement

The most remarkable development of the high pressure research was of paramount interest after the invention of the diamond anvil cell (DAC) [232,233,234] in 1958. DAC is used to perform various studies: X-ray diffraction, electrical conductivity measurement, magnetism, optical, Raman, IR, X-ray absorption, NMR and spectroscopy also. Diamond anvil cell (DAC) is a simple device used to create very high pressures. The structure of diamond anvil cell mainly comprises of a pair of diamond anvils and a metallic gasket shown schematically in Figure 2-37. The gasket contains a hole in which a sample and ruby are placed in a hydrostatic medium [234]. Here, ruby act as a pressure gauge and the diamond is optically transparent over wide range of wavelength; the ultraviolet, visible, infrared, and X-ray spectral range. For the measurement with DAC, very tiny samples are required. Sample used in DAC can be solid or liquid and since diamonds are quite inert, so a wide range of substances can be studied. Diamond plays an important role in DAC because of some extraordinary properties. They provide very low birefringence, low photoluminescence, and offer resistance to abrasion. Moreover, diamond is the hardest substance; so it ensures generation of highest pressure.[236]

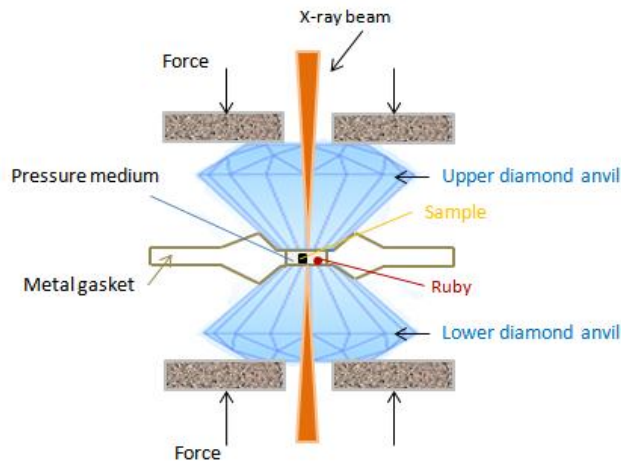


Figure 2-37: A schematic diagram of DAC.

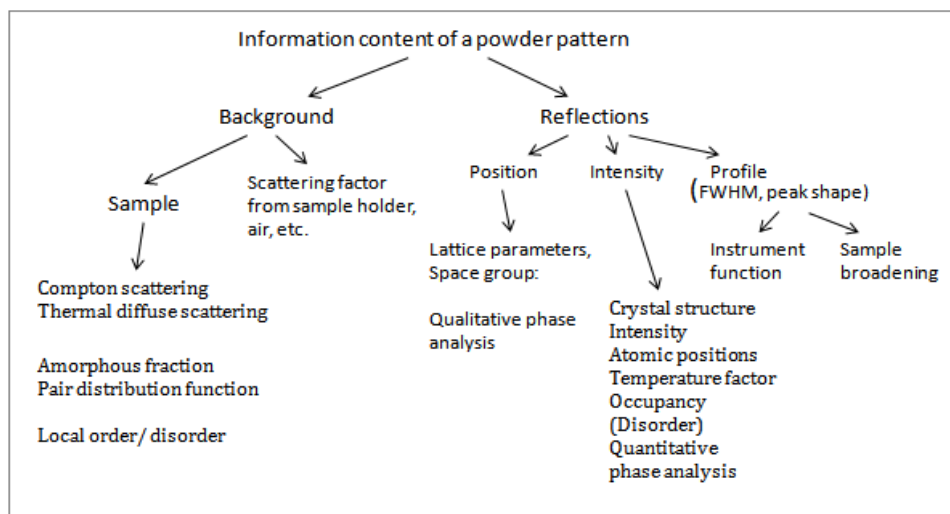
The three main parts of DAC comprises of alignment assembly, sliding system and the mechanism of application of load. The main principle is that a force is applied on the external surface of the diamond cell which exerts great pressures inside by pressing the tips of two diamonds together on the sample. This pressure squeezes the gasket and sample confined in a high-pressure chamber. The pressure is made hydrostatic by surrounding the sample with a fluid-like medium inside the gasket. Further, the entire system is connected into the experimental equipment for optical access. Light is then guided onto the cell and transmission and reflections on the sample are examined. Pressure can be applied in several ways; by using a screw-design, double diaphragm or a membrane unit. There are two strategies for pressure measurement: using ruby fluorescence method or by using equation of state (EOS) of a standard which is the one we used.

At present, different designs of DACs are available which are optimized for the measurement techniques, sample requirements, and other experimental conditions. In our case, for high pressure X-ray diffraction studies, we use membrane diamond anvil cell (MDAC). The schematic diagram and detailed description are given in the paper [232]. The advantage of using membrane cell; is that it is possible to change the load smoothly and maintain the parallelism of the diamonds under pressure, the whole process can be remote control and easily programmed with time. In this kind of cell, the force is generated by inflation of the membrane. This cell can be used to perform various measurements such as control of gasket indentation, low-temperature performance of the cell, study of phase transitions and also the measurement of refractive index of a homogeneous medium.

In our work, we performed high pressure X-ray diffraction of our sample using MDAC, mainly to study the phase transition. The entire measurements were carried out at the Material Science Powder Diffraction (MSPD) beamline at the ALBA-CELLS synchrotron (Barcelona). The details of the beamline source and optics used are given in the reference [237]. To conduct the experiments, after synthesis, the samples were grinded into powder form. A very small amount of powder was trapped between the two diamond anvils (Boehler-Almax design). The measurements were performed up to 20 GPa with a focused incident monochromatic X-ray beam of wavelength ($\lambda=0.4246\text{\AA}$) corresponding to Sn K-edge. The powder samples were loaded into the gasket (Inconel X750) preindented to 40microns. The pressure chamber was 150 microns in diameter. The pressure was measured using the EOS of Cu. The diffraction patterns were recorded by the detector and 2D Debye-Scherrer circles were obtained and transformed into 1D pattern using FIT 2D software. [237,238]

2.3.3 Refinement Method

The extraction of useful information from the powder diffraction patterns is done by using various patterns fitting method. Two of them, Rietveld and le Bail are described in this section. In our work, these two refinement methods are implemented using the software FULLPROF. The information content in diffraction pattern is shown below in the flowchart 2.3.



Flowchart 2.3: the information content in diffraction pattern.

2.3.3.1 Rietveld Refinement

Rietveld refinement method was first introduced by Hugo M. Rietveld in 1967, to refine the crystal structures from the powder diffraction data [239]. It is also known as whole powder pattern structural refinement method (WPPR). In this method, the least square refinement is carried out until the best fit is obtained between the observed powder diffraction pattern and the calculated pattern. The model parameters that are refined include the atomic positions, the scale factor, the lattice parameters, the background, instrumental factors (geometric or optical), diffraction optic effects, and the specimen aberration (such as specimen displacement, broadening and transparency).

The diffraction pattern is iterated i th times to obtain the best fit with the intensity value y_i . The factor which is necessary to be minimized in the least square fit is the residual (S_y) given as:

$$S_y = \sum_i (w_i(y_i - y_{ci}))^2 \quad \text{..... (2.2a)}$$

Where, $w_i = 1/y_i$, and y_i is the observed intensity and y_{ci} is the calculated intensity at the i th step and \sum is the total data points recorded at i th step.

Further, to determine the calculated intensity (y_{ci}), we can consider a powder diffraction pattern as a collection of individual reflection profiles. Each profile contains information about the peak height, peak position, a breadth and an integrated area under each peak. The area is proportional to the Bragg intensity (I_{hkl}), where h, k, l are the Miller indices (K). The intensity (I_K) is related to the square of the absolute value of the structure factor, $|F_K|^2$. The calculated intensity y_{ci} is then determined from $|F_K|^2$ values obtained from the structural model by taking the sum of the contribution of neighboring Bragg reflections and the background.

$$y_{ci} = s \sum_k [L_k |F_k|^2 \emptyset (2\theta_i - 2\theta_k) P_k A + y_{bi}] \quad \text{..... (2.2b)}$$

where, s is the scale factor, K represents the Miller indices, L_k contains the Lorentz, polarization, and multiplicity factors, \emptyset is the reflection profile function, P_k is the preferred orientation function, A is the absorption factor and y_{bi} is the background intensity at the i th step.

Since the adjustable parameters and intensities are related in a non-linear manner, the initial model must be close to the correct model otherwise the non-linear least square fit will not necessarily converge to a global minimum and instead it could diverge to a false minimum. The idea of criteria

of best fit can be quantified with several R-values developed by the users of Rietveld method. The most commonly used residual R- value is R_p (R-pattern) and R_{wp} (R-weighted pattern) given as:

$$R_{wp} = \{ \sum w_i (y_i(\text{obs}) - y_i(\text{calc}))^2 / \sum w_i (y_i(\text{obs}))^2 \}^{1/2} \quad \text{..... (2.2c)}$$

$$R_p = \{ \sum |y_i(\text{obs}) - y_i(\text{calc})| / \sum (y_i(\text{obs})) \} \quad \text{..... (2.2d)}$$

Another useful numerical criterion is the Goodness-of-fit (S) given by the relation:

$$S = [S_y / (N - P)]^{1/2} \quad \text{..... (2.2e)}$$

S value of 1.3 or less is considered to be satisfactory. N is the number of observations and P is the number of adjusted parameters.

This method is most successfully used nowadays to determine structure of materials, component of chemical mixtures and also analyze the phases.

2.3.3.2 Le Bail Refinement

The measured powder diffraction patterns of the material often consist of overlapped Bragg peaks, so the restoration of the Bragg intensities is not so easy. Their actual value can be determined by integrating the area under each observed peak. The whole powder pattern decomposition (WPPD) technique provides a systematic procedure to decompose a powder pattern into its component Bragg reflections and extract the integrated intensities. The most commonly used WPPD method is the le Bail algorithm developed by Armel le Bail. The le Bail model is easy to incorporate inside an existing Rietveld code. For the le Bail method, value of unit cell, position of Bragg peaks and space group of the material must be known. But the structural factors and the associated structural parameters are not required for the analysis. Le Bail refinement also follows the least square minimization process like as the Rietveld method. Here, the intensities are refined by minimizing the difference between the calculated pattern and the experimentally observed pattern. The lattice parameters, profile parameters and background parameters are refined during each iteration cycle.

Le Bail method calculates the intensities by using the Rietveld decomposition equation. As same as Rietveld, experimentally observed intensity $y_i(\text{obs})$ is partitioned among all the peaks (p). In the first iteration, initially, all of the intensities are set to an arbitrary value. These are considered as a calculated value. This process leads to an 'observed' intensity of a particular peak given as:

$$(I_{\text{obs}})_1 = \sum_{i=0}^{n-1} [(y_i(\text{obs})) \left\{ \frac{(y_{i1})_{\text{calc}}}{\sum_{j=0}^{p-1} (y_{ij})_{\text{calc}}} \right\}] \quad \text{..... (2.3)}$$

Where, y_{i1} is the calculated intensity of peak '1' and $(I_{\text{obs}})_1$ is the 'observed intensity of peak '1'.

According to this relation, the I_{obs} of a particular peak '1' depend on the experimental observed intensity and the ratio of the calculated intensity of peak '1' and the total calculated intensities of all the peaks. After the first cycle, the lattice, background and profile parameters are refined and these sets of refined parameters are then used for calculating new set of I_{obs} . The process is iterated again and again; new set of I_{obs} is updated in further refinement cycles. Following this, iteration is continuing until good agreement obtained between the observed and calculated powder pattern.

2.3.4 Thermal analysis by Differential Scanning Calorimeter (DSC)

Differential scanning calorimetry or DSC is a thermal analysis technique that was first developed by E.S. Watson and M.J.O'Neill in 1962 and then commercially launched in 1963 at Pittsburgh Conference on Analytical Chemistry and Applied Spectroscopy. It is used to characterized the physical properties of a wide variety of materials and analyze their changes with temperature. In this technique, the difference in heat flow required in order to raise the temperature of a sample and a reference is recorded as a function of temperature. There are two types of DSC: power compensated DSC and heat flux DSC. In power compensated DSC (Figure 2-38b), the temperatures of the sample and the reference are operated independently using separate identical furnaces, while in heat flux DSC (Figure 2-38a), the whole assembly is enclosed in a single furnace.

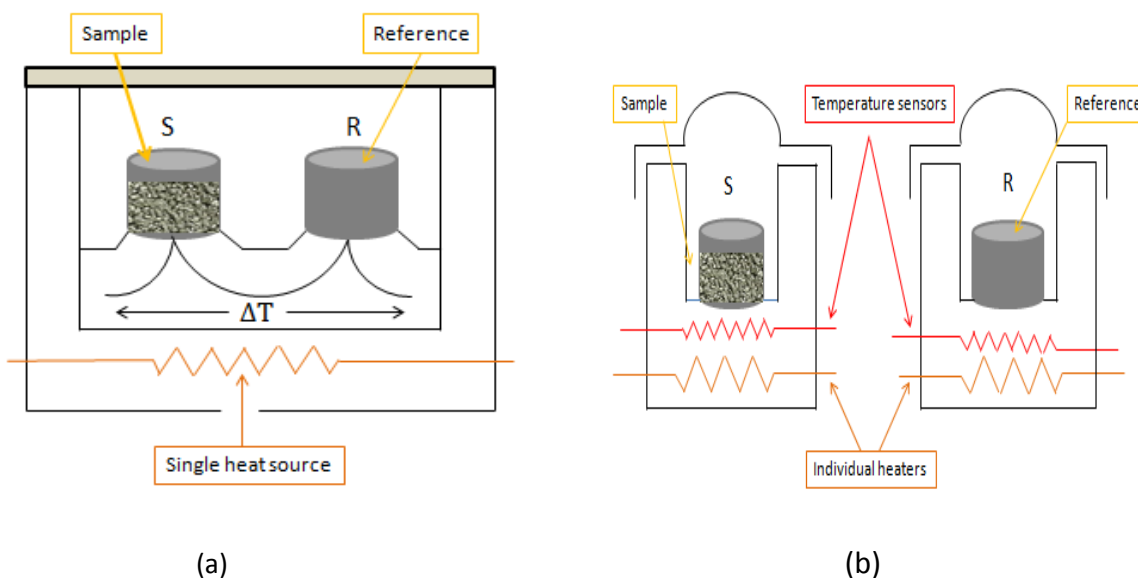


Figure 2-38: A schematic drawing of (a) Heat flux DSC; (b) power-compensated DSC.

DSC becomes a most useful thermal analysis technique due to its various advantages. Only a small amount of material (range from 0.5mg-100mg) is required, which ensures uniform temperature distribution and high resolution. In addition, the sample preparation, experimental set-up and interpretation of results can be done easily. It can analyze both solids and liquids samples. The strong point of using DSC is the speed with which it detects the transitions in materials. Using this technique, it is possible to observe specific events like crystallization, glass transition, melting, oxidation, decomposition as well as any other chemical reactions. In addition, it can also determine the thermal stability and the reaction kinetics of a material.

The DSC chamber consists of a sample holder and a reference holder enclosed in the same furnace. The DSC measurements for our study were performed using a Setaram Setsys Evolution equipment shown in Figure 2-39.



Figure 2-39: DSC (Setaram Setsys Evolution equipment).

Here in this instrument, the sample is placed into an alumina crucible and the reference is usually an empty alumina crucible. The sample and empty reference crucibles are heated at constant heat flow. The whole chamber is encapsulated in an inert atmosphere to prevent oxidation of samples at high temperatures. Both the sample and reference are maintained at nearly same temperature throughout the experiment. Here we present one of our result of DSC experiment (or DSC thermogram) shown in Figure 2-40 as an example. It shows a plot of heat flow Vs sample temperature in degree Celsius. The curve is associated with endothermic peak as a function of temperature or time. Such peak arrival corresponds to a given phase transition of the sample under study. The temperature at the onset of transition can be calculated by taking the average of two values of temperature obtained by drawing the tangent lines on the curve itself. On other side, it is valuable to know the mathematical background related to heat flow. As, DSC is carried out at constant pressure, heat flow is equivalent to change in enthalpy. The heat capacity (C_p) is also related to the heat flow. Mathematically, it can be expressed as,

$$\left(\frac{dq}{dT}\right)_p = \left(\frac{dH}{dT}\right)_p = C_p \quad \text{..... (2.4)}$$

Where, the heat flow is measured in mcal sec^{-1} . The total enthalpy change of the event can be calculated by integrating the area under the peak.

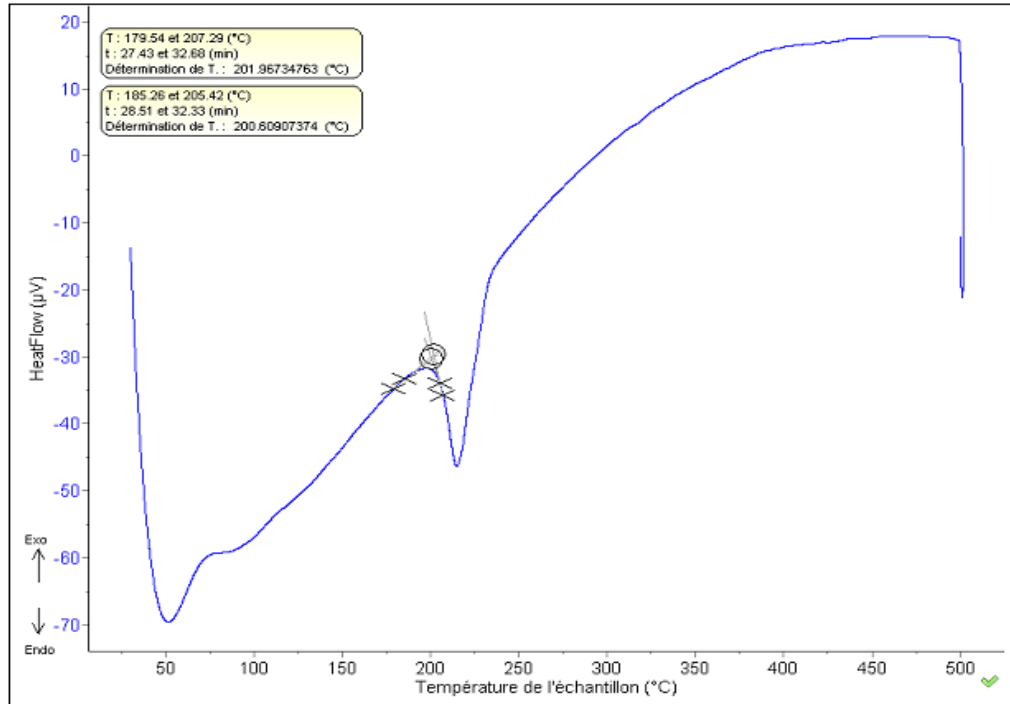


Figure 2-40: Diagram of DSC Heat flow curve Vs Temperature of sample.

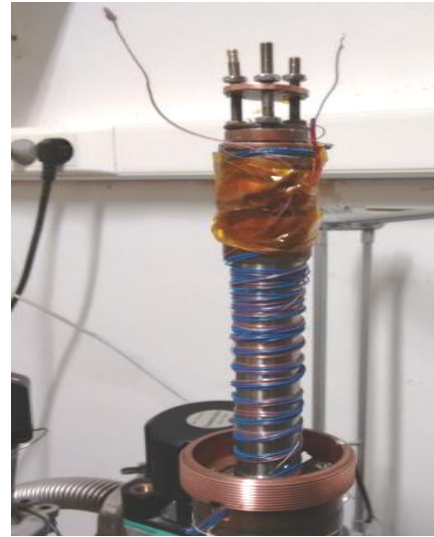
2.4 Transport property measurement techniques/ Electrical characterization

2.4.1 Seebeck coefficient measurement

Seebeck coefficient measurement of materials at low temperatures (30K-300K) was performed using differential method. The experiment was carried out using the instrumental set up constructed in the laboratory shown in Figure 2-41.



(a)



(b)

Figure 2-41: (a) Instrument to measure Seebeck coefficient and resistivity and (b) zoom view of sample holder part.

In the differential method, a gradient of temperature (ΔT) is applied across the material which results in a potential difference (ΔV). Seebeck coefficient does not depend on the sample geometry and is simply defined by a measurement of voltage at two points on the sample divide by the temperature difference between these two points,

$$S = \frac{\Delta V}{\Delta T} \quad \dots\dots\dots (2.5)$$

For the Seebeck measurement, the powder sample are sintered (SPS) and then cut into a rectangular parallelepiped bar shape pellet. The whole measurement were made under vacuum condition and the densified bar is placed vertically inside the instrument. The schematic diagram of sample holder set-up is shown in Figure 2-42.

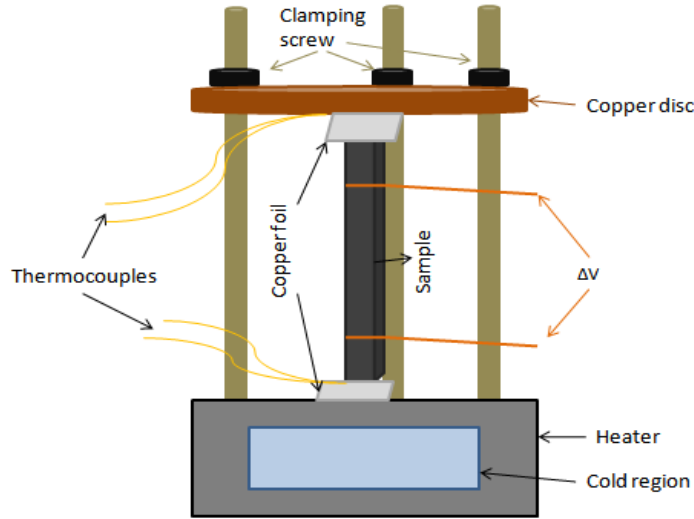


Figure 2-42: Schematic diagram of sample holder set-up.

According to the schematic diagram, the bar is held between the heating base and the copper plate. The copper plate is equipped with three screws which make the bar to stand in a vertical position until the measurement is over. The temperature and potential difference was measured by the thermocouples which are sandwiched between copper foils and the sample. The copper plate at the top and the heating base at the bottom hold the thermocouples tightly to provide a good contact with the sample. Thus, ensures good thermal and electrical contacts. After the sample has been fixed, the device is tightly covered with a steel tube which keeps the sample in a constant vacuum environment. In Figure 2-42, the wires (orange colour) on the right hand side measures the resistivity and the thermocouples (yellow colour) on left hand side measures both ΔV and ΔT simultaneously. Here, the S value was not just measure with $\Delta V/\Delta T$ but from a linear fit of ΔV vs ΔT obtained during measurements. The thermal gradient is regulated and preset by using the computer software. All measurements were controlled by the computer and raw data is automatically saved. In the Seebeck coefficient measurement, the current supply is open circuit with no current flowing through the sample. The calibration of the device was made on a superconducting material ($S = 0 \mu V.K^{-1}$) and a skutterudite. While measuring the Seebeck coefficient, we need to consider the contribution of the copper wires ($S_{Cu-wire}$) connected to the bar to the value of the thermoelectric power is around $1-2 \mu V.K^{-1}$. Thus, the Seebeck coefficient is measures as:

$$S = \frac{\Delta V}{\Delta T} + S_{Cu-wire} \quad \dots\dots (2.6)$$

The electrical resistivity and the Seebeck coefficients were carried out using the same device shown in Figure 2-41. For resistivity measurement, two new contacts were made near the ends of the bar. The copper wires at the end were pasted with silver glue and the contacts were connected with this wire by welding with tin. This two points (voltage probes) measures the voltage difference with the application of current across the thermocouples. The voltage and current, data acquisitions were fully automated and controlled by the computer software. Thus, the sample resistance (R) can be known from the data obtained and the resistivity (ρ) was calculated from the relation:

$$\rho = \frac{R \times A}{l} \quad \dots\dots\dots (2.7)$$

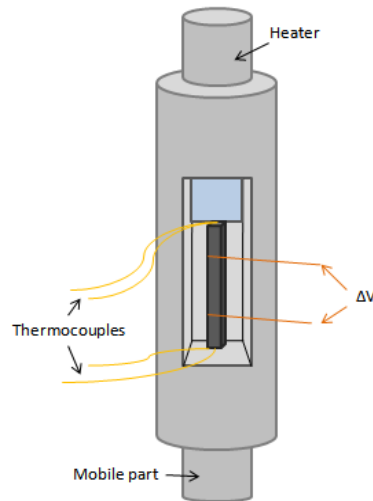
Where, A is the cross-sectional area of the sample and l is the distance between the copper wires (or two contacts).

2.4.2 Seebeck and Resistivity measurement at high temperature

High temperature measurement of Seebeck coefficient and resistivity was performed with a device built in our laboratory. A schematic diagram and the actual set –up is shown in Figure 2-43 (a) and (b) respectively.



(a)



(b)

Figure 2-43: Measurement at high temperature: (a) the actual set –up in the laboratory and (b) the schematic diagram.

With this instrumental set-up, the measurement can be carried out under controlled atmosphere including vacuum and a reducing atmosphere for oxygen sensitive material. We can measure the thermoelectric power (S) and the electrical resistivity (ρ) within the temperature range (300K-1200K). The whole instrument assembly was built with the materials which are stable at high temperature. A sintered sample was cut into bar-shape and the measurement was done following the same method as in the case of low-temperature measurement. A detailed description of the instrument and the method of measurement are given in the paper [240].

2.4.3 Hall Effect measurement

The Hall Effect measurement is important for characterizing the electrical transport properties of metals and semiconductors. The assembly of PPMS is used to perform Hall measurement within temperature range (10K-400K). A schematic diagram for Hall measurement is shown in Figure 2-44.

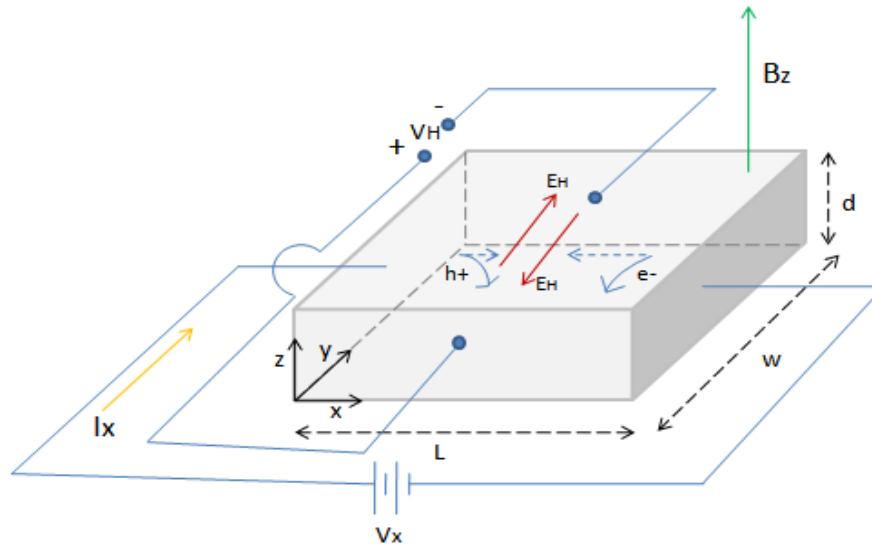


Figure 2-44: Geometry for measuring Hall Effect.

The sintered sample was cut into square shape to use for the measurement purpose. The contacts were made with copper wires and attached on the body of sample by soldering with indium. The principle behind the Hall Effect is explained below.

Hall Effect was discovered by E.H. Hall in 1879. According to this effect, when a sample with an applied current I_x is placed in a magnetic field perpendicular to the current flow, the charge carriers

will experience a force. Depending on the type of material, there will be a build-up of net charge and this further induces an electric field in y-direction perpendicular to both the current and the magnetic field. In steady state, the magnetic field force is completely balanced by the induced electric field force given as:

$$qE_y = qv_x B_z \quad \text{..... (2.8a)}$$

Where, v_x is the velocity of the charge particle in x-direction.

The induced electric field (Hall field, E_H) produces a voltage across the material known as Hall voltage (V_H):

$$V_H = E_H W \quad \text{..... (2.8b)}$$

Where, W is the width of the material shown in the geometry.

The polarity of the Hall voltage determines whether the material is n-type (-ve charge carrier) or p-type (+ve charge carrier). The Hall measurement system can be used to determine several parameters such as: carrier concentration (n), Hall coefficient, resistivity and the mobility of charge carriers. From the relation of Hall voltage, the hall coefficient can be related to the carrier concentration,

$$V_H = \frac{I_x B_z}{ned} \quad \text{..... (2.8c)}$$

$$R_H = \frac{V_H d}{I_x B_z} = \frac{E_y}{j_x B_z} = \frac{1}{ne} \quad \text{..... (2.8d)}$$

Where, e is the electronic charge and j_x is the current density. The value of R_H is +ve for p-type and -ve for n-type. Another important parameter is the Hall resistivity ρ_H which is expressed as the ratio of the electric field E_y and the current density j_x , in accordance with the Drude model.

$$\rho_H = \frac{E_y}{j_x} \quad \text{..... (2.8e)}$$

From experimental point of view, the Hall coefficient is measured by taking the variation of Hall resistivity with the magnetic field and the slope will give R_H as:

$$R_H = \frac{d\rho_H}{dB} \quad \text{..... (2.8f)}$$

On the other hand, if the carrier concentration values from Hall effect measurements as well as electrical resistivity measurements is known, then the Hall mobility can be calculated as:

$$\mu_H = \frac{1}{\rho n e} \quad \text{..... (2.8g)}$$

During measurement, the factors which are essential to be considered are to have good ohmic contact, flat, symmetric and homogenous sample, and also to avoid any kind of heating of the sample or thermal gradients.

2.4.4 Specific heat measurement

The heat capacity or specific heat of a substance is defined as the amount of heat per unit mass required to raise the temperature of it by one degree. It is expressed in unit of thermal energy per degree temperature. The heat capacity of our samples is measured using PPMS. In PPMS, the Quantum Design heat capacity option measures the heat capacity at constant pressure given by the relation:

$$C_p = \left(\frac{dQ}{dT} \right)_p \quad \text{..... (2.9a)}$$

Where, dQ is the amount of heat transferred to the substance resulting in an increase in temperature dT.

There are several different techniques which are optimized to measure specific heat capacity depending on sample size. The technique with which we measure the specific heat capacity of our sample in PPMS is relaxation technique developed by Bachmann et al. in 1972 [241]. According to this technique, each measurement cycle contains a heating period followed by a cooling period. In each cycle, the heat capacity option adjusts the thermal response to a model which accounts for both the thermal relaxation of the sample platform to the bath temperature and also the relaxation between the sample platform and the sample itself. The schematic diagram of the whole assembly which is used to determine specific heat capacity in PPMS is shown in Figure 2-45.

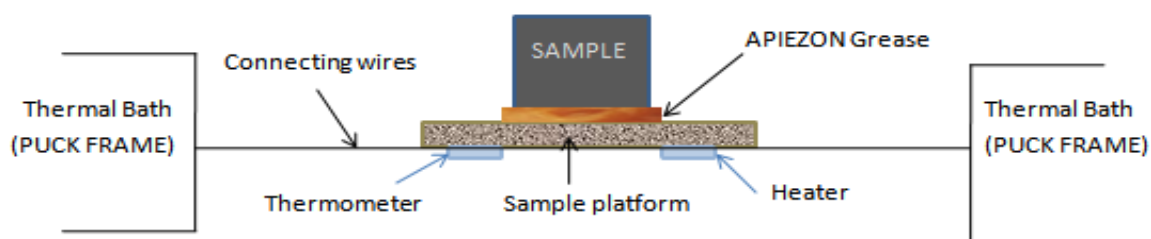


Figure 2-45: Schematic diagram of assembly to measure the heat capacity in PPMS heat capacity option.

According to the figure, the calorimeter puck consists of a resistive platform heater, platform thermometer and puck thermometer. The structure is provided with eight small thermally conducting wires that support the sample platform (2mm*2mm) and suspend it in the middle of the puck frame. Moreover, the wires also provide a good electrical and thermal connection among several parts. The sample is mounted to the sample platform by using a thin layer of grease (Apiezon N Grease). During the measurement, a Cryopump High -vacuum option is used to provide adequate vacuum of 0.01 mTorr such that the conductance of the wires dominates the thermal conductance between the sample platform and the thermal bath. This in turn produces a heat link to the bath with a large time constant, so that the platform and sample reach at sufficient thermal equilibrium condition during each measurement. The whole assembly is enclosed within a thermal radiation shield which protects the sample platform and the sample from any unwanted heat.

Before each measurement, it is important to perform the addenda (C_a) measurement. It is the measurement of the heat capacity of the sample platform (C_p) along with the grease. C_p is treated as a value equal to C_a . The software first measures the temperature response of the sample platform to the applied heat and fits it to a desired model. Immediately after, the sample is mounted and the total heat capacity is measured. The software then calculates the actual heat capacity of the sample (C_s) by subtracting the addenda part from the total heat capacity. So, for this, two separate measurements are required: one with and one without a sample on the sample platform. All this measurement is based on two-tau model with schematic diagram shown in Figure 2-46.

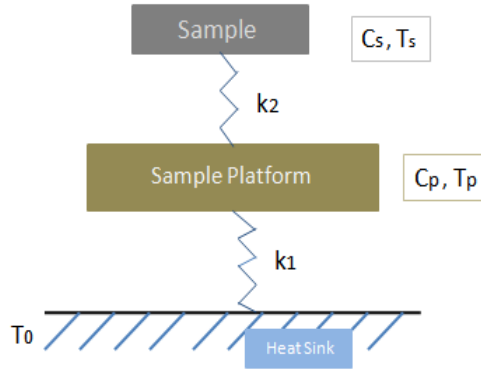


Figure 2-46: Specific heat measurement.

To model the thermal response for heat capacity the heat balance equations are:

$$P(t) = C_p \frac{dT_p}{dt} + \kappa_s (T_p - T_s) + \kappa_p (T_p - T_0) \quad \text{.....(2.9b)}$$

$$0 = C_s \frac{dT_s}{dt} + \kappa_s (T_s - T_p) \quad \text{..... (2.9c)}$$

Where, C_s and C_p are the heat capacity of the sample and the platform with their respective temperature T_s and T_p . κ_s is the thermal conductance between the sample and the sample platform and κ_p is the thermal conductance between the heat sink and the sample platform. T_0 is the temperature of the heat sink which is held nearly at a constant temperature T_p .

2.4.5 Thermal diffusivity measurement (LASER FLASH method)

One of the most attractive methods for measuring thermal conductivity (κ) is to determine first the thermal diffusivity (α), specific heat (C_p) and the density (ρ) as a function of temperature and then compute the value of thermal conductivity from the given relation:

$$\kappa(T) = \alpha(T)\rho(T)C_p(T) \quad \text{..... (2.10)}$$

Thermal diffusivity which defines how quickly a body can change its temperature is measured by using the laser flash method. It is expressed in the unit m^2/s . Simple geometrical method was used to measure the density of the material. And, precise value of specific heat can be obtained either by using DSC (Differential Scanning Calorimetry) or by PPMS (Physical property measurement system).

The thermal diffusivity of the given materials was measured utilizing a NETZSCH model LFA 457 MicroFlash apparatus and schematic diagram shown in Figure 2-47(a) and (b) respectively. The main principle behind the laser flash technique was first described by Parker in 1961 and it's become useful world-wide due to its wide temperature range for measurement.

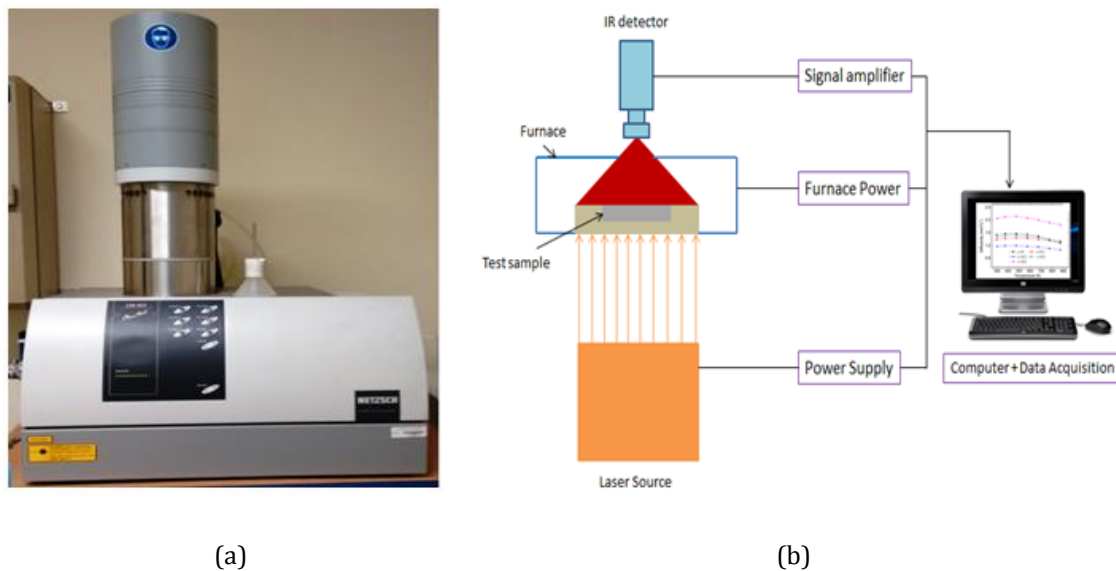


Figure 2-47: (a) LFA 457MicroFlash apparatus and (b) schematic diagram of LFA.

In a laser flash technique (LFA), at first, the samples were placed in the sample holder under inert gas environment. The sample is usually a disk or square in shape. At the beginning, the sample is aligned properly between a neodymium (Nd) glass laser ($1.06\ \mu\text{m}$ wavelength) and an indium antimonide (InSb) IR detector inside the furnace. The laser pulse is guided by a mirror to the sample. The furnace is provided with a thermocouple mounted on the side of the sample holder which controls the sample and its surrounding temperature. Once, the sample reaches and stabilizes at the desired temperature say T_0 , an instantaneous laser beam is fired several times on the front face of the sample, defined as a “shot”. During each shot, the front surface absorbs the laser beam energy causing a heat flux lines to travel parallel through the sample thickness; there is no heat flow in the plane of the sample shown in Figure 2-48. This results in a rise in temperature at the rear face which is then monitored as a function of time with a detector (InSb-detector, liquid nitrogen cooled). Further, the detected signal is amplified before being transferred to the computer for future analysis. Moreover, use of adjustable filters between the laser and the furnace allows keeping the sample temperature in the optimum range.

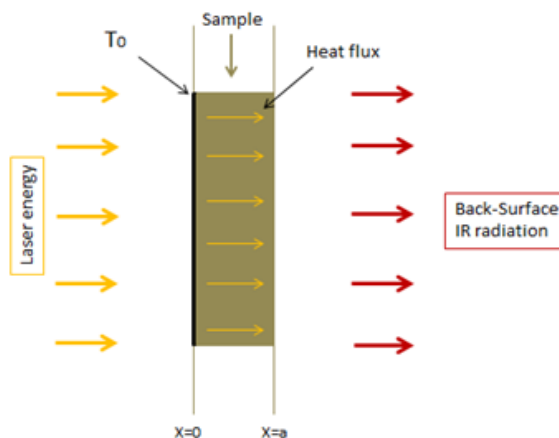


Figure 2-48: Schematic drawing of through-plane heat flow in LFA method.

Sample preparation: For laser flash experiment, a well dense sintered sample is required. The sample was first polish and cut into desire shape with appropriate size. The faces of the sample were made flat and parallel, so that it can be fitted easily within the sample holder. The system is equipped with sample holders for various sample shapes and sizes; for e.g., it can be a disc or a square form. The sample holders possess very low thermal conductivity in order to maintain a heat insulated environment surrounding the sample. With LFA instrument, it is possible to measure three samples at the same time. Disk-shaped samples with diameter of 10-12mm and square shape sample with length side 8mm were prepared. The thickness of the sample lied between 1-2mm. The sample was coated with graphite aerosol for surface blackening, it is also important for the emissivity. It increases the energy absorbed on the laser side and the temperature signal on the backside of the sample. The picture of sample holders is shown in Figure 2-49.



(a)



(b)

Figure 2-49: (a) sample holder with different shapes and sizes (b) Square sample holder with square shape sample.

Advantages of LFA method: It is a non-contact and non-destructive method. It has the capability to analyze multi-layer samples. It measures sample with simple geometry and preparation of sample

is an easy task. It can measure a broad range of thermal diffusivity value ($0.01\text{-}1000\text{ mm}^2/\text{s}$) with a high level of accuracy and reproducibility. The LFA 457 Microflash is designed as a cost-effective, easy-to-operate, and allows measurement with temperature range from room temperature to 1100°C . The vertical arrangement of sample holder, furnace and detector makes it easy to install the sample inside. This in turn, provides an optimum signal-to-noise ratio of the detector signal. The LFA technique is of paramount interest as the measurements are less time consuming and more productive. In spite of the positive sides, flash method has some limitations. The equipment is usually expensive and special care need to be taken while dealing with porous and non-homogeneous materials. [242,243]

Chapter 3

Experimental Results on solid solution AgBiSe₂-AgBiS₂

3.1 Motivation behind this chapter

This chapter presents the study of the solid solution and the study of the phase transitions. A detailed investigation on the synthesis and the structural characterization of the solid solution ($\text{AgBiSe}_{2-x}\text{S}_x$, x varies from 0 to 2) by X-ray diffraction and by thermal analysis using DSC (Differential scanning calorimeter) has been carried out. Moreover, this chapter contains the experimental results that were obtained during high temperature and high pressure XRD study. The main objective of this study is to understand how to trap the cubic phase, of prime interest for application, and also because of the low thermal conductivity which could be obtained for intermediate compositions.

3.2 Results of synthesis

The instruments and technique used for the synthesis purpose during the whole PhD work are already mentioned in the section 2.2.1. Here, in the following section, we mention about the raw materials, their respective mass value and the end products obtained on completion of heat treatments.

3.2.1 Raw materials and Calculation of compositions

The specifications of the raw materials used for the synthesis are tabulated in chapter 2. The first idea of our work is to synthesize the compounds belonging to the solid solution $\text{AgBiSe}_{2-x}\text{S}_x$. To make it fruitful, it is required to determine the appropriate synthesis conditions. Some of the previous works on AgBiSe_2 were mentioned in chapter 1. At the beginning, our work started with the compound AgBiSe_2 with the idea of getting the correct synthesis condition for each crystal structure and then extending these conditions to the whole solid solution.

Synthesis of AgBiSe_2 : The samples of chemical composition AgBiSe_2 (2g) were prepared by mixing uniformly adequate proportions of raw materials, Ag, Bi and Se in a glove box. The powder was grinded using agate mortar manually and then pressed into bar-shape pellets. The pellets were sealed in an evacuated silica tube, heated up to (500°C) [222] for 48 hr and slowly cooled down to room temperature. The obtained ingot was crushed into fine powder and structural analysis was carried out by X-ray powder diffraction (XRD). The powder XRD pattern of the sample is shown in Figure 3-50. The result obtained does not match the expected one, the room temperature hexagonal phase of AgBiSe_2 . Our result contradicts with the one mentioned in the literature [222]. As we see

here, the peaks may correspond to hexagonal phase but not well synthesized, the peaks are not sharp enough, and rhombohedral and/or cubic phase might also be present. According to the XRD analysis, in Figure 3-50, the hexagonal phase matched with the database pattern with reference code (01-029-1441) and rhombohedral phase match with the reference code (01-085-0704). The possibility of the mixed phases shows that the synthesis was ineffective. The reason could be the choice of furnace; which may be not well calibrated or may be the tube was not placed accurately in the effective heating zone. The choice of temperature could be another factor behind this failure. But, it is hard to give a definitive explanation of this difference in results at this stage. Thus, to understand this discrepancy, it is important to perform the thermal analysis using DSC.

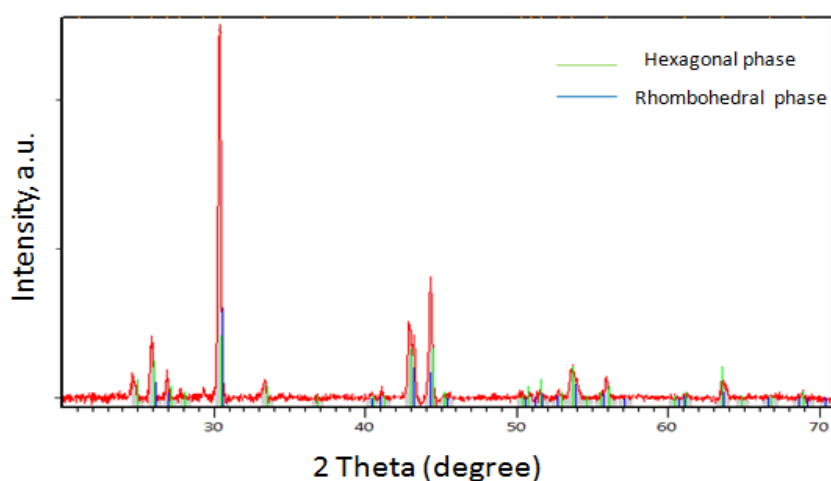


Figure 3-50: XRD pattern of AgBiSe_2 sample.

For the DSC measurement, at first the solid mass obtained after synthesis was crushed and grounded into powder manually using agate mortar. The adequate amount of powder about 80.2mg of the synthesized AgBiSe_2 sample was weighed using weighing machine. After, we poured the measured mass into a small alumina crucible suitable for the DSC measurement. The heat flow curve obtained after measurement is shown in Figure 3-51. Two clearly visible endothermic peaks are observed in the curve; representing two phase transition points ($\alpha \rightarrow \beta \rightarrow \gamma$). The temperatures at the onset of the two transitions are marked in the curve itself. This temperature value corresponds to the temperature of phase transition. The temperatures at which the first and second transition occurs are 217°C and 307°C respectively. The first synthesis which we performed failed to obtain the room temperature phase accurately. From these DSC results, the probable reason could be the short synthesis time. Indeed, the annealing temperature was above the transitions and even if the sample was slowly cooled down, the annealing time below 217°C was too short to give it a single

hexagonal phase but too long to trap the cubic phase. So, for future synthesis, two things could be applied; one is to perform two step synthesis (sec.3.2.2) instead of one single step and another is to do further annealing after synthesis at a temperature lower than the transition temperature for long time. Following this, we could expect the room temperature hexagonal phase.

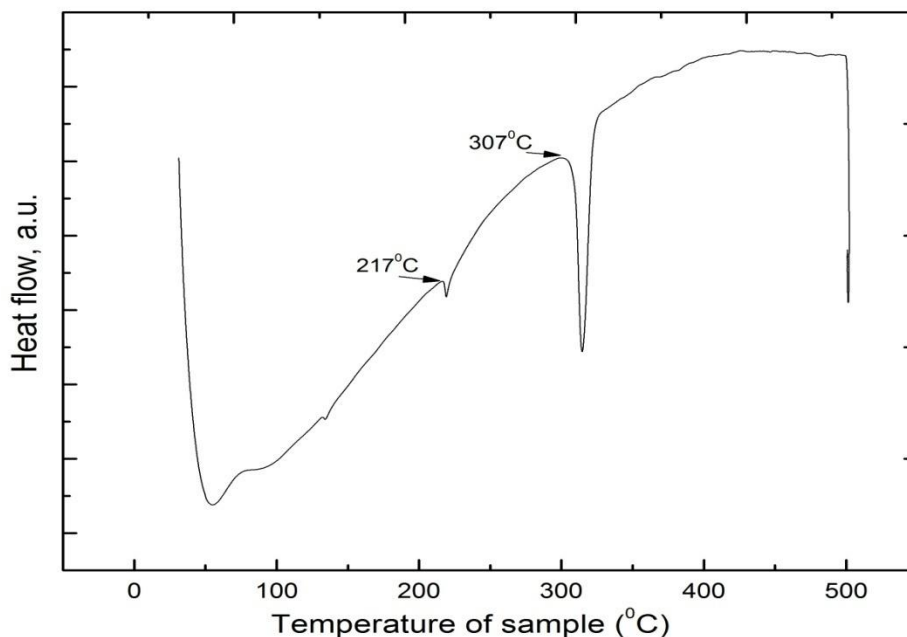


Figure 3-51: Heat flow curve of AgBiSe₂.

Based on the result obtained, AgBiSe₂ was synthesized again along with all other compositions. The whole synthesis steps were described in details in the following section.

At first, we began our synthesis with one composition AgBiSe_{0.5}S_{1.5}, by following the two step synthesis process. The precursors were weighed, mixed, grinded manually and finally pressed into pellets. They were then sealed in a silica tube under argon atmosphere and placed vertically inside the furnace. The details of heat treatment are mentioned in section 3.2.2. The XRD result obtained is shown in Figure 3-52.

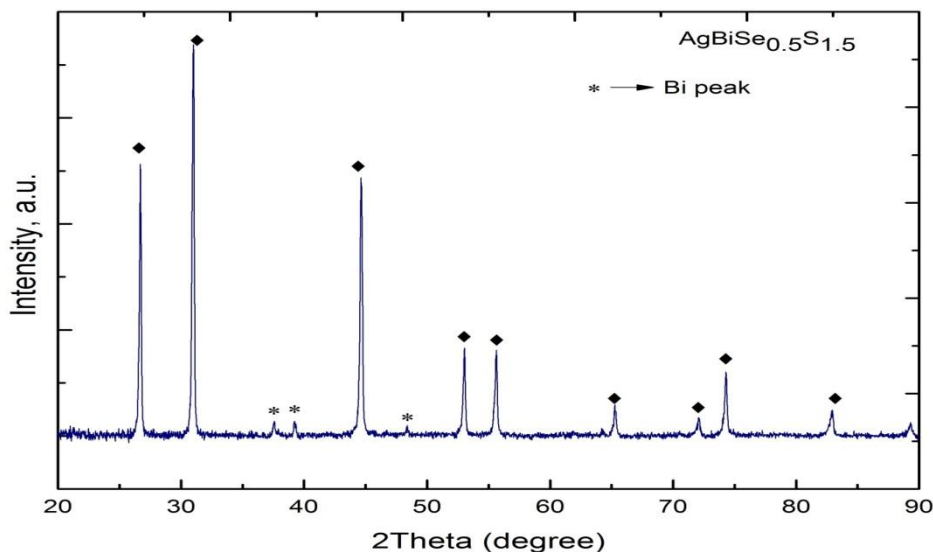


Figure 3-52: XRD pattern of composition $\text{AgBiSe}_{0.5}\text{S}_{1.5}$.

Here, in this XRD analysis, we observe a single cubic pattern matched with the XRD database pattern with reference code (01-089-3673), the main cubic peaks are indicated with a symbol (◆). This pattern also contains the secondary phase of bismuth indicated by a (*) symbol in the pattern itself. This means that the final synthesis product contains little bismuth and that there are no traces of silver, selenium and sulfur according to the XRD result; as silver is slightly sticky and selenium and sulfur are volatile in nature, it indicates an excess of Bi in the synthesis. So, as per this result, we choose to do the future synthesis by preparing the samples with less bismuth in it.

At first, we prepared the samples with the nominal composition (2% deficiency of Bi) $\text{AgBi}_{0.98}\text{Se}_{2-x}\text{S}_x$ belonging to the solid solution of AgBiSe_2 - AgBiS_2 . In total, there is a set of 21 possible compositions by varying x value from 0 to 2 with steps of 0.1. These compositions were synthesized by following one step solid state reaction. The reaction is shown below:





For $\text{AgBi}_{0.98}\text{Se}_{2-x}\text{S}_x$,



A sample of total mass 4.5g was prepared for each composition by mixing desired amount of precursors. The mass of each precursor was weighed in stoichiometric amount to form 4.5 gram in total. The calculated mass values of precursors are given in annex A. During this step of weighing, the silver powder is very fine and sticks to the aluminum foil, so the quantity of silver powder was measured in slight excess in order to compensate for non stoichiometry of silver. Once all the

precursors were weighed, they were mixed and grinded manually by agate mortar. The powder sample of 4.5g was then turned into bar shape pellets by using a proper system and pressing device, shown in Table 4. Out of 4.5g of sample, we made total eight bar shape pellet each of mass 0.5625g.

Table 4: Systems to make bar shape pellet.

 <p>Steps of arranging the whole system → used for making bar shape pellet</p>	 <p>Weighing machine → Used to measure mass of precursors</p>	 <p>Uniaxial pressing device → Used to make bar shape</p>	 <p>Bar shape pellet → each of size 3*3*12 mm³</p>
---	--	---	--

3.2.2 Heat treatment and water quenching

This section mainly contains the details of the synthesis steps followed to obtain the room temperature hexagonal phase and high temperature cubic phase for all the compositions.

The most common way of reacting precursors to form the various compositions is solid state synthesis. This is possible by heat treating the stoichiometric amount of starting material in a controlled atmosphere or vacuum. The strategy is to first increase the temperature below the melting point of the compounds and held until the elements react and then cooled down at a controlled rate to room temperature to obtain the final product. Alternatively, the temperature is raised further in the beginning for melting the starting material and achieves proper mixing before the cooling step.

At the very beginning, the mixture of high purity precursors (Ag, Bi, Se, and S) was placed in a smaller diameter silica crucible, schematically shown in Figure 3-53. It was then sealed within a

silica tube under argon atmosphere before being heated inside the furnace. The whole preparation for the heat treatment is shown below:

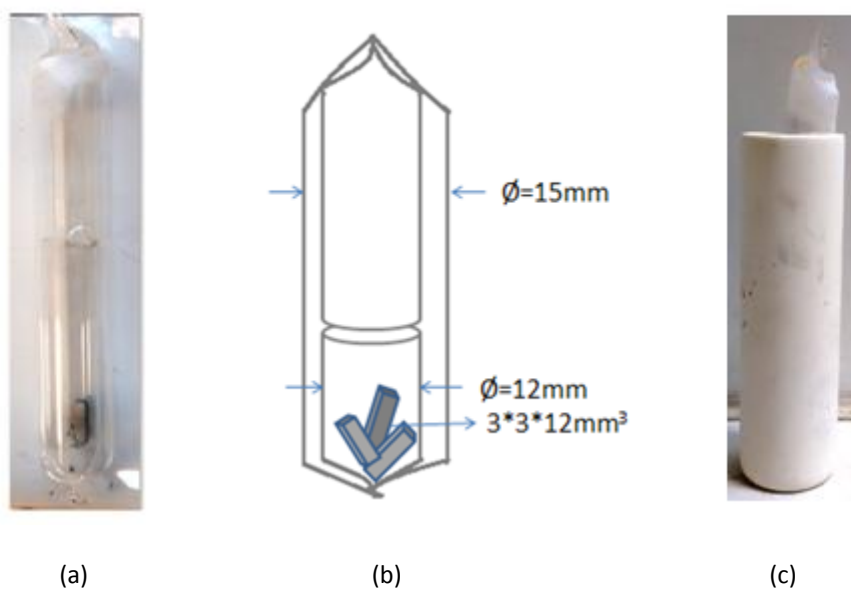


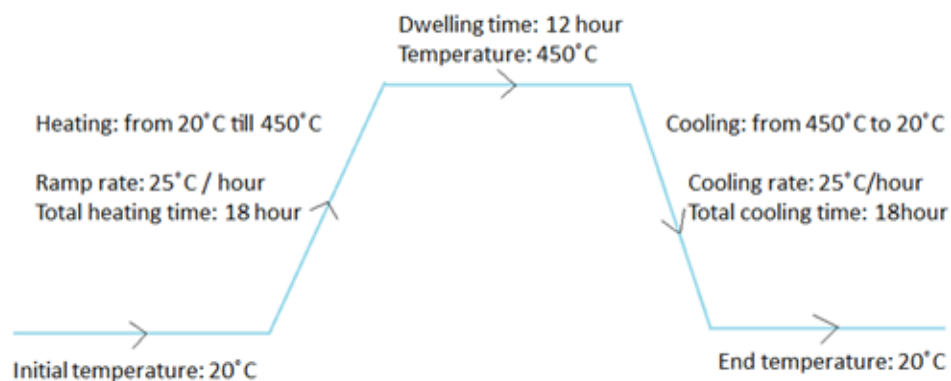
Figure 3-53:(a) Sealed silica glass tube with material inside (bar shape pellet) (b) Schematic drawing of sealed silica tube with bar shape pellets, (c) the very same sealed silica tube inside alumina crucible before being placed inside furnace.

As we see in Figure 3-53(b), for sealing, a small glass tube was placed above the small crucible; this is to make the mouth of upper sealed glass much stronger. Indeed, if the synthesis route requires water quenching, then this kind of sealing is very helpful. It prevents breaking of glass tube. Moreover, due to this upper glass tube, the small crucible is far enough from the point of sealing and is never in contact with the flame; which is good for the material inside. Indeed, if in case, the contact occurs, it may result in volatilization of the elements and in turn disturb the whole stoichiometry. So, to avoid such situation, proper sealing as we mentioned above is appropriate. The heat treatment carried out for two series of composition $\text{AgBiSe}_{1-x}\text{S}_{1+x}$ and $\text{AgBiSe}_{1+x}\text{S}_{1-x}$ are described below:

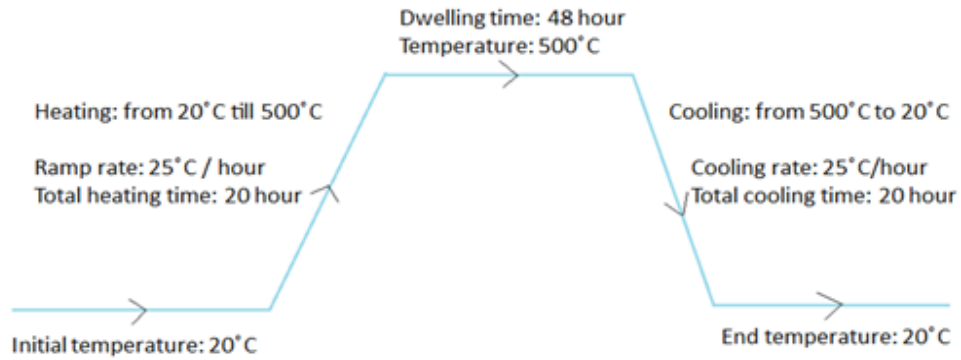
- i) Heat treatment route to trap the cubic phase for these two series:

According to table (annex A), the samples were prepared exactly with this mass value and then sealed inside silica glass tube as shown in Figure 3-53(a). The tubes were then placed vertically inside the high temperature furnace. From the literature on BiAgSeS [186] and from the DSC results, we get the idea of temperature required to synthesize this particular compound but in our

case we use different dwelling time. Our conditions are described here. Firstly, for the compounds belonging to $\text{AgBiSe}_{1-x}\text{S}_{1+x}$, the first heat treatment was carried out at 450°C , dwelled for 12 hours and then slowly cooled down to room temperature. The heating and cooling ramp rate is set at 25°C/hr . Normally, we could choose fast heating rate (for ex. 100°C/hr) but due to the presence of sulfur in our compound, the heating rate was slowed down. The fast heating rate may make sulfur and selenium quickly react with silver and bismuth and lead to explosion inside the furnace due to exothermic reaction. Moreover, if it is heated too quickly, the sulfur may volatilize leading to result that sulfur maybe lack in our compound or the tube may explode due to overpressure. Oppositely, if heated slowly, sulfur may first react slowly with silver and bismuth to form some intermediate compounds, and won't volatilize at high temperature. Secondly, for the compounds belongs to $\text{AgBiSe}_{1+x}\text{S}_{1-x}$: the materials were held at 500°C , dwelled for 48 hours and slowly cooled down to room temperature. The heating and cooling rate was same as mentioned before. The first step initiates the reaction between the precursors (Ag, Bi, Se and S) and prevents the breaking of tubes during second treatment at high temperature. The layout of first heat treatment is shown in Figure 3-54.



(a)



(b)

Figure 3-54: Schematic drawing of first heat treatment conditions for two series (a) $\text{AgBiSe}_{1-x}\text{S}_{1+x}$ and (b) $\text{AgBiSe}_{1+x}\text{S}_{1-x}$.

The second heat treatment for both series was carried out at elevated temperature 850°C to facilitate complete mixing, and was held for 48 hours and then rapidly water quenched at room temperature. At this particular temperature, we noticed that the whole mixture inside the tube is in liquid state before being dipped into the water. The main idea behind this water quenching is to freeze the high temperature cubic phase at room temperature, as the cubic phase is only stable at high temperature. So, this quenching helps to trap this phase and to avoid any phase transformation during the cooling. In other words, water quenching procedure cools down the sample in very short time, that time is too short for a phase to change; as a result it retains the high temperature phase. The layout of second heat treatment is shown in Figure 3-55.

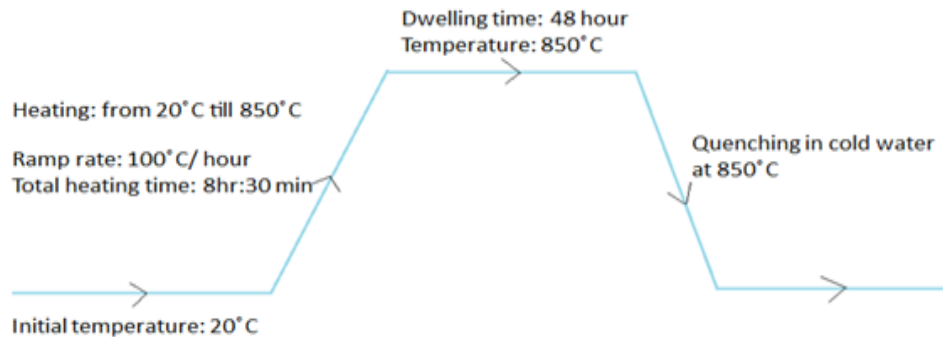


Figure 3-55: Schematic drawing of second heat treatment condition.

- ii) Heat treatment route to obtain the hexagonal phase for the two series $\text{AgBiSe}_{1-x}\text{S}_{1+x}$ and $\text{AgBiSe}_{1+x}\text{S}_{1-x}$:

In this case, the first heat treatment conditions were the same as shown in Figure 3-54. Soon after this, the materials were heated to 850°C at the rate 100°C/hr , held for 48 hours. During this time, the elements were melted and were completely dissolved in the melt. After, the tube was cooled down with a speed 100°C/hr to room temperature. The whole synthesis process was carried out using both high temperature furnace and cylindrical furnace as shown in Table 3. As there was no water quenching step immediately after second heating, so it is convenient to use cylindrical furnace along with the vertical one. Here, we didn't follow the water quenching step. As the samples were cooled down slowly, it takes long time to go to room temperature, so it has enough time to initiate the phase change. The schematic drawing of second heat treatment condition is shown below in Figure 3-56.

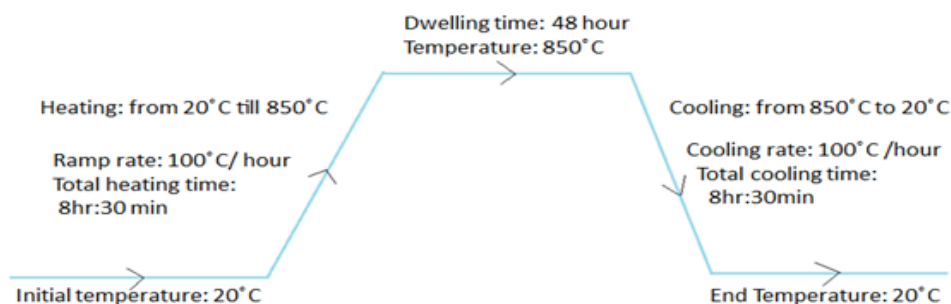


Figure 3-56: Schematic drawing of second heat treatment for both the series $\text{AgBiSe}_{1-x}\text{S}_{1+x}$ and $\text{AgBiSe}_{1+x}\text{S}_{1-x}$.

After the synthesis, the samples were hammered out of the sealed silica tube. The ingots obtained were solid dense big chunks with silvery shine shown in Figure 3-57.



Figure 3-57: Ingot obtained after synthesis using (a) vertical furnace and b) horizontal cylindrical furnace.

Further annealing was run after the second heat treatment. The as synthesized solid chunks were sealed again and kept at 140°C (a small furnace in the lab) for prolonged annealing time (one month). The choice of this temperature came from the DSC analysis; the phase transition was at low temperature, so the annealing temperature should be lower than this temperature and also it requires longer time as the diffusion process is very slow at this lower temperature. Another factor is the time in this diffusion process, the longer the time, the more uniform the phase will be; so we kept all our 21 samples together inside the furnace to obtain the hexagonal phase.

3.3 Result of structural and thermal analysis

For structural investigations, the series of samples with composition $\text{AgBiSe}_{2-x}\text{S}_x$ were characterized by X-ray diffraction (XRD). The lattice parameters were determined from the X-ray patterns by the Le Bail refinement method. We choose to do the Le Bail refinement instead of Reitveld refinement because at the beginning our Reitveld refinements of the hexagonal phase patterns were not satisfying. Indeed, the hexagonal structure of AgBiSe_2 consists of an ordered arrangement of silver and bismuth. In our first attempts, we failed to obtain a good refinement of the intensities of the peaks using Reitveld method; the probable reason could be a partial disordering of the atoms in our structure which we failed to simulate from laboratory XRD patterns.

3.3.1 Powder X-ray diffraction (PXRD)

Powder X-ray diffraction studies of all the samples were performed at room temperature under the specification; 2θ varies from 20° to 120° with step size 0.00835° and time per step 500. The final diffraction patterns were extracted after long execution time (more than 12hrs). The small step and long time helps in increasing the resolution and the quality of measurements. For short execution time at large angles, the intensity will be small for small peaks as in the same order of magnitude as noise; so it's difficult to detect the small peaks. On the other hand, for the long execution time, the noise level remains same but the intensity of the peaks grows and can be easily detected. This means we improve the overall signal to noise ratio by performing the measurements for longer time, especially at the large angles where intensities are low. Thus, the long execution time provides a XRD pattern with larger number of peaks preferable for the precise refinement. The first XRD analysis of long time annealed samples (sec. 3.2.2) were shown in Figure 3-58(a) & (c). Two XRD full scale patterns are shown separately below in Figure 3-58(b,d), to clearly observe the peaks at higher angle. All the diffraction lines for every sample match well with the standard

diffraction data. The patterns reveal that the materials with the nominal composition $\text{AgBi}_{0.98}\text{Se}_{2-x}\text{S}_x$ consist of the main hexagonal phase with a space group (P -3 m 1). Moreover, there is no evidence of any secondary phase within the detection limits of powder XRD.

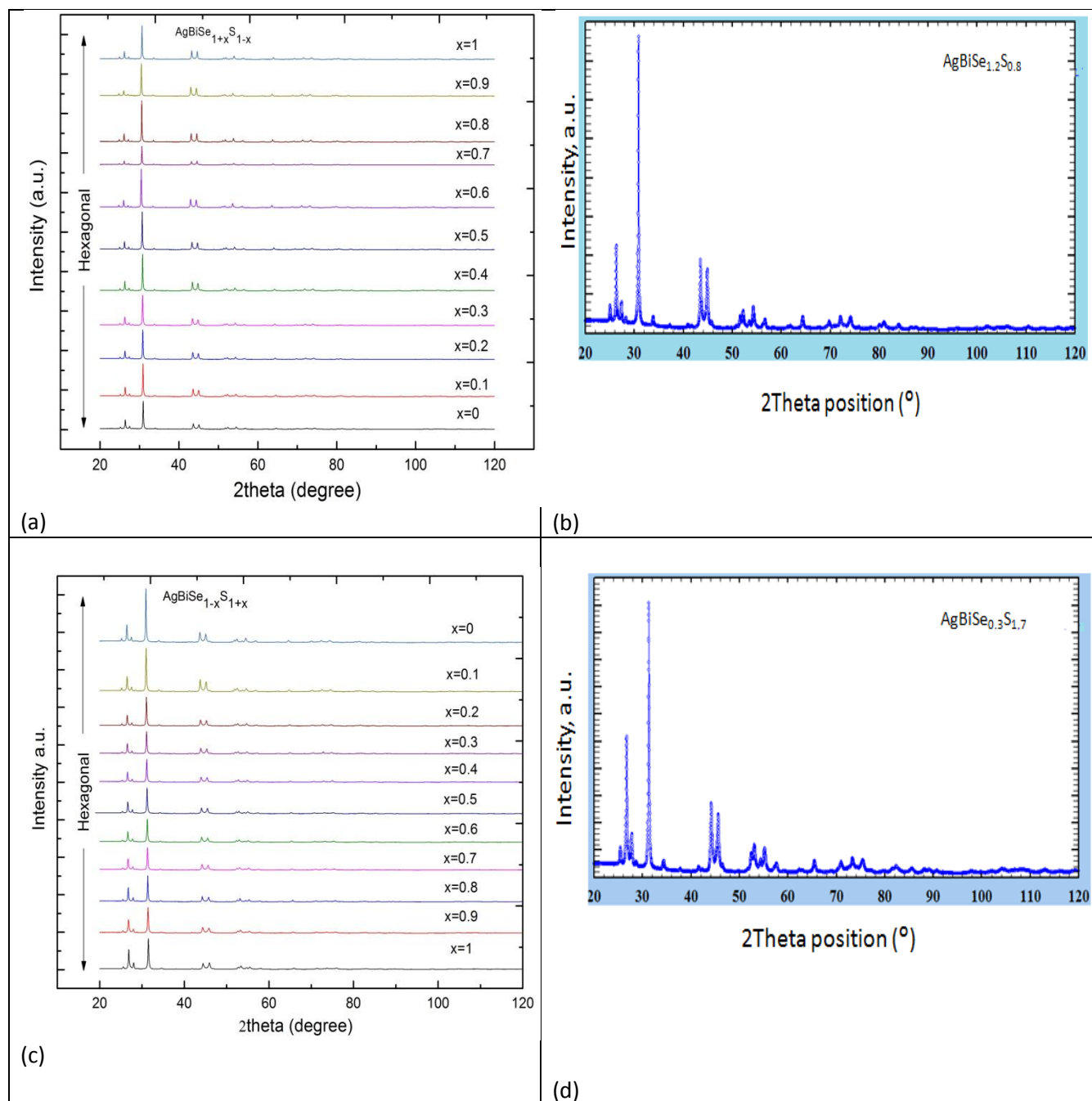


Figure 3-58: (a-d) XRD patterns of $\text{AgBiSe}_{1+x}\text{S}_{1-x}$ and $\text{AgBiSe}_{1-x}\text{S}_{1+x}$ samples: reveals hexagonal phase.

The second XRD analyses of quenched samples at room temperature are shown in Figure 3-59(a,c). Two XRD full scale patterns are shown separately below in Figure 3-59(b,d), to clearly observe the peaks at higher angle. All patterns are assigned to cubic phase (Fm-3m group) without any indication of secondary phase impurities.

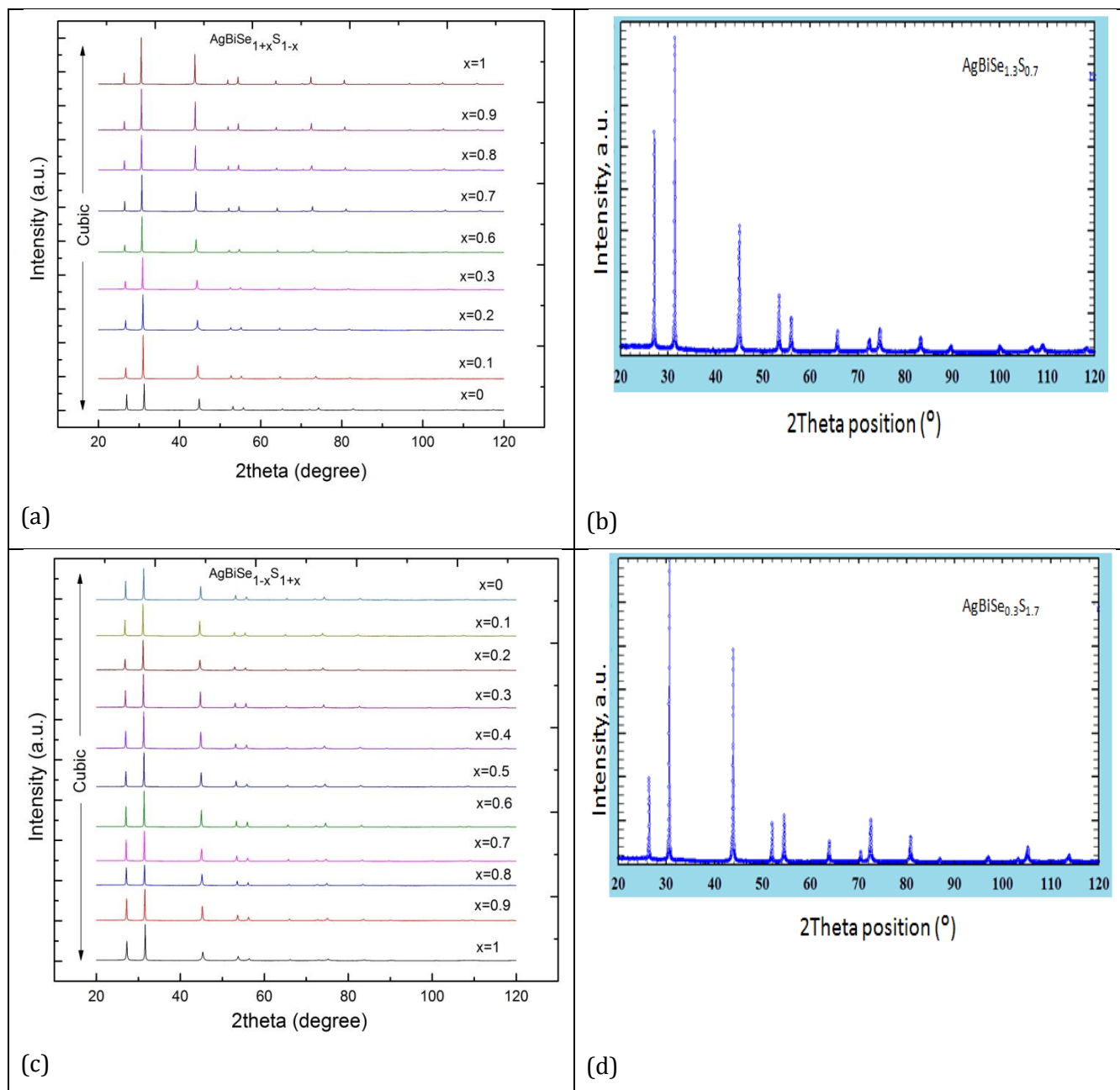


Figure 3-59: (a-d) XRD patterns of $\text{AgBiSe}_{1+x}\text{S}_{1-x}$ and $\text{AgBiSe}_{1-x}\text{S}_{1+x}$ samples: reveals cubic phase.

If we observe the XRD patterns carefully, the peaks are shifted little from each other, Figure 3-60 demonstrates that the XRD peaks slightly shift to the lower angles with the increasing Se percentage or in other words with decreasing S percentage. The shift could indicate a variation of the lattice parameters.

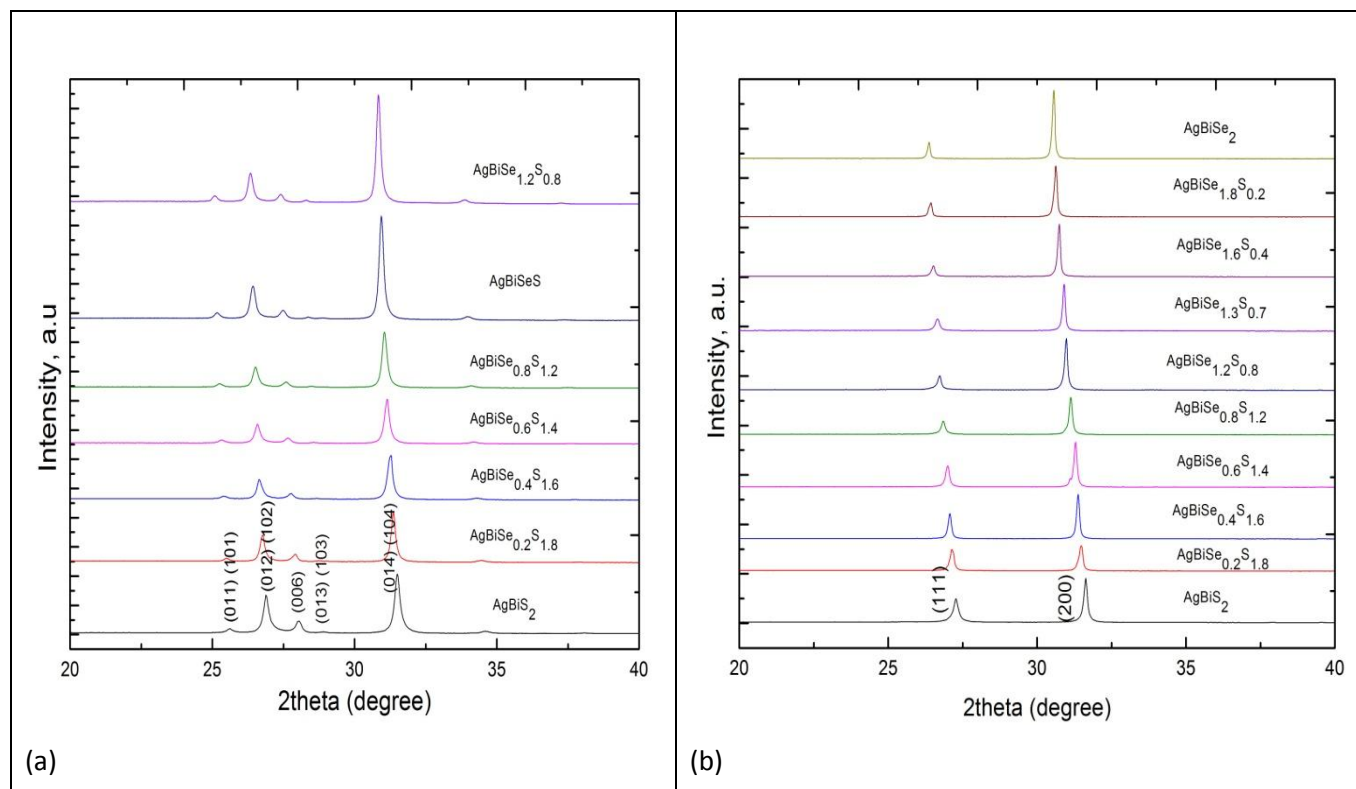


Figure 3-60: Regular shift in the XRD peaks (a) samples with hexagonal phase and (b) samples with cubic phase.

Till now, we observed that all compositions of the solid solution possess both the hexagonal and cubic phase. Particularly, to compare with the literature, here, we have summarized the XRD pattern in one single plot, in Figure 3-61. It shows that both the compounds AgBiSe_2 and AgBiS_2 , crystallizes in a hexagonal and cubic phase, depending on the synthesis process.

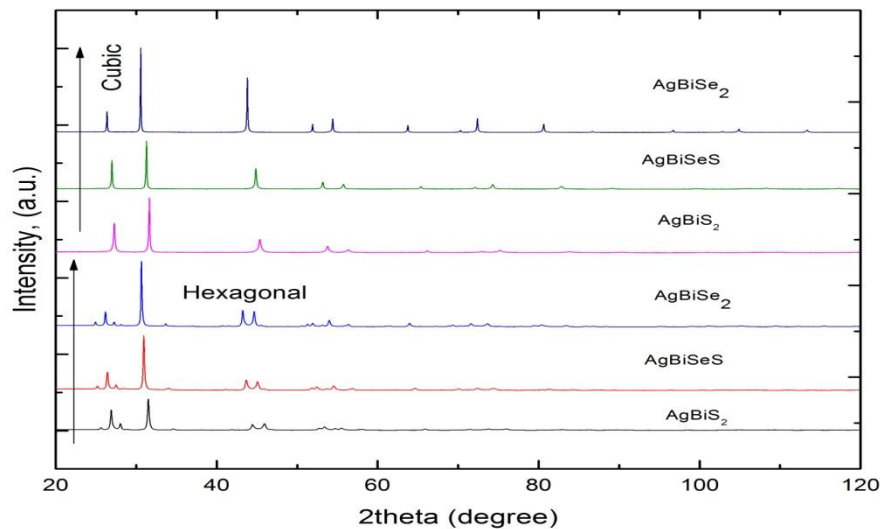
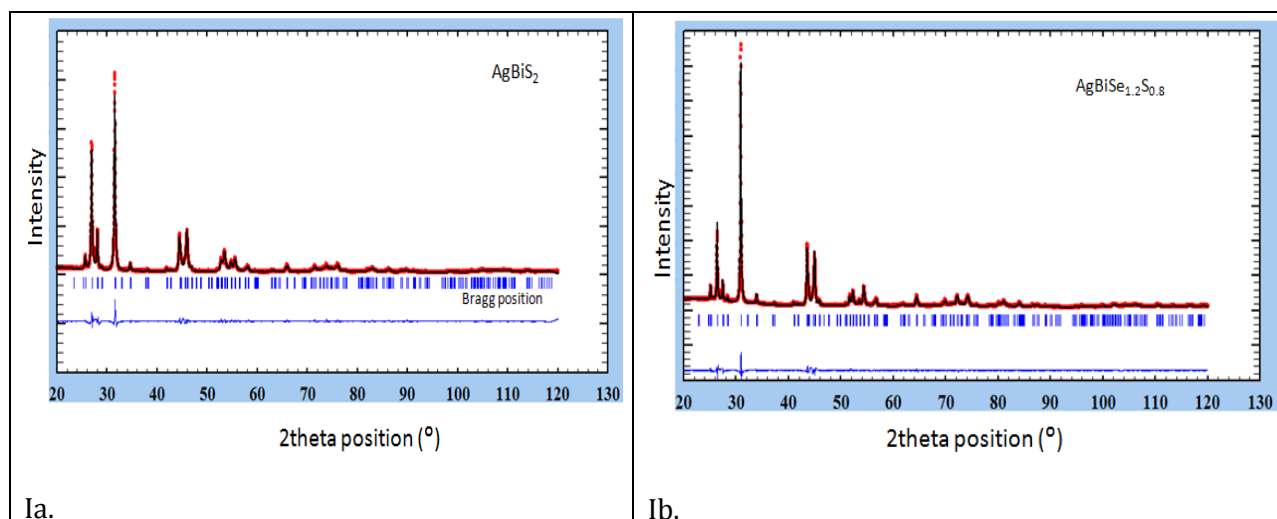


Figure 3-61: XRD plots for comparison.

3.3.1.1 Determination of lattice parameters

From the powder XRD data patterns (sec.3.3.1), the lattice parameters were calculated using Le Bail refinement with FULLPROF software. Here, in this refinement, the intensities of the individual peaks are no longer treated as least-squares parameters and are never refined. As a result, each cycle of least-squares is very fast since the matrix remains small. Here, we have shown the examples of some refinement for both the phase in Figure 3-62. Figure 3-62 reveals a good agreement between the observed XRD patterns and the refinements which are evidenced by the small residual. The obtained lattice parameters value for both the hexagonal and cubic phase samples are tabulated in Table 5.



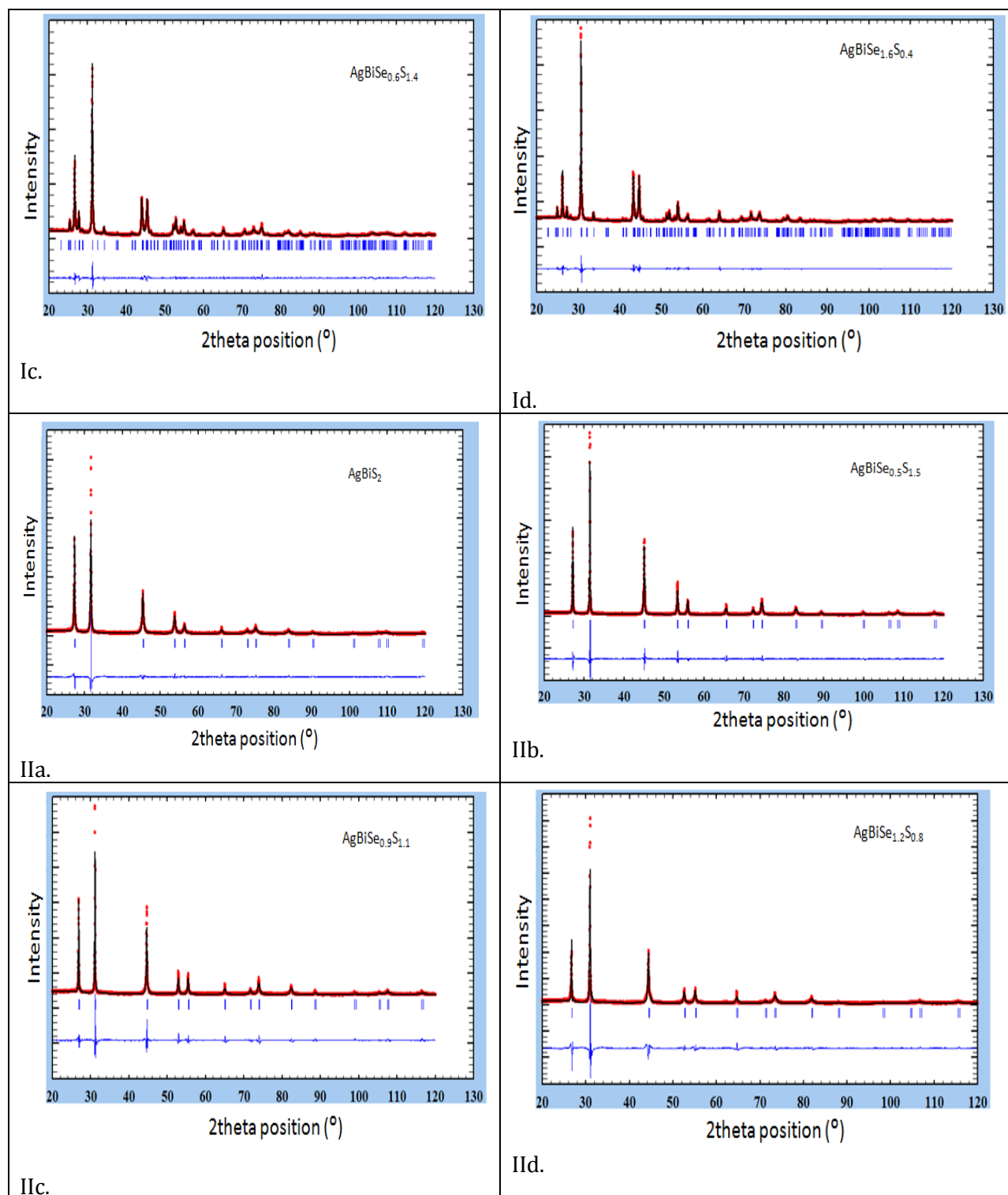


Figure 3-62: Refinement pattern of samples with hexagonal (Ia-Id) and cubic (IIa-IId) phase; the solid black line represents the refinements performed, the red line represents the measured XRD patterns and the blue line at the bottom is the residual.

Table 5: Lattice parameter values for all the samples with hexagonal phase and cubic phase. For the gap in the “cubic” column, see below.

Compositions	Hexagonal		Cubic
	a (Å)=b(Å)	c (Å)	a=b=c (Å)
AgBiSe ₂	4.070	19.047	5.647
AgBiSe _{0.1} S _{1.9}	4.076	19.078	5.659
AgBiSe _{0.2} S _{1.8}	4.083	19.104	5.667
AgBiSe _{0.3} S _{1.7}	4.088	19.154	5.680
AgBiSe _{0.4} S _{1.6}	4.095	19.185	5.686
AgBiSe _{0.5} S _{1.5}	4.101	19.220	5.694
AgBiSe _{0.6} S _{1.4}	4.108	19.257	5.706
AgBiSe _{0.7} S _{1.3}	4.116	19.291	5.713
AgBiSe _{0.8} S _{1.2}	4.122	19.324	5.725
AgBiSe _{0.9} S _{1.1}	4.128	19.355	5.730
AgBiSeS	4.137	19.390	5.739
AgBiSe _{1.1} S _{0.9}	4.143	19.418	5.753
AgBiSe _{1.2} S _{0.8}	4.149	19.444	5.760
AgBiSe _{1.3} S _{0.7}	4.155	19.487	5.766
AgBiSe _{1.4} S _{0.6}	4.163	19.508	-
AgBiSe _{1.5} S _{0.5}	4.169	19.538	-
AgBiSe _{1.6} S _{0.4}	4.176	19.563	5.801
AgBiSe _{1.7} S _{0.3}	4.183	19.591	5.811
AgBiSe _{1.8} S _{0.2}	4.189	19.621	5.821
AgBiSe _{1.9} S _{0.1}	4.194	19.647	5.832
AgBiSe ₂	4.199	19.659	5.833

Based on these refinements, the lattice parameters are plotted in Figure 3-63(a & b).

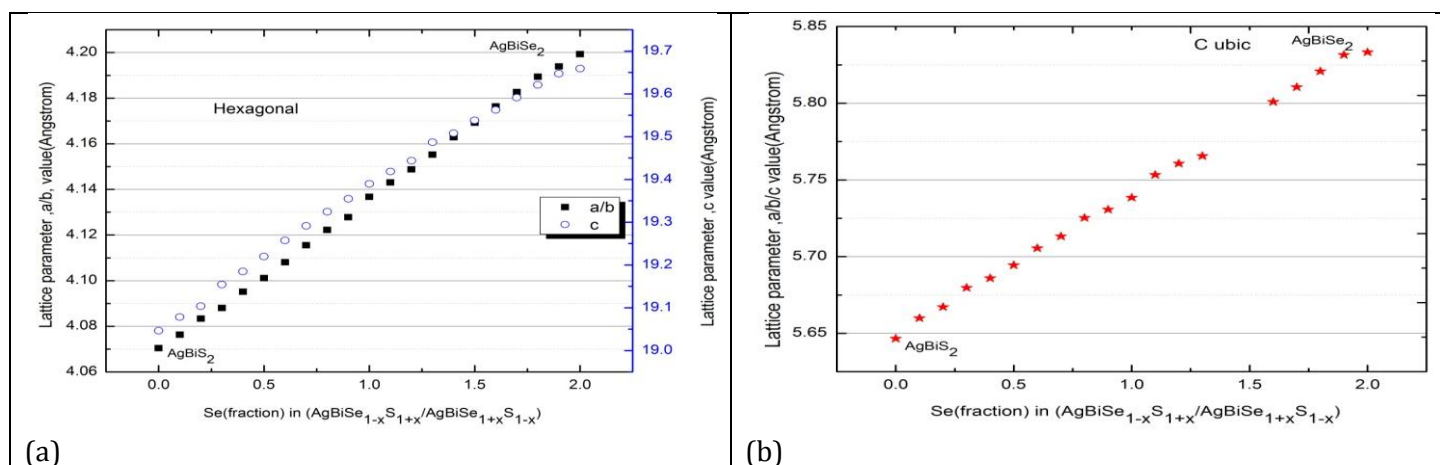


Figure 3-63: Lattice parameters Vs Se content in $(\text{AgBiSe}_{1+x}\text{S}_{1-x})$ and $(\text{AgBiSe}_{1-x}\text{S}_{1+x})$; (a) samples with hexagonal phase and (b) samples with cubic phase.

Figure 3-60 and Figure 3-63 shows a systematic peak shift towards lower angle and the linear expansion in the lattice parameters with increasing Se content (or decreasing S content) indicating the Vegard's law for the complete solid solution. The ionic radius of Se is larger than that of S. So, as higher content of Se is introduced in the solid solution in comparison to the sulfur, the unit cell undergoes a systematic expansion, and this result in a monotonous increase in the lattice parameters with Se percentage. The linear dependence of the lattice parameters also indicates a complete homogeneous solid solution with no miscibility gap. In Figure 3-63(b), we notice a gap in the linear plot, this appears due to unavailability of two samples $\text{AgBiSe}_{1.5}\text{S}_{0.5}$ and $\text{AgBiSe}_{1.4}\text{S}_{0.4}$; as we were unable to collect the two samples due to imperfect quenching and silica tubes got damaged. The detailed description is presented in the following paragraph.

At first, if we consider the rock-salt structure, the expected lattice parameter value for the AgBiSe_2 is 6.14 Å, if we assume ionic bonding with ionic radii of Ag^+ (1.15 Å), Bi^{3+} (1.03 Å) and Se^{2-} (1.98 Å). In our case, we got the experimental value 5.83 Å. This implies that the compound is not fully ionic, but which is relevant as the Se is not so electronegative in nature. So, it is expected to show slight covalent character. Secondly, the expected lattice parameter for AgBiS_2 with ionic radius of S^{2-} (1.84 Å) is 5.86 Å, if it's fully ionic. In our case, we have obtained the value 5.64 Å, which means it's also not fully ionic but closer to the expected value. This calculation shows that with sulfur, the ionic nature is a little bit more pronounced as compared to the Se; because sulfur is more electronegative than selenium. Further, the ionic radius of Se is 1.98 Å and for S the value is 1.84 Å. If we calculate, the size of Se is 7.6% larger than the size of S. Our structure contains half chalcogens and half metals and metals will not change, so, if the chalcogen size increases by 7.6%, the lattice parameter should increase by 3.8%. So, if we increase the lattice value of AgBiS_2 (5.64 Å) by 3.8%, the lattice value for AgBiSe_2 is 5.85 Å. But, in our case the experimental lattice value is 5.83 Å, slightly smaller, which means the bonding will be slightly more covalent with Se content. And also, the lattice parameter value in our case increased by 3.4% not so far from the expected one. The lattice parameters increase linearly, it means this is only linked with the increase in size and leads to expansion of the structure. And also the overlap of the orbital's is quite similar. For the hexagonal phase also, the experimental percentage increase is 3.2% which is also very close to the expected one. Hence, as in our case, the lattice parameters vary linearly in both the cases, which means it only depends on the size, no other physical reason behind this. Moreover, it confirms that there is a complete solid solution with no miscibility gap.

3.3.2 DSC (Differential Scanning calorimetry)

To examine the phase transitions of the obtained samples accurately, the DSC heat flow curves were measured, using hexagonal phase samples shown in 3.3.1. This thermal analysis was done in the temperature range from 30°C to 500°C. The mass of the sample used ranged from 80.2 to 80.5 mg. The first DSC analyses of the samples with nominal composition $\text{AgBiSe}_{1-x}\text{S}_{1+x}$ ($0.1 \leq x \leq 1$) are shown in Figure 3-64. It reveals the presence of only one endothermic peak suggesting the presence of one phase transition which can be designated as ($\alpha \rightarrow \gamma$). For one sample ($x=0.6$), we noticed another peak marked with an arrow in the curve with the temperature value, this peak corresponds to the peak of selenium whose melting point is close to the temperature. The heat flow curves show a systematic shift of the endothermic peaks (dotted area) towards higher value of temperature with increasing Se content (or with decreasing S content) in $\text{AgBiSe}_{1-x}\text{S}_{1+x}$. Moreover, there is no second phase transition for these samples, with a direct transition from room temperature hexagonal phase to high temperature cubic phase, and no other intermediate phase for these samples.

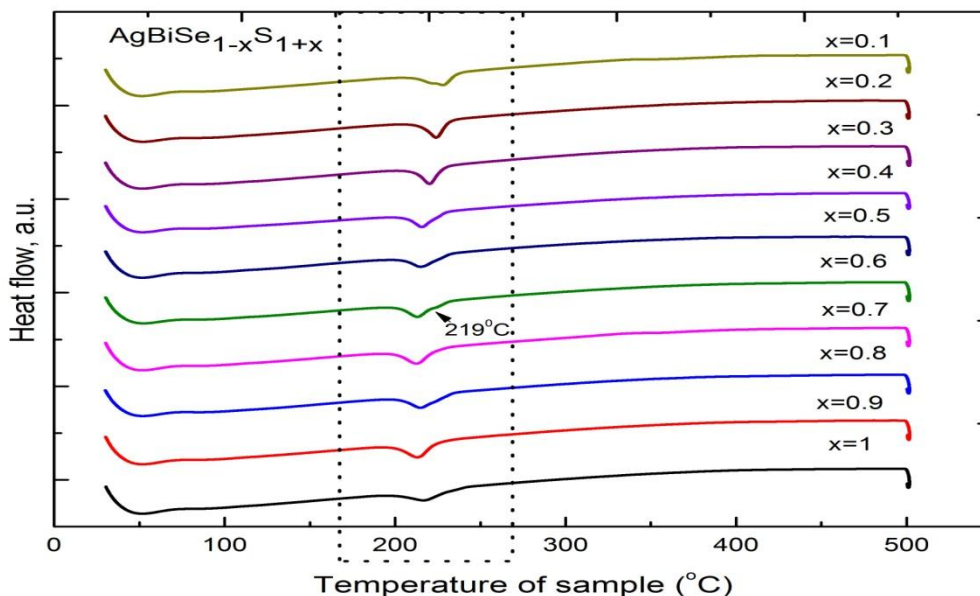
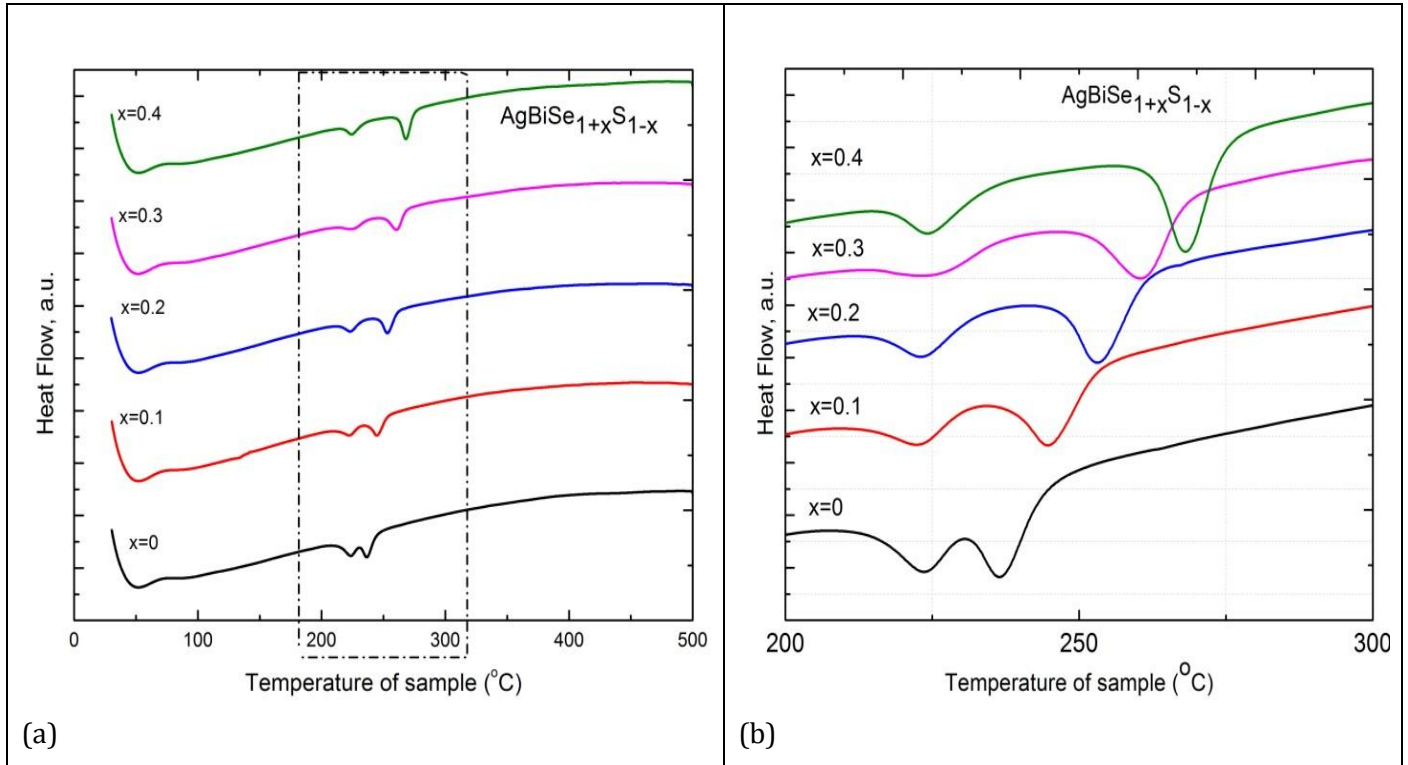


Figure 3-64: DSC curves of solid solution $\text{AgBiSe}_{1-x}\text{S}_{1+x}$ ($0.1 \leq x \leq 1$) indicate one phase transition for all the compositions.

The second DSC heat flow curves recorded for the other compositions $\text{AgBiSe}_{1+x}\text{S}_{1-x}$, ($0 \leq x \leq 1$) are shown in Figure 3-65(a & c). In the Figure 3-65(a) and (c), two clearly visible endothermic peaks are spotted for all the samples; representing two phase transition points which can be noted as ($\alpha \rightarrow \beta \rightarrow \gamma$). The DSC plots are zoomed at the particular region of transition and are shown in Figure 3-

65(b) and (d). In accordance to DSC result, XRD results also show two different phases for this composition $\text{AgBiSe}_{1+x}\text{S}_{1-x}$; namely room temperature hexagonal phase and high temperature cubic phase. But the intermediate phase was not observed in the XRD patterns and is yet to find out. However, a rhombohedral phase has been observed in the literature for AgBiSe_2 . Also, there is a regular shift of the endothermic peaks to the higher temperature with the increasing Se content in the solid solutions. The effective transition zone is marked within the graph itself. Here, we noticed that the magnitude of the peaks changes going from one composition to another. This change could be analyzed by integrating the area under the each curve which gives the enthalpy change during the transition. We plotted the area under the peaks for all curves in Figure 3-66. In Figure 3-66 (a), we can notice that the area values are nearly same whereas Figure 3-66 (b) shows a variation.



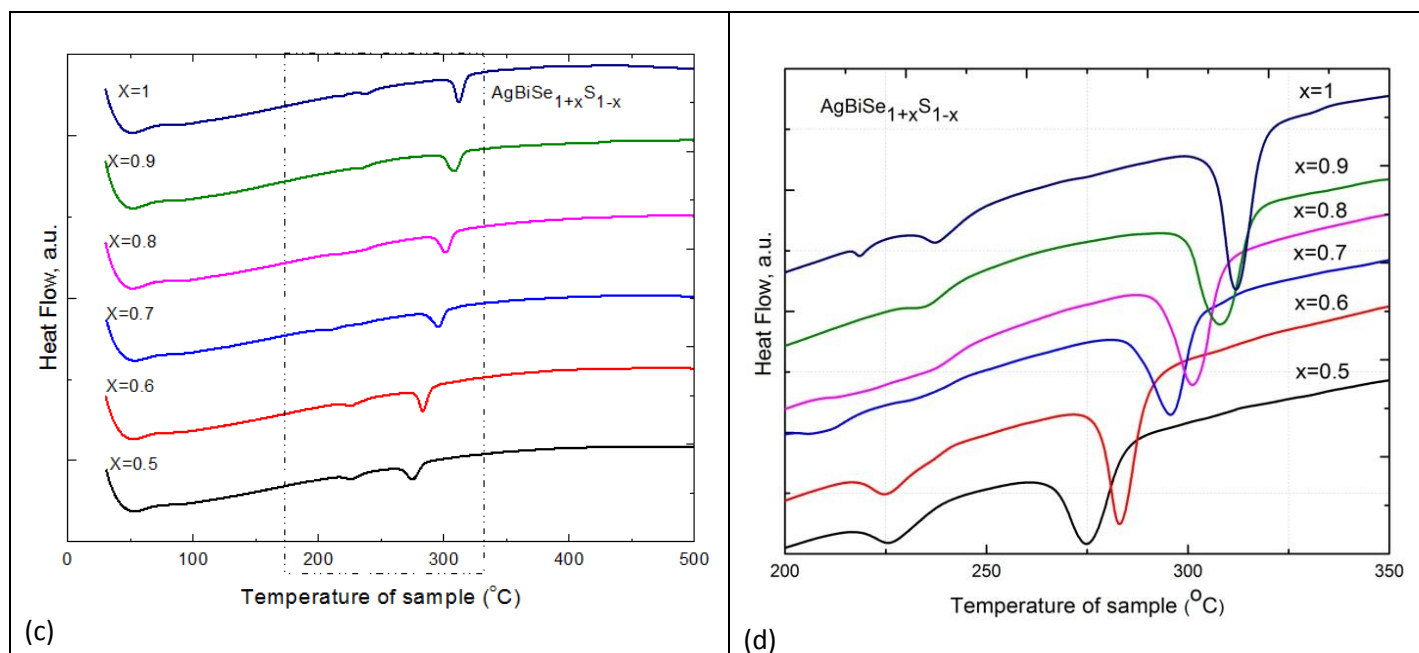


Figure 3-65: (a-d) DSC curves of solid solutions $\text{AgBiSe}_{1-x}\text{S}_{1+x}$ ($0 \leq x \leq 1$) indicate phase transition ($\alpha \rightarrow \beta \rightarrow \gamma$).

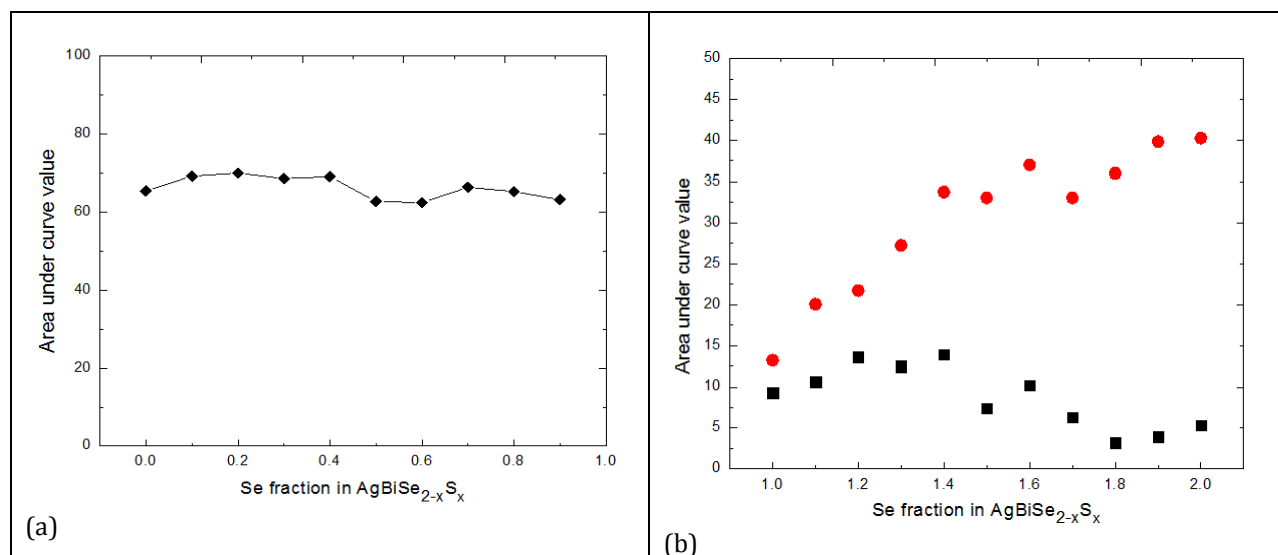


Figure 3-66: Plots of area under the curve values of $\text{AgBiSe}_{2-x}\text{S}_x$ vs. the selenium fraction; (a) samples with one phase transition and (b) samples with two phase transition.

We can see that the enthalpy change during the second phase transition in $\text{AgBiSe}_{1+x}\text{S}_{1-x}$ ($0 \leq x \leq 1$) increases when the selenium fraction increases. However, we are not able to give an explanation to this phenomenon.

Therefore, on the basis of the XRD patterns and DSC analyses, we conclude that for the solid solution with compositions $\text{AgBiSe}_{1-x}\text{S}_{1+x}$ ($0.1 \leq x \leq 1$), only one phase transition point (phase change, $\alpha \rightarrow \beta$) is present whereas for $\text{AgBiSe}_{1+x}\text{S}_{1-x}$ ($0 \leq x \leq 1$), two phase transition points ($\alpha \rightarrow \beta \rightarrow \gamma$) are present. The intermediate phase is not yet proved by XRD, however the rhombohedral phase has been observed in the literature for AgBiSe_2 . The heat flow curves also give information about the temperatures corresponding to the transition point for each sample. The corresponding phase diagram is shown in Figure 3-67, with the temperature Vs the concentration of Selenium in the compounds.

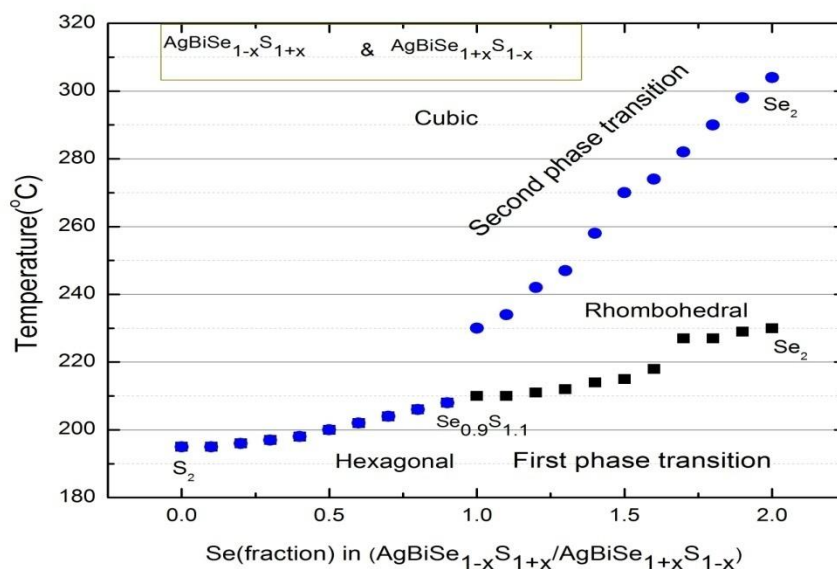
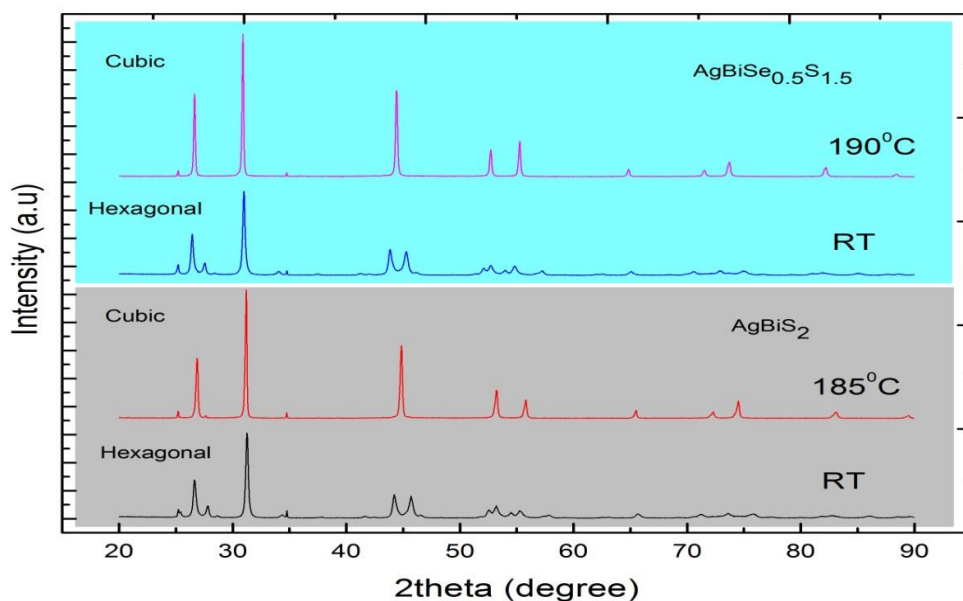


Figure 3-67: Structural phase diagram with temperature from DSC curve Vs Se content in the solid solutions.

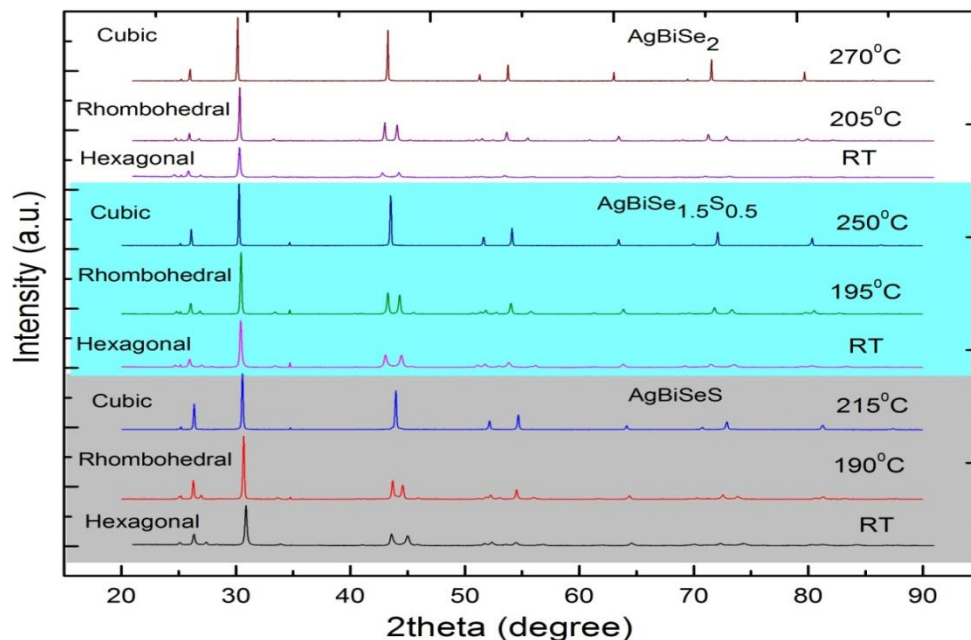
3.3.2.1 Comparative study (DSC and HT-XRD)

Further, to confirm the DSC results, temperature dependent XRD was performed for five selected samples, shown in Figure 3-68. We choose here these five samples to cover the whole range of compositions of the solid solution from pure AgBiSe_2 to pure AgBiS_2 . From DSC we noticed that some samples show one phase transition while some other shows two phase transition. So, to do the analysis, five samples are chosen according to that. The patterns clearly show that for the two samples AgBiS_2 and $\text{AgBiSe}_{0.5}\text{S}_{1.5}$, the structural transition from the hexagonal (space group $P-3m1$) to the cubic phase ($F-3m1$) is direct. On the contrary, for the other compositions, the transition occurs as hexagonal-rhombohedral (space group $R-3m$)-cubic phase. This result is in well consistency with the DSC one. However, due to some errors in the calibration of the HT-XRD

furnace, the temperatures noted down during the HT-XRD experiments were slightly different from the actual one. Hence, we can the transition temperatures are slightly higher than what we observed in DSC. Here, we distinguish between the two patterns hexagonal and rhombohedral by observing the differences in the peaks; first within the angle range 20° to 30° , hexagonal pattern contains four peak (the relative intensity of the fourth one is very small) while the rhombohedral pattern contains three peaks. In addition, we observed two peaks with greater intensity lying between the angles 40° to 50° , the distance between them is not similar for both the patterns. The distance is slightly larger in hexagonal pattern as compare to the rhombohedral one. However, these differences are rather faint which makes it difficult to differentiate these two patterns (especially if a mixture of both phases is present).



(a)



(b)

Figure 3-68: Temperature dependent XRD patterns of samples: revealing the type of phases.

These XRD patterns were refined using the Le Bail refinement method to obtain the lattice parameters. Here, we have shown some of the examples of refined patterns in Figure 3-69. The small residual gives a clear-cut evidence of a good agreement between the observed pattern and the refined pattern. The red stars symbol in the refined patterns shows the peak which arises from the sample holder, and does not belongs to the main pattern. From these refinements, the lattice parameters and volume per formula unit for each specific sample were determined and presented in Table 6.

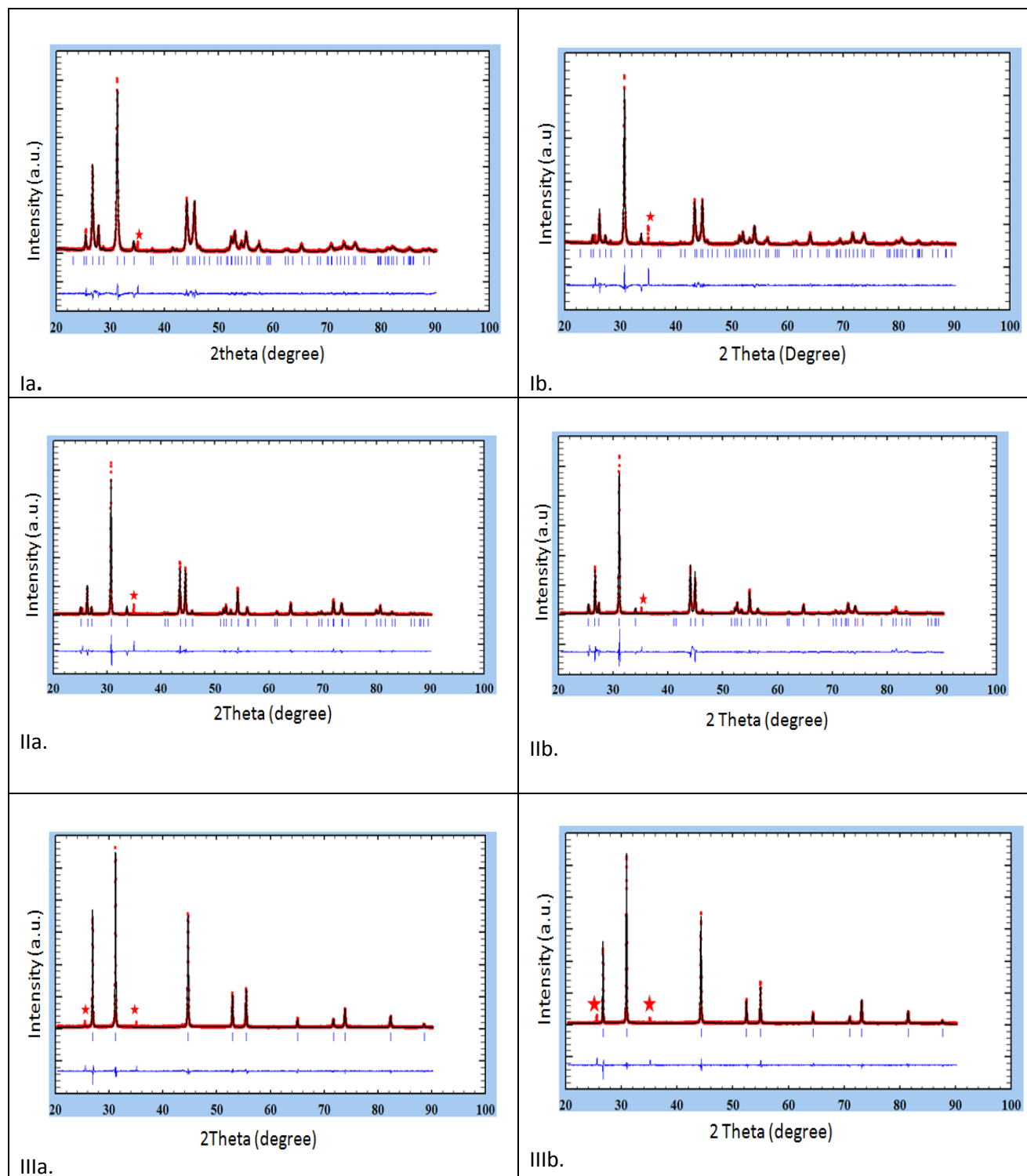


Figure 3-69: The picture of refined XRD patterns; the solid black line represents the refinements performed, the red line represents the measured XRD patterns and the blue line at the bottom is the residual: Hexagonal pattern (Ia & Ib), rhombohedral pattern (IIa & IIb) and cubic patterns (IIIa & IIIb).

Table 6: Lattice parameters values determined by Le Bail refinement. The values of volume per formula unit are calculated from the parameters.

AgBiS ₂				
Structure name	Temp. (°C)	a/b (Å)	c (Å)	Volume/Z (Å ³)
Hexagonal	25	4.069	19.042	91.011
Hexagonal	50	4.070	19.056	91.099
Hexagonal	150	4.072	19.144	91.617
Cubic	185	5.672	5.672	91.257
Cubic	195	5.679	5.679	91.557
Cubic	205	5.681	5.681	91.654
Cubic	215	5.684	5.684	91.806
AgBiSe _{0.5} S _{1.5}				
Hexagonal	25	4.099	19.215	93.196
Hexagonal	50	4.099	19.231	93.292
Hexagonal	150	4.099	19.305	93.678
Hexagonal	170	4.094	19.310	93.418
Cubic	190	5.726	5.726	93.860
Cubic	200	5.729	5.729	94.014
Cubic	210	5.731	5.731	94.116
AgBiSeS				
Hexagonal	25	4.135	19.379	95.648
Hexagonal	50	4.136	19.407	95.698
Rhombohedral	195	4.106	19.577	95.290
Cubic	210	5.778	5.778	96.470
Cubic	215	5.779	5.779	96.487
Cubic	220	5.780	5.780	96.524
Cubic	225	5.781	5.781	96.575
Cubic	230	5.786	5.786	96.840
AgBiSe _{1.5} S _{0.5}				
Hexagonal	25	4.167	19.530	97.913
Hexagonal	50	4.170	19.562	98.189
Hexagonal	150	4.171	19.638	98.604
Hexagonal	190	4.143	19.624	97.245
Rhombohedral	195	4.151	19.680	97.897
Rhombohedral	200	4.146	19.633	97.583
Rhombohedral	210	4.146	19.663	97.702
Rhombohedral	220	4.149	19.700	97.879
Cubic	250	5.837	5.837	99.446
Cubic	255	5.838	5.838	99.499
Cubic	260	5.839	5.838	99.532
AgBiSe ₂				
Hexagonal	25	4.198	19.659	99.996
Hexagonal	50	4.198	19.682	100.175
Hexagonal	150	4.199	19.752	100.578
Hexagonal	170	4.199	19.765	100.615
Rhombohedral	190	4.184	19.766	99.866
Rhombohedral	205	4.185	19.804	100.136
Cubic	270	5.894	5.894	102.382
Cubic	280	5.896	5.896	102.490

Based on the Table 6, plots are made below in Figure 3-70(a-c); depicting the variation of lattice parameters with respect to experimental temperature and the temperature dependence of volume per formula unit for each compound.

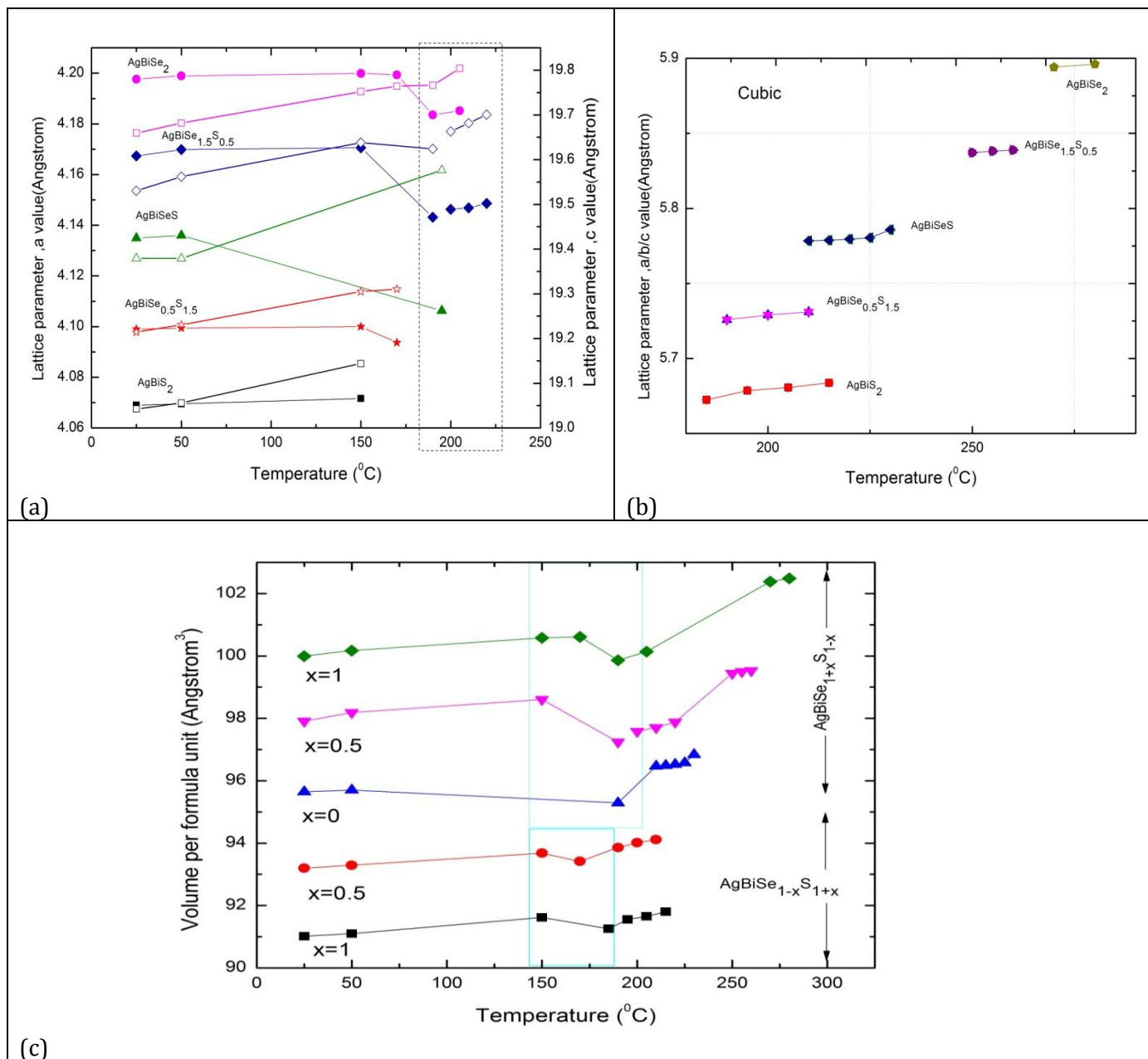


Figure 3-70: (a) shows the lattice parameters variations with temperature, for hexagonal part and rhombohedral part (dotted box), where solid symbol represents the 'a' value and open symbol represents the 'c' value, (b) shows the lattice parameter for the cubic part and (c) plot of volume per formula unit as a function of temperature for the five selected samples.

From Figure 3-70(a) and (b), the lattice parameter plots show the expansion when the selenium fraction increases from one composition to another, and also the thermal expansion for each composition. However, a drop in the values occurs in each case at the phase transition point. The drop in lattice parameter values from hexagonal to rhombohedral is marked with a dotted box shown in the plot itself. Figure 3-70(c) reveals that there is sudden drop in volume which occurs with the increase of temperature near the transition, as shown by the sky-blue box. Again, with further rise in temperature, the volume increases again. This volume change may come from the rearrangement of atomic position. This sudden collapse may affect strongly the material, in other words, detrimental for TE applications, as the materials will break down due to this volume change upon thermal cycling. The collapse in the volume could be understood from the structure shown in Figure 3-71. Figure 3-71 (a) and (b) shows the hexagonal and cubic structure of AgBiSe_2 . In the hexagonal unit cell, half of the cubic polyhedral which surround the Bi/Ag are shown for clarity, and in the cubic unit cell one octahedron around Ag/Bi mixed position in the structure is shown. The polyhedra in case of the hexagonal structure is a distorted cube. While, in the case of the rhombohedral structure, the polyhedra are slightly distorted octahedra. So, moving from hexagonal to rhombohedral and to cubic, there is first a complete rearrangement of the polyhedral which occurs from hexagonal to rhombohedral (or from hexagonal to cubic in the case of only one transition is present), which results in change in volume, and then a disorder-order transition from rhombohedral to cubic. Therefore, we can relate this structural difference with the volume shrinkage in Figure 3-70 (c) at the transition point marked with the box in the figure itself. Moreover, in the table and the curves, we can also notice that the coefficient of thermal expansion is larger in the cubic phase than in the hexagonal one. Therefore in relation to the results explained above, the suppression of the phase transitions is the prime requirement for the applications.

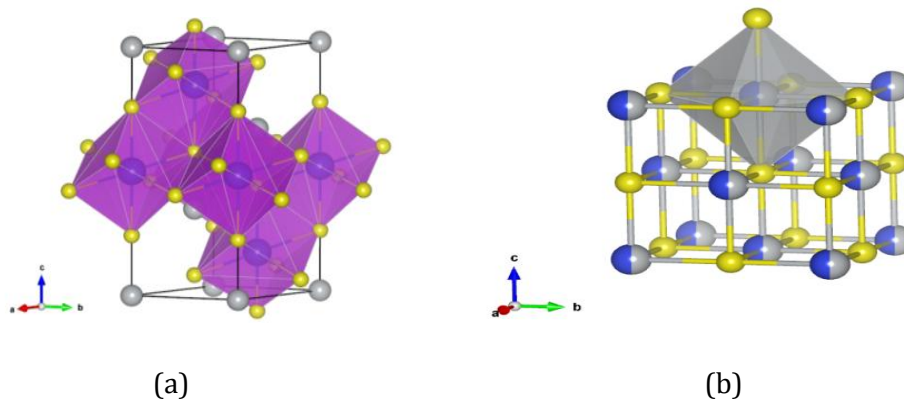


Figure 3-71: Structure of AgBiSe_2 ; (a) hexagonal AgBiSe_2 with Bi or Ag polyhedral and AgBiSe_2 with cubic octahedral.

3.3.3 High pressure measurements

The structural behavior of one sample AgBiSe_2 (this composition corresponds to the end number of the solid solution and possesses the largest temperature for the transitions) was investigated under high pressure conditions. We performed two separate measurements with powder of AgBiSe_2 , one with cubic phase obtained through quenching and another with hexagonal phase obtained after one month annealing. The study of high pressure XRD was performed to check if we get the phase transition (cubic phase by applying pressure), which could mean then through chemical pressure, it would be possible to stabilize this cubic phase. The XRD patterns collected at different pressure in the two different cases are shown below. The evolution of the diffraction patterns with increasing pressure is shown in Figure 3-72 and Figure 3-73. For Figure 3-72, the XRD patterns show no structural changes in the range of experimental pressure up to 18.20 GPa. All the patterns are single cubic phase. Every pattern contains the same peak over the range of 2θ ($2-18^\circ$). There is no appearance and disappearance of new peak in any of these patterns while moving from low to high pressure, thus it represents no phase change behavior. However, upon close examination, a supplementary peak can be observed in some patterns with low intensity. It corresponds to Copper (marked with *), as it was used for the pressure calibration. Further, we noticed that there is a shift in the peaks while moving from low pressure to the higher ones, which corresponds to the contraction of the unit cell with the pressure, which was expected.

For hexagonal sample AgBiSe_2 , the evolution of XRD patterns were examined and plotted in Figure 3-73. At first, from 0.106 GPa to 0.994 GPa, the patterns resembles the hexagonal phase and no significant changes are observed until 0.994 GPa. But, soon after that, in 1.394 GPa XRD pattern, we noticed a change in the pattern, which resembles to rhombohedral structure. There is a disappearance of peak noticed which we observed in the hexagonal pattern marked with a symbol (\blacklozenge) within the curve itself (the intensity of this peak is very low). This change clearly indicates a structural phase transition of AgBiSe_2 , beginning near 1.394 GPa and completing around 13.894 GPa. On other side, a new peak emerges in the patterns from 1.394 GPa to 12.739 GPa, marked with a symbol (\bullet) in the patterns. This peak is same as marked in Figure 3-72, corresponding to the copper. Another change in structure is noticed after 15.995 GPa, which resembles to cubic phase.

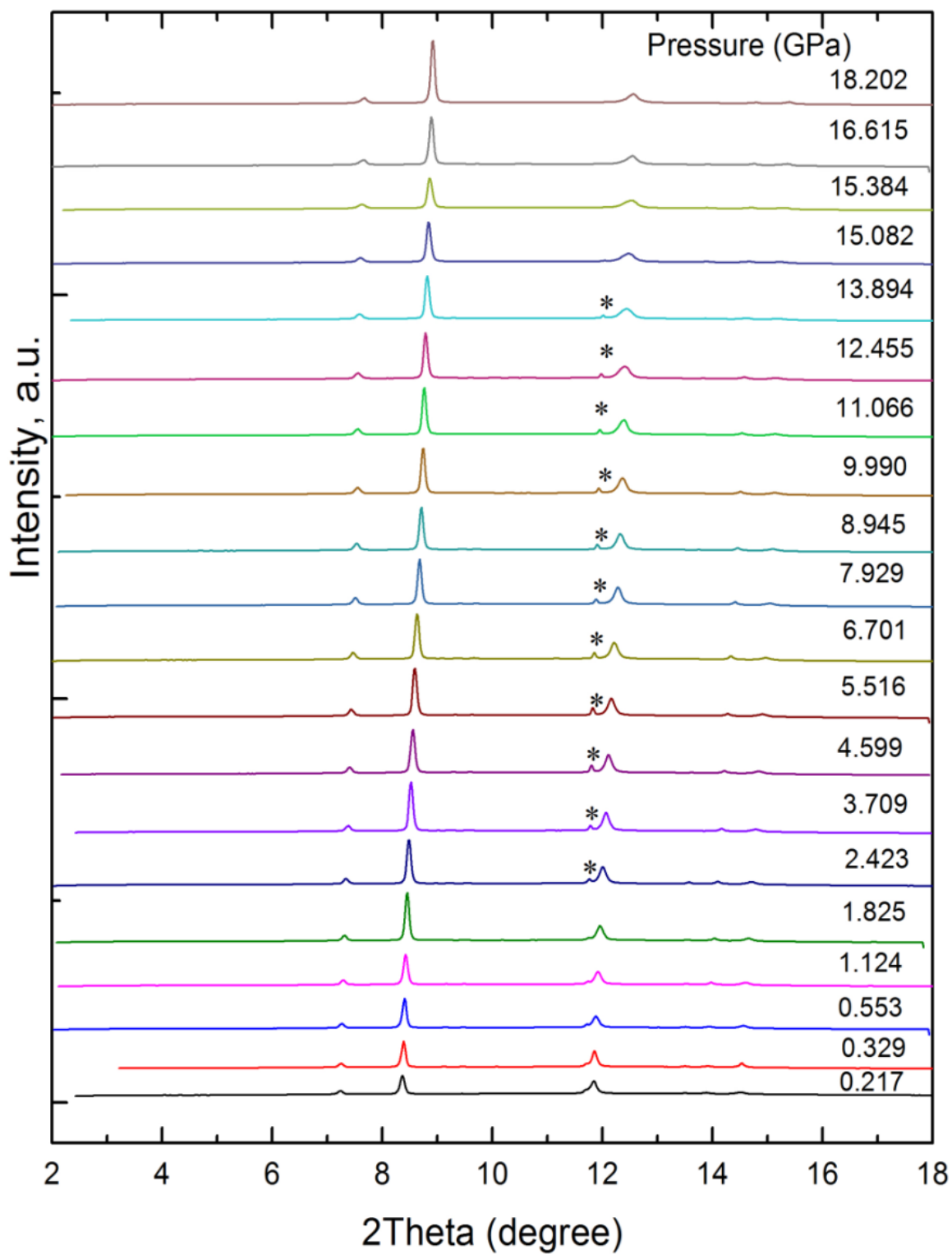


Figure 3-72: High pressure X-ray diffraction patterns of cubic-AgBiSe₂; the black symbol (*) indicates the appearance of a new peak in the XRD patterns is due to copper.

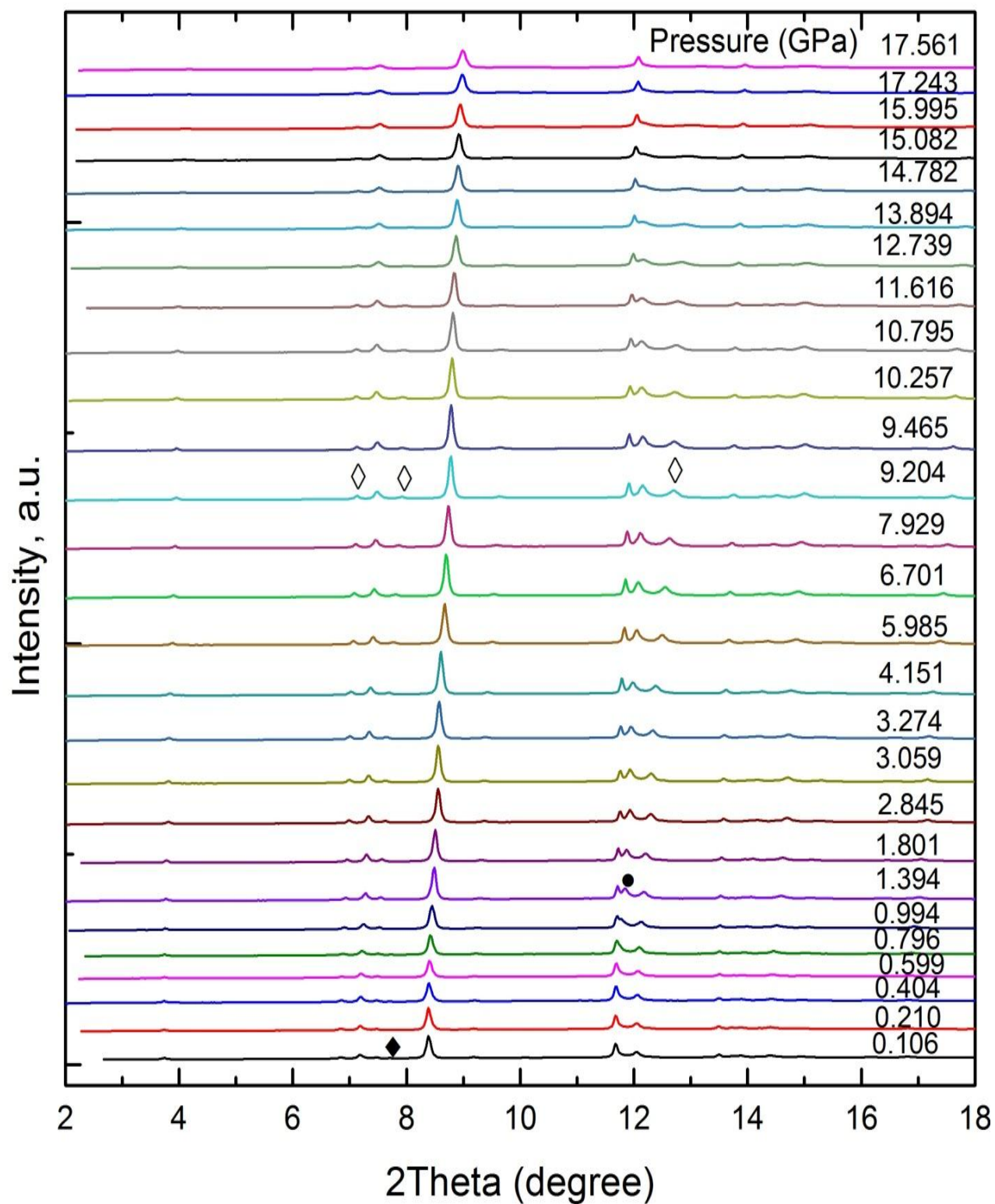


Figure 3-73: High pressure X-ray diffraction patterns of AgBiSe_2 (Hexagonal): Above 0.99GPa, the patterns show several changes, the pressure induced phase transition is found in this case.

We noticed that the three peaks marked in Figure 3-73 for the pattern 9.204GPa (rhombohedral) disappeared in the pattern 17.243GPa till the end pressure. Hence, this result revealed another structural phase transition of sample AgBiSe_2 after the rhombohedral phase. Along with the phase change, we observed a shift in the peak position which corresponds again to the contraction of the unit cell with the applied pressure. So, from this observation, we can conclude that the phase change can be obtained by applying pressure, and in future if we use chemical pressure in our compositions, we could be able to stabilize the cubic phase, prior to the application purpose. The lattice parameter value in both the cases (Figure 3-72 and Figure 3-73) are not mention here because the refinement performed on these patterns does not show a small residual, which means the observed pattern and the refined pattern are not in a good agreement with each other, thus difficult to evaluate the correct lattice value.

3.4 Conclusion

In summary, all compositions belonging to the solid solution $\text{AgBiSe}_2\text{-AgBiS}_2$ have been synthesized with the correct heat treatment conditions. We have performed the structural characterization using XRD and further structural analysis using Le bail refinement; showing the nature of phases (both hexagonal and cubic phase) exists in all such compositions. Further, the thermal analysis has been studied using DSC which confirmed the presence of phase transition in these compositions. So far, we have succeed in obtaining the two phases namely, hexagonal and cubic phase, and from the high temperature XRD, we observed the rhombohedral phase too for the selected composition. For future study, it would be interesting to trap the intermediate phase for all other compositions which shows two phase transition events obtained through DSC results. For that purpose, one could keep the sample for long annealing time at the particular temperature (should be noted down from the DSC heat flow curve) where this intermediate phase exists and may do the water quenching at this temperature in order to freeze this phase. In this chapter, we have also investigated the structural behavior under high pressure which shows the phase change under pressure. So, in the following chapter, we will mainly focused on the chemical pressure applied on our samples in order to stabilize the cubic phase or in other word to suppress the phase transition which we observed in this chapter.

Chapter 4

Suppression of phase transition through substitution

4.1 Motivation and organization of the chapter

From the results of the previous chapter, we notice that a transition from hexagonal phase to cubic phase is obtained at high pressure, thus our idea in this chapter is to use chemical pressure in order to stabilize this phase, which is promising for applications. Here, partial substitution has been applied to the compounds belonging to solid solution in order to suppress the phase transition; making it valuable for TE application. In this respect, we present in this chapter the effect of the substitution on the solid solution, method of synthesis and structural analysis performed on the samples.

4.2 Synthesis and structural characterization of substituted solid solutions

4.2.1 Introduction

Earlier, it has been reported that the Ag-Sb based chalcogenide compounds mainly $\text{AgSb}(\text{Ch})_2$ crystallized as a rock-salt NaCl type structure (Fm-3m) [174,176,177]. Two such examples are AgSbTe_2 and AgSbSe_2 [178,191]. Moreover, recent investigations point out enhanced TE performances of these materials reached due to elemental doping or substitution.

We choose to do isovalent substitution in order to finely control the crystal structure without disturbing the electronic structure. Our primary goal was to suppress the phase transitions which we noticed in chapter 3. Moreover, the result of the pressure XRD study showed that if the pressure is applied to the hexagonal phase, it can transform to the cubic phase, which means by applying chemical pressure we could stabilize the cubic phase. In this respect, after going through literature, we choose to substitute bismuth (Bi) by antimony (Sb); these two element belongs to the same family or same column in the periodic table (group V element), possess same valence and very similar properties. We choose antimony because AgSbSe_2 remains cubic without undergoing any kind of phase transition, so it should stabilize the cubic phase. And as the size of Sb is smaller than Bi, the chemical pressure obtained by the substitution could lead to the stabilization of the cubic phase. This kind of substitution should not change drastically the electrical properties because the elements are similar. Moreover, it could be a good choice to see the effect of substitution on the thermal conductivity by using the differences in size and mass between them.

The first tests were conducted on the compound AgBiSe_2 with Sb substitution ($\text{AgBi}_{1-x}\text{Sb}_x\text{Se}_2$) in order to find out the correct Sb concentration to suppress the phase transition. Later, the substitution was done on five chosen compounds with compositions which span the full range of

the solid solution $\text{AgBiSe}_2\text{-AgBiS}_2$. The whole synthesis and results based on the substitution are presented in the following sections.

4.2.2 Method of synthesis

All the samples were prepared by conventional solid state reactions method . The process was carried out by considering the melting point of Ag (961.8°C), Bi (271.4°C), Se (220.8°C), S (115.2°C) and Sb (630.6°C) which are the basic raw materials. At first, the stoichiometric amounts of starting materials were weighed and mixed in appropriate ratios for the desired compositions inside the glove box, and then pressed into bar shape pellets (Table 4). The tubes containing such pellets were then sealed under argon atmosphere and treated with adequate heating conditions. The vertical furnace used for the heat treatment was given in Table 3.

4.2.3 Substitution with antimony (Sb)

4.2.3.1 Heat treatment

This section contains the detailed synthesis conditions which were applied during the study. A schematic drawing for the heat treatment of $\text{AgBi}_{1-x}\text{Sb}_x\text{Se}_2$ is shown in Figure 4-74. Our conditions are described here. The first heat treatment was carried out at 400°C, dwelled for 30 minutes and then heated further at 850°C, held for 48hrs followed by slowly cooling down to room temperature. The heating and cooling ramp rate is mention in the diagram itself.

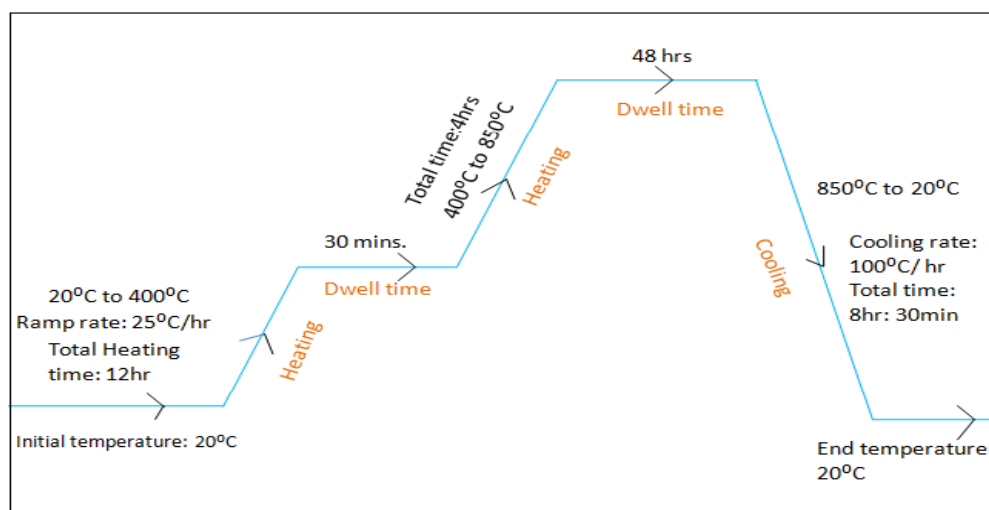


Figure 4-74: A schematic drawing for the heat treatment of composition $\text{AgBi}_{1-x}\text{Sb}_x\text{Se}_2$.

4.2.3.2 PXRD (Powder X-ray diffraction)

For the first synthesis event, the X-ray diffraction was carried out with the specification; 2θ varies from 20° to 80° , with step size ($^\circ$) 0.0167 and time per step (s) 60. The total execution time was 30minutes. The XRD patterns of total set of ten samples are plotted in Figure 4-75. The detailed pictures of XRD patterns for selected sample are shown below in Figure 4-76.

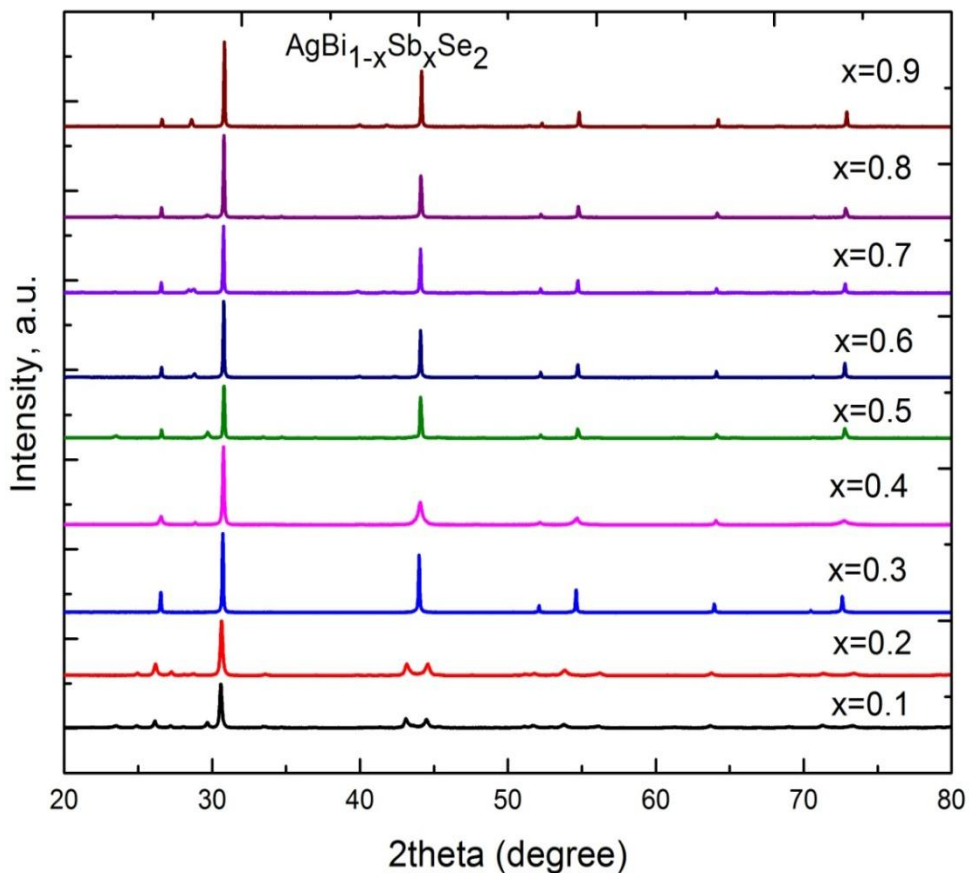


Figure 4-75: XRD patterns of first ten set of samples; $\text{AgBi}_{1-x}\text{Sb}_x\text{Se}_2$, ($0.1 \leq x \leq 0.9$).

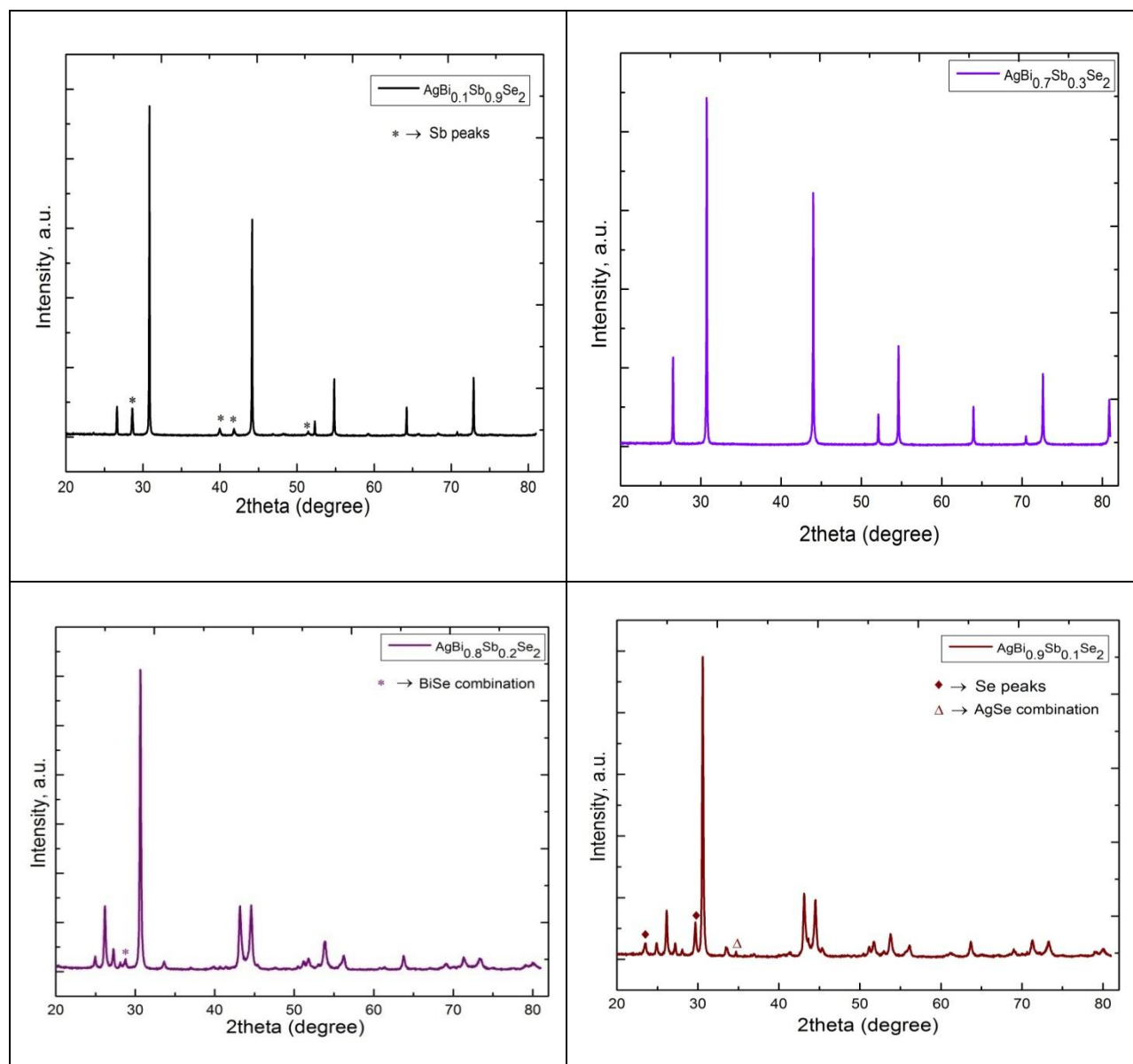


Figure 4-76: XRD patterns of samples belong to $\text{AgBi}_{1-x}\text{Sb}_x\text{Se}_2$; secondary peaks are marked with the symbols shown in each picture.

The Figure 4-76 shows the example of four selected XRD patterns out of the ten samples. Here, we have shown two patterns, $\text{AgBi}_{0.1}\text{Sb}_{0.9}\text{Se}_2$ and $\text{AgBi}_{0.7}\text{Sb}_{0.3}\text{Se}_2$, as others ($x \geq 0.3$) are nearly same (shown in annex C). The first pattern belongs to the sample $\text{AgBi}_{0.1}\text{Sb}_{0.9}\text{Se}_2$; the main peaks correspond to the peaks of cubic AgSbSe_2 (matched with the reference code 96-901-1029 in the database). The secondary peaks of antimony (Sb) were observed in this pattern, marked with a (*) symbol at the top of each peaks. In comparison with all other compositions the pattern of $\text{AgBi}_{0.7}\text{Sb}_{0.3}\text{Se}_2$ as shown in Figure 4-76 does not show any kind of presence of secondary phases.

The pattern also matches with the cubic pattern (reference code 96-901-1020), obtained from the database. On the other hand, the other two patterns namely, $\text{AgBi}_{0.8}\text{Sb}_{0.2}\text{Se}_2$ and $\text{AgBi}_{0.9}\text{Sb}_{0.1}\text{Se}_2$, show a hexagonal phase (matched the hexagonal pattern of AgBiSe_2 with reference code 96-901-1024), besides they contain secondary phases too. For the $\text{AgBi}_{0.8}\text{Sb}_{0.2}\text{Se}_2$, the secondary peaks occurred due to the presence of BiSe combination and for $\text{AgBi}_{0.9}\text{Sb}_{0.1}\text{Se}_2$, due to presence of Se and AgSe combination in the final compound. Hence, this analysis shows that $x=0.3$ or 30% of Sb is the lowest Sb amount that enables to get the cubic phase: as we noticed here, for $x=0.1, 0.2$, it is hexagonal and for $x \geq 0.3$, it is cubic. So, for further analysis of phase transition, thermal analysis using DSC was performed for each of these compositions in order to confirm these observations.

4.2.3.3 Thermal analysis (DSC)

The thermal analysis of the samples mentioned in section 4.2.3.2 was carried out using DSC and the heat flow curves obtained are plotted in Figure 4-77. The thermal analysis was done in the temperature range from RT to 500°C . The mass of the sample used ranged from 80.1 to 80.4 mg. In Figure 4-77, for the samples $x=0.8, 0.5$ and 0.1 , the three peaks surrounded by a box after 200°C are due to the selenium, as the melting point of selenium is 220.8°C ; we obtained the secondary peaks of Se in the XRD patterns of these samples. In addition, in the same samples, we notice a peak between 100°C and 150°C , shown in the figure itself. This may arise due to another secondary phase which we found in the XRD results of three of these compositions (refer to Figure 4-76 and Annex C). For the sample $x=0.2$ and 0.1 , we obtained hexagonal phase at RT along with the secondary phases (Figure 4-76). Here in DSC, the other peaks in these two samples correspond to the phase transition. The temperatures corresponding to the peaks are marked with arrows on the curves themselves. With increasing amount of Sb fraction, the peaks shift to lower temperature. The composition $\text{AgBi}_{0.7}\text{Sb}_{0.3}\text{Se}_2$ ($x=0.3$) does not show any transition peak in the heat flow curve, which means there is no phase transition throughout the temperature range. So, from the combined results of DSC and XRD, we can say that $\text{AgBi}_{0.7}\text{Sb}_{0.3}\text{Se}_2$ contains only cubic phase in the whole temperature range. In other words, Sb substitution (30%) suppresses the phase transition in AgBiSe_2 , due to the effect of chemical pressure, similarly to the observations made in our pressure XRD study.

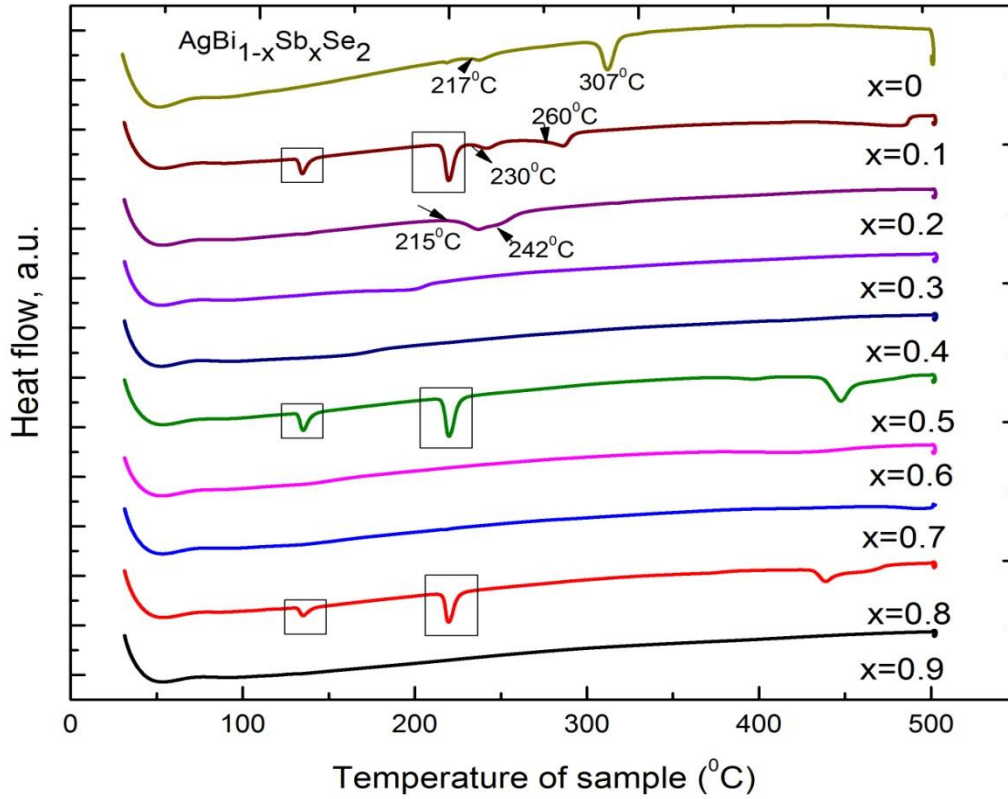


Figure 4-77: Heat flow DSC curves of $\text{AgBi}_{1-x}\text{Sb}_x\text{Se}_2$, ($0.1 \leq x \leq 0.9$).

4.2.4 Substitution on solid solution AgBiSe_2 - AgBiS_2

4.2.4.1 Introductions

Based on the XRD and DSC analysis, we choose to substitute Sb with 30% in other five compositions, namely, $\text{AgBi}_{0.7}\text{Sb}_{0.3}\text{Se}_2$, $\text{AgBi}_{0.7}\text{Sb}_{0.3}\text{S}_2$, $\text{AgBi}_{0.7}\text{Sb}_{0.3}\text{Se}_{0.5}\text{S}_{1.5}$, $\text{AgBi}_{0.7}\text{Sb}_{0.3}\text{SeS}$, $\text{AgBi}_{0.7}\text{Sb}_{0.3}\text{Se}_{1.5}\text{S}_{0.5}$. This choice of similar Sb fraction for all compositions came from the fact that when S content increases in the solid-solution (AgBiSe_2 - AgBiS_2), the transitions shift towards the lower temperature value, and should thus be more easily suppressed. In other words, we can say that 30% Sb should satisfy the idea of suppression of the phase transition for all the selected compositions. To cover the whole range of solid solution, we choose these five samples with $S=0, 0.5, 1, 1.5, 2$.

4.2.4.2 Heat treatment

For the second synthesis event involving the compositions $\text{AgBi}_{0.7}\text{Sb}_{0.3}\text{Se}_{1-x}\text{S}_{1+x}$ and $\text{AgBi}_{0.7}\text{Sb}_{0.3}\text{Se}_{1+x}\text{S}_{1-x}$, the similar heating treatment was applied as shown in Figure 4-74. After synthesis, the samples were hammered out of the sealed silica tube. The ingots obtained were solid and dense big chunks with silvery shine luster shown in Figure 4-78.



Figure 4-78: Picture of ingot; a solid chunk obtained after synthesis.

To investigate the results of synthesis, XRD was carried out and the whole information was given in the section below. In the meanwhile, we observed that among the five samples, the XRD pattern of $\text{AgBi}_{0.7}\text{Sb}_{0.3}\text{Se}_2$ resembles the single cubic phase but not in an adequate way; the peaks are not sharp. But, for the same composition with less powder (1g instead of 4.5g) when synthesized at the beginning, the XRD result was pure single cubic phase with sharp peaks. The two results are compared in Figure 4-79. The difference between the two results may arise due to incomplete reaction with large amount of powder (4.5g). The dwelling time may be not long enough so that the atoms diffuse properly to give the desired end product.

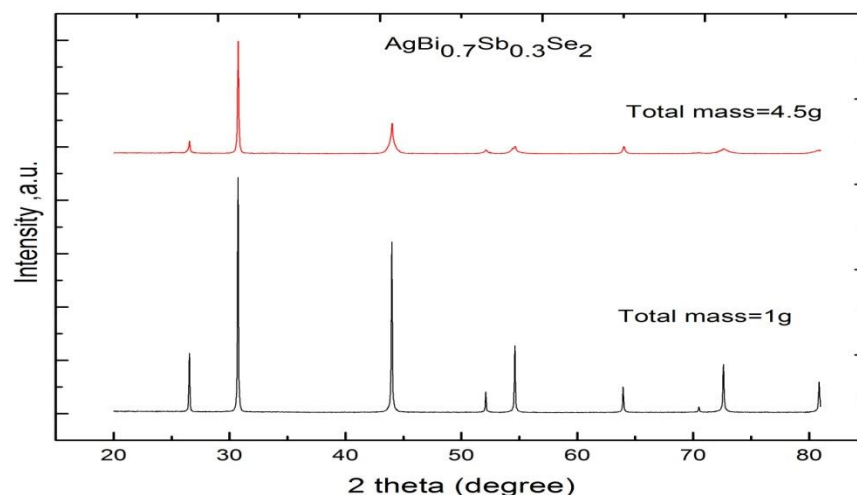


Figure 4-79: Comparison of XRD patterns of $\text{AgBi}_{0.7}\text{Sb}_{0.3}\text{Se}_2$ compound with two different mass values.

The above experimental results lead us to do further annealing of $\text{AgBi}_{0.7}\text{Sb}_{0.3}\text{Se}_2$, the one with (4.5g). We regrind the powder and made pellets again and followed a new heat treatment. The synthesis was carried out at a temperature slightly lower than the melting temperature; so that reaction will complete and the pellets will retain their shape on completion of synthesis. A schematic drawing for this heat treatment is shown below in Figure 4-80. The sample was heated to 650°C at the rate 100°C/hr , held for 72 hours and was cooled down with a speed 100°C/hr to room temperature. The longer annealing time allows the diffusion process to be effective enough to give a complete reaction.

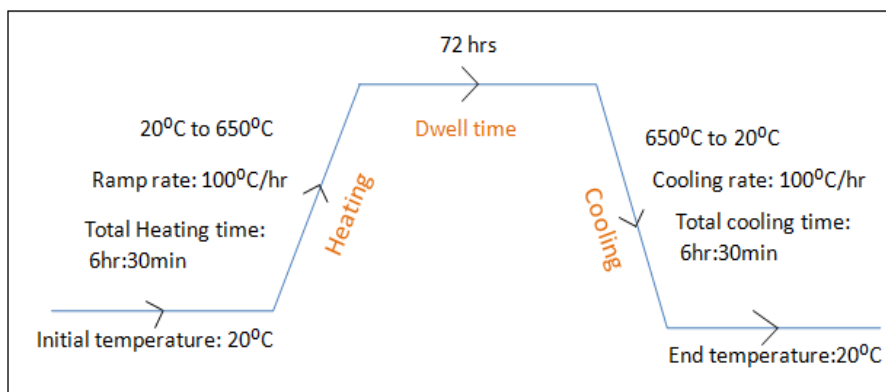


Figure 4-80: A schematic drawing of further annealing of composition $\text{AgBi}_{0.7}\text{Sb}_{0.3}\text{Se}_2$.

After synthesis, the annealed samples were taken out of the sealed tube shown in Figure 4-81. The shape of the pellets remained same and they possess a silvery shine color.



Figure 4-81: Picture representing the pellets of annealed sample $\text{AgBi}_{0.7}\text{Sb}_{0.3}\text{Se}_2$.

4.2.4.3 PXRD (Powder X-ray diffraction)

The XRD patterns obtained for the final five Sb (30%) substituted compounds are shown in Figure 4-82. The X-ray diffraction was carried out with the specifications; 2θ varies from 20° to 120° , with step size ($^\circ$) 0.00835 and time per step (s) 500. The total execution time was 13hr: 22min: 45sec. The data obtained demonstrates that all five compounds achieve the cubic phase at room temperature without quenching after substitution. This means, with such kind of substitution, we have been able to suppress the phase transition, irrespective of the selenium-sulfur fraction in the compositions. Besides, the peaks are sharp, which shows a good crystallinity of the samples and a complete reaction.

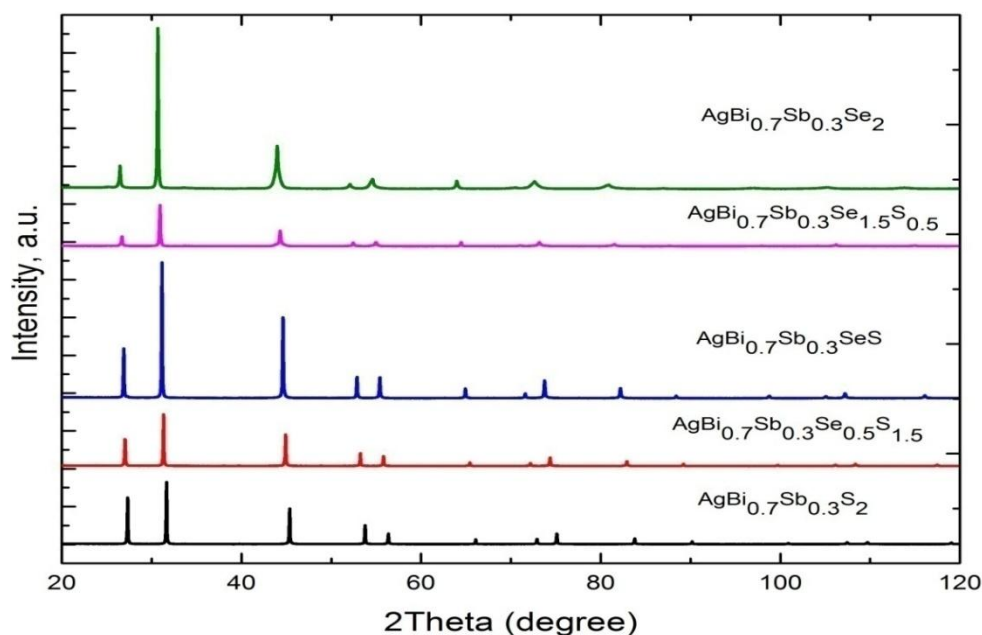


Figure 4-82: The XRD patterns of Sb substituted five samples belongs to the solid solutions $\text{AgBi}_{0.7}\text{Sb}_{0.3}\text{Se}_{1-x}\text{S}_{1+x}$ and $\text{AgBi}_{0.7}\text{Sb}_{0.3}\text{Se}_{1+x}\text{S}_{1-x}$; reveals the cubic phase.

We also notice that the XRD peaks slightly shift to the lower angles with the increasing Se percentage shown in Figure 4-83. The reason could come from the variation of lattice parameters with the increasing Se content, similar to the Sb-free compositions mentioned in chapter 3.

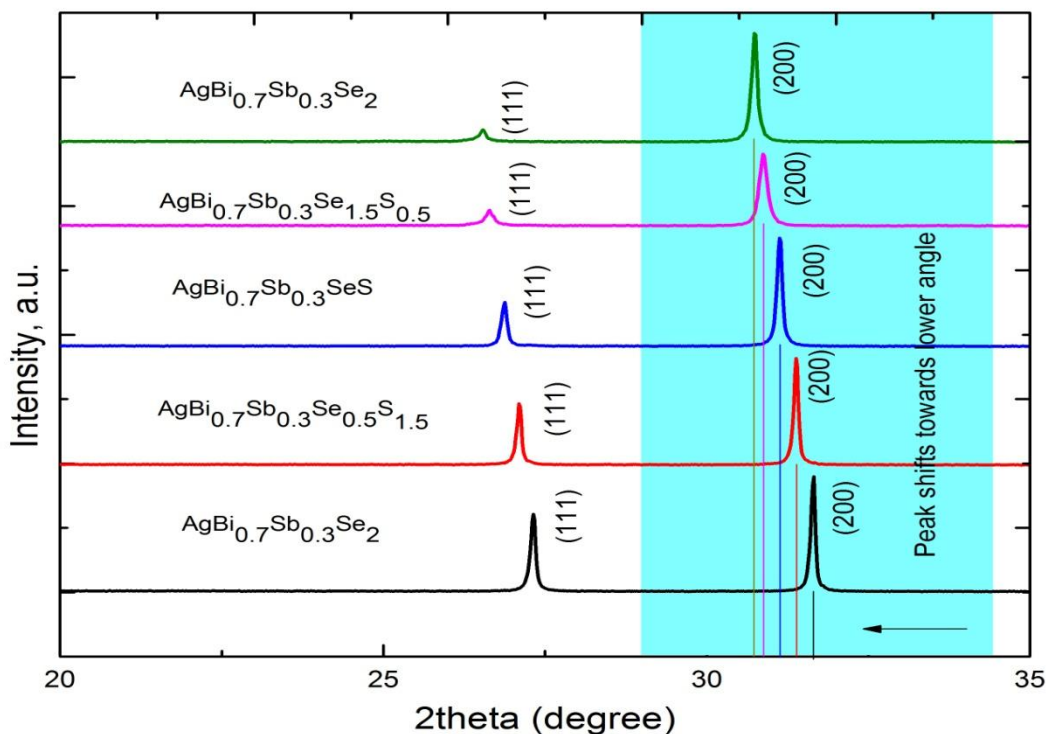


Figure 4-83: Regular shift in the XRD peaks of Sb substituted samples.

4.2.4.4. Determination of lattice parameters

The PXRD patterns were refined using Le Bail refinement to obtain the lattice parameters value of the five samples. The refinement was done with FULLPROF software. One example of refined patterns is shown below in Figure 4-84. It shows a good agreement between the observed XRD patterns and the refinement which is evidenced by the small residual. We obtained the same for other compositions also. The lattice parameters values for the five samples are tabulated in Table 7.

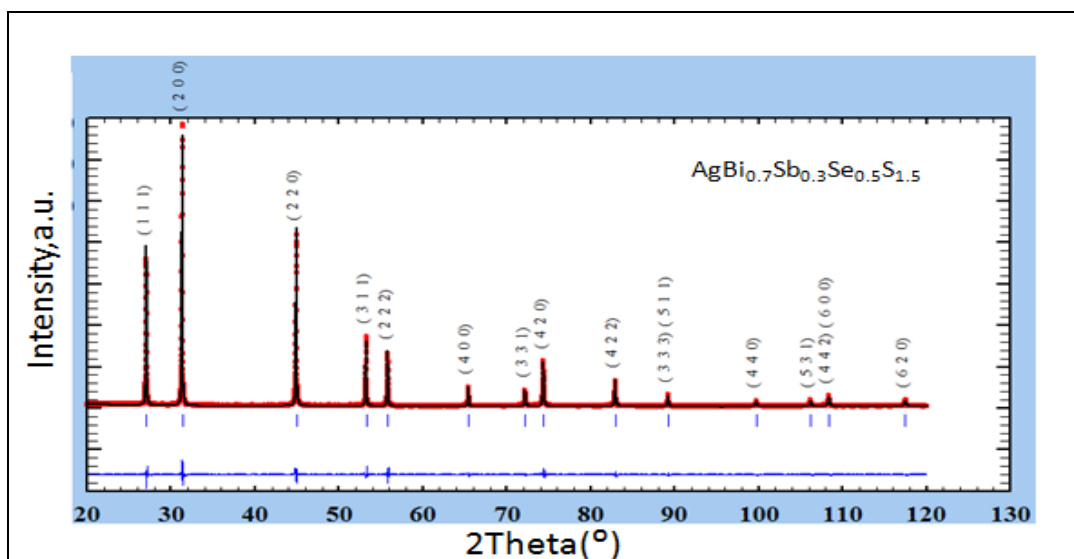


Figure 4-84: Refinement pattern of $\text{AgBi}_{0.7}\text{Sb}_{0.3}\text{Se}_{0.5}\text{S}_{1.5}$: Single cubic phase (space group $Fm\bar{3}m$); the solid black line represents the refinements performed, the red line represents the measured XRD patterns and the blue line at the bottom is the residual.

Table 7: Lattice parameters values determined by Le Bail refinement. The values of volume/Z are calculated from the parameters.

Compositions	a/b/c (Å)	Volume/Z (Å ³)
$\text{AgBi}_{0.7}\text{Sb}_{0.3}\text{S}_2$	5.654	90.359
$\text{AgBi}_{0.7}\text{Sb}_{0.3}\text{Se}_{0.5}\text{S}_{1.5}$	5.699	92.528
$\text{AgBi}_{0.7}\text{Sb}_{0.3}\text{SeS}$	5.742	94.669
$\text{AgBi}_{0.7}\text{Sb}_{0.3}\text{Se}_{1.5}\text{S}_{0.5}$	5.780	96.551
$\text{AgBi}_{0.7}\text{Sb}_{0.3}\text{Se}_2$	5.815	98.306

Based on the Table 7, the lattice parameters and the volume per formula unit with respect to the increase in Se content in the compounds are plotted in Figure 4-85. The shifts in the peaks in XRD patterns can be understood by the almost linear expansion in the lattice parameter with increasing Se content. Moreover, the nature of graph satisfies the Vegards law for the substituted solid solutions. The ionic radius of Se is larger than that of S. So, as higher content of Se is introduced in the solid solution in comparison to the sulfur, the unit cell undergoes a systematic expansion, and this result shows that the presence of Sb does not create any miscibility gap and thus there is a monotonous increase in lattice parameters. The almost linear dependency of lattice parameters also shows a complete homogeneous solid solution with no miscibility gap.

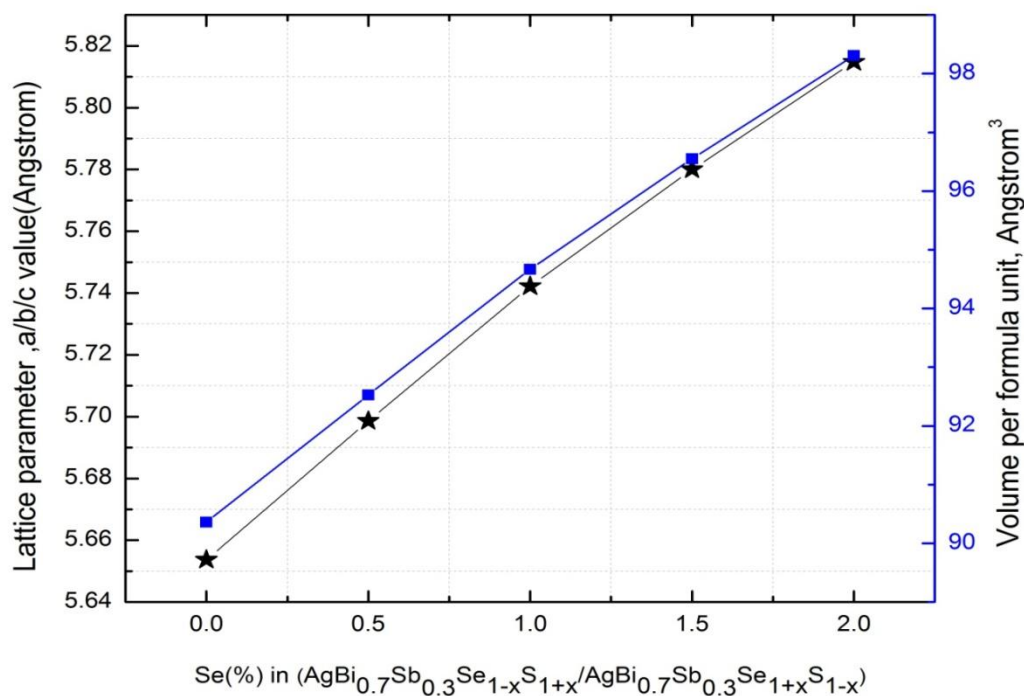


Figure 4-85: The lattice parameters variations and volume per formula unit as a function of selenium content in the compounds.

4.2.4.5 DSC (Differential scanning calorimeter)

We obtained the cubic phase for all the five samples at RT; to prove that there is no phase transition in these samples; the DSC measurement was carried out. The thermal analysis was done in the temperature range from RT to 500°C. The mass of the sample used ranged from 80.1 to 80.4 mg. The heat flow curves obtained are plotted in Figure 4-86. It reveals that there is no endothermic peak corresponds to the phase transition for all the five samples. That means, all the samples possess single cubic phase characteristic. But, we noticed two small endothermic peaks marked in a dotted area for $\text{AgBi}_{0.7}\text{Sb}_{0.3}\text{S}_2$ and $\text{AgBi}_{0.7}\text{Sb}_{0.3}\text{Se}_{0.5}\text{S}_{1.5}$; the temperature of melting is very close to the melting point of bismuth (271.4°C). These traces of Bi originate from the fact that we didn't use 2% deficiency of Bi for these syntheses, as contrary to the synthesis mentioned in chapter 3.

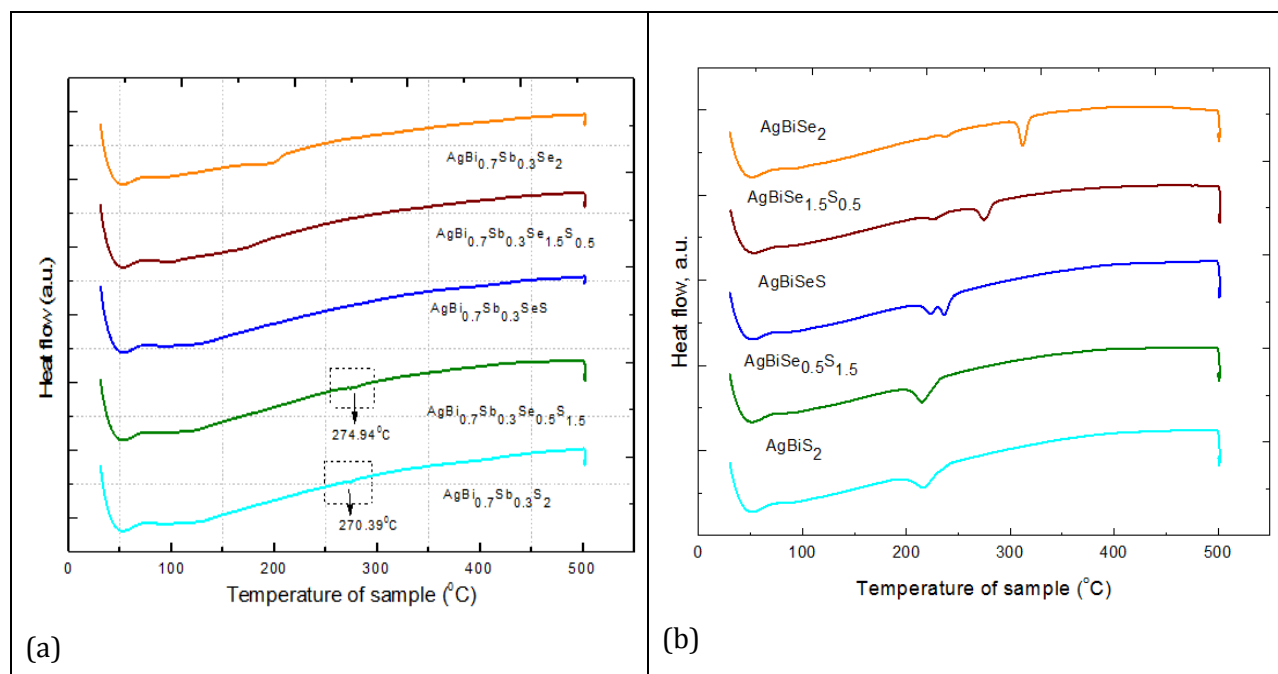


Figure 4-86: (a) Heat flow DSC curves of Sb substituted samples; reveals no phase transition and (b) Heat flow DSC curves of samples without substitution; reveals phase transition in the samples.

For comparison, we have plotted the heat flow curve of same five compositions without any Sb-substitution in Figure 4-86b. This Figure 4-86b makes easier to compare the changes which occurred after substitution in those samples. At first, for $\text{AgBi}_{0.7}\text{Sb}_{0.3}\text{S}_2$ and $\text{AgBi}_{0.7}\text{Sb}_{0.3}\text{Se}_{0.5}\text{S}_{1.5}$, we noticed one endothermic peak in Figure 4-86b, which corresponds to phase transition as explained in chapter 3, whereas no such peak observed throughout the whole temperature range for these two samples with Sb substitution in Figure 4-86a. For other three samples, namely, $\text{AgBi}_{0.7}\text{Sb}_{0.3}\text{SeS}$, $\text{AgBi}_{0.7}\text{Sb}_{0.3}\text{Se}_{1.5}\text{S}_{0.5}$, and $\text{AgBi}_{0.7}\text{Sb}_{0.3}\text{Se}_2$, we obtained endothermic peaks too which implies the presence of phase transition in these compositions, shown in Figure 4-86b. But, in Figure 4-86a, again no such peak was observed for these three samples all over the temperature range. Combining this two results of DSC (Figure 4-86a and Figure 4-86b), we can say that with substitution, we were able to suppress the phase transition in our samples.

4.3 Conclusion

In summary, the substituted samples have been synthesized by solid state reaction followed by cooling down to room temperature without water quenching. We have performed the structural

and thermal analysis using powder X-ray diffraction (PXRD) and DSC. The insights gained from the experimental results reveal no structural phase transition up to the experimental limit. Our findings revealed that through Sb-substitution, it is possible to suppress the phase transition in the solid solution $\text{AgBiSe}_2\text{-AgBiS}_2$ due to the application of the chemical pressure, as it was a prerequisite for the applications. The next step of the study would be the n-type doping of the samples which will be in the next chapter.

Chapter 5

Influence of doping on solid solution (AgBiSe₂-AgBiS₂)

5.1 Motivation and organization of the chapter

The result obtained in chapter 4 showed that the antimony substitution on bismuth site for the solid solution is effective in suppressing the phase transition. Here in, we present the effect of doping on the Sb-substituted solid solutions.

5.2 Synthesis of solid solutions with Niobium (Nb) doping on Silver (Ag) site

5.2.1 Introduction

Earlier, in our laboratory, work had been done with AgBiSe_2 with Nb doping which shows enhanced TE properties by increasing the carrier concentration. Moreover, the ZT of 1 at 773K was achieved through Nb doping [222], in turn making this material suitable for medium temperature TE applications. Following this result, we also choose Nb for doping in our Sb-substituted solid solutions, with the same amount as the one used in the prior study.

While doping, it is important to choose an element which possesses more or less as the same size with the element to be doped. In our case, the ionic radius of Nb is smaller than that of Ag, which in turn conserves the required structure. We performed doping on five compounds which are mentioned in (Annex D) (they were chosen in order to span the complete range of compositions of the solid solution) with 2% and 4% of Nb doped in Ag site, following the same synthesis process as the one used in chapter 4. This in turn helps to reproduce and compare the results for undoped and doped samples. The whole synthesis and the experimental results based on the doping will be presented in the following sections.

5.2.2 Method of synthesis

The Nb doped samples were synthesized by solid state reactions method. The respective compositions were mentioned in Annex D. The samples were made using nominal stoichiometric powder mixtures of silver (Ag), bismuth (Bi), antimony (Sb), selenium (Se), sulfur (S) and niobium (Nb) inside the glove box. After being uniformly mixed in an agate mortar, the mixtures were shaped into pellets by uniaxial pressure (Table 4). The pellets were sealed in an evacuated silica tubes under argon atmosphere and then placed in a vertical furnace (Table 3) to carry out the synthesis.

5.2.3 Raw materials and calculation of compositions

The details of starting precursors were listed in chapter 2. The synthesis event were based on the five compositions; $\text{Ag}_{1-x}\text{Nb}_x\text{Bi}_{0.7}\text{Sb}_{0.3}\text{S}_2$, $\text{Ag}_{1-x}\text{Nb}_x\text{Bi}_{0.7}\text{Sb}_{0.3}\text{Se}_{0.5}\text{S}_{1.5}$, $\text{Ag}_{1-x}\text{Nb}_x\text{Bi}_{0.7}\text{Sb}_{0.3}\text{SeS}$, $\text{Ag}_{1-x}\text{Nb}_x\text{Bi}_{0.7}\text{Sb}_{0.3}\text{Se}_{1.5}\text{S}_{0.5}$, $\text{Ag}_{1-x}\text{Nb}_x\text{Bi}_{0.7}\text{Sb}_{0.3}\text{Se}_2$. With Nb doping of 2% and 4% ($x=0.02, 0.04$), a set of ten samples were prepared, calculation of compositions of two samples and mass value of all the precursors for all the Nb-doped samples mention in annex D.

5.2.4 Heat treatment

All the samples undergo the similar two step heat treatment shown in Figure 5-87. We followed the same procedure as mentioned in section 4.2.3. The first heat treatment was carried out at 400°C, held for 30 minutes and then heated further at 850°C, held for 48hrs followed by slowly cooling down to room temperature. The heating ramp rate is 25°C/hr and cooling ramp rate is set at 100°C/hr.

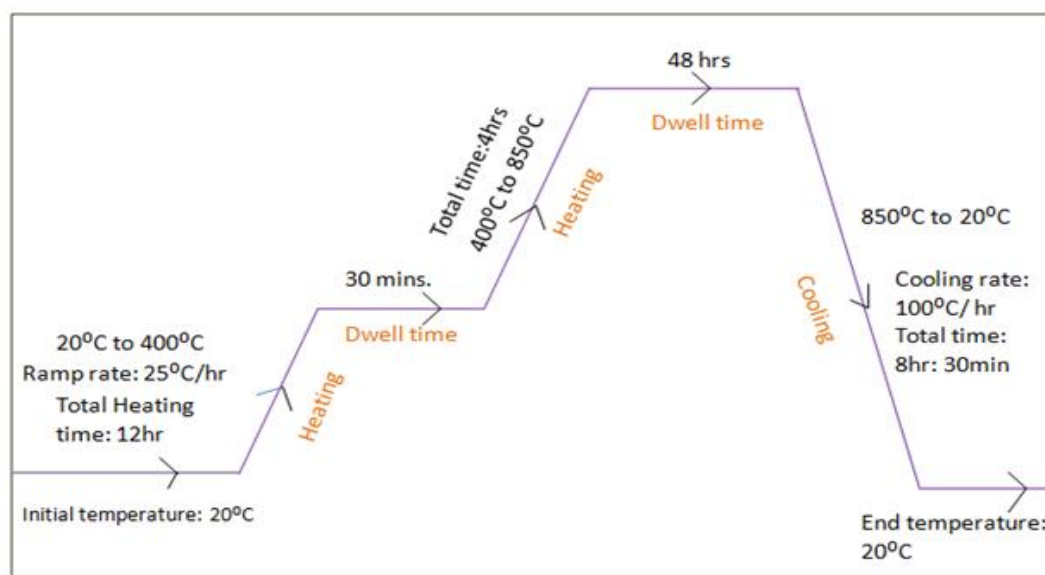


Figure 5-87: A schematic drawing for the heat treatment.

After synthesis, the samples were hammered out of the sealed silica tube. The obtained ingots, shown in Figure 5-88, are a solid big chunks with silvery shine luster; similar for all the samples.



Figure 5-88: Picture of ingot; a solid chunk obtained after synthesis.

This solid mass was crushed and grinded into fine powder with agate mortar manually and then prepared for the XRD analysis. The results are presented shown in the following section.

5.3 Result of Structural and thermal analysis

5.3.1 PXRD (Powder X-ray diffraction)

The X-ray diffraction characterization was carried out with the specifications; 2θ varies from 20° to 120° , with step size ($^\circ$) 0.00836 and time per step (s) 500. The total execution time was 13hr: 22min: 45sec. The XRD pattern of two samples are shown in Figure 5-89 as example, and for the others the patterns look similar. The PXRD patterns for the doped samples at RT shows that the main diffraction peaks correspond to the cubic phase for both $x=0.02$ and $x=0.04$. This observance shows that the small fraction of Nb doping in Sb substituted samples does not change the phase behavior at RT in comparison with the undoped Sb-substituted samples. For both the undoped and doped Sb-substituted samples, the cubic phase was trapped at RT without undergoing any quenching.

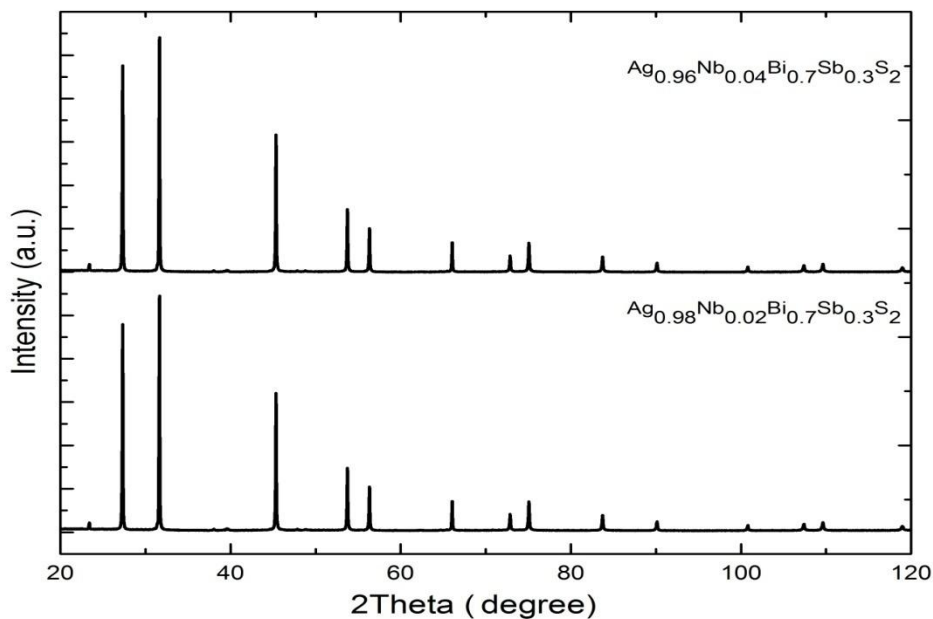


Figure 5-89: XRD patterns of Nb doped sample for $x=0.02$ and $x=0.04$.

Further, we have noticed a regular shift in the diffraction peaks towards the lower angle when the Se fraction increases for the both the cases; $x=0.02$ and $x=0.04$ samples, shown in Figure 5-90. This shifting behavior can be understood from the variation of lattice parameter values.

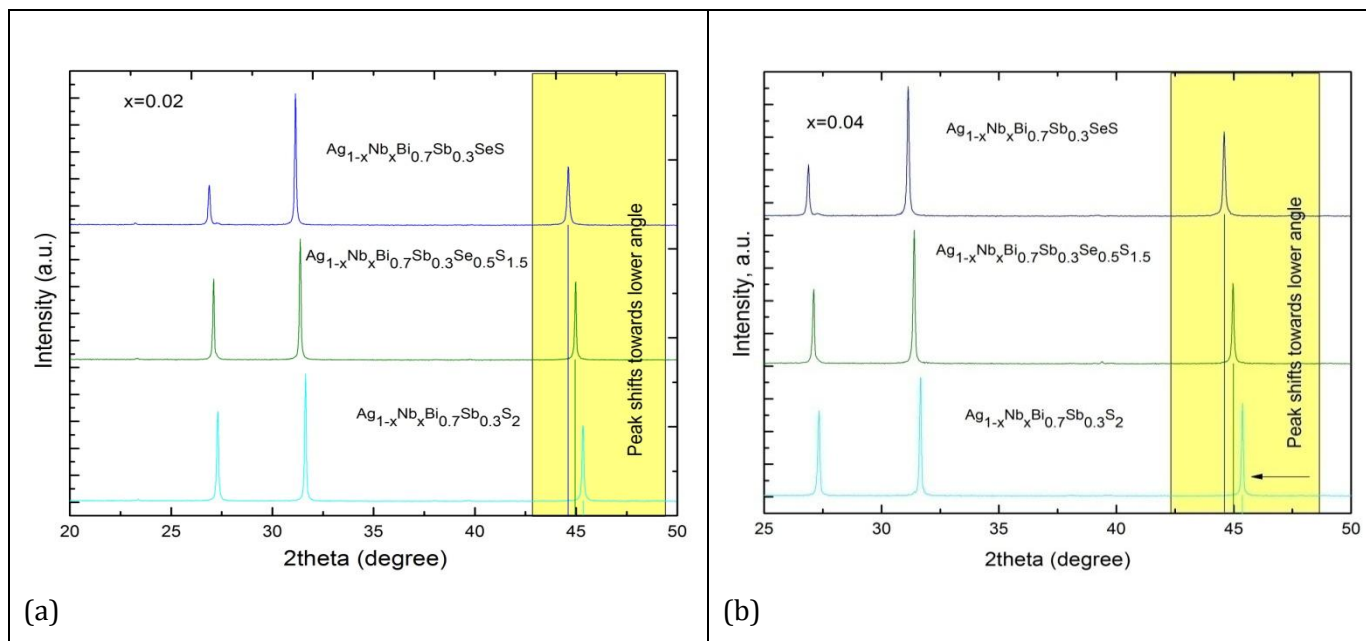


Figure 5-90: Shifting in diffraction peaks of doped samples; (a) $x=0.02$ and (b) $x=0.04$.

5.3.2 Determination of lattice parameters

The PXRD patterns were refined using Le Bail refinement to obtain the lattice parameters value of the set ten of samples. The refinement was done with FULLPROF software. The two refined patterns are shown below in Figure 5-91 as an example, for the other samples, we obtained the same. It shows a good agreement between the observed XRD patterns and the refinements which is evidenced by the small residual. Here in this pattern, we notice the presence of faint amount of secondary phase. The lattice parameters values for the ten samples were tabulated in Table 8.

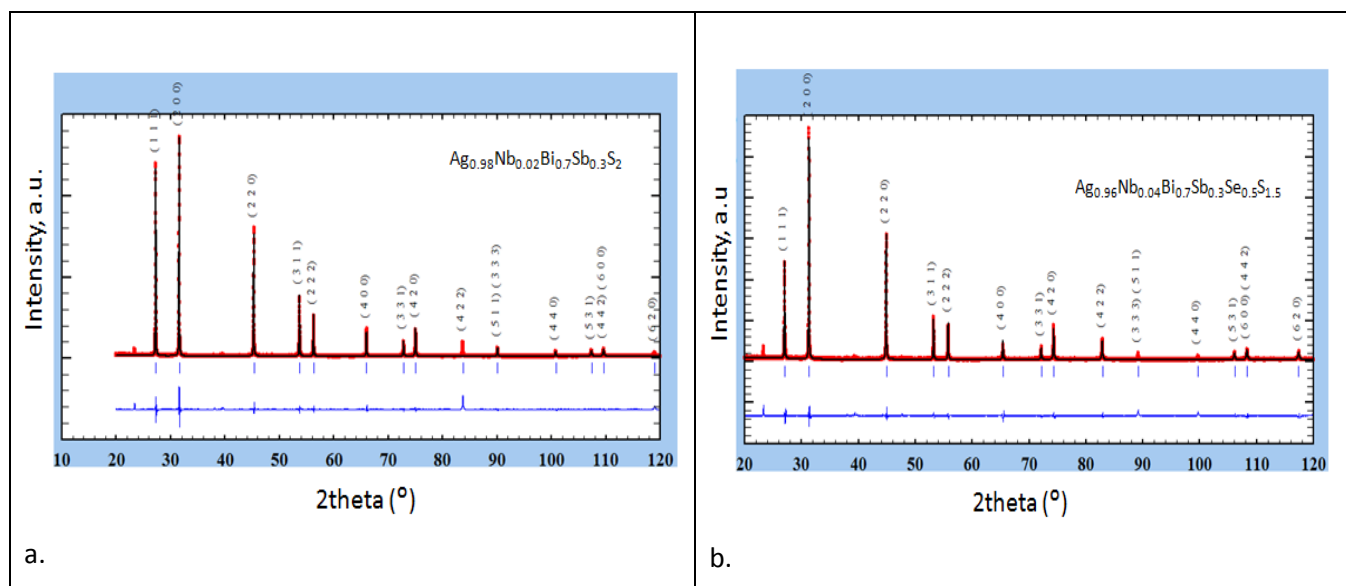


Figure 5-91: Refinement pattern of doped samples; Single cubic phase (space group $Fm\bar{3}m$); the solid black line represents the refinements performed, the red line represents the measured XRD patterns and the blue line at the bottom is the residual.

Table 8: Lattice parameters values determined by Le Bail refinement.

Compositions	a/b/c(Å) (x=0.02)	a/b/c(Å) (x=0.04)
$Ag_{1-x}Nb_xBi_{0.7}Sb_{0.3}S_2$	5.656	5.656
$Ag_{1-x}Nb_xBi_{0.7}Sb_{0.3}Se_{0.5}S_{1.5}$	5.702	5.702
$Ag_{1-x}Nb_xBi_{0.7}Sb_{0.3}SeS$	5.746	5.746
$Ag_{1-x}Nb_xBi_{0.7}Sb_{0.3}Se_{1.5}S_{0.5}$	5.783	5.788
$Ag_{1-x}Nb_xBi_{0.7}Sb_{0.3}Se_2$	5.814	5.811

Based on the Table 8, the lattice parameters with respect to the increase in Se content in the compounds were plotted in Figure 5-92. The shifts in the peaks in XRD patterns can be understood by the almost linear expansion in the lattice parameter with increasing Se content. Moreover, the evolution of lattice parameters nature of graph satisfies the Vegards law for the doped solid solution for both the cases $x=0.02$ and $x=0.04$. The ionic radius of Se is larger than that of S. So, as higher content of Se is introduced in the solid solution in comparison to the sulfur, the unit cell undergoes a systematic expansion, and this result shows that the small fraction of Nb does not create any negative effects on the solid solutions and maintains the monotonous increase in lattice parameters with Se percentage. The almost linear dependency of lattice parameters also shows a complete homogeneous solid solution with no miscibility gap, similarly to the undoped solid solution.

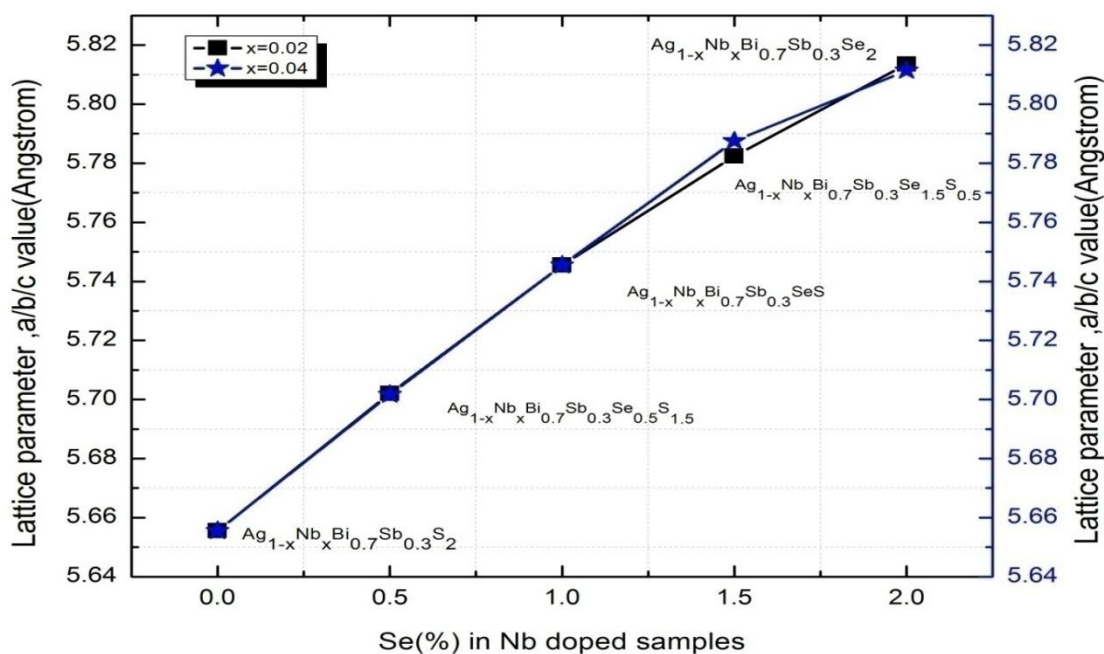


Figure 5-92: The lattice parameters variations of doped samples vs. selenium content in the compounds.

5.3.3 DSC (Differential scanning calorimeter)

The DSC measurements were carried out on the set of samples. The thermal analysis was done in the temperature range from RT to 500°C. The mass of the samples used ranged from 80.1 to 80.4 mg. The heat flow curves obtained are plotted in Figure 5-93. We checked all DSC measurements with three cycles of heat flow for each sample. The result reveals that there is no endothermic peak

corresponding to the phase transition for all the five samples, in comparison with the one which we obtained in Figure 4-86b. But, we noticed two small endothermic peaks marked in a box for $\text{AgBi}_{0.7}\text{Sb}_{0.3}\text{S}_2$ and $\text{AgBi}_{0.7}\text{Sb}_{0.3}\text{Se}_{0.5}\text{S}_{1.5}$ in Figure 5-93(a) and (b); the temperature of melting is very close to the melting point of bismuth (271.4°C) and this endothermic peak does not belong to the transition. And, the peak observed in case of $\text{Ag}_{1-x}\text{Nb}_x\text{Bi}_{0.7}\text{Sb}_{0.3}\text{Se}_2$ (for both $x=0.04$ and $x=0.02$) indicated with an arrow does not belong to the transition. We checked the first and second heating heat flow curve for these compositions, one of them is shown in annex D. We noticed that the peak which appeared in the first heating disappeared in the second heating. This may occur if there is a little trace of secondary phase present in the sample, which volatilize at high temperature.

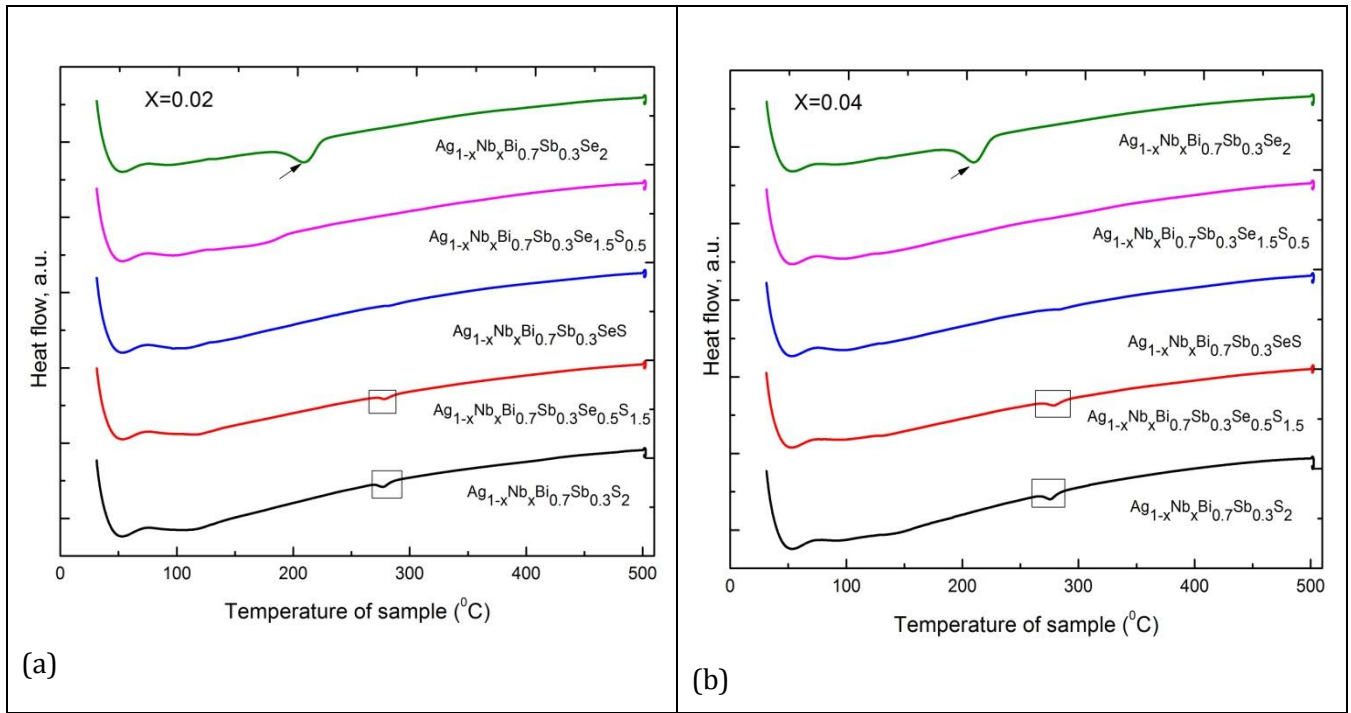


Figure 5-93: Heat flow DSC curves of Nb doped samples: (a) $x=0.02$ and (b) $x=0.04$.

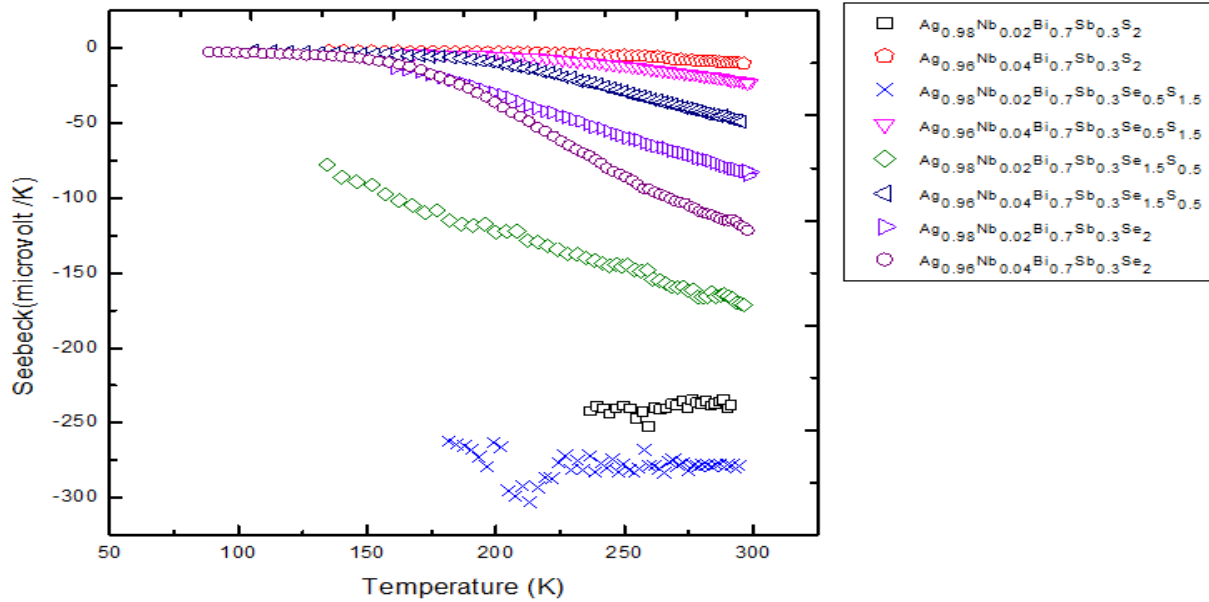
Hence, from the results of DSC obtained for undoped and doped samples, we can conclude that very small amount of Nb doping does not change the phase behavior of the samples. And, the idea of suppressing the phase transition is still maintained after doping.

5.4 Densification of samples

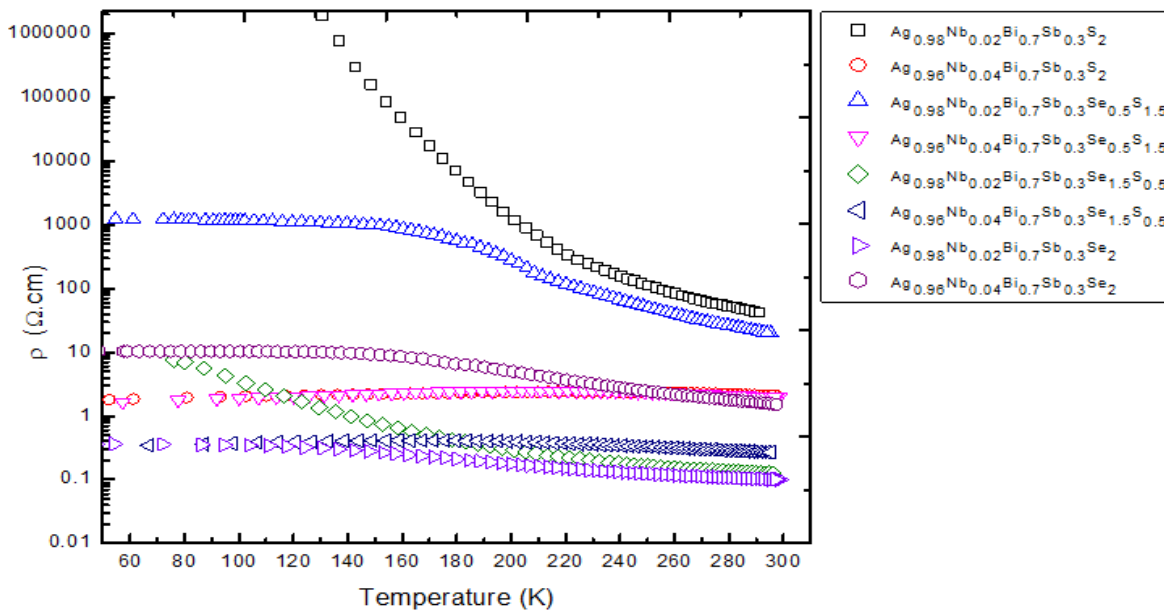
The obtained samples after synthesis were grounded by hand in agate mortar and subsequently densified using spark plasma sintering (SPS) system at 400°C with holding time of 10 min in a $\varnothing=15\text{mm}$ graphite mold under an axial compressive stress of 75MPa in an argon atmosphere. The obtained dense pellets, with thickness of 2.89mm were polished and cut into a square shape pellet. But, some of the samples while polishing broke down into several pieces, so we were unable to cut it into the desired shape required for the measurement. The possible reason could be the grinding method as we grinded chunks manually, the grains are not too small in size; and no optimization of the microstructure was carried out before SPS. Another possibility is that our sample contains small amounts of elemental Bi and Se that can melt, come out and results in cracks in the sintered pellet. For the Seebeck and electrical resistivity measurements, we cut the samples into bars as shown in chapter 2. The thermal diffusivity and the Seebeck and electrical resistivity were measured on the square and bar shape samples respectively.

5.5 Transport properties measurements

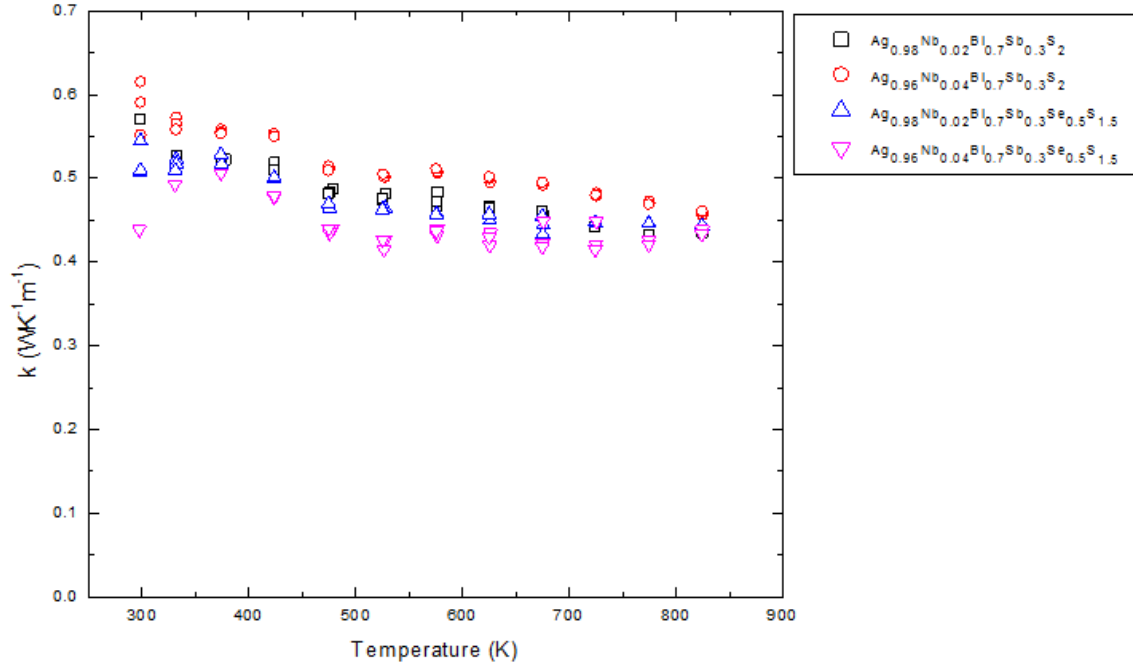
The Seebeck coefficient, electrical resistivity and thermal diffusivity were measured by using the instruments already mentioned in chapter 2. Here, in this section, we presented the results obtained with the sintered samples. The temperature dependences of S and ρ for selected compositions $\text{Ag}_{1-x}\text{Nb}_x\text{Bi}_{0.7}\text{Sb}_{0.3}\text{S}_2$, $\text{Ag}_{1-x}\text{Nb}_x\text{Bi}_{0.7}\text{Sb}_{0.3}\text{Se}_{0.5}\text{S}_{1.5}$, $\text{Ag}_{1-x}\text{Nb}_x\text{Bi}_{0.7}\text{Sb}_{0.3}\text{Se}_{1.5}\text{S}_{0.5}$ and $\text{Ag}_{1-x}\text{Nb}_x\text{Bi}_{0.7}\text{Sb}_{0.3}\text{Se}_2$ ($x=0.02, 0.04$) over the temperature range 50-300K are shown in Figure 5-94(a) and (b). These compositions correspond to the pellets that were large enough for the measurements after polishing.



(a)



(b)



(c)

Figure 5-94: Temperature dependence of (a) S , (b) ρ from 50 to 300K and (c) κ from 300 to 825K for $\text{Ag}_{1-x}\text{Nb}_x\text{Bi}_{0.7}\text{Sb}_{0.3}\text{S}_2$, $\text{Ag}_{1-x}\text{Nb}_x\text{Bi}_{0.7}\text{Sb}_{0.3}\text{Se}_{0.5}\text{S}_{1.5}$, $\text{Ag}_{1-x}\text{Nb}_x\text{Bi}_{0.7}\text{Sb}_{0.3}\text{Se}_{1.5}\text{S}_{0.5}$ and $\text{Ag}_{1-x}\text{Nb}_x\text{Bi}_{0.7}\text{Sb}_{0.3}\text{Se}_2$

Table 9: The room temperature value of $|S|$, ρ , κ and ZT for selected compositions.

Composition name	$ S $ ($\mu\text{V/K}$)	ρ ($\Omega\cdot\text{cm}$)	κ ($\text{WK}^{-1}\text{m}^{-1}$)	ZT
$\text{Ag}_{0.98}\text{Nb}_{0.02}\text{Bi}_{0.7}\text{Sb}_{0.3}\text{S}_2$	238	42.8	0.57	6.9×10^{-5}
$\text{Ag}_{0.96}\text{Nb}_{0.04}\text{Bi}_{0.7}\text{Sb}_{0.3}\text{S}_2$	9	2.1	0.62	1.8×10^{-6}
$\text{Ag}_{0.98}\text{Nb}_{0.02}\text{Bi}_{0.7}\text{Sb}_{0.3}\text{Se}_{0.5}\text{S}_{1.5}$	278	19.9	0.51	2.2×10^{-4}
$\text{Ag}_{0.96}\text{Nb}_{0.04}\text{Bi}_{0.7}\text{Sb}_{0.3}\text{Se}_{0.5}\text{S}_{1.5}$	23	1.9	0.44	1.8×10^{-5}
$\text{Ag}_{0.98}\text{Nb}_{0.02}\text{Bi}_{0.7}\text{Sb}_{0.3}\text{Se}_{1.5}\text{S}_{0.5}$	171	0.1	-	-
$\text{Ag}_{0.96}\text{Nb}_{0.04}\text{Bi}_{0.7}\text{Sb}_{0.3}\text{Se}_{1.5}\text{S}_{0.5}$	49	0.3	-	-
$\text{Ag}_{0.98}\text{Nb}_{0.02}\text{Bi}_{0.7}\text{Sb}_{0.3}\text{Se}_2$	81	0.1	-	-
$\text{Ag}_{0.96}\text{Nb}_{0.04}\text{Bi}_{0.7}\text{Sb}_{0.3}\text{Se}_2$	121	1.5	-	-

In Figure 5-94 (a), we observed negative value of S with semiconductor-like behavior for all compositions with x value 0.02 and 0.04, which indicates that for all x , these five compositions behave as an n-type semiconductor over the temperature range (50-300K). Moreover, the value of

|S| increases for $\text{Ag}_{0.96}\text{Nb}_{0.04}\text{Bi}_{0.7}\text{Sb}_{0.3}\text{S}_2$, $\text{Ag}_{0.96}\text{Nb}_{0.04}\text{Bi}_{0.7}\text{Sb}_{0.3}\text{Se}_{0.5}\text{S}_{1.5}$, $\text{Ag}_{0.96}\text{Nb}_{0.04}\text{Bi}_{0.7}\text{Sb}_{0.3}\text{Se}_{1.5}\text{S}_{0.5}$, $\text{Ag}_{0.98}\text{Nb}_{0.02}\text{Bi}_{0.7}\text{Sb}_{0.3}\text{Se}_{1.5}\text{S}_{0.5}$, and $\text{Ag}_{0.96}\text{Nb}_{0.04}\text{Bi}_{0.7}\text{Sb}_{0.3}\text{Se}_2$, $\text{Ag}_{0.98}\text{Nb}_{0.02}\text{Bi}_{0.7}\text{Sb}_{0.3}\text{Se}_2$ with increasing temperature from 50K to 300K, while for two other composition $\text{Ag}_{0.98}\text{Nb}_{0.02}\text{Bi}_{0.7}\text{Sb}_{0.3}\text{S}_2$ and $\text{Ag}_{0.98}\text{Nb}_{0.02}\text{Bi}_{0.7}\text{Sb}_{0.3}\text{Se}_{0.5}\text{S}_{1.5}$, the |S| value are constant. This constant value could be analyzed from the resistivity curve, as the nature of the curve shows that these two compositions are very resistive. Here, we tabulated the room temperature value of |S|, ρ , κ and ZT in Table 9. We observed that the value of |S| and ρ for first six compositions decreases from Nb fraction 0.02 to 0.04, which indicates an effective doping; increase in Nb fraction increases the carrier concentration which leads to lowering of seebeck coefficient. So, we can say that the doping is effective for n-type doping which means that by adding antimony in our compositions, the doping behavior remain same. The temperature dependence of the thermal conductivity κ for only four compositions $\text{Ag}_{1-x}\text{Nb}_x\text{Bi}_{0.7}\text{Sb}_{0.3}\text{S}_2$ and $\text{Ag}_{1-x}\text{Nb}_x\text{Bi}_{0.7}\text{Sb}_{0.3}\text{Se}_{0.5}\text{S}_{1.5}$ ($x=0.02, 0.04$) is plotted in Figure 5-94(c). All this samples possess large electrical resistivity, which means for all of them the electrical contribution to the thermal conductivity is almost zero. This indicate that the thermal conductivity we observed is mostly only the lattice thermal conductivity and the value for all the compositions are very low mentioned in Table 9. We observed that the κ value decreases with temperature for all the compositions ($x=0.02, 0.04$) over the range 300-900K which arised due to umklapp phonon-phonon scattering. And, from the Table 9, we noticed low κ value for both doping fraction for both the composition. Moreover, we observed the ZT value is very small because the power factor is too small due to large resistivity, which means that the doping level is not optimum here. And the very low thermal conductivity for all samples means that with optimized power factor, ZT values could be large.

5.6 Conclusion and future work

In summary, firstly we have performed the structural characterization and thermal analysis of the Nb-doped samples using XRD and DSC. We noticed that the small fraction of Nb doping in Sb substituted samples does not change the phase behavior at RT in comparison with the undoped samples. Indeed, the DSC results confirmed the absence of any phase transition in these doped samples. In the second half part of our study, from the Seebeck coefficient and resistivity measurements, we have concluded that with antimony in our compositions the band structure changes a little as compared to the antimony-free composition, which means that the optimum niobium content added in AgBiSe_2 (as mention in literature 222) is not the same here. So, a new optimization should be carried out, as we have seen already that the doping with Nb is effective.

Secondly, we can say that the optimum doping level will probably be depending on the S to Se content; as for the same Nb doping content, the value mention in Table 9 changes from pure S to pure Se. So, the optimization should be performed for all the compositions (or selected compositions spanning the whole composition range of the solid solution. Following this, in future, the optimization of carrier concentration has to be performed again. Moreover, we obtained very low value of thermal conductivity, which means in future for all of the compositions if we are able to optimize the power factor, the ZT will be high as the thermal conductivity is intrinsically very low. And, as we already obtained a very low value of κ , nanostructuring is not required in future to diminish the κ value. Here, in this chapter, we were not able to show the result of property measurements for some of the samples, as the sintered pellets broke during polishing. In this respect, in future, one should optimize the SPS conditions to avoid such situation, for example by applying the ball milling method prior to SPS.

Chapter 6

**The effect of ionized impurity scattering
on the TE performances of rock salt**

$\text{AgPb}_m\text{SnSe}_{2+m}$

6.1 Organization of the chapter

Here, we present a supplementary chapter based on the results obtained with rock salt material $\text{AgPb}_m\text{SnSe}_{2+m}$. The chapter is divided into two parts: first part contains the details of the synthesis process and the second part shows the study of thermoelectric performances of $\text{AgPb}_m\text{SnSe}_{2+m}$ samples.

6.2 Introduction

At present, several approaches have been developed to enhance the thermopower including modifying the band structure by electronic resonant states [249], quantum confinement effects [250], band convergence [251], energy barrier filtering [252,253] and intensifying impurity scattering of the carriers [254] to enhance the Seebeck coefficient. Among these, the carrier impurity scattering effect on the Seebeck coefficient has been recently investigated in skutterudites [254]. The important known facts regarding this scattering include: this effect results in reduction of the carrier mobility leading to a deterioration of the electrical conductivity [256]; and as the carrier scattering probability by ionized impurity is inversely related to $\varepsilon^{3/2}$ and v^3 , where ε is the energy of the carriers and v is the drift velocity [255], so, the carriers with lower energy are more scattered than the higher energy ones which on other way helps to raise the value of Seebeck coefficient. Therefore, to implement such ideas, it is necessary to find an effective strong ionized impurity scattering center, which could control the concentration of carriers in order to reduce the degradation of the electrical conductivity due to much lower mobility while improving the Seebeck coefficient. Thus, this overall could put a positive impact on the improvement of TE performances.

As per the recent reports, AgSnSe_2 and PbSe both possess the rock salt structure type. AgSnSe_2 has acquired much attention due to its characteristic of natural valence-skipping and also it possesses a very short mean-free path of the carriers showing the existence of intrinsically strong electron scattering possibly due to the valence fluctuations of Sn [258]. On the other side, PbSe is not a good applicant for TE performance as compared to PbTe due to the greater separation of its two key valence bands. But, still work has been made with this material as it's contain lower cost Se as compared to Te, and has higher melting and operation temperature but contains no scarce element like tellurium in its composition. Till date, solid solution is considered to be an effective way to enhance the TE performance. Here, in this report, we showed the TE performance of a novel PbSe-AgSnSe_2 solid solution $\text{AgPb}_m\text{SnSe}_{2+m}$ with limited AgSnSe_2 fraction influenced by the ionized impurity scattering of the charge carriers. In AgSnSe_2 , half of the Sn is $2+$ and half is $4+$, so average

charge is 3+ which is as same as the Bi (3+) in AgBiSe₂. In addition, it contains Ag and Se (-2) which is similar as the AgBiCh₂. This study is a collaborative work with another group (Lin Pan, College of Materials Science and Engineering, University of Technology Nanjing, China) and the context is linked with my thesis work as it possesses the same rock-salt structure like I-V-VI₂ group. My role in the experimental work included densification by SPS, shaping of pellets, XRD analysis, thermal diffusivity measurements, and low temperature Seebeck coefficient and electrical resistivity measurements.

6.3 Synthesis of solid solution

At first, the synthesis of AgSnSe₂ was done by simple solid state method. The nominal amount of raw materials Ag (shots, 99.99%), Sn (shots, 99.99%) and Se (granules, 99.99%) were first properly mixed and grounded, and after it has been sealed in an evacuated silica tube under argon atmosphere. After, the ingot was held at 1073 K for 12 h, cooled down to 673 K in 8 h, followed by water-quenching. The sample was then taken out of the silica tubes and grounded manually using agate mortar and after was pressed into pellets under uniaxial stress (250 MPa). Those pellets were heated again with the same thermal treatment. The second synthesis event was done for PbSe. Here, again the raw materials Pb (granules, 99.99%) and Se (granules, 99.99%) were mixed and grounded manually and then sealed in an evacuated silica tube. The synthesis was done by melting and solidifying the raw materials together at 1423 K for 6 h. And finally, from the above prepared two materials AgSnSe₂ and PbSe, the compounds belonging to the solid solution AgPb_mSnSe_{m+2} ($m = \infty, 100, 50, 25$) were obtained by mixing, melting and solidifying AgSnSe₂ and PbSe together with mole ratio 1: m at 1423 K in an evacuated silica tubes under argon atmosphere. For the synthesis, the ingots were held at 1423 K for 6 h, cooled down to 673 K in 8 h, and then subsequently water-quenched. The resultant samples were obtained after following this above mentioned three synthesis events.

After, the samples were grounded, followed by densification using a spark plasma sintering (SPS) system (SPS-511S) at 873 K with holding time of 10 min in a $\varnothing=15$ mm graphite mold under an uniaxial compressive stress of 100 MPa in an argon atmosphere. After SPS, the samples were polished to remove the graphite from the surface and were then cut into proper dimensions suitable for the measurements using a diamond saw. For thermal stability tests, the pellet with composition AgPb_mSnSe_{2+m} ($m = 25$) was further annealed at 773 K for one week in an evacuated silica tube before performing the measurements.

6.4 Methods and devices used for characterization

The instruments used for materials characterizations were mentioned earlier in chapter 2. The results of the experiments performed are discussed in the following section.

6.5 Results and discussion

6.5.1 Structural characterization results

Figure 6-95(a) shows the X-ray diffraction patterns for all the samples obtained at room temperature. According to this Figure 6-95 (a), the main diffraction peaks correspond to the PbSe (JCPD No.06-0354) phase, for $\text{AgPb}_m\text{SnSe}_{2+m}$ samples and no other secondary phases were observed in these patterns. Using Rietveld refinement, the lattice parameters values were calculated from the XRD patterns and were plotted as shown in Figure 6-95 (b). Here, we can see that the lattice constant a monotonically decreases with increasing AgSnSe_2 content; the resultant refined pattern obtained for all the samples were shown in Figure 6-96.

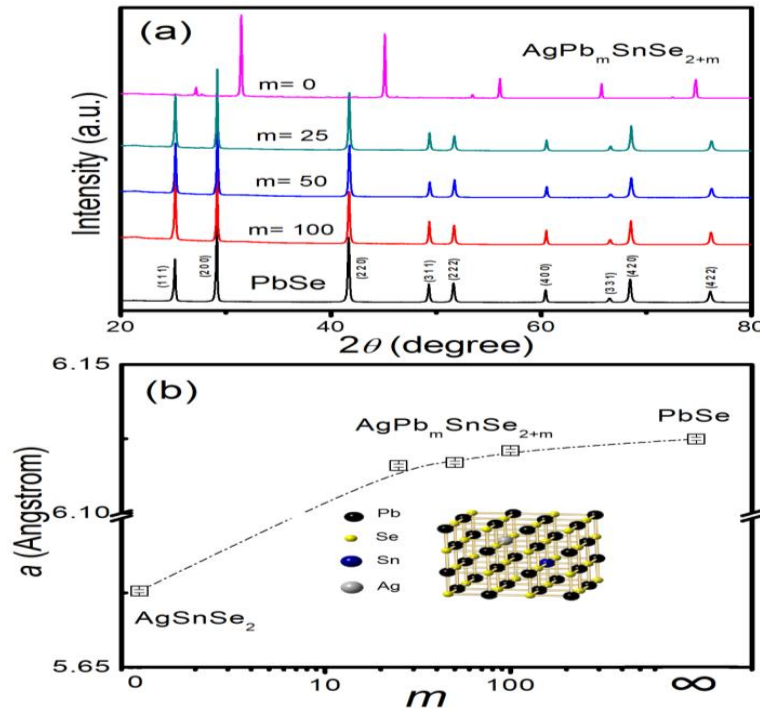


Figure 6-95: Powder XRD patterns (a) and lattice constants (b) of $\text{AgPb}_m\text{SnSe}_{2+m}$ ($m = \infty, 100, 50, 25, 0$).

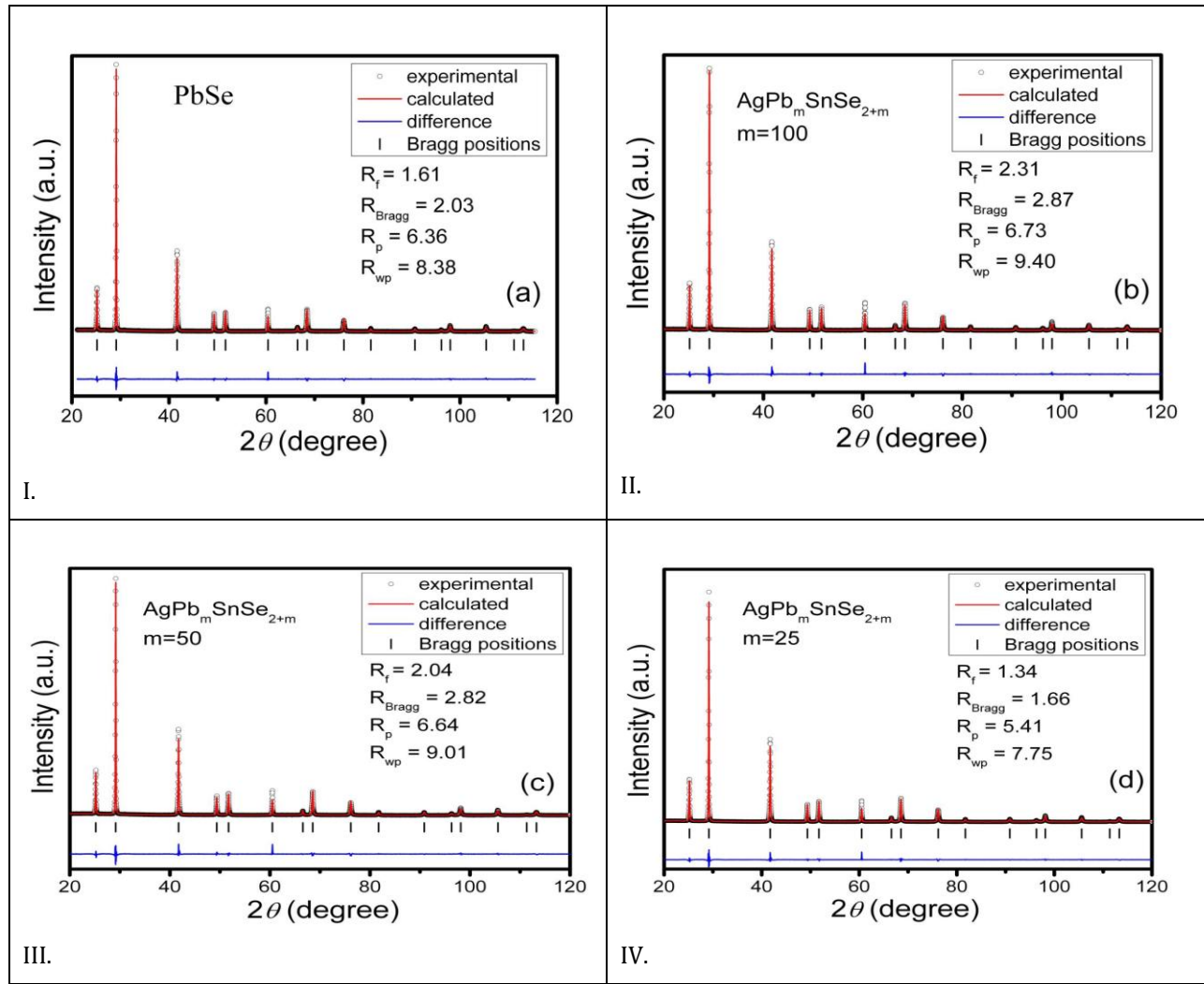


Figure 6-96: Rietveld refinements of $\text{AgPb}_m\text{SnSe}_{2+m}$ ($m = \infty, 100, 50, 25$) at room temperature.

6.5.2 Results of electrical and thermal property measurements

6.5.2.1 Seebeck and Resistivity measurements

At first, the temperature dependences of electrical resistivity ρ and Seebeck coefficient S for $\text{AgPb}_m\text{SnSe}_{2+m}$ ($m = \infty, 100, 50, 25$) in the range of 25 K – 889 K are plotted in Figure 6-97(a,b). As per the Figure 6-97, we observe that for pristine PbSe, the ρ and S value increases with increasing temperature from 50 K to 595 K, and below 595K the S is positive which indicates a p -type degenerate semiconductor behavior. However, with further heating above 595K, S value reaches a maximum and then again starts to decrease and changes to negative values around 840 K. In the

meantime, we notice that when temperature rises up to 693K, ρ value starts to decrease. This kind of electrical transport behavior may unambiguously correspond to a two bands conduction mechanism, where both the holes and electrons take part in conduction. The presence of both the carriers can be understood well from the variation of S , as it is positive at low temperature and then into negative at high temperature. On the other hand, for the rest three samples of $\text{AgPb}_m\text{SnSe}_{2+m}$ ($m = 100, 50, 25$), ρ first increases when heating and then decreases, leaving a flat peak around temperature 173 K, 187 K and 201 K respectively. But, with further rise in temperature, it keeps on falling and then rises again, leaving a flat valley around 345 K, 401 K, and 399 K respectively. Compare to the PbSe, other samples showed increasing S value with rising temperature throughout the entire temperature range. Thus, it implies the suppression of bipolar carriers conduction in $\text{AgPb}_m\text{SnSe}_{2+m}$ ($m = 100, 50, 25$) as compared to PbSe.

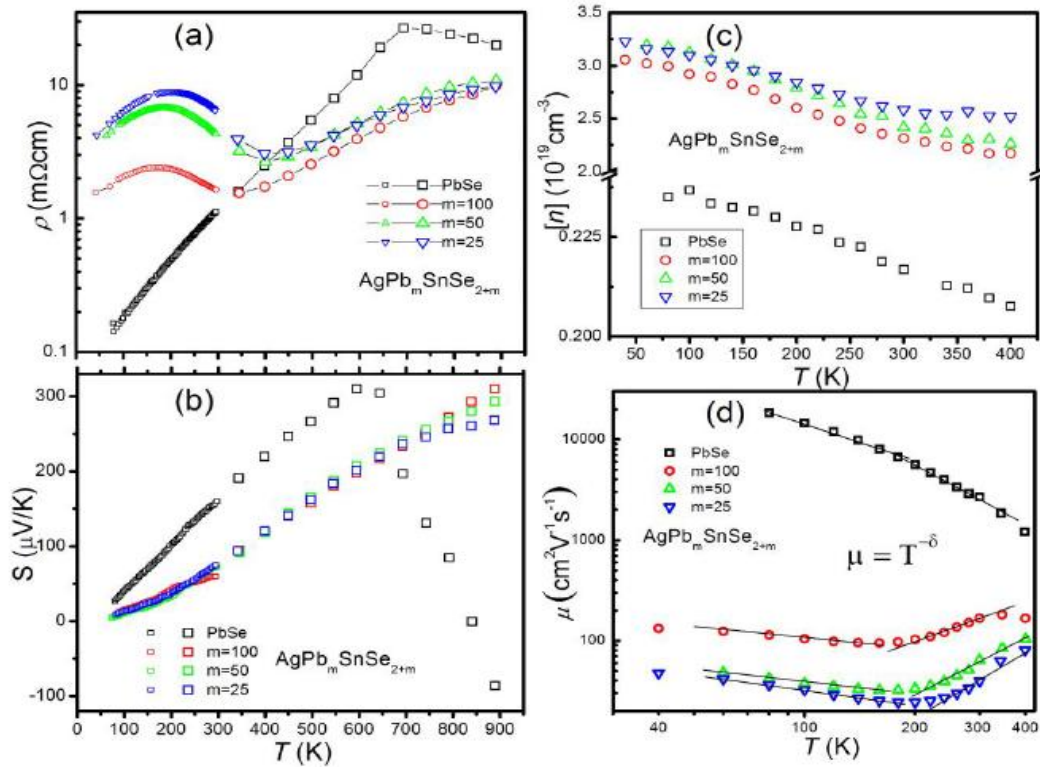


Figure 6-97: Temperature dependences of (a) electrical resistivity, (b) Seebeck coefficient, (c) carriers concentration and (d) hole mobility of $\text{AgPb}_m\text{SnSe}_{2+m}$ ($m = \infty, 100, 50, 25$).

6.5.2.2 Hall Effect measurements

To perform the Hall Effect measurements, the resistivity relation which is important to note is given by $\rho = 1/ne\mu$, where n is the carriers concentration, e is the electronic charge (C), and μ is the mobility of the holes. In order to obtain a better understanding of the role of AgSnSe_2 in the system, Hall-effect analysis was performed. At first, the carriers concentration $[n]$ for $\text{AgPb}_m\text{SnSe}_{2+m}$ ($m = \infty, 100, 50, 25$) samples were calculated using the Hall coefficients relation $R_H = 1 / ne$, where e is the electronic charge and plotted in Figure 6-97(c). The figure shows that the concentration of holes of all samples decreases with increasing temperature. This behavior could be relate to the absence of interband excitations from heavy-hole band Σ to light-hole band L of $\text{AgPb}_m\text{SnSe}_{2+m}$ ($m = \infty, 100, 50, 25$) or not obvious below room temperature [264]. Moreover, the carrier concentration of $\text{AgPb}_m\text{SnSe}_{2+m}$ increases monotonically over the entire temperature range with the increase of AgSnSe_2 content. Even, such type of variation of carriers concentration of $\text{AgPb}_m\text{SnSe}_{2+m}$ ($m = 100, 50, 25$), rules out any “thermal activation” behavior in these samples.

Further experiments were conducted to obtain the temperature dependence of the mobility of all the samples shown in the Figure 6-97(d), which scales with the power exponent δ of $\mu \approx T^{-\delta}$. Here, we observe that the mobility μ of pristine PbSe decreases monotonically over the entire temperature range, while μ of $\text{AgPb}_m\text{SnSe}_{2+m}$ ($m = 100, 50, 25$) decreases first and then increases, leaving a flat valley around 160 K ($m = 100$) and 180K ($m = 50, 25$) respectively. Then, with further heating, μ of $\text{AgPb}_m\text{SnSe}_{2+m}$ ($m = 100$) keeps increasing first and then falls, leaving a maximum around 350 K. The very same behavior of μ is expected for $\text{AgPb}_m\text{SnSe}_{2+m}$ ($m=50, 25$) also, μ of $\text{AgPb}_m\text{SnSe}_{2+m}$ ($m = 50, 25$) should also exhibit a peak located around 400 ~ 450 K but due to the temperature limit of the measurements, these two peaks cannot be observed in Figure 6-97(d). A detailed explanation of the scattering effect is described below in the following paragraphs.

The relaxation time τ and a transport effective mass m^* is related to mobility by the relation: $\mu = e\tau / m^*$. According to the Matthiesen’s rule, τ can be expressed as:

$$\tau^{-1} = \tau_{h-h}^{-1} + \tau_{h-GB}^{-1} + \tau_{h-II}^{-1} + \tau_{h-ph}^{-1} + \dots \quad \text{..... 6.1}$$

Where $h-h$ refers to hole-hole scattering, $h-GB$ to hole-grain boundaries scattering, $h-II$ to hole-ionized impurities scattering, and $h-ph$ to hole-phonons scattering.

All these scattering processes depend on the temperature and the concentration of carriers. Here, we can neglect the contribution of τ_{h-h} , as it is effective only at very low temperatures, τ_{h-ll} is neglected too in pristine PbSe as the concentration of carriers is low in PbSe (meaning that the concentration of ionized impurities is also low. Among all the scattering mechanism, τ_{h-ph} is considered as the main contributor to τ at high temperature, as phonon modes are activated at this temperature. Under this hypothesis, μ obeys a power law $\mu \approx T^{-\delta}$, where $\delta=s-r$ is composed of the scattering parameter (i.e., $r = -1/2$ for acoustic phonon scattering, 0 for neutral impurity scattering, and $3/2$ for ionized impurity scattering, ...) and the number of phonons participating to a scattering process (i.e., $s = 1$ for one-phonon process, 2 for two-phonon process, and $s = 0$ for non-phonon scattering processes) [265]. Here, for $\text{AgPb}_m\text{SnSe}_{2+m}$ ($m = \infty, 100, 50, 25$), the power exponents δ close to room temperature are 1.8, -1.4, -1.5 and -1.7, respectively. More precisely, in the degenerate p -type PbSe sample, the mobility follows $\mu \approx T^{-1.2}$ at 80 – 160 K and $\mu \approx T^{-1.8}$ above 180 K, indicating $r = -1/2$ (acoustic phonon scattering with one-phonon process) over the entire temperature range. The lower exponent at low temperature may originate from the contribution of h -GB scattering. However, for the degenerate $\text{AgPb}_m\text{SnSe}_{2+m}$ ($m = 100, 50, 25$) samples below 160 K, the mobility showed $\mu \approx T^{-0.35}, T^{-0.45}, T^{-0.5}$ indicates which implies that the carrier scattering mechanisms are a combination of various mechanisms. Further, with increasing temperature above 180 K, the mobility of $\text{AgPb}_m\text{SnSe}_{2+m}$ ($m = 100, 50, 25$) samples, the value of $\mu \approx T^{1.4}, T^{1.5}, T^{1.7}$ indicating that the main carrier scattering mechanism is the ionized impurity scattering above 180 K. Again, heating to 350 K, δ value of $\text{AgPb}_m\text{SnSe}_{2+m}$ ($m = 100$) changes to positive, which means acoustic phonon scattering will become the dominated scattering mechanism again at high temperature, due to the excitation of phonon modes.

The strength of ionized impurity scattering is mainly determined by the concentration of impurity centers N_i , their charge states v , the carrier concentration n , the dielectric constant ϵ and the density of states effective mass m_d^* [266]. According to Brooks' and Herring's derivations, the carrier relaxation time of ionized impurity scattering is proportional to $m_d^{*1/2}$ and inversely proportional to N_i and v^2 . [254, 266] Thus, a highly charged impurity with high screened Coulomb potential will more effectively scatter the lower energy electrons and lead to larger average electron energy and results in larger value of Seebeck coefficient. Here, strong ionized impurity scattering in the $\text{AgPb}_m\text{SnSe}_{2+m}$ system could originate from the valence fluctuations of Sn with charge states Sn^{4+} and Sn^{2+} . The large impurity scattering leads to the strong decrease of the mobility, but contributes to limit the decrease of S that should be observed with the much larger n .

6.5.2.3 Specific heat measurements

Figure 6-98 shows the heat capacity C_p of pristine PbSe and $\text{AgPb}_m\text{SnSe}_{2+m}$ ($m = 25$) as a function of temperature from 2 K to 400 K. According to the plot, C_p of pristine PbSe and $\text{AgPb}_m\text{SnSe}_{2+m}$ ($m = 25$) shows the similar type of variation over the entire temperature range. Even, $m = 50$ and $m = 100$ showed the identical behavior. The heat capacity of pristine PbSe reaches a value of 50 J/mol K at room temperature which is exactly the same as the expected classical high temperature Dulong-Petit lattice heat capacity value. The inset in Figure 6-98 shows the low temperature data of pristine PbSe and $\text{AgPb}_m\text{SnSe}_{2+m}$ ($m = 25$) plotted as C_p / T versus T^2 allowing a conventional fit by [268],

$$\frac{C_p(T)}{T} = \gamma + \beta T^2 \quad \text{..... 6.2}$$

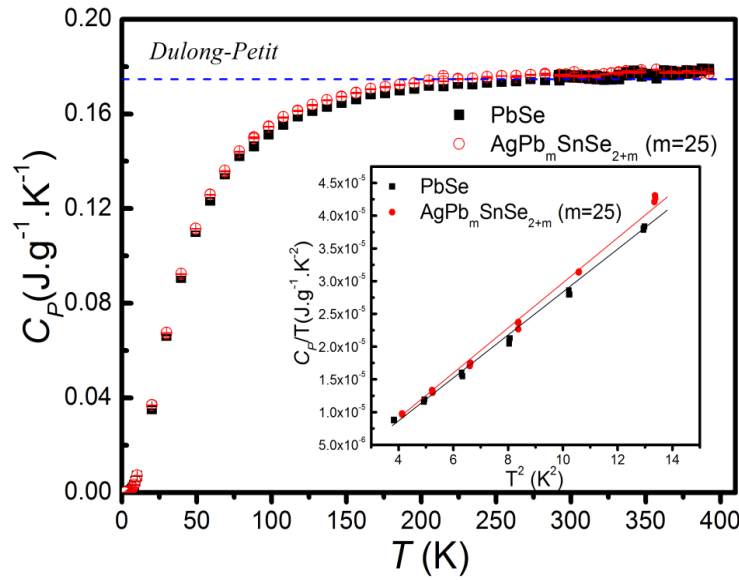


Figure 6-98: The heat capacity C_p of PbSe and $\text{AgPb}_m\text{SnSe}_{2+m}$ ($m = 25$) as a function of temperature from 2 K to 400 K. The inset shows the low- T C_p of PbSe and $\text{AgPb}_m\text{SnSe}_{2+m}$ ($m = 25$) plotted as C_p / T versus T^2 .

The above fit leads to almost identical values of β , which means that the Debye temperature is the same for all the samples, and near about zero value of γ for all materials, which means that the Fermi level is very close to the band edge and that materials can be mostly considered as single band.

6.5.2.4 Thermal conductivity measurements

Figure 6-99 (a) shows the temperature dependence of the thermal conductivity κ for $\text{AgPb}_m\text{SnSe}_{2+m}$ ($m = \infty, 100, 50, 25$). This figure depicts that λ of pristine PbSe at room temperature is $1.82 \text{ Wm}^{-1}\text{K}^{-1}$. It decreases first due to the intensified phonon-phonon umklapp processes and then increases with heating, leaving a valley around 570 K. This behavior comes from the bipolar diffusion i.e. more minority carriers (electrons here) jump across the band in the narrow band pristine PbSe with rising temperature and the formed diffusing electron-hole pairs lead to an additional thermal conductivity contribution. However, λ for $\text{AgPb}_m\text{SnSe}_{2+m}$ ($m = 100, 50, 25$) decreases with heating over the entire temperature range which means that the bipolar contribution to the thermal conductivity has been suppressed. Comparing with pristine PbSe, the total thermal conductivity λ of $\text{AgPb}_m\text{SnSe}_{2+m}$ ($m = 50, 25$) drops remarkably in the whole temperature range while λ of $\text{AgPb}_m\text{SnSe}_{2+m}$ ($m = 100$) strengthened below 750K.

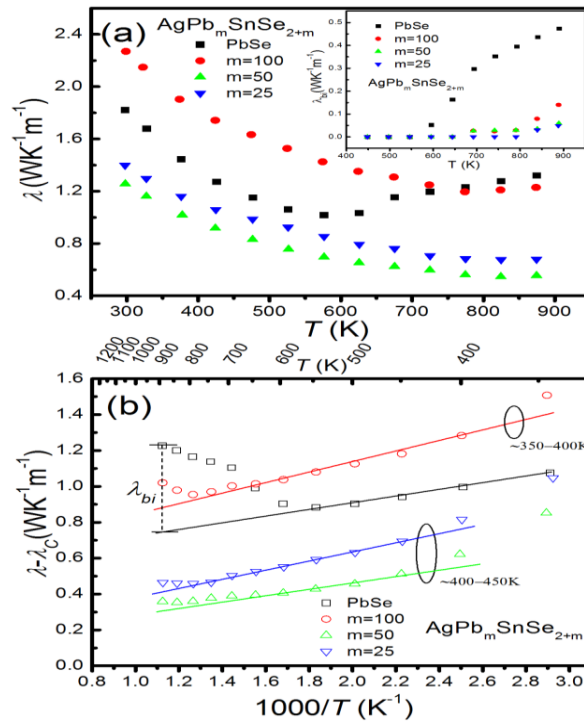


Figure 6-99: (a) Temperature dependence of thermal conductivity of $\text{AgPb}_m\text{SnSe}_{2+m}$ ($m = \infty, 100, 50, 25$) from 300 K to 875 K. The inset in (a) shows bipolar thermal conductivity as a function of temperature for $\text{AgPb}_m\text{SnSe}_{2+m}$ ($m = \infty, 100, 50, 25$). (b) The difference of total and carrier thermal conductivity $\lambda - L\sigma T$ as a function of temperature for $\text{AgPb}_m\text{SnSe}_{2+m}$ ($m = \infty, 100, 50, 25$), the solid line is a linear fit of the lattice thermal conductivity at temperature ranges from room temperature to 875 K, deviation of thermal conductivity indicating a significant bipolar thermal conductivity.

The total thermal conductivity λ can be expressed as:[269] $\lambda = \lambda_{\text{lat}} + \lambda_c + \lambda_{\text{bi}} = \lambda_{\text{lat}} + L\sigma T + \lambda_{\text{bi}}$, where λ_{lat} , λ_c and λ_{bi} refer to lattice, carrier and bipolar contributions to the thermal conductivity, respectively, and L is the Lorenz number which is obtained by fitting the Seebeck coefficient to the reduced chemical potential [7]. Here we have plotted the difference of total and carrier thermal conductivity ($\lambda - L\sigma T$) as a function of temperature. It shows that $(\lambda - L\sigma T)$ decreases linearly when heating from room temperature for pristine PbSe, which confirms that the acoustic phonon scattering is predominant. On the other hand, $(\lambda - L\sigma T)$ of $\text{AgPb}_m\text{SnSe}_{2+m}$ ($m = 100$) starts to decrease linearly above 350 K, while above 400 ~ 450K for $\text{AgPb}_m\text{SnSe}_{2+m}$ ($m = 50, 25$). It indicates that acoustic phonon scattering becomes the dominant scattering process above 350 K ($m = 100$) and 400 ~ 450K ($m = 50, 25$) for $\text{AgPb}_m\text{SnSe}_{2+m}$. It also confirms that the bipolar contribution has been mostly suppressed with the presence of AgSnSe_2 as the linear fit only deviates at very high temperature.

6.5.2.5 Figure of merit value

Here, from the combination of the electrical and thermal transport properties over the range of 340 – 890K, the figure of merit ZT is plotted shown in Figure 6-100. It shows that ZT of pristine PbSe reaches 0.49 at 344 K, climbs to a maximum of 0.6 at 448 K, and then starts to fall down to below 0.1 above 694 K due to the bipolar contribution. However, for $\text{AgPb}_m\text{SnSe}_{2+m}$ samples, ZT monotonically increases with temperature in the entire temperature range. The maximum ZT value of 1.3 at 889 K is obtained for $\text{AgPb}_m\text{SnSe}_{2+m}$ ($m = 50$). Therefore, the results indicate that the high temperature TE properties of PbSe can be remarkably improved by the introduction of slight amounts of AgSnSe_2 to form $\text{AgPb}_m\text{SnSe}_{2+m}$, by suppressing the bipolar contribution to the thermal conductivity while maintaining reasonably large S values due to ionized impurity scattering of the carriers.

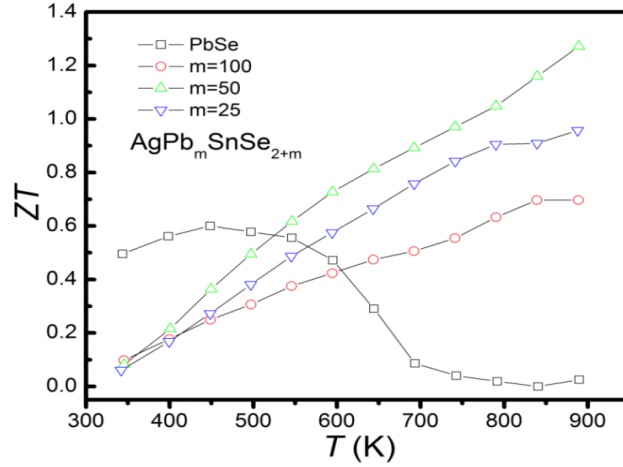


Figure 6-100: ZT of $\text{AgPb}_m\text{SnSe}_{2+m}$ ($m = \infty, 100, 50, 25$) in the range 340 K to 890 K.

6.6 Conclusion

We successfully synthesized the solid solution $\text{AgPb}_m\text{SnSe}_{2+m}$ ($m = 100, 50, 25$) samples with a rock salt structure. The temperature dependence of the holes mobility μ combined with the difference between total and carrier thermal conductivity $\lambda - L\sigma T$, showed that ionized impurity scattering becomes predominant in $\text{AgPb}_m\text{SnSe}_{2+m}$ near room temperature (180 – 350 K for ($m = 100$), 180 – 400 ~ 450 K for ($m = 50, 25$)), although acoustic phonon scattering remains the main scattering mechanism at higher temperature. The introduction of AgSnSe_2 within the PbSe matrix can synergistically optimize the electrical and thermal transport properties. It enhances the Seebeck coefficient by boosting the scattering factor, improves the electric conductivity by the increase of the concentration of holes coupled to a limited degradation of their mobility, and reduces the total thermal conductivity by suppressing the bipolar contribution to the thermal conductivity. Therefore, thanks to this introduction of ionized impurity scattering, ZT of $\text{AgPb}_m\text{SnSe}_{2+m}$ ($m = 50$) reaches 1.3 at 889 K, and could most probably be further improved through the optimization of the concentration of charge carriers by doping.

Conclusion and perspectives

The goal of the thesis was to explore the solid solution $\text{AgBiSe}_2\text{-AgBiS}_2$, belonging to the class of ternary chalcogenides of type I-V-VI₂. Mainly, it includes the structural characterization, study of phase transition and transport property measurements.

The samples belonging to the solid solution $\text{AgBiSe}_2\text{-AgBiS}_2$ have been synthesized after the optimization of the heat treatment conditions. We have performed the structural characterization using XRD and further structural analysis using Le bail refinement; showing a complete solid solution without miscibility gap and that exists for all compositions. The thermal analysis confirmed the presence of the phase transitions for these compositions, with a shift of the temperature of transition as a function of the sulfur/selenium fraction. We have succeeded in obtaining single phase compounds for the two phases namely, hexagonal and cubic phase, and from the high temperature XRD, we observed the rhombohedral phase too for the selected composition ($x=1$ to 2 in $\text{AgBiSe}_{2-x}\text{S}_x$). Moreover, we obtained the phase change of the material from hexagonal to cubic under high pressure. For future study, it would be interesting to trap the intermediate (rhombohedral) phase for all compositions which shows two phase transition events obtained through DSC results. The most probable way to achieve this would be to keep sample for long annealing time (several weeks, as the temperature is rather low) at the particular temperature (should be noted down from the DSC heat flow curve) where this intermediate phase exists and do the water quenching at this temperature in order to stabilize this phase. So, in the following step of the study, we mainly focused on the chemical pressure applied on our samples in order to stabilize the cubic phase or in other word to suppress the phase transition which we observed in all compositions of the solid-solution.

Following the phase transition from hexagonal phase to cubic phase observed under high pressure, substitution method was applied on solid solution in order to suppress the phase transition. We have chosen to substitute bismuth with antimony, so by means of chemical pressure, we hoped to freeze the cubic phase; prior to the applications. The substituted samples have been synthesized by solid state reaction followed by slow cooling down to room temperature without water quenched. The insights gained from the experimental results revealed no structural phase transition up to the experimental limit, as was expected, meaning that the cubic phase has been stabilized by chemical pressure. Here we have performed substitution on selected composition spanning the whole range of the solid-solution, so it means chemical pressure with 30% Sb on the Bi site can stabilize the cubic phase in all compositions from AgBiS_2 to AgBiSe_2 .

Doping attempts were carried out in the Sb-substituted samples in order to observe its influence on solid solution. The results obtained confirmed that the small fraction of Nb doping in Sb substituted samples does not change the phase behavior at RT in comparison with the undoped samples. The DSC results confirmed the absence of phase transition too. The transport properties measurements show the negative value of S for all compositions ($x=0.02, 0.04$), indicating n-type semiconducting behavior over the range (50-300K). The value of $|S|$ and ρ for first six compositions decreases from Nb fraction 0.02 to 0.04; which means that as expected, increase in Nb fraction increases the carrier concentration which leads to lowering of Seebeck coefficient. This suggests that the doping is effective for n-type doping which means that by adding antimony in our compositions, the doping behavior remains the same. However, the values of the power factor were very low, so, we can conclude that with antimony in our composition the band structure changes slightly compared to the antimony free composition, which means that the optimum niobium content added in AgBiSe_2 (as mentioned in literature [222]) is not the same for Sb-substituted samples. So, in future a new optimization should be carried out, to find the optimum Nb level. Moreover, the optimum doping level will probably be depending on the S to Se content suggesting that further optimization of carrier concentration is required. Here, we achieved very low value of κ for the compositions ($x=0.02, 0.04$) over the range 300-900K. In addition, all these samples possess large electrical resistivity, which shows that the electrical contribution to the thermal conductivity is almost zero. This result concludes that the thermal conductivity we observed is mostly only the lattice thermal conductivity. Further, the low κ value suggests that in future for all of the compositions if we are able to optimize the power factor, the ZT will be large as the thermal conductivity is intrinsically very low. All the transport properties measurements were carried out on selected compositions, unfortunately, we could not perform on all other samples; as the sintered pellets broke during polishing. In this respect, we can suggest to apply the ball milling method before SPS in order to avoid such a situation. We expect that it would be possible then to explore the properties on all other samples.

During my PhD, we worked in collaboration with another group (Lin Pan, College of Materials Science and Engineering, University of Technology Nanjing, China) on solid solution $\text{AgPb}_m\text{SnSe}_{2+m}$ which possesses the same rock-salt structure as AgBiCh_2 . The results obtained showed that the ionized impurity scattering becomes predominant in $\text{AgPb}_m\text{SnSe}_{2+m}$ near room temperature (180 – 350 K) for ($m = 100$), 180 – 400 ~ 450 K for ($m = 50, 25$)), although acoustic phonon scattering remains the main scattering mechanism at higher temperature. Further, the introduction of AgSnSe_2 within the PbSe matrix can optimize the electrical and thermal transport properties. It enhances the Seebeck coefficient by boosting the scattering factor, improves the electric

conductivity by the increase of the concentration of holes coupled to a limited degradation of their mobility, and reduces the total thermal conductivity by suppressing the bipolar contribution to the thermal conductivity. Here, we achieved ZT value of 1.3 at 889K for $\text{AgPb}_m\text{SnSe}_{2+m}$ ($m = 50$) which suggests that the introduction of ionized impurity scattering is effective. In future, it would be better to do optimization of the carrier concentration by doping in order to enhance ZT value further.

The PhD thesis work allowed discovering the structural behavior of the chalcogenide materials AgBiSe_2 - AgBiS_2 , the existence of phase transition for all the compositions, characterization and transport properties measurements of materials using various instruments, and the effect of substitution and doping on the structural behavior of the materials.

Annex

A.

Calculation of compositions belonging to solid solution (AgBiSe₂-AgBiS₂).

The general formula used to calculate the mass m of each precursor is shown below:

$$n_{\text{Ag Bi}_{0.98}\text{Se}_{2-x}\text{S}_x} \text{ (mol)} = \frac{m \text{ (g)}}{M_{\text{Ag Bi}_{0.98}\text{Se}_{2-x}\text{S}_x} \left(\frac{\text{g}}{\text{mol}} \right)}$$

The calculated masses of precursors for all composition are shown in the table below.

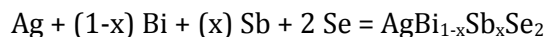
Table: Calculated mass value of precursors for composition AgBi_{0.98}Se_{2-x}S_x.

AgBi _{0.98} Se _{2-x} S _x	m (Ag),g	m(Bi), g	m(Se), g	m(S), g
AgBi _{0.98} SeS	1.146	2.175	0.839	0.340
AgBi _{0.98} Se _{0.9} S _{1.1}	1.159	2.199	0.763	0.379
AgBi _{0.98} Se _{0.8} S _{1.2}	1.172	2.224	0.686	0.418
AgBi _{0.98} Se _{0.7} S _{1.3}	1.185	2.250	0.607	0.458
AgBi _{0.98} Se _{0.6} S _{1.4}	1.199	2.276	0.527	0.499
AgBi _{0.98} Se _{0.5} S _{1.5}	1.213	2.303	0.444	0.541
AgBi _{0.98} Se _{0.4} S _{1.6}	1.227	2.330	0.359	0.584
AgBi _{0.98} Se _{0.3} S _{1.7}	1.242	2.358	0.273	0.628
AgBi _{0.98} Se _{0.2} S _{1.8}	1.257	2.387	0.184	0.673
AgBi _{0.98} Se _{0.1} S _{1.9}	1.272	2.416	0.093	0.719
AgBi _{0.98} S ₂	1.288	2.446	-	0.766
AgBi _{0.98} Se _{1.1} S _{0.9}	1.133	2.151	0.912	0.303
AgBi _{0.98} Se _{1.2} S _{0.8}	1.121	2.128	0.985	0.267
AgBi _{0.98} Se _{1.3} S _{0.7}	1.109	2.105	1.055	0.231
AgBi _{0.98} Se _{1.4} S _{0.6}	1.097	2.083	1.124	0.196
AgBi _{0.98} Se _{1.5} S _{0.5}	1.086	2.061	1.192	0.161
AgBi _{0.98} Se _{1.6} S _{0.4}	1.074	2.040	1.258	0.128
AgBi _{0.98} Se _{1.7} S _{0.3}	1.063	2.019	1.323	0.095
AgBi _{0.98} Se _{1.8} S _{0.2}	1.053	1.998	1.387	0.063
AgBi _{0.98} Se _{1.9} S _{0.1}	1.042	1.978	1.449	0.031
AgBi _{0.98} Se ₂	1.032	1.958	1.510	-

B.

Calculation of compositions of Sb-substituted compound.

The one step solid-state reaction applied is:



The calculated masses of precursors for all the respective compounds are tabulated in the table below:

Table: Calculated mass value of precursors for composition $\text{AgBi}_{1-x}\text{Sb}_x\text{Se}_2$

X value	m(Ag), g	m (Bi), g	m (Sb), g	m (Se), g
0.1	0.4629	0.8072	0.0523	0.6777
0.2	0.4717	0.7307	0.1065	0.6906
0.3	0.4809	0.6522	0.1629	0.7041
0.4	0.4905	0.5701	0.2215	0.7180
0.5	0.5004	0.4847	0.2824	0.7325
0.6	0.5107	0.3958	0.3459	0.7477
0.7	0.5215	0.3031	0.4120	0.7634
0.8	0.5327	0.2064	0.4810	0.7799
0.9	0.5444	0.1055	0.5531	0.7970
1	0.5564	-	0.6280	0.8145

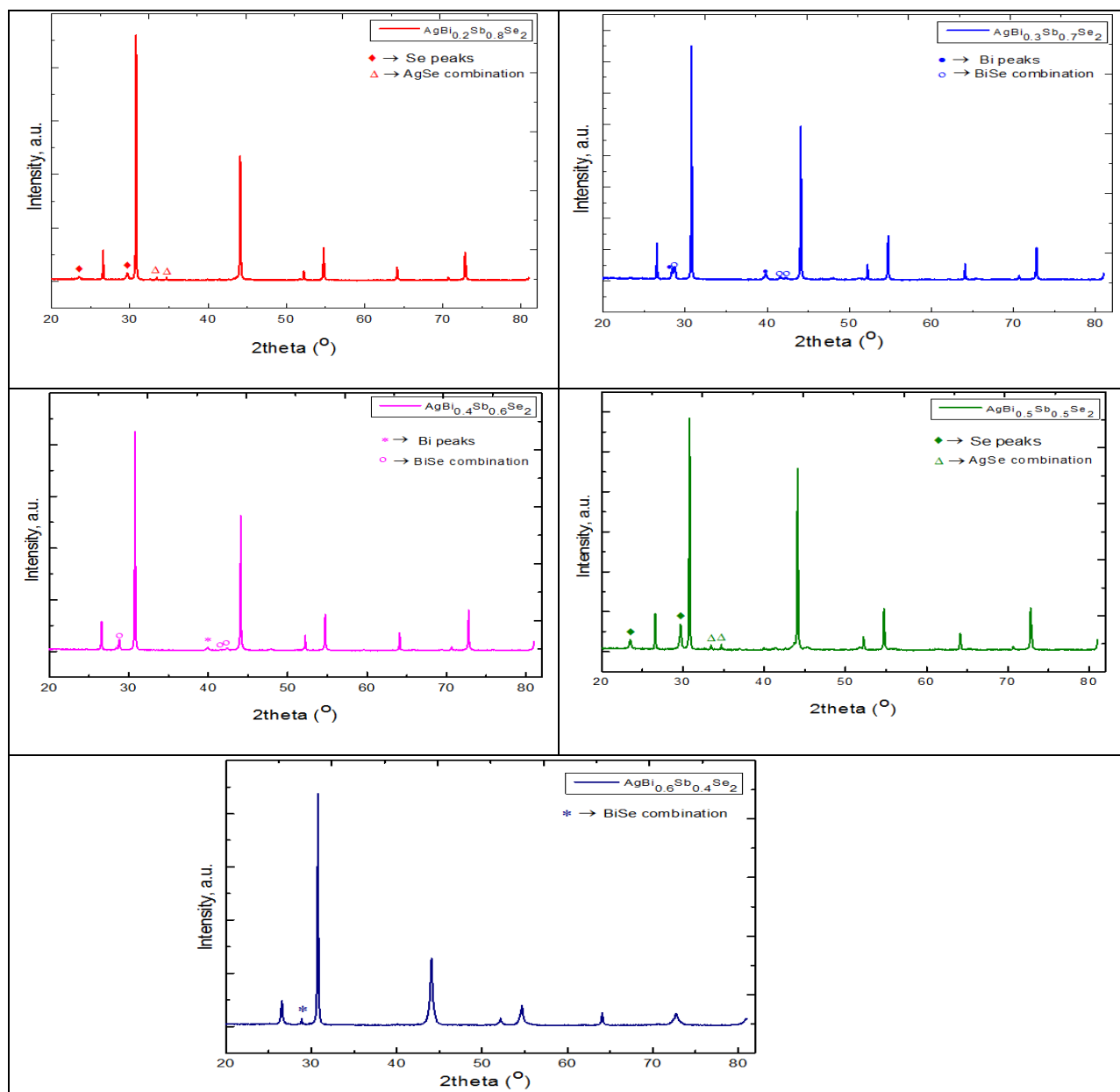
The calculated masses of precursors for Sb substituted solid solution are given below:

Composition	m (Ag), g	m (Bi), g	m (Sb), g	m (Se), g	m (S), g
$\text{AgBi}_{0.7}\text{Sb}_{0.3}\text{S}_2$	1.3681	1.8554	0.4633	-	0.8132
$\text{AgBi}_{0.7}\text{Sb}_{0.3}\text{Se}_{0.5}\text{S}_{1.5}$	1.2833	1.7403	0.4347	0.4697	0.5721
$\text{AgBi}_{0.7}\text{Sb}_{0.3}\text{SeS}$	1.2084	1.6387	0.4092	0.8846	0.3591
$\text{AgBi}_{0.7}\text{Sb}_{0.3}\text{Se}_{1.5}\text{S}_{0.5}$	1.1417	1.5483	0.3866	1.2537	0.1697
$\text{AgBi}_{0.7}\text{Sb}_{0.3}\text{Se}_2$	1.0820	1.4674	0.3664	1.5843	0.8132

C.

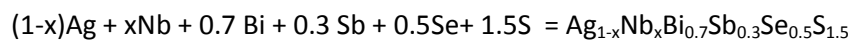
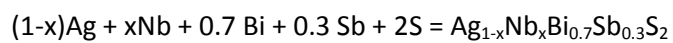
XRD patterns of Sb-substituted AgBiSe_2 samples.

The pattern of $\text{AgBi}_{0.2}\text{Sb}_{0.8}\text{Se}_2$; the main peaks correspond to the peaks of cubic AgSbSe_2 (reference code 96-901-1029). Here, we noticed secondary peaks arise due to the presence of Se in the compound (marked as ♦) and another two due to the AgSe combination (marked as Δ). The pattern of $\text{AgBi}_{0.3}\text{Sb}_{0.7}\text{Se}_2$; the main peaks matched with cubic mention before and secondary peaks appear due to the presence of Bi (marked as •) and BiSe combination (marked as ○). The pattern $\text{AgBi}_{0.4}\text{Sb}_{0.6}\text{Se}_2$ contains the same type of secondary phases as the $\text{AgBi}_{0.3}\text{Sb}_{0.7}\text{Se}_2$. The pattern of $\text{AgBi}_{0.5}\text{Sb}_{0.5}\text{Se}_2$ shows the similar kind of secondary phases as $\text{AgBi}_{0.2}\text{Sb}_{0.8}\text{Se}_2$. In case of $\text{AgBi}_{0.6}\text{Sb}_{0.4}\text{Se}_2$, we noticed only one secondary peak marked in the pattern itself.



D.

The one step solid-state reaction for Nb –doped samples:



The general formula used to calculate the mass m of each precursor is given below:

$$n_{\text{Ag}_{1-x}\text{Nb}_x\text{Bi}_{0.7}\text{Sb}_{0.3}\text{S}_2} (\text{mol}) = \frac{m (\text{g})}{M_{\text{Ag}_{1-x}\text{Nb}_x\text{Bi}_{0.7}\text{Sb}_{0.3}\text{S}_2} \left(\frac{\text{g}}{\text{mol}} \right)}$$

$$n_{\text{Ag}_{1-x}\text{Nb}_x\text{Bi}_{0.7}\text{Sb}_{0.3}\text{Se}_{0.5}\text{S}_{1.5}} (\text{mol}) = \frac{m (\text{g})}{M_{\text{Ag}_{1-x}\text{Nb}_x\text{Bi}_{0.7}\text{Sb}_{0.3}\text{Se}_{0.5}\text{S}_{1.5}} \left(\frac{\text{g}}{\text{mol}} \right)}$$

Table (a): Calculated mass value of precursors with 2% of Nb doped, (x=0.02).

Composition	m (Ag), g	m (Nb), g	m (Bi), g	m (Sb), g	m (Se), g	m (S), g
$\text{Ag}_{0.98}\text{Nb}_{0.02}\text{Bi}_{0.7}\text{Sb}_{0.3}\text{S}_2$	1.3419	0.0236	1.8569	0.4637	-	0.8139
$\text{Ag}_{0.98}\text{Nb}_{0.02}\text{Bi}_{0.7}\text{Sb}_{0.3}\text{Se}_{0.5}\text{S}_{1.5}$	1.2586	0.0221	1.7417	0.4349	0.4701	0.5726
$\text{Ag}_{0.98}\text{Nb}_{0.02}\text{Bi}_{0.7}\text{Sb}_{0.3}\text{SeS}$	1.1851	0.0208	1.6399	0.4095	0.8853	0.3594
$\text{Ag}_{0.98}\text{Nb}_{0.02}\text{Bi}_{0.7}\text{Sb}_{0.3}\text{Se}_{1.5}\text{S}_{0.5}$	1.1196	0.0197	1.5494	0.3869	1.2546	0.1698
$\text{Ag}_{0.98}\text{Nb}_{0.02}\text{Bi}_{0.7}\text{Sb}_{0.3}\text{Se}_2$	1.0611	0.0187	1.4684	0.3666	1.5853	-

Table (b): Calculated mass value of precursors with 4% of Nb doped, (x=0.04).

Composition	m (Ag), g	m (Nb), g	m (Bi), g	m (Sb), g	m (Se), g	m (S), g
$\text{Ag}_{0.96}\text{Nb}_{0.04}\text{Bi}_{0.7}\text{Sb}_{0.3}\text{S}_2$	1.3156	0.0472	1.4693	0.4641	-	0.8146
$\text{Ag}_{0.96}\text{Nb}_{0.04}\text{Bi}_{0.7}\text{Sb}_{0.3}\text{Se}_{0.5}\text{S}_{1.5}$	1.2339	0.0443	1.5505	0.4352	0.4705	0.5730
$\text{Ag}_{0.96}\text{Nb}_{0.04}\text{Bi}_{0.7}\text{Sb}_{0.3}\text{SeS}$	1.1617	0.0417	1.6412	0.4098	0.8859	0.3597
$\text{Ag}_{0.96}\text{Nb}_{0.04}\text{Bi}_{0.7}\text{Sb}_{0.3}\text{Se}_{1.5}\text{S}_{0.5}$	1.0976	0.0394	1.7431	0.3872	1.2555	0.1699
$\text{Ag}_{0.956}\text{Nb}_{0.04}\text{Bi}_{0.7}\text{Sb}_{0.3}\text{Se}_2$	1.0401	0.0373	1.8585	0.3669	1.5864	-

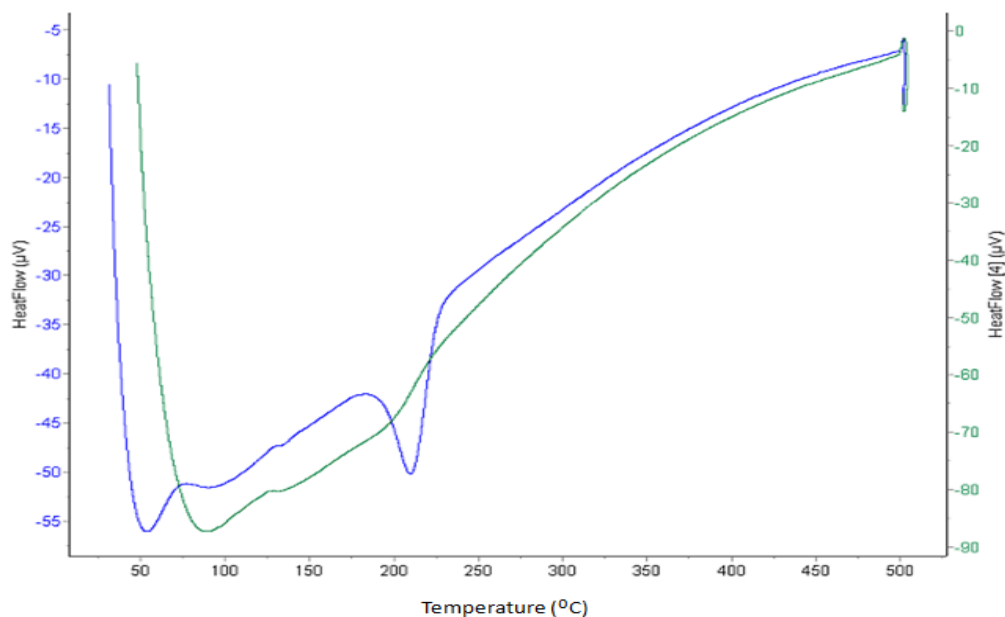


Figure: Plot of DSC result of Nb-doped sample ($\text{Ag}_{0.96}\text{Nb}_{0.04}\text{Bi}_{0.7}\text{Sb}_{0.3}\text{Se}_2$) with two heating cycles: blue curve for first heating and green curve for second heating.

Bibliography

- [1] T. Seebeck, Magnetic polarization of metals and minerals, 265: 1822-1823.
- [2] J.C. Peltier, Ann. Phys. Chim. 1834, LV1, 371.
- [3] W. Thomson Mathematical and Physical Papers 1, p. 175, 1851.
- [4] W. Thomson Proceedings of the Royal Society of Edinburgh 91, 1851.
- [5] T.M. Tritt and M.A. Subramanian, "Thermoelectric Materials, Phenomena, and Applications,".
- [6] F. J. DiSalvo, "Thermoelectric Cooling and Power Generation," *Science*, vol. 285, no. 5428. p. 703–706, 1999.
- [7] Rowe, D.M., Thermoelectric Handbook Macro to Nano. 2005, Boca Raton: CRC press.
- [8] Goldsmid, H.J. CRC Handbook of Thermoelectric, 1995, CRC Press: Boca Raton.
- [9] L. Onsager, " Reciprocal relations in irreversible processes I, " *Physical Review* 37, p. 405, 1931.
- [10] L. Onsager, " Reciprocal relations in irreversible processes II, " *Physical Review* 38, p. 2265, 1931.
- [11] J. H. Goldsmid. Introduction to thermoelectricity , Springer, 2009.
- [12] Ioffe A.F. (1960), Physics of semiconductors. Academic Press, New York.
- [13] Kittel C (2005), Introduction to Solid state physics. Chemical Industry Press, Beijing.
- [14] E. Altenkrich *Physikalische Zeitschrift* 10, p. 560, 1909.
- [15] E. Altenkrich *Physikalische Zeitschrift* 12, p. 920, 1910.
- [16] J. Zheng, "Recent advances on thermoelectric materials," *Front. Phys. China*, vol. 3, no. 3, pp. 269–279, 2008.
- [17] X. Zhang and L.-D. Zhao, "Thermoelectric materials: Energy conversion between heat and electricity," *J. Mater.*, vol. 1, no. 2, pp. 92–105, 2015.
- [18] G. Slack, "New Materials and Performance Limits for Thermoelectric Cooling, ed. DM Rowe," in *CRC Handbook of Thermoelectrics. ed. DM Rowe*, 1995, p. 407.
- [19] G. Mahan, B. Sales, and J. Sharp, "Thermoelectric Materials: New Approaches to an Old Problem," *Phys. Today*, vol. 50, no. 3, p. 42, 1997.
- [20] G. S. Nolas, J. Sharp, and H. J. Goldsmid, *Thermoelectrics : basic principles and new materials developments*. 2001.
- [21] A. Shakouri, "Recent Developments in Semiconductor Thermoelectric Physics and Materials," *Annual Review of Materials Research*, vol. 41, no. 1. pp. 399–431, 2011.
- [22] G. J. Snyder and E. S. Toberer, "Complex thermoelectric materials," *Nat. Mater.*, vol. 7, no. 2, pp. 105–114, 2008.

- [23] S. B. Riffat and X. Ma, "Thermoelectrics: A review of present and potential applications," *Appl. Therm. Eng.*, vol. 23, no. 8, pp. 913–935, 2003
- [24] L. E. Bell, "Cooling, heating, generating power, and recovering waste heat with thermoelectric systems," *Science*, vol. 321, no. 5895, pp. 1457–1461, 2008.
- [25] M. Zebarjadi, K. Esfarjani, M. S. Dresselhaus, Z. F. Ren, and G. Chen, "Perspectives on thermoelectrics: from fundamentals to device applications," *Energy & Environmental Science*, vol. 5, no. 1. p. 5147, 2012.
- [26] T. M. Tritt, H. Böttner, and L. Chen, "Thermoelectrics: Direct Solar Thermal Energy Conversion," *MRS Bull.*, vol. 33, no. 04, pp. 366–368, 2008.
- [27] J. Yang and T. Caillat, "Thermoelectric Materials for Space and Automotive Power Generation," *MRS Bull.*, vol. 31, no. 03, pp. 224–229, 2006.
- [28] Pustovalov AA (1986) Radioisotopic thermoelectric generators for implanted electrocardiostimulant. Atomic energy:60,125-129.
- [29] UV Lazarenko (1988) Radioisotopic power source for a feeding autonomous apparatus of a type-artificial heart. Atomic energy:64,110-114.
- [30] X. Yu, Y. Wang, Y. Liu, T. Li, H. Zhou, X. Gao, F. Feng, T. Roinila, and Y. Wang, "CMOS MEMS-based thermoelectric generator with an efficient heat dissipation path," *J. Micromechanics Microengineering*, vol. 22, no. 10, p. 105011, 2012.
- [31] A. F. Ioffe, Semiconductors, Thermoelement and thermoelectric cooling, 1957.
- [32] D. Zhao and G. Tan, "A review of thermoelectric cooling: Materials, modeling and applications," *Applied Thermal Engineering*, vol. 66, no. 1–2. pp. 15–24, 2014
- [33] H. J. Goldsmid, "Theory of Thermoelectric Refrigeration," *Springer*, 2009.
- [34] C. Ugalde, J. Anzurez, and I. I. Lázaro, "Thermoelectric coolers as alternative transducers for solar energy harvesting," in *Proceedings - 2010 IEEE Electronics, Robotics and Automotive Mechanics Conference, CERMA 2010*, 2010, pp. 637–641.
- [35] R. Chein and G. Huang, "Thermoelectric cooler application in electronic cooling," *Appl. Therm. Eng.*, vol. 24, no. 14–15, pp. 2207–2217, 2004.
- [36] M. Bojić, G. Savanović, N. Trifunović, L. Radović, and D. Šaljić, "Thermoelectric cooling of a train carriage by using a coldness-recovery device," *Energy*, vol. 22, no. 5, pp. 493–500, 1997.
- [37] A. B. Kustas, A. L. Jurgensmeyer, D. D. Williams, B. D. Dickman, T. H. Bradley, T. C. Lipsey, and B. D. Minor, "High Efficiency Thermoelectric Coolers for use in Firefighter Applications," pp. 1–11
- [38] Yazawa K, Shakouri A, "Energy payback optimization of termoelectric power generating systems," proc. ASME Int.Mech. Eng. Congr. Expo. (IMECE2010), Vancouver, p. IMECE2010-37957.
- [39] a V Shevelkov, "Chemical aspects of the design of thermoelectric materials," *Russ. Chem. Rev.*, vol. 77, no. 1, pp. 1–19, 2008.

- [40] H. Alam, S. Ramakrishna, "A review on the enhancement of figure of merit from bulk to nano-thermoelectric materials," *Nano Energy. Rev.*, 2 (2013), 190-212.
- [41] J. R. Sootsman, D. Y. Chung, and M. G. Kanatzidis, "New and old concepts in thermoelectric materials," *Angewandte Chemie - International Edition*, vol. 48, no. 46. pp. 8616–8639, 2009.
- [42] O. Yamashita and S. Tomiyoshi, "Effect of Annealing on Thermoelectric Properties of Bismuth Telluride Compounds," *Japanese Journal of Applied Physics*, vol. 42, no. Part 1, No. 2A. pp. 492–500, 2003.
- [43] D. H. Kim and T. Mitani, "Thermoelectric properties of fine-grained Bi_2Te_3 alloys," *J. Alloys Compd.*, vol. 399, no. 1–2, pp. 14–19, 2005.
- [44] J. Yang, T. Aizawa, A. Yamamoto, and T. Ohta, "Thermoelectric properties of p-type $(\text{Bi}_2\text{Te}_3)_x(\text{Sb}_2\text{Te}_3)_{1-x}$ prepared via bulk mechanical alloying and hot pressing," *J. Alloys Compd.*, vol. 309, no. 1–2, pp. 225–228, 2000.
- [45] G. Wang and T. Cagin, "Electronic structure of the thermoelectric materials Bi_2Te_3 and Sb_2Te_3 from first-principles calculations," *Phys. Rev. B*, vol. 76, no. 7, pp. 1–8, 2007.
- [46] C. B. Satterthwaite and R. W. J. Ure, "Electrical and thermal properties of Bi_2Te_3 ," *Phys. Rev.*, vol. 108, no. 5, pp. 1164–1170, 1957.
- [47] Z. H. Dughaish, "Lead telluride as a thermoelectric material for thermoelectric power generation," *Phys. B Condens. Matter*, vol. 322, no. 1–2, pp. 205–223, 2002. *Energy Environ Sci* 4:2090-2096.
- [48] Lalonde A, Pei YZ, Synder G.J. , "Reevaluation of $\text{PbTe}_{1-x}\text{I}_x$ as high performance n-type thermoelectric material ," *Energy Environ Sci* 4:2090-2096.
- [49] Pei YZ, L.A., Iwanaga S et al , "High thermoelectric figure of merit in heavy hole dominated PbTe ," *Energy Environ Sci* 4:2085-2089,2011.
- [50] Pei YZ, L.A., Iwanaga S et al , "Covergence of electronic bands for high performance bulk thermoelectrics.," *Nature* 473: 66-69.
- [51] Pei YZ, Wang H, Synder GJ. , "Band engineering of thermoelectric materials," *Adv. Mater* 2012;24:6125-35.
- [52] Gibbs ZM, Kim H, Wang H, White RL, Drymiotis F, K.M, et al "Temperature dependent band gap in PbX ($\text{X}=\text{S}, \text{Se}, \text{Te}$). *Appl Phys Lett* 2013;103.
- [53] Pei YZ, Wang H, Gibbs ZM, LaLonde AD, Synder Gj. "Thermopower enhancemnet in $\text{Pb}_{1-x}\text{Mn}_x\text{Te}$ alloys and its effect on thermoelectric efficiency. *Npg Asia Mater* 2012;4
- [54] Zhao LD, Wu HJ, Hao SQ, Wu CI, Zhou XY, Biswas K, et al.. "All-scale hierarchical thermoelectrics: MgTe in PbTe facilitates valence band convergence and suppresses bipolar thermal transport for high performance". *Energy Environ Sci* 2013;6:3346-55.
- [55] C.H., Z.L., S.X. Dou., "Recent progress in thermoelectric materials", *Chinese Science Bulletin*, 59 (18), 2073-2091, 2014.

- [56] Y. Gelbstein, Z. Dashevsky, and M. P. Dariel, "High performance n-type PbTe-based materials for thermoelectric applications," *Phys. B Condens. Matter*, vol. 363, no. 1–4, pp. 196–205, 2005.
- [57] I. Kudman, "Thermoelectric properties of p-type PbTe-PbSe alloys," *J. Mater. Sci.*, vol. 7, no. 9, pp. 1027–1029, 1972.
- [58] H. Wang, Y. Pei, A. D. Lalonde, and G. J. Snyder, "Heavily doped p-type PbSe with high thermoelectric performance: An alternative for PbTe," *Adv. Mater.*, vol. 23, no. 11, pp. 1366–1370, 2011.
- [59] He JQ, Sootsman JR, G. SN et al, "On the origin of increased phonon scattering in nanostructured PbTe based thermoelectric materials," *J Am Chem Soc*, vol. 132, pp. 8669–8675, 2010.
- [60] Sootsman JR, Kong HJ, Uher C, "Large enhancements in the thermoelectric power factor of bulk PbTe at high temperature by synergistic nanostructuring," *Angew Chem Int Ed*, vol. 47, pp. 8618–8622, 2008.
- [61] Pei YZ, Lensch-Falk J, Tobber ES, "High thermoelectric performance in PbTe due to large nanoscale Ag₂Te precipitates and La doping," *Adv. Funct Mater.*, vol. 21, pp. 241–249, 2011.
- [62] Hsu KF, Loo S, Guo F, "Cubic AgPb_mSbTe_{2+m}: bulk thermoelectric materials with high figure of merit," *Science.*, 303, pp. 818–821, 2004.
- [63] Poudeu PFP, Downey AD, "High thermoelectric figure of merit and nanostructuring in bulk p-type Na_{1-x}Pb_mSb_yTe_{m+2}," *Angew Chem Int Ed*, vol. 45, pp. 3835–3839, 2006.
- [64] Biswas K, He JQ, Zhang QC,, "Strained endotail nanostructures with high thermoelectric figure of merit," *Nat Chem.*, 3, pp. 160–166, 2011.
- [65] Kanishka B, He JQ, Ivan DB,, "High performance bulk thermoelectrics with all-scale hierarchical architectures," *Nature* 489, pp. 414–418, 2012.
- [66] Ibanez M, Zamani R, Gorsse S et al, "Core-shell nanoparticle as building blocks for the bottom-up production of functional nanocomposites: PbTe-PbS thermoelectric properties," *ACS Nano* 7, pp. 2573–2586, 2013.
- [67] Rogacheva EI, Tavrina TV, Nashchekina ON, "Quantum size effects in PbSe quantum wells," *Appl Phys Lett*, vol. 80, pp. 2690–2692, 2002.
- [68] Zhang QY, Wang H, Liu WS, "Enhancement of thermoelectric figure-of-merit by resonant states of aluminium doping in lead selenide," *Energy Environ Sci.*, 5, pp. 5246–5251, 2012.
- [69] J. W. Sharp, "Some properties of GeTe-based thermoelectric alloys," *Proc. ICT'03. 22nd Int. Conf. Thermoelectr. (IEEE Cat. No. 03TH8726)*, 2003.
- [70] L. Xu, H. Q. Wang, and J. C. Zheng, "Thermoelectric properties of PbTe, SnTe, and GeTe at high pressure: An Ab initio study," in *Journal of Electronic Materials*, 2011, vol. 40, no. 5, pp. 641–647
- [71] B. Abeles, D. S. B. G. D. Cody, and J. P. Dismukes, "Thermal conductivity of Ge-Si alloys at high temperatures," *Phys. Rev.*, vol. 125, pp. 44–46, 1962.
- [72] A. Samarelli, L. Ferre Llin, S. Cecchi, J. Frigerio, D. Chrastina, G. Isella, E. M??ller Gubler, T.

- Etzelstorfer, J. Stangl, Y. Zhang, J. M. R. Weaver, P. S. Dobson, and D. J. Paul, "Prospects for SiGe thermoelectric generators," *Solid. State. Electron.*, vol. 98, pp. 70–74, 2014.
- [73] O. Yamashita and N. Sadatomi, Thermoelectric properties of $\text{Si}_{1-x}\text{Ge}_x$ with alloy and dopant segregations, *Journal of Applied Physics* 88(1), p. 245, 2000.
- [74] B. B. Iversen, A. E. C. Palmqvist, D. E. Cox, G. S. Nolas, G. D. Stucky, N. P. Blake, and H. Metiu, "Why are clathrates good candidates for thermoelectric materials?," *J. Solid State Chem.*, vol. 149, no. 2, pp. 455–458, 2000.
- [75] M. Christensen, S. Johnsen, and B. B. Iversen, "Thermoelectric clathrates of type I.," *Dalton Trans.*, vol. 39, no. 4, pp. 978–992, 2010.
- [76] J. F. Meng, N. V. C. Shekar, J. V. Badding, and G. S. Nolas, "Threefold enhancement of the thermoelectric figure of merit for pressure tuned $\text{Sr}_8\text{Ga}_{16}\text{Ge}_{30}$," *J. Appl. Phys.*, vol. 89, no. 3, pp. 1730–1733, 2001.
- [77] J. D. Bryan and G. D. Stucky, " $\text{Eu}_4\text{Ga}_8\text{Ge}_{16}$: A new four-coordinate clathrate network," *Chem. Mater.*, vol. 13, no. 2, pp. 253–257, 2001.
- [78] E. Toberer, M. Christensen, B. Iversen, and G. Snyder, "High temperature thermoelectric efficiency in $\text{Ba}_8\text{Ga}_{16}\text{Ge}_{30}$," *Physical Review B*, vol. 77, no. 7. 2008.
- [79] A. Saramat, G. Svensson, A. E. C. Palmqvist, C. Stiewe, E. Mueller, D. Platzek, S. G. K. Williams, D. M. Rowe, J. D. Bryan, and G. D. Stucky, "Large thermoelectric figure of merit at high temperature in Czochralski-grown clathrate $\text{Ba}_8\text{Ga}_{16}\text{Ge}_{30}$," *J. Appl. Phys.*, vol. 99, no. 2, p. 023708, 2006.
- [80] N. P. Blake, D. Bryan, S. Lattner, L. Møllnitz, G. D. Stucky, and H. Metiu, "Structure and stability of the clathrates $\text{Ba}_8\text{Ga}_{16}\text{Ge}_{30}$, $\text{Sr}_8\text{Ga}_{16}\text{Ge}_{30}$, $\text{Ba}_8\text{Ga}_{16}\text{Si}_{30}$, and $\text{Ba}_8\text{In}_6\text{Sn}_{30}$," *J. Chem. Phys.*, vol. 114, no. 22, pp. 10063–10074, 2001.
- [81] S. Paschen, V. Pacheco, A. Bentien, A. Sanchez, W. Carrillo-Cabrera, M. Baenitz, B. B. Iversen, Y. Grin, and F. Steglich, "Are type-I clathrates Zintl phases and 'phonon glasses and electron single crystals'?, " in *Physica B: Condensed Matter*, 2003, vol. 328, no. 1–2, pp. 39–43.
- [82] G. S. Nolas, J. L. Cohn, G. A. Slack, and S. B. Schujman, "Semiconducting Ge clathrates: Promising candidates for thermoelectric applications," *Appl. Phys. Lett.*, vol. 73, no. 2, pp. 178–180, 1998.
- [83] H. Kleinke, "New bulk materials for thermoelectric power generation: clathrates and complex antimonides," *Chemistry of Materials*, vol. 22, no. 3. pp. 604–611, 2010.
- [84] B. Chen, J.-H. Xu, C. Uher, D. T. Morelli, G. P. Meisner, J.-P. Fleurial, T. Caillat, and A. Borshchevsky, "Low-temperature transport properties of the filled skutterudites $\text{CeFe}_{4-x}\text{Co}_x\text{Sb}_{12}$," *Physical Review B*, vol. 55, no. 3. pp. 1476–1480, 1997.
- [85] X. Shi, S. Bai, L. Xi, J. Yang, W. Zhang, L. Chen, and J. Yang, "Realization of high thermoelectric performance in n-type partially filled skutterudites," *Journal of Materials Research*, vol. 26, no. 15. pp. 1745–1754, 2011.
- [86] M. Puyet, A. Dauscher, B. Lenoir, M. Dehmas, C. Stiewe, E. Müller, and J. Hejtmanek, "Beneficial effect of Ni substitution on the thermoelectric properties in partially filled $\text{CaCo}_{4-x}\text{Ni}_x\text{Sb}_{12}$

- skutterudites," *J. Appl. Phys.*, vol. 97, no. 8, p. 083712, 2005.
- [87] M. Puyet, B. Lenoir, A. Dauscher, and M. Dehmas, "High temperature transport properties of partially filled $\text{Ca}_x\text{Co}_4\text{Sb}_{12}$ skutterudites," *J. Appl. ...*, 2004.
 - [88] D. J. Singh and I. I. Mazin, "Calculated thermoelectric properties of La-filled skutterudites," *Phys. Rev. B*, vol. 56, no. 4, pp. R1650–R1653, 1997.
 - [89] J. S. Dyck, W. Chen, C. Uher, L. Chen, X. Tang, and T. Hirai, "Thermoelectric properties of the n-type filled skutterudite $\text{Ba}_{0.3}\text{Co}_4\text{Sb}_{12}$ doped with Ni," *J. Appl. Phys.*, vol. 91, no. 6, pp. 3698–3705, 2002.
 - [90] X. Tang, Q. Zhang, M. Niino, and T. Goto, and T. Hirai, "Synthesis and thermoelectric properties of double-atom-filled skutterudite $\text{R}_y\text{M}_x\text{Co}_{4-x}\text{Sb}_{12}$ (R: Ce, Ba, Y; M: Fe, Ni)," *Journal of Applied Physics* 97, p. 093712, 2005.
 - [91] Y. Yongkwan Dong, P. Puneet, T. Tritt and G. S. Nolas, "High temperature thermoelectric properties of p-type skutterudites $\text{Yb}_x\text{Co}_3\text{FeSb}_{12}$," *Physica Status Solidi RRL* 7(6), p. 418, 2013.
 - [92] C. Uher, J. Yang, S. Hu, D. T. Morelli, and G. P. Meisner, "Transport properties of pure and doped MnNiSn (M=Zr, Hf)," *Phys. Rev. B - Condens. Matter Mater. Phys.*, vol. 59, no. 13, pp. 8615–8621, 1999.
 - [93] Q. Shen, L. Zhang, L. Chen, T. Goto, and T. Hirai, "Thermoelectric properties of ZrNiSn-based half-Heusler compounds by solid state reaction method," *J. Mater. Sci. Lett.*, vol. 20, no. 24, pp. 2197–2199, 2001.
 - [94] Q. Shen, L. Chen, T. Goto, T. Hirai, J. Yang, G. P. Meisner, and C. Uher, "Effects of partial substitution of Ni by Pd on the thermoelectric properties of ZrNiSn-based half-Heusler compounds," *Appl. Phys. Lett.*, vol. 79, no. 25, pp. 4165–4167, 2001.
 - [95] S. Sakurada and N. Shutoh, "Effect of Ti substitution on the thermoelectric properties of (Zr,Hf)NiSn half-Heusler compounds," *Appl. Phys. Lett.*, vol. 86, no. 8, pp. 1–3, 2005.
 - [96] X. Yan, G. Joshi, W. Liu, Y. Lan, H. Wang, S. Lee, J. W. Simonson, S. J. Poon, T. M. Tritt, G. Chen, and Z. F. Ren, "Enhanced thermoelectric figure of merit of p-type half-heuslers," *Nano Lett.*, vol. 11, no. 2, pp. 556–560, 2011.
 - [97] T. Zhu, C. Fu, H. Xie, Y. Liu, and X. Zhao, "High Efficiency Half-Heusler Thermoelectric Materials for Energy Harvesting," *Advanced Energy Materials*, vol. 5, no. 19, 2015.
 - [98] B. Balke, J. Barth, M. Schwall, G. H. Fecher, and C. Felser, "An alternative approach to improve the thermoelectric properties of half-Heusler compounds," in *Journal of Electronic Materials*, 2011, vol. 40, no. 5, pp. 702–706.
 - [99] M. S. Lee, F. P. Poudeu, and S. D. Mahanti, "Electronic structure and thermoelectric properties of Sb-based semiconducting half-Heusler compounds," *Phys. Rev. B - Condens. Matter Mater. Phys.*, vol. 83, no. 8, 2011.
 - [100] S. R. Brown, S. M. Kauzlarich, F. Gascoin, and G. J. Snyder, " $\text{Yb}_{14}\text{MnSb}_{11}$: New High Efficiency Thermoelectric Material for Power Generation," *Chem. Mater.*, vol. 18, no. 7, pp. 1873–1877,

2006.

- [101] S. M. Kauzlarich, S. R. Brown, and G. J. Snyder, "Zintl phases for thermoelectric devices.," *Dalton Trans.*, no. 21, pp. 2099–2107, 2007.
- [102] C. a Cox, E. S. Toberer, A. a Levchenko, S. R. Brown, G. J. Snyder, A. Navrotsky, and S. M. Kauzlarich, "Structure, heat capacity, and high-temperature thermal properties of $\text{Yb}_{14}\text{Mn}_{1-x}\text{Al}_x\text{Sb}_{11}$," *Chem. Mater.*, vol. 21, no. 7, pp. 1354–1360, 2009.
- [103] E. S. Toberer, C. A. Cox, S. R. Brown, T. Ikeda, A. F. May, S. M. Kauzlarich, and G. Jeffrey Snyder, "Traversing the metal-insulator transition in a zintl phase: Rational enhancement of thermoelectric efficiency in $\text{Yb}_{14}\text{Mn}_{1-x}\text{Al}_x\text{Sb}_{11}$," *Adv. Funct. Mater.*, vol. 18, no. 18, pp. 2795–2800, 2008.
- [104] E. S. Toberer, S. R. Brown, T. Ikeda, S. M. Kauzlarich, and G. J. Snyder, "High thermoelectric efficiency in lanthanum doped $\text{Yb}_{14}\text{MnSb}_{11}$," *Appl. Phys. Lett.*, vol. 93, no. 6, 2008.
- [105] C. A. Cox, S. R. Brown, G. J. Snyder, and S. M. Kauzlarich, "Effect of Ca doping on the thermoelectric performance of $\text{Yb}_{14}\text{MnSb}_{11}$," *J. Electron. Mater.*, vol. 39, no. 9, pp. 1373–1375, 2010.
- [106] I. Terasaki, Y. Sasago, and K. Uchinokura, "Large thermoelectric power in NaCo_2O_4 single crystals," *Physical Review B*, vol. 56, no. 20. pp. R12685–R12687, 1997.
- [107] I. Terasaki, "Transport properties and electronic states of the thermoelectric oxide NaCo_2O_4 ," in *Physica B: Condensed Matter*, 2003, vol. 328, no. 1–2, pp. 63–67.
- [108] M. Ohtaki and E. Maeda, "Microstructures and Thermoelectric Properties of NaCo_2O_4 Prepared by Double-step Sintering.," *J. Japan Soc. Powder Powder Metall.*, vol. 47, no. 11, pp. 1159–1164, 2000.
- [109] Y. Liu, Y. Lin, Z. Shi, C. W. Nan, and Z. Shen, "Preparation of $\text{Ca}_3\text{Co}_4\text{O}_9$ and improvement of its thermoelectric properties by spark plasma sintering," *J. Am. Ceram. Soc.*, vol. 88, no. 5, pp. 1337–1340, 2005.
- [110] H. Ohta, K. Sugiura, and K. Koumoto, "Recent progress in oxide thermoelectric materials: P-type $\text{Ca}_3\text{Co}_4\text{O}_9$ and n-Type SrTiO_3 ," *Inorganic Chemistry*, vol. 47, no. 19. pp. 8429–8436, 2008.
- [111] Y. Cui, J. R. Salvador, J. Yang, H. Wang, G. Amow, and H. Kleinke, "Thermoelectric Properties of Heavily Doped n-Type SrTiO_3 Bulk Materials," *J. Electron. Mater.*, vol. 38, no. 7, pp. 1002–1007, 2009.
- [112] S. Ohta, T. Nomura, H. Ohta, and K. Koumoto, "High-temperature carrier transport and thermoelectric properties of heavily La- Or Nb-doped SrTiO_3 single crystals," *J. Appl. Phys.*, vol. 97, no. 3, 2005.
- [113] R. Funahashi, I. Matsubara, and S. Sodeoka, "Thermoelectric properties of $\text{Bi}_2\text{Sr}_2\text{Co}_2\text{O}_x$ polycrystalline materials," *Appl. Phys. Lett.*, vol. 76, no. 17, pp. 2385–2387, 2000.
- [114] P. Jood, R. J. Mehta, Y. Zhang, G. Peleckis, X. Wang, R. W. Siegel, T. Borca-Tasciuc, S. X. Dou, and G. Ramanath, "Al-doped zinc oxide nanocomposites with enhanced thermoelectric properties,"

- Nano Lett.*, vol. 11, no. 10, pp. 4337–4342, 2011.
- [115] M. Ohtaki, K. Araki, and K. Yamamoto, “High thermoelectric performance of dually doped ZnO ceramics,” in *Journal of Electronic Materials*, 2009, vol. 38, no. 7, pp. 1234–1238.
 - [116] D. Bérardan, C. Byl, and N. Dragoe, “Influence of the preparation conditions on the thermoelectric properties of Al-doped ZnO,” *J. Am. Ceram. Soc.*, vol. 93, no. 8, pp. 2352–2358, 2010.
 - [117] H. Kaga, R. Asahi, and T. Tani, “Thermoelectric Properties of Doped (ZnO) m In₂O₃,” *Jpn. J. Appl. Phys.*, vol. 43, no. 6A, pp. 3540–3543, 2004.
 - [118] D. Berardan, E. Guilmeau, A. Maignan, and B. Raveau, “In₂O₃:Ge, a promising n-type thermoelectric oxide composite,” *Solid State Commun.*, vol. 146, no. 1–2, pp. 97–101, 2008.
 - [119] K. Koumoto, I. Terasaki, and R. Funahashi, “Complex Oxide Materials for Potential Thermoelectric Applications,” *MRS Bulletin*, vol. 31, no. 03, pp. 206–210, 2006.
 - [120] M. Ohtaki, “Recent aspects of oxide thermoelectric materials for power generation from mid-to-high temperature heat source,” *J. Ceram. Soc. Japan*, vol. 119, no. 1395, pp. 770–775, 2011.
 - [121] J. W. Fergus, “Oxide materials for high temperature thermoelectric energy conversion,” *Journal of the European Ceramic Society*, vol. 32, no. 3, pp. 525–540, 2012.
 - [122] L. D. Hicks and M. S. Dresselhaus, “Effect of quantum-well structures on the thermoelectric figure of merit,” *Phys. Rev. B*, vol. 47, no. 19, pp. 12727–12731, 1993.
 - [123] M. S. Dresselhaus, G. Chen, M. Y. Tang, R. G. Yang, H. Lee, D. Z. Wang, and Z. F. Ren, “New Directions for Nanoscale Thermoelectric Materials Research,” *Mater. Res.*, vol. 886, pp. 1–10, 2006.
 - [124] L. D. Hicks and M. S. Dresselhaus, “Thermoelectric figure of merit of a one-dimensional conductor,” *Phys. Rev. B*, vol. 47, no. 24, pp. 16631–16634, 1993.
 - [125] M. S. Dresselhaus, G. Chen, M. Y. Tang, R. Yang, H. Lee, D. Wang, Z. Ren, J. P. Fleurial, and P. Gogna, “New directions for low-dimensional thermoelectric materials,” *Adv. Mater.*, vol. 19, no. 8, pp. 1043–1053, 2007.
 - [126] J. R. Szczech, J. M. Higgins, and S. Jin, “Enhancement of the thermoelectric properties in nanoscale and nanostructured materials,” *J. Mater. Chem.*, vol. 21, no. 12, p. 4037, 2011.
 - [127] T. Koga, S. B. Cronin, M. S. Dresselhaus, J. L. Liu, and K. L. Wang, “Experimental proof-of-principle investigation of enhanced Z sub 3D T in (00,” *Appl. Phys. Lett.*, vol. 77, no. 10, pp. 1490–1492, 2000.
 - [128] L. D. Hicks, T. C. Harman, and M. S. Dresselhaus, “Use of quantum-well superlattices to obtain a high figure of merit from nonconventional thermoelectric materials,” *Appl. Phys. Lett.*, vol. 63, no. 23, pp. 3230–3232, 1993.
 - [129] T. C. Harman, P. J. Taylor, D. L. Spears, and M. P. Walsh, “Thermoelectric quantum-dot superlattices with high ZT,” *J. Electron. Mater.*, vol. 29, no. 1, pp. L1–L2, 2000.

- [130] R. Venkatasubramanian, E. Siivola, T. Colpitts, and B. O'Quinn, "Thin-film thermoelectric devices with high room-temperature figures of merit," *Nature*, vol. 413, no. 6856, pp. 597–602, 2001.
- [131] J. C. Caylor, K. Coonley, J. Stuart, T. Colpitts, and R. Venkatasubramanian, "Enhanced thermoelectric performance in PbTe-based superlattice structures from reduction of lattice thermal conductivity," *Appl. Phys. Lett.*, vol. 87, no. 2, 2005.
- [132] D. Vashaee and A. Shakouri, "Thermionic power generation at high temperatures using SiGeSi superlattices," *J. Appl. Phys.*, vol. 101, no. 5, pp. 13–18, 2007.
- [133] X. Fan, G. Zeng, C. LaBounty, J. E. Bowers, E. Croke, C. C. Ahn, S. Huxtable, A. Majumdar, and A. Shakouri, "SiGeC/Si superlattice microcoolers," *Appl. Phys. Lett.*, vol. 78, no. 11, pp. 1580–1582, 2001.
- [134] T. Koga, X. Sun, S. B. Cronin, and M. S. Dresselhaus, "Carrier pocket engineering to design superior thermoelectric materials using GaAs/AlAs superlattices," *Appl. Phys. Lett.*, vol. 73, no. 20, pp. 2950–2952, 1998.
- [135] J. M. O. Zide, D. Vashaee, Z. X. Bian, G. Zeng, J. E. Bowers, A. Shakouri, and A. C. Gossard, "Demonstration of electron filtering to increase the Seebeck coefficient in $\text{In}_{0.53}\text{Ga}_{0.47}\text{As}/\text{In}_{0.53}\text{Ga}_{0.28}\text{Al}_{0.19}\text{As}$ superlattices," *Phys. Rev. B - Condens. Matter Mater. Phys.*, vol. 74, no. 20, pp. 1–5, 2006.
- [136] A. Mavrokefalos, N. T. Nguyen, M. T. Pettes, D. C. Johnson, and L. Shi, "In-plane thermal conductivity of disordered layered W Se₂ and $(\text{W})_x(\text{W Se}_2)_y$ superlattice films," *Appl. Phys. Lett.*, vol. 91, no. 17, pp. 24–26, 2007.
- [137] T. C. Harman, P. J. Taylor, B.E. LaForge and M. P. Walsh, "Quantum dot superlattice thermoelectric materials and devices," *Science (New York, NY)*, 297, pp. 2229–2232, 2002.
- [138] T. C. Harman, G.W. Turner, B.E. LaForge and M. P. Walsh, "Nanostructured Thermoelectric Materials," *J. Electron. Mater.* 2005, 34, L19.
- [139] L. D. Hicks, T. C. Harman, X. Sun, and M. S. Dresselhaus, "Experimental study of the effect of quantum-well structures on the thermoelectric figure of merit," *Phys. Rev. B*, vol. 53, no. 16, pp. R10493–R10496, 1996.
- [140] E. I. Rogacheva, O. N. Nashchekina, A. V. Meriuts, S. G. Lyubchenko, M. S. Dresselhaus, and G. Dresselhaus, "Quantum size effects in n-PbTe/p-SnTe/n-PbTe heterostructures," *Appl. Phys. Lett.*, vol. 86, no. 6, pp. 1–3, 2005.
- [141] A. Shakouri, "Thermoelectric, thermionic and thermophotovoltaic energy conversion," *Proceedings of the International Conference on Thermoelectrics (2005)*, 492–497.
- [142] I. Chowdhury, R. Prasher, K. Lofgreen, G. Chrysler, S. Narasimhan, R. Mahajan, D. Koester, R. Alley, and R. Venkatasubramanian, "On-chip cooling by superlattice-based thin-film thermoelectrics," *Nat. Nanotechnol.*, vol. 4, no. 4, pp. 235–238, 2009.
- [143] A. I. Hochbaum, R. Chen, R. D. Delgado, W. Liang, E. C. Garnett, M. Najarian, A. Majumdar, and P. Yang, "Enhanced thermoelectric performance of rough silicon nanowires," *Nature*, vol. 451, no. 7175, pp. 163–167, 2008.

- [144] A. I. Boukai, Y. Bunimovich, J. Tahir-Kheli, J.-K. Yu, W. A. Goddard, and J. R. Heath, "Silicon nanowires as efficient thermoelectric materials.," *Nature*, vol. 451, no. 7175, pp. 168–71, 2008.
- [145] C. J. Vineis, A. Shakouri, A. Majumdar, and M. G. Kanatzidis, "Nanostructured thermoelectrics: Big efficiency gains from small features," *Adv. Mater.*, vol. 22, no. 36, pp. 3970–3980, 2010.
- [146] P. F. P. Poudeu, J. D'Angelo, A. D. Downey, J. L. Short, T. P. Hogan, and M. G. Kanatzidis, "High thermoelectric figure of merit and nanostructuring in bulk p-type $\text{Na}_{1-x}\text{PbmSb}_{y}\text{Te}_{m+2}$," *Angew. Chemie - Int. Ed.*, vol. 45, no. 23, pp. 3835–3839, 2006.
- [147] B. Poudel, Q. Hao, Y. Ma, Y. Lan, A. Minnich, B. Yu, X. Yan, D. Wang, A. Muto, D. Vashaee, X. Chen, J. Liu, M. S. Dresselhaus, G. Chen, and Z. Ren, "High-thermoelectric performance of nanostructured bismuth antimony telluride bulk alloys.," *Science*, vol. 320, no. 5876, pp. 634–638, 2008.
- [148] T. C. Harman, D. L. Spears, and M. P. Walsh, "PbTe/Te superlattice structures with enhanced thermoelectric figures of merit," *Journal of Electronic Materials*, vol. 28, no. 1. pp. L1–L5, 1999.
- [149] L. Shi, J. Jiang, G. Zhang, and B. Li, "High thermoelectric figure of merit in silicon-germanium superlattice structured nanowires," *Appl. Phys. Lett.*, vol. 101, no. 23, 2012.
- [150] G. Zeng, J. E. Bowers, J. M. O. Zide, A. C. Gossard, W. Kim, S. Singer, A. Majumdar, R. Singh, Z. Bian, Y. Zhang, and A. Shakouri, "ErAs: InGaAs/InGaAlAs superlattice thin-film power generator array," *Appl. Phys. Lett.*, vol. 88, no. 11, 2006.
- [151] H. Uchino, Y. Okamoto, T. Kawahara, and J. Morimoto, "The study of the origin of the anomalously large thermoelectric power of Si/Ge superlattice thin film," *Japanese J. Appl. Physics, Part 1 Regul. Pap. Short Notes Rev. Pap.*, vol. 39, no. 4 A, pp. 1675–1677, 2000.
- [152] H. L. Ni, X. B. Zhao, T. J. Zhu, X. H. Ji, and J. P. Tu, "Synthesis and thermoelectric properties of Bi_2Te_3 based nanocomposites," *J. Alloys Compd.*, vol. 397, no. 1–2, pp. 317–321, 2005.
- [153] W. Liu, X. Yan, G. Chen, and Z. Ren, "Recent advances in thermoelectric nanocomposites," *Nano Energy*, vol. 1, no. 1. pp. 42–56, 2012.
- [154] Z. Ren, Y. Ma, Q. Hao, B. Poudel, yucheng Lan, B. Yu, D. Wang, and G. Chen, "Enhanced Thermoelectric Figure-of-Merit in p-Type Nanostructured Bismuth Antimony Tellurium Alloys Made from Elemental Chunks," *NANO Lett.*, vol. 8, no. 8, pp. 2580–2584, 2008.
- [155] W. Xie, J. He, H. J. Kang, X. Tang, S. Zhu, M. Laver, S. Wang, J. R. D. Copley, C. M. Brown, Q. Zhang, and T. M. Tritt, "Identifying the specific nanostructures responsible for the high thermoelectric performance of $(\text{Bi,Sb})_2\text{Te}_3$ nanocomposites," *Nano Lett.*, vol. 10, no. 9, pp. 3283–3289, 2010.
- [156] X. Yan, B. Poudel, Y. Ma, W. S. Liu, G. Joshi, H. Wang, Y. Lan, D. Wang, G. Chen, and Z. F. Ren, "Experimental Studies on Anisotropic Thermoelectric Properties and Structures of n-Type $\text{Bi}_{2-x}\text{Te}_{3-x}\text{Se}_x$," *Nano Lett.*, vol. 10, no. 9, pp. 3373–3378, 2010.
- [157] W. Xie, X. Tang, Y. Yan, Q. Zhang, and T. M. Tritt, "Unique nanostructures and enhanced thermoelectric performance of melt-spun BiSbTe alloys," *Appl. Phys. Lett.*, vol. 94, no. 10, 2009.
- [158] Y. Q. Cao, X. B. Zhao, T. J. Zhu, X. B. Zhang, and J. P. Tu, "Syntheses and thermoelectric properties

- of Bi₂Te₃Sb₂Te₃ bulk nanocomposites with laminated nanostructure,” *Appl. Phys. Lett.*, vol. 92, no. 14, pp. 8–11, 2008.
- [159] K. Biswas, J. He, I. D. Blum, Chun-IWu, T. P. Hogan, D. N. Seidman, V. P. Dravid, and M. G. Kanatzidis, “Corrigendum: High-performance bulk thermoelectrics with all-scale hierarchical architectures,” *Nature*, vol. 490, no. 7421, pp. 570–570, 2012.
 - [160] G. Joshi, H. Lee, Y. Lan, X. Wang, G. Zhu, D. Wang, R. W. Gould, D. C. Cuff, M. Y. Tang, M. S. Dresselhaus, G. Chen, and Z. Ren, “Enhanced thermoelectric figure-of-merit in nanostructured p-type silicon germanium bulk alloys,” *Nano Lett.*, vol. 8, no. 12, pp. 4670–4674, 2008.
 - [161] X. W. Wang, H. Lee, Y. C. Lan, G. H. Zhu, G. Joshi, D. Z. Wang, J. Yang, a. J. Muto, M. Y. Tang, J. Klatsky, S. Song, M. S. Dresselhaus, G. Chen, and Z. F. Ren, “Enhanced thermoelectric figure of merit in nanostructured n-type silicon germanium bulk alloy,” *Appl. Phys. Lett.*, vol. 93, no. 19, p. 193121, 2008.
 - [162] D.G.Cahill, S.K.Watson and R.O.Pohl, “Lower limit to the thermal conductivity of disordered crystals,” *Physical Review B*, 46 (1992)6131–6140.
 - [163] C.Chiritescu, D.G.Cahill, N.Nguyen, D.Johnson, A.Bodapati, P. Keblinski, et al., “Ultralow thermal conductivity in disordered layered WSe₂ crystals,” *Science*(NewYork,NY) 315 (2007)351–353.
 - [164] B. Wolfing, C. Kloc, J. Teubner, and E. Bucher, “High performance thermoelectric Tl₉BiTe₆ with an extremely low thermal conductivity,” *Phys. Rev. Lett.*, vol. 86, no. 19, pp. 4350–4353, 2001.
 - [165] K. Kurosaki, A. Kosuga, H. Muta, and S. Yamanaka, “Thermoelectric properties of thallium compounds with extremely low thermal conductivity,” *Mater. Trans.*, vol. 46, no. 7, pp. 1502–1505, 2005.
 - [166] K. Kurosaki, A. Kosuga, H. Muta, M. Uno, and S. Yamanaka, “Ag₉TlTe₅: A high-performance thermoelectric bulk material with extremely low thermal conductivity,” *Appl. Phys. Lett.*, vol. 87, no. 6, p. 061919, 2005.
 - [167] J. W. Sharp, B. C. Sales, D. G. Mandrus, and B. C. Chakoumakos, “Thermoelectric properties of Tl₂SnTe₅ and Tl₂GeTe₅,” *Appl. Phys. Lett.*, vol. 74, no. 25, pp. 3794–3796, 1999.
 - [168] D.-Y. Chung, T. Hogan, P. Brazis, M. Rocci-Lane, C. Kannewurf, M. Bastea, C. Uher, and M. G. Kanatzidis, “CsBi₄Te₆: A high-performance thermoelectric material for low- temperature applications,” *Science (80-.)*, vol. 287, no. 5455, pp. 1024–1027, 2000.
 - [169] P. W. Brazis, M. Rocci, D.-Y. Chung, M. G. Kanatzidis, and C. R. Kannewurf, “Transport properties of doped CsBi₄Te₆ thermoelectric materials,” *Materials Research Society Symposium Proceedings*, vol. 545, no. Thermoelectric Materials 1998–The Next Generation Materials for Small-Scale Refrigeration and Power Generation Applications. pp. 75–80, 1999.
 - [170] C. Wood, “Materials for thermoelectric energy conversion,” *Reports Prog. Phys.*, vol. 51, no. 4, pp. 459–539, 1988.
 - [171] R. Detemple, D. Wamwangi, M. Wuttig, and G. Bihlmayer, “Identification of Te alloys with suitable phase change characteristics,” *Appl. Phys. Lett.*, vol. 83, no. 13, pp. 2572–2574, 2003.

- [172] L. Yu, R. S. Kokenyesi, D. A. Keszler, and A. Zunger, "Inverse design of high absorption thin-film photovoltaic materials," *Adv. Energy Mater.*, vol. 3, no. 1, pp. 43–48, 2013.
- [173] K.Wang, C.Steimer, R.Detemple, D. Wamwangi, M.Wutting, "Assessment of Se-based phase change alloy as a candidate for non-volatile electronic memory applications, *Appl. Phys. A81* (2005) 1601-1605.
- [174] D. T. Morelli, V. Jovovic, and J. P. Heremans, "Intrinsically minimal thermal conductivity in cubic I-V-VI₂ semiconductors," *Phys. Rev. Lett.*, vol. 101, no. 3, 2008.
- [175] J.Wernick, K.Benson, New semiconducting ternary compounds, *J.Phys Chem. Solids* 3 (1957) 157-159.
- [176] S.Geller, J.H. Wernick, Ternary semiconducting compounds with sodium chloride structure: AgSbSe₂, AgSbTe₂, AgBiS₂, AgBiSe₂, *Acta Crystallogr.* 12 (1959) 46-54.
- [177] K. Hoang and S. D. Mahanti, "Atomic and electronic structures of I-V-VI₂ ternary chalcogenides", *Journal of Science: Advanced Materials and Devices* 1 (2016) 51-56.
- [178] H. Wang, J.-F. Li, M. Zou, and T. Sui, "Synthesis and transport property of AgSbTe₂ as a promising thermoelectric compound," *Appl. Phys. Lett.*, vol. 93, no. 20, p. 202106, 2008.
- [179] J.Xu, H.Li, B.Du, X.Tang, Q. Zhang, C.Uher, "High thermoelectric figure of merit and nanostructuring in bulk AgSbTe₂, *J. Mater. Chem.* 20 (2010) 6138-6143.
- [180] K. Hoang, S. D. Mahanti, J. R. Salvador, and M. G. Kanatzidis, "Atomic ordering and gap formation in Ag-Sb-based ternary chalcogenides," *Phys. Rev. Lett.*, vol. 99, no. 15, pp. 1–4, 2007.
- [181] V. Jovovic and J. P. Heremans, "Measurements of the energy band gap and valence band structure of AgSbTe₂" *Phys. Rev. B*, vol. 77, no. 24, p. 245204, 2008.
- [182] L.-H. Ye, K. Hoang, a. J. Freeman, S. D. Mahanti, J. He, T. M. Tritt, and M. G. Kanatzidis, "First-principles study of the electronic, optical, and lattice vibrational properties of AgSbTe₂," *Phys. Rev. B*, vol. 77, no. 24, p. 245203, 2008.
- [183] M. D. Nielsen, V. Ozolins, and J. P. Heremans, "Lone pair electrons minimize lattice thermal conductivity," *Energy Environ. Sci.*, vol. 6, no. 2, pp. 570–578, 2013.
- [184] H.Shinya, A. Masago, T. Fukushima, H. Katayama-Yoshida, "Inherent instability by antibonding coupling in AgSbTe₂, *Jpn. J. Appl. Phys.* 55 (2016) 041801.
- [185] R. Wolfe, J. H. Wernick, and S. E. Haszko, "Anomalous Hall effect in AgSbTe₂," *J. Appl. Phys.*, vol. 31, no. 11, pp. 1959–1964, 1960.
- [186] J. Ma, O. Delaire, a F. May, C. E. Carlton, M. a McGuire, L. H. VanBebber, D. L. Abernathy, G. Ehlers, T. Hong, a Huq, W. Tian, V. M. Keppens, Y. Shao-Horn, and B. C. Sales, "Glass-like phonon scattering from a spontaneous nanostructure in AgSbTe₂," *Nat. Nanotechnol.*, vol. 8, no. 6, pp. 445–51, 2013.
- [187] P. A. Sharma, J. D. Sugar, and D. L. Medlin, "Influence of nanostructuring and heterogeneous nucleation on the thermoelectric figure of merit in AgSbTe₂," *J. Appl. Phys.*, vol. 107, no. 11, 2010.

- [188] R. Kumar, A. Cornelius, E. Kim, Y. Shen, S. Yoneda, C. Chen, and M. Nicol, "Pressure induced structural phase transition in AgSbTe_2 ," *Phys. Rev. B*, vol. 72, no. 6, p. 060101, 2005.
- [189] K. Wojciechowski, J. Tobola, M. Schmidt, and R. Zybala, "Crystal structure, electronic and transport properties of AgSbSe_2 and AgSbTe_2 ," *J. Phys. Chem. Solids*, vol. 69, no. 11, pp. 2748–2755, 2008.
- [190] K. T. Wojciechowski and M. Schmidt, "Structural and thermoelectric properties of AgSbTe_2 - AgSbSe_2 pseudobinary system," *Phys. Rev. B*, vol. 79, no. 18, p. 184202, 2009.
- [191] S. Berri, D. Maouche, and Y. Medkour, "Ab initio study of the structural, electronic and elastic properties of AgSbTe_2 , AgSbSe_2 , Pr_3AlC , Ce_3AlC , Ce_3AlN , La_3AlC and La_3AlN compounds," *Phys. B-Condensed Matter*, vol. 407, no. 17, pp. 3320–3327, 2012.
- [192] R. S. Kumar, A. Sekar, N. V. Jaya, and S. Natarajan, "Synthesis and high pressure studies of the semiconductor AgSbSe_2 ," *J. Alloys Compd.*, vol. 285, no. 1–2, pp. 48–50, 1999.
- [193] V. Jovovic and J. P. Heremans, "Doping Effects on the Thermoelectric Properties of AgSbTe_2 ," *J. Electron. Mater.*, vol. 38, no. 7, pp. 1504–1509, 2009.
- [194] B. L. Du, H. Li, and X. F. Tang, "Enhanced thermoelectric performance in Na-doped p-type nonstoichiometric AgSbTe_2 compound," *J. Alloys Compd.*, vol. 509, no. 5, pp. 2039–2043, 2011.
- [195] R. Mohanraman, R. Sankar, F. C. Chou, C. H. Lee, and Y. Y. Chen, "Enhanced thermoelectric performance in Bi-doped p-type AgSbTe_2 compounds," *J. Appl. Phys.*, vol. 114, no. 16, 2013.
- [196] B. Du, H. Li, J. Xu, X. Tang, and C. Uher, "Enhanced figure-of-merit in Se-doped p-type AgSbTe_2 thermoelectric compound," *Chem. Mater.*, vol. 22, no. 19, pp. 5521–5527, 2010.
- [197] H. Zhang, J. Luo, H.-T. Zhu, Q.-L. Liu, J.-K. Liang, J.-B. Li, and G.-Y. Liu, "Synthesis and thermoelectric properties of Mn-doped AgSbTe_2 compounds," *Chinese Phys. B*, vol. 21, no. 10, p. 106101, 2012.
- [198] B. K. Min, B. S. Kim, I. H. Kim, J. K. Lee, M. H. Kim, M. W. Oh, S. D. Park, and H. W. Lee, "Electron transport properties of La-doped AgSbTe_2 thermoelectric compounds," *Electron. Mater. Lett.*, vol. 7, no. 3, pp. 255–260, 2011.
- [199] R. Mohanraman, R. Sankar, K. M. Boopathi, F.-C. Chou, C.-W. Chu, C.-H. Lee, and Y.-Y. Chen, "Influence of In doping on the thermoelectric properties of an AgSbTe_2 compound with enhanced figure of merit," *J. Mater. Chem. A*, vol. 2, no. 8, p. 2839, 2014.
- [200] B. Du, H. Li, and X. Tang, "Effect of Ce substitution for Sb on the thermoelectric properties of AgSbTe_2 compound," *J. Electron. Mater.*, vol. 43, no. 6, pp. 2384–2389, 2014.
- [201] R. Mohanraman, R. Sankar, F. C. Chou, C. H. Lee, Y. Iizuka, I. P. Muthuselvam, and Y. Y. Chen, "Influence of nanoscale Ag_2Te precipitates on the thermoelectric properties of the Sn doped P-type AgSbTe_2 compound," *APL Mater.*, vol. 2, no. 9, pp. 1–8, 2014.
- [202] K. Wojciechowski, M. Schmidt, J. Tobola, M. Koza, A. Olech, and R. Zybala, "Influence of doping on structural and thermoelectric properties of AgSbSe_2 ," *J. Electron. Mater.*, vol. 39, no. 9, pp. 2053–2058, 2010.

- [203] S. Cai, Z. Liu, J. Sun, R. Li, W. Fei, and J. Sui, "Enhancement of thermoelectric properties by Na doping in Te-free p-type AgSbSe₂," *Dalt. Trans.*, vol. 44, no. 3, pp. 1046–1051, 2015.
- [204] S. N. Guin, A. Chatterjee, and K. Biswas, "Enhanced thermoelectric performance in p-type AgSbSe₂ by Cd-doping," *RSC Adv.*, vol. 4, no. 23, p. 11811, 2014.
- [205] S. N. Guin, D. S. Negi, R. Datta, and K. Biswas, "Nanostructuring, carrier engineering and bond anharmonicity synergistically boost the thermoelectric performance of p-type AgSbSe₂-ZnSe," *J. Mater. Chem. A*, vol. 2, no. 12, pp. 4324–4331, 2014.
- [206] S. N. Guin, A. Chatterjee, D. S. Negi, R. Datta, and K. Biswas, "High thermoelectric performance in tellurium free p-type AgSbSe₂," *Energy Environ. Sci.*, vol. 6, no. 9, pp. 2603–2608, 2013.
- [207] D. Li, X. Y. Qin, T. H. Zou, J. Zhang, B. J. Ren, C. J. Song, Y. F. Liu, L. Wang, H. X. Xin, and J. C. Li, "High thermoelectric properties for Sn-doped AgSbSe₂," *J. Alloys Compd.*, vol. 635, pp. 87–91, 2015.
- [208] Z. Liu, J. Shuai, H. Geng, J. Mao, Y. Feng, X. Zhao, X. Meng, R. He, W. Cai, and J. Sui, "Contrasting the Role of Mg and Ba Doping on the Microstructure and Thermoelectric Properties of p-Type AgSbSe₂," *ACS Appl. Mater. Interfaces*, vol. 7, no. 41, pp. 23047–23055, 2015.
- [209] S. N. Guin and K. Biswas, "Sb deficiencies control the hole transport and boost the thermoelectric performance of p-type AgSbSe₂," *J. Mater. Chem. C*, vol. 2, p. DOI: 10.1039/c5tc01429h, 2015.
- [210] B. A. Cook, M. J. Kramer, X. Wei, J. L. Harringa, and E. M. Levin, "Nature of the cubic to rhombohedral structural transformation in (AgSbTe₂)₁₅(GeTe)₈₅ thermoelectric material," *J. Appl. Phys.*, vol. 101, no. 2007, p. 053715, 2007.
- [211] E. a Skrabek and D. S. Trimmer, "Properties of the general TAGS system," *CRC Handb. Thermoelectr.*, pp. 267–275, 1995.
- [212] J. R. Salvador, J. Yang, X. Shi, H. Wang, and A. A. Wereszczak, "Transport and mechanical property evaluation of (AgSbTe)_{1-x}(GeTe)_x (x=0.80, 0.82, 0.85, 0.87, 0.90)," *J. Solid State Chem.*, vol. 182, no. 8, pp. 2088–2095, 2009.
- [213] S. H. Yang, T. J. Zhu, T. Sun, J. He, S. N. Zhang, and X. B. Zhao, "Nanostructures in high-performance (GeTe)(x)(AgSbTe(2))(100-x) thermoelectric materials.," *Nanotechnology*, vol. 19, no. 24, p. 245707, 2008.
- [214] E. M. Levin, S. L. Bud'Ko, and K. Schmidt-Rohr, "Enhancement of thermopower of TAGS-85 high-performance thermoelectric material by doping with the rare earth dy," *Adv. Funct. Mater.*, vol. 22, no. 13, pp. 2766–2774, 2012.
- [215] Y. Chen, C. M. Jaworski, Y. B. Gao, H. Wang, T. J. Zhu, G. J. Snyder, J. P. Heremans, and X. B. Zhao, "Transport properties and valence band feature of high-performance (GeTe)₈₅(AgSbTe₂)₁₅ thermoelectric materials," *New J. Phys.*, vol. 16, 2014.
- [216] Y. Chen, B. He, T. J. Zhu, and X. B. Zhao, "Thermoelectric properties of non-stoichiometric AgSbTe₂ based alloys with a small amount of GeTe addition," *J. Phys. D Appl. Phys*, vol. 45, pp. 115302–5, 2012.

- [217] K. F. Hsu, S. Loo, F. Guo, W. Chen, J. S. Dyck, C. Uher, T. Hogan, E. K. Polychroniadis, and M. G. Kanatzidis, "Cubic AgPb(m)SbTe_{2+m} : bulk thermoelectric materials with high figure of merit.," *Science*, vol. 303, no. 5659, pp. 818–821, 2004.
- [218] M. Zhou, J. F. Li, and T. Kita, "Nanostructured AgPbmSbTe_{m+2} system bulk materials with enhanced thermoelectric performance," *J. Am. Chem. Soc.*, vol. 130, no. 13, pp. 4527–4532, 2008.
- [219] E. Quarez, K. Hsu, R. Pcionek, N. Frangis, E. K. Polychroniadis, and M. G. Kanatzidis, "Nanostructuring , Compositional Fluctuations , and Atomic Ordering in the Thermoelectric Materials AgPbmSbTe_{2+m} . The Myth of Solid Solutions Lead Antimony Silver Tellurium), several members of which," *J. Am. Chem. Soc.*, vol. 127, pp. 9177–9190, 2005.
- [220] S. N. Guin, V. Srihari, and K. Biswas, "Promising thermoelectric performance in n-type AgBiSe_2 : effect of aliovalent anion doping," *J. Mater. Chem. A*, vol. 3, no. 2, pp. 648–655, 2015.
- [221] D. S. Parker, A. F. May, and D. J. Singh, "Benefits of carrier-pocket anisotropy to thermoelectric performance: The case of p-type AgBiSe_2 ," *Phys. Rev. Appl.*, vol. 3, no. 6, pp. 1–10, 2015.
- [222] L. Pan, D. Berardan, and N. Dragoë, "High Thermoelectric Properties of n - Type AgBiSe_2 ," vol. 3, 2012.
- [223] C. Xiao, X. Qin, J. Zhang, R. An, J. Xu, K. Li, B. Cao, J. Yang, B. Ye, and Y. Xie, "High thermoelectric and reversible p-n-p conduction type switching integrated in dimetal chalcogenide," *J. Am. Chem. Soc.*, vol. 134, no. 44, pp. 18460–18466, 2012.
- [224] S. N. Guin and K. Biswas, "Cation disorder and bond anharmonicity optimize the thermoelectric properties in kinetically stabilized rocksalt AgBiS_2 nanocrystals," *Chem. Mater.*, vol. 25, no. 15, pp. 3225–3231, 2013.
- [225] S. Berri, D. Maouche, N. Bouarissa, and Y. Medkour, "First principles study of structural, electronic and optical properties of AgSbS_2 ," *Materials Science in Semiconductor Processing*, vol. 16, no. 6, pp. 1439–1446, 2013.
- [226] G. Tan, F. Shi, H. Sun, L.-D. Zhao, C. Uher, V. P. Dravid, and M. G. Kanatzidis, " $\{\text{SnTe}\}$ - $\{\text{AgBiTe}\}_2$ as an efficient thermoelectric material with low thermal conductivity," *J. Mater. Chem. A*, vol. 2, no. 48, pp. 20849–20854, 2014.
- [227] D. Wu, Y. Pei, Z. Wang, H. Wu, L. Huang, L. D. Zhao, and J. He, "Significantly Enhanced Thermoelectric Performance in n-type Heterogeneous BiAgSeS composites," *Adv. Funct. Mater.*, 24, pp. 7763–7771, 2014.
- [228] Y.L. Pei, H. Wu, J. Sui, J. Li, D. Berardan, C. Barreateau, L. Pan, N. Dragoë, W.S. Liu, J. He and L.D. Zhao, "High thermoelectric performance in n-type BiAgSeS due to intrinsically low thermal conductivity," *Energy Environ. Sci.*, 6, pp. 1750–1755, 2013.
- [229] R. Mohanraman, T.W. Lan et al., "Engineering Nanostructural Routes for Enhancing Thermoelectric Performance: Bulk to Nanoscale," vol.3, Article 63, 2015.
- [230] J.H. Wernick, " Constitution of the AgSbS_2 - PbS , AgBiS_2 - PbS and AgBiS_2 - AgBiSe_2 Systems", the American mineralogist, vol. 45, 1960.

- [231] M. Suárez, a Fernández, and J. Menéndez, "Challenges and Opportunities for Spark Plasma Sintering: A Key Technology for a New Generation of Materials," *Sinter. Appl.*, p. 319, 2013.
- [232] R. Letoullec, J. P. Pinceaux, and P. Loubeyre, "The membrane diamond anvil cell: A new device for generating continuous pressure and temperature variations," *High Press. Res.*, vol. 1, no. 1, pp. 77–90, 1988.
- [233] I. L. Spain and D. J. Dunstan, "The technology of diamond anvil high-pressure cells: II. Operation and use," *J. Phys. E.*, vol. 22, no. 11, pp. 923–933, 2000.
- [234] I. L. Spain and D. J. Dunstan, "The technology of diamond anvil high-pressure cells: I. Principles, design and construction," *J. Phys. E.*, vol. 22, pp. 913–933, 1989.
- [235] D. J. Dunstan, "Theory of the gasket in diamond anvil high-pressure cells," *Rev. Sci. Instrum.*, vol. 60, no. 12, pp. 3789–3795, 1989.
- [236] A. Katrusiak, "High-pressure crystallography," *Acta Crystallogr. Sect. A Found. Crystallogr.*, vol. 64, no. 1, pp. 135–148, 2008.
- [237] F. Fauth, I. Peral, C. Popescu, M. Knapp, "The new Material Science Powder Diffraction beamline at ALBA Synchrotron," *Powder Diffraction*, vol. 28, supplement S2, pp. S360–S370, 2013.
- [238] D. Errandonea, C. Popescu, S. N. Achary, a. K. Tyagi, and M. Bettinelli, "In situ high-pressure synchrotron X-ray diffraction study of the structural stability in NdVO₄ and LaVO₄," *Mater. Res. Bull.*, vol. 50, pp. 279–284, 2014.
- [239] A Profile Refinement Method for Nuclear and Magnetic Structures", Rietveld, H.M. (1969), *J. Appl. Cryst.*, **22**, 65–71.
- [240] C. Byl, D. Bérardan, and N. Dragoe, "Experimental setup for measurements of transport properties at high temperature and under controlled atmosphere," *Meas. Sci. Technol.*, vol. 23, no. 3, p. 035603, 2012.
- [241] R. Bachmann, F.J. Disalvo, T.H. Gelaballe, R.L. Greene, R.E. Howard, C.N. King, H.C. Kirsch, K. Lee, R.E. Schawall, H.U. Thomas, and R.B. Zubeck, "Heat capacity measurements on small samples at low temperatures," *Review of Scientific Instruments* 43, p. 205, 1972.
- [242] M. Sheindlin, D. Halton, M. Musella, and C. Ronchi, "Advances in the use of laser-flash techniques for thermal diffusivity measurement," *Rev. Sci. Instrum.*, vol. 69, no. 3, pp. 1426–1436, 1998.
- [243] T. Baba and A. Ono, "Improvement of the laser flash method to reduce uncertainty in thermal diffusivity measurements," *Meas. Sci. Technol.*, vol. 12, no. 12, pp. 2046–2057, 2001.
- [244] S. Diouf and A. Molinari, "Densification mechanisms in spark plasma sintering: Effect of particle size and pressure," *Powder Technol.*, vol. 221, pp. 220–227, 2012.
- [245] S. X. Song, Z. Wang, and G. P. Shi, "Heating mechanism of spark plasma sintering," *Ceram. Int.*, vol. 39, no. 2, pp. 1393–1396, 2013.
- [246] S. Iwanaga, E. S. Toberer, A. Lalonde, and G. J. Snyder, "A high temperature apparatus for measurement of the Seebeck coefficient," *Rev. Sci. Instrum.*, vol. 82, no. 6, 2011.

- [247] M. Gunes, M. Parlak, and M. Ozenbas, "An instrument for the high temperature measurement of the Seebeck coefficient and electrical resistivity," *Meas. Sci. Technol.*, vol. 25, no. 5, p. 055901, 2014.
- [248] M. Cutler and N. F. Mott, "Observation of Anderson Localization in an electron gas," *Phys. Rev.*, vol. 181, no. 3, pp. 1336–1339, 1969; P. M. Chaikin, and G. Beni, "Thermopower in the correlated hopping regime," *Phys. Rev B.*, vol. 13, no. 2, pp. 647–651, 1976.
- [249] J. P. Heremans, V. Jovovic, E. S. Toberer, A. Saramat, K. Kurosaki, A. Charoenphakdee, S. Yamanaka, G. J. Snyder, "Enhancement of Thermoelectric Efficiency in PbTe by Distortion of the Electronic Density of States," *Science.*, vol. 321, pp. 554, 2008; J. P. Heremans, B. Wiendlocha, A. M. Chamoire, "Environmental Science Resonant levels in bulk thermoelectric semiconductors," *Energy Environ. Sci.* pp. 5510–5530, 2012.
- [250] T. C. Harman, P. J. Taylor, M. P. Walsh, B. E. Laforge, T. C. Harman, P. J. Taylor, M. P. Walsh, and B. E. Laforge, "Quantum Dot Superlattice Thermoelectric Materials and Devices," *Science*, vol. 297, no. 5590, pp. 2229–32, 2002; Y. Tian, M. R. Sakr, J. M. Kinder, D. Liang, M. J. Macdonald, R. L. J. Qiu, H. Gao, and X. P. A. Gao, "One-Dimensional Quantum Confinement Effect Modulated Thermoelectric Properties in InAs Nanowires," *Nano lett.*, vol. 12, pp. 6492, 2012.
- [251] Y. Pei, X. Shi, A. LaLonde, H. Wang, L. Chen, and G. J. Snyder, "Convergence of electronic bands for high performance bulk thermoelectrics," *Nature*, vol. 473, no. 7345, pp. 66–69, 2011; W. Liu, X. Tan, K. Yin, H. Liu, X. Tang, J. Shi, Q. Zhang, and C. Uher, "Convergence of Conduction Bands as a Means of Enhancing Thermoelectric Performance of n-Type $\text{Mg}_{2-\text{Si}}_{1-\text{x}}\text{Sn}_\text{x}$ Solid Solutions," *Phys. Rev B*, vol. 108, pp. 1–5, 2012.
- [252] J. Martin, L. Wang, L. Chen, and G. S. Nolas, "Enhanced Seebeck coefficient through energy-barrier scattering in PbTe nanocomposites," *Phys. Rev. B*, vol. 79, pp. 1–5, 2009.
- [253] C. Ou, J. Hou, T. Wei, B. Jiang, S. Jiao, J. Li, and H. Zhu, "High thermoelectric performance of all-oxide heterostructures with carrier double-barrier filtering effect," *NPG Asia Mater*, vol. 7, no. 5, pp. e182–10, 2015.
- [254] S. Wang, J. Yang, L. Wu, P. Wei, W. Zhang, and J. Yang, "On Intensifying Carrier Impurity Scattering to Enhance Thermoelectric Performance in Cr-Doped $\text{Ce}_\text{y}\text{Co}_{4-\text{Sb}}_{12}$," *Adv. Funct. Mater.*, vol. 25, pp. 6660, 2015.
- [255] D. Chattopadhyay, "Electron scattering by ionized impurities in semiconductors," *Rev. Mod. Phys.*, vol. 53, no. 4, pp. 745–768, 1981.
- [256] H. Jin, B. Wiendlocha, J. P. Heremans, "P-type doping of elemental bismuth with indium, gallium and tin: a novel doping mechanisms in solids," *Energy Environ Sci.* vol. 8, pp. 2027, 2015.
- [257] A. Wold, R. Brec, "STRUCTURE NaCl DES PHASES $\text{Ag}_\text{x}\text{Sn}_{1-\text{x}}\text{X}$ ($\text{X}=\text{S}, \text{Se}$)," *Mater. Res. Bull.*, vol. 11, no. 6, pp. 761–766, 1976.
- [258] Z. Ren, M. Kriener, A. A. Taskin, S. Sasaki, K. Segawa, and Y. Ando, "Anomalous metallic state above the upper critical field of the conventional three-dimensional superconductor AgSnSe_2 with strong intrinsic disorder," *Phys. Rev. B*, pp. 1–6, 2013.
- [259] G. T. Alekseeva, E. A. Gurieva, P. P. Konstantinov, L. V. Prokof'eva, G. T. Alekseeva, E. A. Gurieva,

- P. P. Konstantinov, L. V. Prokof'eva, "Defects in sodium-doped lead and tin chalcogenides: Formation, Interaction and the influence of the defects on the electronic spectrum," vol. 30, no. 9, pp. 864-867, 1996; H. Wang, Y. Pei, A. D. Lalonde, and G. J. Snyder, "Heavily doped p-type PbSe with high thermoelectric performance: An alternative for PbTe," *Adv. Mater.*, vol. 23, no. 11, pp. 1366-1370, 2011; E. K. Chere, Q. Zhang, E. K. Chere, K. Mcenaney, M. Yao, and F. Cao, "Enhancement of Thermoelectric Performance of n-Type PbSe by Cr Doping with Optimized Carrier Concentration Enhancement of Thermoelectric Performance of n-Type PbSe by Cr Doping with Optimized Carrier Concentration," *Adv. Energy Mater.*, no. 5, pp. 1407977-1-8, 2015.
- [260] I. I. Ravich, B. A. Efimova, I. A. Smirnov, "Semiconducting Lead Chalcogenides, in *Monographs in Semiconductor Physics*," vol. 5, Springer, USA 1970.
- [261] V. A. Online, L. D. Zhao, H. J. Wu, S. Q. Hao, C. I. Wu, X. Y. Zhou, K. Biswas, J. Q. He, T. P. Hogan, C. Uher, C. Wolverton, V. P. Dravid, and M. G. Kanatzidis, "Environmental Science All-scale hierarchical thermoelectrics : MgTe in PbTe," *Energy Environ Sci.*, vol. 6, pp. 3346-3355, 2013; Z. Zhou, C. Uher, A. Jewell, and T. Caillat, "Influence of point-defect scattering on the lattice thermal conductivity of solid solution $\text{Co}_{1-x}\text{Sb}_x$," *Phys. Rev. B*, vol. 71, pp. 235209-1-6, 2005; G. Jiang, J. He, T. Zhu, C. Fu, X. Liu, and L. Hu, "High Performance $\text{Mg}_2(\text{Si}, \text{Sn})$ Solid Solutions : a Point Defect Chemistry Approach to Enhancing Thermoelectric Properties," *Adv. Funct. Mater.*, vol. 24, pp. 3776-3781, 2014; L. Hu, T. Zhu, X. Liu, X. Zhao, "Point Defect Engineering of High Performance Bismuth-Telluride-Based Thermoelectric Materials," *Adv. Funct. Mater.*, vol. 24, no. 33, pp. 5211-5218, 2014.
- [262] Q. Zhang, F. Cao, K. Lukas, W. Liu, K. Esfarjani, C. Opeil, D. Broido, D. Parker, D. J. Singh, G. Chen, Z. Ren, "Study of the Thermoelectric Properties of Lead Selenide Doped with Boron , Gallium , Indium , Thallium ," *J. Am. Chem. Soc.*, vol. 134, no. 42, pp. 17731-17738, 2012.
- [263] M. K. Han, K. Hoang, H. Kong, R. Pcionek, C. Uher, K. M. Paraskevopoulos, S. D. Mahanti, M. G. Kanatzidis, "Substitution of Bi for Sb and Its Role in the Thermoelectric Properties and Nanostructuring in $\text{Ag}_{1-x}\text{Pb}_{18}\text{MTe}_{20}$ (M : Bi , Substitution of Bi for Sb and its Role in the Thermoelectric Properties and Nanostructuring in $\text{Ag}_1 - x \text{Pb}_{18} \text{MTe}_{20}$ (M) Bi , Sb)," *Chem. Mater.*, vol. 39, no. 20, pp. 3512-3520, 2008.
- [264] L. D. Zhao, S. Hao, S. H. Lo, C. I. Wu, X. Zhou, Y. Lee, H. Li, K. Biswas, T. P. Hogan, C. Uher, C. Wolverton, V. P. Dravid, M. G. Kanatzidis, "All scale hierarchical thermoelectrics: MgTe in PbTe facilitates valence band convergence and suppresses bipolar thermal transport for high performance," *J. Am. Chem. Soc.*, vol. 135, pp. 7364, 2013.
- [265] K. Ahn, C.-P. Li, C. Uher, M. G. Kanatzidis, "Thermoelectric properties of the compounds $\text{AgPb}_m\text{LaTe}_{m+2}$," *Chem Mater.*, vol. 22, pp. 876-882, 2010.
- [266] H. Brooks, "Theory of the Electrical Properties of Germanium and Silicon," *Adv. Electron. El. Phys.*, vol. 7, pp. 85-182, 1955.
- [267] Y. Lee, S. H. Lo, J. Androulakis, C. I. Wu, L. D. Zhao, D. Y. Chung, T. P. Hogan, V. P. Dravid, M. G. Kanatzidis, "High-Performance Tellurium free Thermoelectrics: All-scale hierarchical structuring of p-type PbSe-MSe systems (M=Ca, Sr, Ba)," *J. Am. Chem. Soc.*, vol. 135, pp. 5152-5160, 2013.
- [268] E. S. R. Gopal, *Specific heat at low temperature*, Plenum Press, USA, 1966.

- [269] G. S. Nolas, H. J. Goldsmid, *Thermal Conductivity of Semiconductors*, Springer US, USA, **2004**.
- [270] E. J. Goldsmid, W. H. Bessey, *Phys. Teach.* **1966**, 4, 1209.
- [271] J. Rodríguez-Carvajal, "Recent advances in magnetic structure determination by neutron power diffraction," *Physica B.*, vol. 192, pp.55-69, 1993.

List of Figures

Figure 1-1: A schematic diagram illustrating the Seebeck effect of two dissimilar material A & B....	11
Figure 1-2: Schematic diagram of Peltier effect between two dissimilar materials A and B.	12
Figure 1-3: Schematic diagram of n and p-type semiconductor showing the effect Peltier effect.	13
Figure 1-4: Schematic diagram of Thompson effect in a single material.	15
Figure 1-5: Waste heat recovery	16
Figure 1-6:(a) Schematic diagram of thermoelectric module and (b) diagram illustrates both power generation (Seebeck effect) and electronic refrigeration (Peltier effect).....	19
Figure 1-7: Dependence of efficiency with ZT. [17].....	22
Figure 1-8: (a) The dependence and variation of s , k , σ and $s^2\sigma$ as a function of carrier concentration n [16]and (b) also ZT variation with carrier concentration[127].	23
Figure 1-9: Schematic illustration of the current state of the TE materials.	29
Figure 1-10: Plot of ZT versus temperature for TE materials (a) p-type and (b) n-type [17].	29
Figure 1-11: Schematic diagram showing the relative energy of the valence bands in PbTe system, with rising solid solution fraction M.[17].....	32
Figure 1-12: Crystal structure of the Type I clathrate. Framework atoms are shown in blue, guest atoms inside the tetrakaidecahedra are orange, and guest atoms inside the pentagonal dodecahedra are in purple [5]......	34
Figure 1-13: The unit cell skutterudite structure of CoSb ₃ ; the transition metals (Co) are at the centre of octahedral formed by pnictogen atoms (Sb), the void cages are filled with blue spheres for clarity [41]......	35
Figure 1-14: Crystal structure of Half-Heusler, TiNiSn, in a unit cell of cubic structure [41].	36
Figure 1-15: The cubic crystal structure of Yb ₁₄ MnSb ₁₁ consists of one [MnSb ₄] ⁹⁻ tetrahedral unit (yellow), one [Sb ₃] ⁷⁻ ion (centres linked by black lines), four Sb ³⁻ ions situated between the [MnSb ₄] ⁹⁻ and [Sb ₃] ⁷⁻ units, and 14Yb ²⁺ ions per formula [41].	37
Figure 1-16: The crystal structure of NaCo ₂ O ₄ is composed of [CoO ₂] ⁻ ionic layers and Na ⁺ ions which occupy half of the interlayer atomic sites. The Co ions [CoO ₂] ⁻ in the layers have an octahedral coordination environment and adopt the CdI ₂ structure type [41].	38
Figure 1-17: Electron density of states of a bulk semiconductor (3D), a quantum well (2D), a quantum wire (1D) and a quantum dot (0D). [125].....	39
Figure 1-18: Calculated ZT as a function of layer thickness (a) in a quantum well structure for layers parallel to the a-b plane (1) and layers parallel to the a-c plane (2). The dashed line corresponds to the ZT for bulk Bi ₂ Te ₃ . [122].....	40
Figure 1-19: Schematic diagram illustrating various phonon scattering mechanisms within a TE material, along with electronic transport of hot and cold electrons. Atomic defects are effective at scattering the short wavelength phonons, but larger embedded nanoparticles are required to scatter mid- and long-wavelength phonons effectively. Grain boundaries can also play an effective role in scattering longer wavelength phonons.[145]	42
Figure 1-20: Nanocomposite thermoelectric material.[39]	44
Figure 1-21: The crystal structure of Tl ₉ BiTe ₆ ; the heavy-atom site disordered being occupied by Bi and Tl. There are two alternating cages of Tl atoms (yellow and blue). (b) The crystal structure of	

Tl ₂ SnTe ₅ is composed of tetrahedral [SnTe ₄] units bridged by Te atoms in square-planar geometry. [41].	46
Figure 1-22: (a) Crystal structure of β -K ₂ Bi ₈ S ₁₃ viewed down to the b-axis. It consists of two Bi/Se building blocks connected at the K/Bi mixed site (blue), the K atoms are in the channels and (b) crystal structure of CsBi ₄ Te ₆ viewed down to b-axis. Cs atoms are located between NaCl-type Bi/Te layers which are composed of [Bi ₄ Te ₆] building units interconnected by Bi-Bi bonds (red) [41].	47
Figure 1-23: Crystal structure of 1-V-VI ₂ compound AgSbSe ₂ [174].	48
Figure 1-24: The schematic representation of (a) harmonicity, (b) anharmonicity and (c) shows the balance phonon transport in harmonicity and an imbalance phonon transport in anharmonicity [17].	50
Figure 1-25: The AgBiS ₂ -AgBiSe ₂ system [230].	53
Figure 1-26: Temperature dependent crystal structure evolution of AgBiSe ₂ . [220]	53
Figure 1-27: Temperature dependence of S, σ , κ , and ZT [223].	54
Figure 1-28: PXRD patterns of pristine AgBiSe ₂ ; showing the structural phase transition from hexagonal to rhombohedral to cubic [222].	55
Figure 1-29: Temperature dependence of ρ and S for (I) AgBi _{1-x} Pb _x Se ₂ from 20-300K, (II) Ag _{1-x} Nb _x BiSe ₂ from 20-773K, and (III) λ and ZT for Ag _{1-x} Nb _x BiSe ₂ from 300-773K [222].	56
Figure 1-30: Temperature dependent (a) electrical conductivity (σ), (b) Seebeck coefficient (S), and (c) Power factor (σS^2), (d) lattice thermal conductivity (κ_{lat}) and finally ZT of AgBiSe ₂ and doped samples [220].	57
Figure 1-31: Crystal structure of high temperature cubic phase of AgBiS ₂ [224].	58
Figure 2-32: Schematic drawing of SPS comprises of a die set-up, the pressing unit and the electric current applied via electrodes.	66
Figure 2-33: A schematic drawing of (a) sintered disc shape pellet, (b) top view of disc, and (c) square and bar shape pellet obtained after cutting.	67
Figure 2-34: Schematic diagram of Bragg diffraction.	68
Figure 2-35: (a) PANalytical Xpert Pro Diffractometer and (b) Bragg Brentano geometry.	68
Figure 2-36: High temperature XRD analysis of AgBiSe _{0.5} S _{1.5} .	69
Figure 2-37: A schematic diagram of DAC.	71
Figure 2-38: A schematic drawing of (a) Heat flux DSC; (b) power-compensated DSC.	76
Figure 2-39: DSC (Setaram Setsys Evolution equipment).	77
Figure 2-40: Diagram of DSC Heat flow curve Vs Temperature of sample.	78
Figure 2-41: (a) Instrument to measure Seebeck coefficient and resistivity and (b) zoom view of sample holder part.	79
Figure 2-42: Schematic diagram of sample holder set-up.	80
Figure 2-43: Measurement at high temperature: (a) the actual set-up in the laboratory and (b) the schematic diagram.	81
Figure 2-44: Geometry for measuring Hall Effect.	82
Figure 2-45: Schematic diagram of assembly to measure the heat capacity in PPMS heat capacity option.	85
Figure 2-46: Specific heat measurement.	86
Figure 2-47: (a) LFA 457MicroFlash apparatus and (b) schematic diagram of LFA.	87

Figure 2-48: Schematic drawing of through-plane heat flow in LFA method.	88
Figure 2-49: (a) sample holder with different shapes and sizes (b) Square sample holder with square shape sample.	88
Figure 3-50: XRD pattern of AgBiSe ₂ sample.	92
Figure 3-51: Heat flow curve of AgBiSe ₂	93
Figure 3-52: XRD pattern of composition AgBiSe _{0.5} S _{1.5}	94
Figure 3-53: (a) Sealed silica glass tube with material inside (bar shape pellet) (b) Schematic drawing of sealed silica tube with bar shape pellets, (c) the very same sealed silica tube inside alumina crucible before being placed inside furnace.	96
Figure 3-54: Schematic drawing of first heat treatment conditions for two series (a) AgBiSe _{1-x} S _{1+x} and (b) AgBiSe _{1+x} S _{1-x}	98
Figure 3-55: Schematic drawing of second heat treatment condition.	98
Figure 3-56: Schematic drawing of second heat treatment for both the series AgBiSe _{1-x} S _{1+x} and AgBiSe _{1+x} S _{1-x}	99
Figure 3-57: Ingot obtained after synthesis using (a) vertical furnace and b) horizontal cylindrical furnace.	99
Figure 3-58: (a-d) XRD patterns of AgBiSe _{1+x} S _{1-x} and AgBiSe _{1-x} S _{1+x} samples: reveals hexagonal phase.	101
Figure 3-59: (a-d) XRD patterns of AgBiSe _{1+x} S _{1-x} and AgBiSe _{1-x} S _{1+x} samples: reveals cubic phase.	102
Figure 3-60: Regular shift in the XRD peaks (a) samples with hexagonal phase and (b) samples with cubic phase.	103
Figure 3-61: XRD plots for comparison.	104
Figure 3-62: Refinement pattern of samples with hexagonal (Ia-IId) and cubic (IIa-IIId) phase; the solid black line represents the refinements performed, the red line represents the measured XRD patterns and the blue line at the bottom is the residual.	105
Figure 3-63: Lattice parameters Vs Se content in (AgBiSe _{1+x} S _{1-x} and AgBiSe _{1-x} S _{1+x}); (a) samples with hexagonal phase and (b) samples with cubic phase.	106
Figure 3-64: DSC curves of solid solution AgBiSe _{1-x} S _{1+x} (0.1 ≤ x ≤ 1) indicate one phase transition for all the compositions.	108
Figure 3-65: (a-d) DSC curves of solid solutions AgBiSe _{1-x} S _{1+x} (0 ≤ x ≤ 1) indicate phase transition (α → β → γ).	110
Figure 3-66: Plots of area under the curve values of AgBiSe _{2-x} S _x vs. the selenium fraction; (a) samples with one phase transition and (b) samples with two phase transition.	110
Figure 3-67: Structural phase diagram with temperature from DSC curve Vs Se content in the solid solutions.	111
Figure 3-68: Temperature dependent XRD patterns of samples: revealing the type of phases.	113
Figure 3-69: The picture of refined XRD patterns; the solid black line represents the refinements performed, the red line represents the measured XRD patterns and the blue line at the bottom is the residual: Hexagonal pattern (Ia & Ib), rhombohedral pattern (IIa & IIb) and cubic patterns (IIIa & IIIb).	114
Figure 3-70: (a) shows the lattice parameters variations with temperature, for hexagonal part and rhombohedral part (dotted box), where solid symbol represents the 'a' value and open symbol	

represents the 'c' value, (b) shows the lattice parameter for the cubic part and (c) plot of volume per formula unit as a function of temperature for the five selected samples.	116
Figure 3-71: Structure of AgBiSe ₂ ; (a) hexagonal AgBiSe ₂ with Bi or Ag polyhedral and AgBiSe ₂ with cubic octahedral.....	117
Figure 3-72: High pressure X-ray diffraction patterns of cubic-AgBiSe ₂ : the black symbol (*) indicates the appearance of a new peak in the XRD patterns is due to copper.....	119
Figure 3-73: High pressure X-ray diffraction patterns of AgBiSe ₂ (Hexagonal): Above 0.99GPa, the patterns show several changes, the pressure induced phase transition is found in this case.	120
Figure 4-74: A schematic drawing for the heat treatment of composition AgBi _{1-x} Sb _x Se ₂	124
Figure 4-75: XRD patterns of first ten set of samples; AgBi _{1-x} Sb _x Se ₂ , (0.1≤x≤0.9).	125
Figure 4-76: XRD patterns of samples belong to AgBi _{1-x} Sb _x Se ₂ ; secondary peaks are marked with the symbols shown in each picture.	126
Figure 4-77: Heat flow DSC curves of AgBi _{1-x} Sb _x Se ₂ , (0.1≤x≤0).	128
Figure 4-78: Picture of ingot; a solid chunk obtained after synthesis.....	129
Figure 4-79: Comparison of XRD patterns of AgBi _{0.7} Sb _{0.3} Se ₂ compound with two different mass values.....	130
Figure 4-80: A schematic drawing of further annealing of composition AgBi _{0.7} Sb _{0.3} Se ₂	130
Figure 4-81: Picture representing the pellets of annealed sample AgBi _{0.7} Sb _{0.3} Se ₂	131
Figure 4-82: The XRD patterns of Sb substituted five samples belongs to the solid solutions AgBi _{0.7} Sb _{0.3} Se _{1-x} S _{1+x} and AgBi _{0.7} Sb _{0.3} Se _{1+x} S _{1-x} ; reveals the cubic phase.....	131
Figure 4-83: Regular shift in the XRD peaks of Sb substituted samples.	132
Figure 4-84: Refinement pattern of AgBi _{0.7} Sb _{0.3} Se _{0.5} S _{1.5} : Single cubic phase (space group F m -3 m); the solid black line represents the refinements performed, the red line represents the measured XRD patterns and the blue line at the bottom is the residual.	133
Figure 4-85: The lattice parameters variations and volume per formula unit as a function of selenium content in the compounds.	134
Figure 4-86: (a) Heat flow DSC curves of Sb substituted samples; reveals no phase transition and (b) Heat flow DSC curves of samples without substitution; reveals phase transition in the samples. ..	135
Figure 5-87: A schematic drawing for the heat treatment.....	139
Figure 5-88: Picture of ingot; a solid chunk obtained after synthesis.....	140
Figure 5-89: XRD patterns of Nb doped sample for x=0.02 and x=0.04.....	141
Figure 5-90: Shifting in diffraction peaks of doped samples; (a) x=0.02 and (b) x=0.04.	141
Figure 5-91: Refinement pattern of doped samples; Single cubic phase (space group F m -3 m); the solid black line represents the refinements performed, the red line represents the measured XRD patterns and the blue line at the bottom is the residual.	142
Figure 5-92: The lattice parameters variations of doped samples vs. selenium content in the compounds.....	143
Figure 5-93: Heat flow DSC curves of Nb doped samples: (a) x=0.02 and (b) x=0.04.	144
Figure 5-94: Temperature dependence of (a) S, (b) ρ from 50 to 300K and (c) κ from 300 to 825K for Ag _{1-x} Nb _x Bi _{0.7} Sb _{0.3} S ₂ , Ag _{1-x} Nb _x Bi _{0.7} Sb _{0.3} Se _{0.5} S _{1.5} , Ag _{1-x} Nb _x Bi _{0.7} Sb _{0.3} Se _{1.5} S _{0.5} and Ag _{1-x} Nb _x Bi _{0.7} Sb _{0.3} Se ₂	147

Figure 6-95: Powder XRD patterns (a) and lattice constants (b) of $\text{AgPb}_m\text{SnSe}_{2+m}$ ($m = \infty, 100, 50, 25, 0$).....	153
Figure 6-96: Rietveld refinements of $\text{AgPb}_m\text{SnSe}_{2+m}$ ($m = \infty, 100, 50, 25$) at room temperature.....	154
Figure 6-97: Temperature dependences of (a) electrical resistivity, (b) Seebeck coefficient, (c) carriers concentration and (d) hole mobility of $\text{AgPb}_m\text{SnSe}_{2+m}$ ($m = \infty, 100, 50, 25$).....	155
Figure 6-98: The heat capacity C_p of PbSe and $\text{AgPb}_m\text{SnSe}_{2+m}$ ($m = 25$) as a function of temperature from 2 K to 400 K. The inset shows the low-T C_p of PbSe and $\text{AgPb}_m\text{SnSe}_{2+m}$ ($m = 25$) plotted as C_p / T versus T^2	158
Figure 6-99: (a) Temperature dependence of thermal conductivity of $\text{AgPb}_m\text{SnSe}_{2+m}$ ($m = \infty, 100, 50, 25$) from 300 K to 875 K. The inset in (a) shows bipolar thermal conductivity as a function of temperature for $\text{AgPb}_m\text{SnSe}_{2+m}$ ($m = \infty, 100, 50, 25$). (b) The difference of total and carrier thermal conductivity $\lambda - L\sigma T$ as a function of temperature for $\text{AgPb}_m\text{SnSe}_{2+m}$ ($m = \infty, 100, 50, 25$), the solid line is a linear fit of the lattice thermal conductivity at temperature ranges from room temperature to 875 K, deviation of thermal conductivity indicating a significant bipolar thermal conductivity.	159
Figure 6-100: ZT of AgPbmSnSe_{2+m} ($m = \infty, 100, 50, 25$) in the range 340 K to 890 K.....	161

List of Tables

Table 1: Comparison of TE properties of metals and semiconductors and insulators at 300K [16]..	24
Table 2: Specifications of raw materials.....	62
Table 3: Picture of instruments used for the synthesis in our laboratory.....	63
Table 4: Systems to make bar shape pellet.	95
Table 5: Lattice parameter values for all the samples with hexagonal phase and cubic phase. For the gap in the “cubic” column, see below.....	106
Table 6: Lattice parameters values determined by Le Bail refinement. The values of volume per formula unit are calculated from the parameters.....	115
Table 7: Lattice parameters values determined by Le Bail refinement. The values of volume/Z are calculated from the parameters.	133
Table 8: Lattice parameters values determined by Le Bail refinement.	142
Table 9: The room temperature value of S , ρ , κ and ZT for selected compositions.....	147

Chalcogénures de type I-V-VI₂ pour applications thermoélectriques

Sunanda MITRA

UNIVERSITÉ PARIS SACLAY, UNIVERSITÉ PARIS-SUD ED 571 :

Sciences chimiques : molécules, matériaux, instrumentation et biosystèmes

Laboratoire : Institut de Chimie Moléculaire et des Matériaux d'Orsay

La conversion d'énergie par effet thermoélectrique (TE), qui peut être utilisée pour convertir de la chaleur perdue en électricité, a reçu une attention soutenue ces dernières décennies. L'efficacité d'un système TE est caractérisé par le facteur de mérite adimensionnel, $ZT = (S^2 \sigma / \kappa) T$, où S , σ , κ , et T sont respectivement le coefficient Seebeck, la conductivité électrique, la conductivité thermique et la température absolue. Récemment, les matériaux à base de chalcogénures de formule générale AgBiCh_2 ont attiré un intérêt au sein de la communauté de la thermoélectricité du fait de leur conductivité thermique faible, qui conduit à des propriétés thermoélectriques prometteuses. Cependant, ces matériaux présentent des transitions structurales qui les rendent inutilisables dans des applications de conversion thermoélectrique. Dans cette thèse, une étude de la solution solide AgBiS_2 - AgBiSe_2 est effectuée, dans le but d'établir son diagramme de phase structural. Des études de diffraction des rayons X en température et sous pression sont effectuées afin de mieux comprendre les transitions structurales observées. L'application d'une pression chimique par substitution partielle du bismuth par l'antimoine permet ensuite de supprimer les transitions de phase en stabilisant la phase haute température. Enfin, des essais préliminaires de dopage ont été effectués afin d'ouvrir la voie à l'optimisation des propriétés thermoélectriques.

1. Etude de la solution solide AgBiS_2 - AgBiSe_2

Au début de ce travail de thèse, peu de données étaient disponibles relatives au diagramme de phase de la solution solide AgBiS_2 - AgBiSe_2 et quant à l'existence même de la solution solide complète. Par ailleurs, si les composés extrêmes AgBiS_2 et AgBiSe_2 avaient été relativement étudiés, ce n'était pas le cas pour les compositions intermédiaires. La première partie de l'étude a donc consisté en l'optimisation des conditions de synthèse des échantillons de composition nominale $\text{AgBiS}_{2-x}\text{Se}_x$ ($x=0$ à 2, par pas de 0.1), en repartant des conditions de la littérature publiées pour AgBiSe_2 , à savoir un mélange stœchiométrique en boîte à gants, un pastillage, puis un recuit à 500°C pendant 48h dans une ampoule de silice scellée sous argon suivi d'un refroidissement lent.

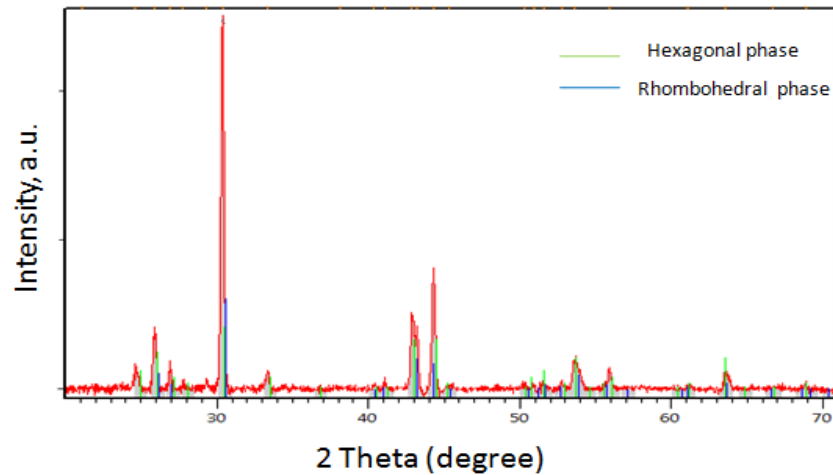


Figure 1: diffractogramme de rayons X de l'échantillon de composition nominale AgBiSe_2 recuit à 500°C 48h suivi d'un refroidissement lent.

Comme le montre la figure 1, ce traitement thermique ne permet pas d'obtenir un échantillon monophasé. En effet, même si les seules phases en présence sont de composition AgBiSe_2 sans trace de phases secondaires, on peut observer ici le mélange d'une phase rhomboédrique et d'une phase hexagonale (sachant qu'une phase cubique aurait dû être obtenue d'après la littérature. Suite à ce résultat, une étude par calorimétrie différentielle à balayage (DSC) a été effectuée, le thermogramme correspondant est représenté sur la figure 2.

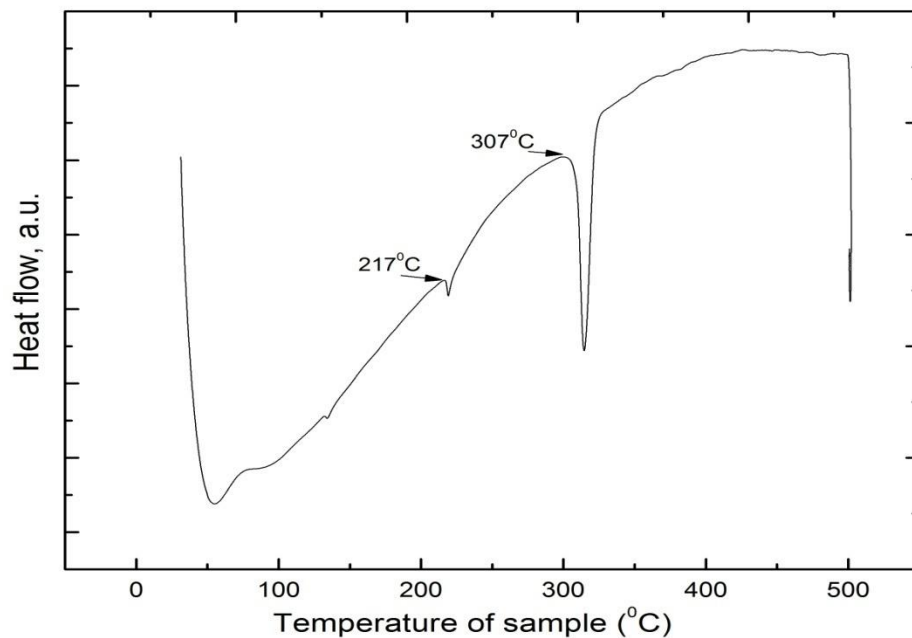


Figure 2: thermogramme de l'échantillon de composition nominale AgBiSe_2 recuit à 500°C 48h suivi d'un refroidissement lent.

Sur ce thermogramme, deux pics endothermiques peuvent être observés, qui correspondent aux transitions structurales hexagonal \rightarrow rhomboédrique et rhomboédrique \rightarrow cubique, à 217°C et 307°C respectivement. On comprend alors pourquoi ce premier échantillon n'était pas monophasé : du fait du refroidissement lent, la phase cubique haute température a le temps de se transformer en phase rhomboédrique lors du refroidissement. En revanche, du fait de la lenteur de la diffusion en phase solide aux températures plus basses, la phase transformation de phase rhomboédrique \rightarrow hexagonale n'est pas achevée en fin de synthèse.

Suite à ces observations, un nouveau protocole de synthèse a été mis en place de manière à obtenir pour chacun des échantillons de la solution solide la phase cubique ou la phase hexagonale (nous verrons par la suite que le domaine d'existence en température de la phase rhomboédrique est assez étroit, et nous n'avons pas essayé d'isoler cette phase pour chacune des compositions) :

- Pour la phase cubique, un premier traitement thermique avec un chauffage lent jusqu'à 450°C ou 500°C pour les échantillons riches respectivement en soufre et en sélénium avec un maintien durant 12h à cette température. L'objectif est ici d'initier de manière « douce » la réaction entre le chalcogène et les métaux, qui est exothermique, et d'éviter une explosion de l'ampoule de silice. Dans un second temps un recuit à 850°C suivi d'une trempe à l'eau, de manière à figer la phase haute température.
- Pour la phase hexagonale, un premier traitement thermique avec un chauffage lent jusqu'à 850°C, avec un maintien à cette température durant 48h de manière à homogénéiser le lingot, puis un refroidissement lent. Dans un second temps un recuit à 120°C durant 1 mois, de manière à permettre la diffusion en phase solide et l'obtention de la phase hexagonale.

Ces nouveaux traitements thermiques ont permis d'obtenir des échantillons monophasés dans les structures cubiques et hexagonales pour chacune des 21 compositions de la solution solide. Un affinement des diffractogrammes de rayons X par la méthode de LeBail a ensuite été effectué pour déterminer les paramètres de maille de chacun des échantillons (les essais d'affinement de Rietveld de la phase hexagonale n'ont pas été satisfaisant, avec des difficultés notables à simuler les intensités des pics de diffraction, vraisemblablement du fait d'un désordre cationique partiel). L'évolution des paramètres de maille en fonction de la composition des échantillons solides pour chacune des deux phases est représentée figure 3. On observe dans les deux cas une augmentation linéaire des paramètres de maille lorsque la fraction de sélénium augmente, obéissant à une loi de Vegard. Cette observation démontre l'existence d'une solution solide complète entre les composés extrêmes AgBiS_2 et AgBiSe_2 . Par ailleurs, l'augmentation des paramètres de maille entre AgBiS_2 et AgBiSe_2 est proche de celle qui peut être estimée à l'aide d'un modèle ionique, ce qui montre que la nature des liaisons chimiques évolue peu avec la fraction de sélénium.

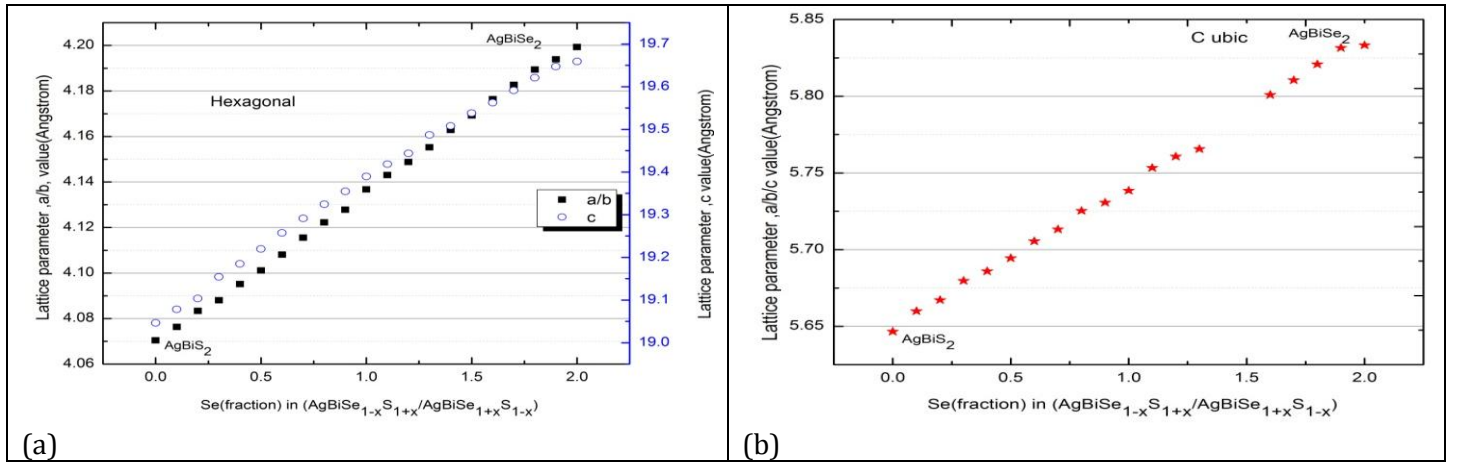


Figure 3: Evolution des paramètres de maille avec la fraction de sélénium dans la phase hexagonale (a) et la phase cubique (b). Deux échantillons sont manquants dans le figure de droite du fait de la rupture de l'ampoule de silice au cours de la trempe à l'eau lors de leur synthèse.

Suite à ce résultat, des analyses DSC ont été effectuées sur tous les échantillons de la série (en utilisant ceux cristallisant en phase hexagonale, afin de construire le diagramme de phase de la solution solide. Dans le cas des échantillons les plus riches en soufre, un seul pic endothermique est observé (figure 4), correspondant à une seule transition structurale. Au contraire dans le cas des échantillons les plus riches en sélénium, deux pics endothermiques sont présents, correspondant à deux transitions structurales (figure 5). Par ailleurs, un net déplacement en température des pics peut être observé lorsque la fraction de sélénium change, ce qui indique une évolution des températures de transition.

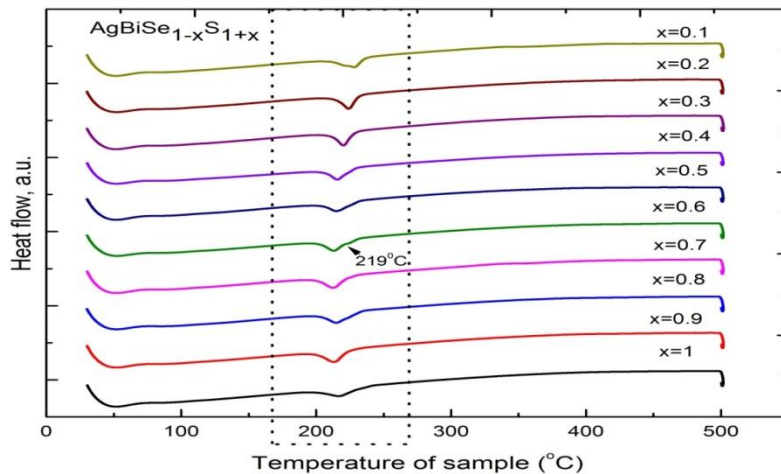


Figure 4: Thermogrammes des échantillons de la solution solide $\text{AgBiSe}_{1-x}\text{S}_{1+x}$. L'épaulement à 219°C correspond au point de fusion du sélénium

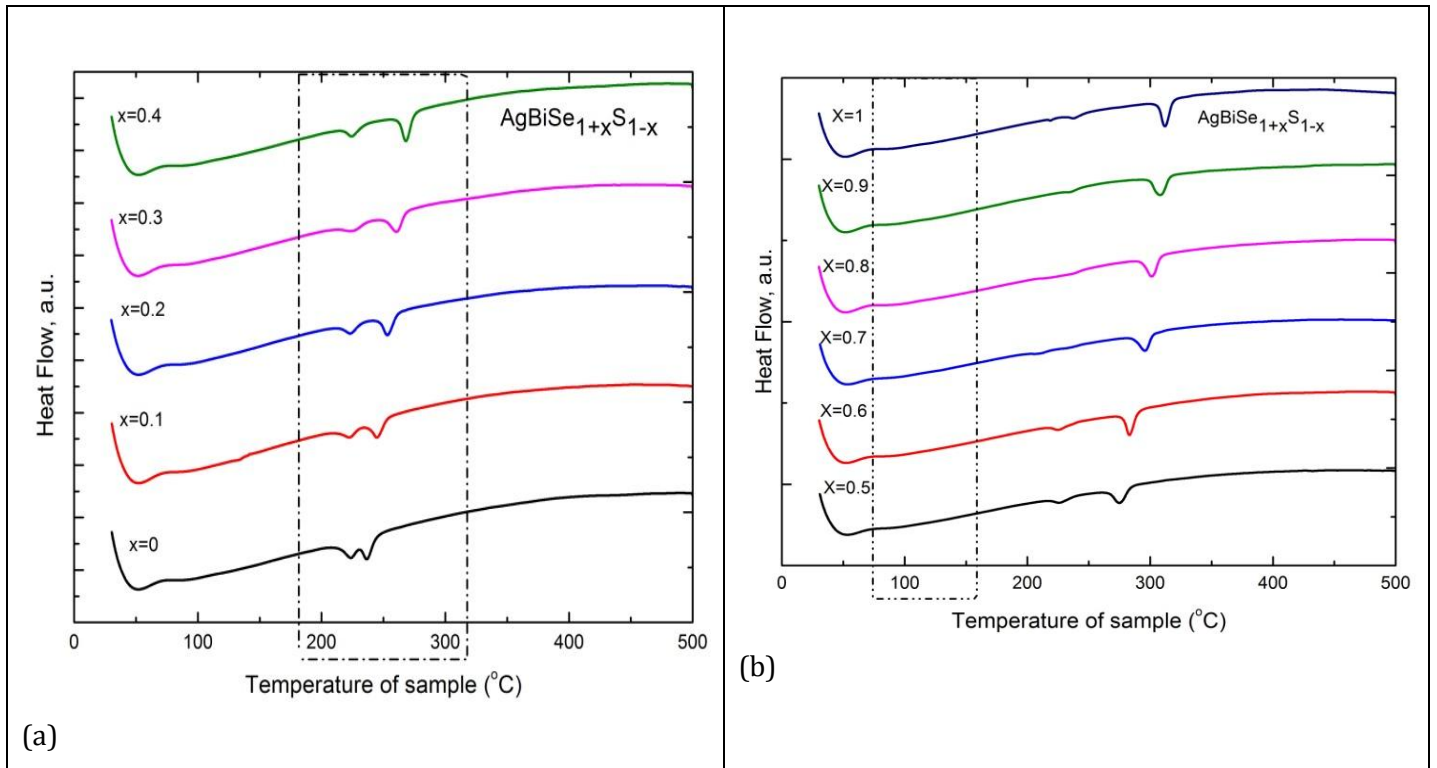


Figure 5: Thermogrammes des échantillons de la solution solide $\text{AgBiSe}_{1+x}\text{S}_{1-x}$.

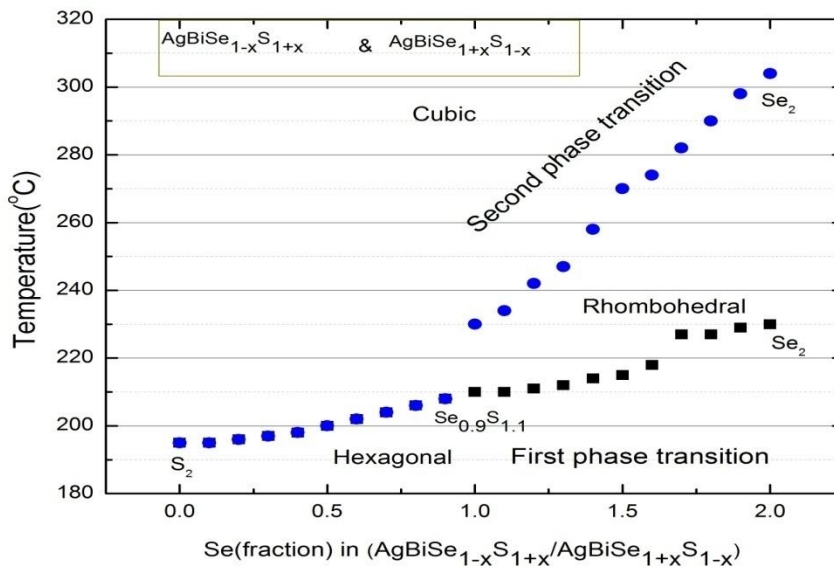


Figure 6: Diagramme de phase structural, montrant la/les température(s) de transition observée(s) par DSC en fonction de la composition de la solution solide.

Sur la base de ces observations, il est donc possible de construire le diagramme de phase de la solution solide, qui est reporté sur la figure 6. Pour les échantillons de la solution solide $\text{AgBiSe}_{1-x}\text{Se}_x$ pour lesquels $x < 1$, une transition directe de la phase hexagonale à la phase cubique est

observée, avec une température de transition qui croît lorsque la fraction de sélénium augmente. Pour les échantillons de la solution solide pour lesquels $x > 1$, une phase intermédiaire rhomboédrique est présente, avec deux transitions structurales successives, depuis la phase hexagonale à basse température vers la phase rhomboédrique, puis la phase cubique à haute température. Les deux températures de transition augmentent avec la fraction de sélénium.

Pour confirmer ces résultats, une étude par diffraction des rayons X en température a été effectuée sur une sélection de compositions. Une sélection des diffractogrammes obtenus est donnée figure 7.

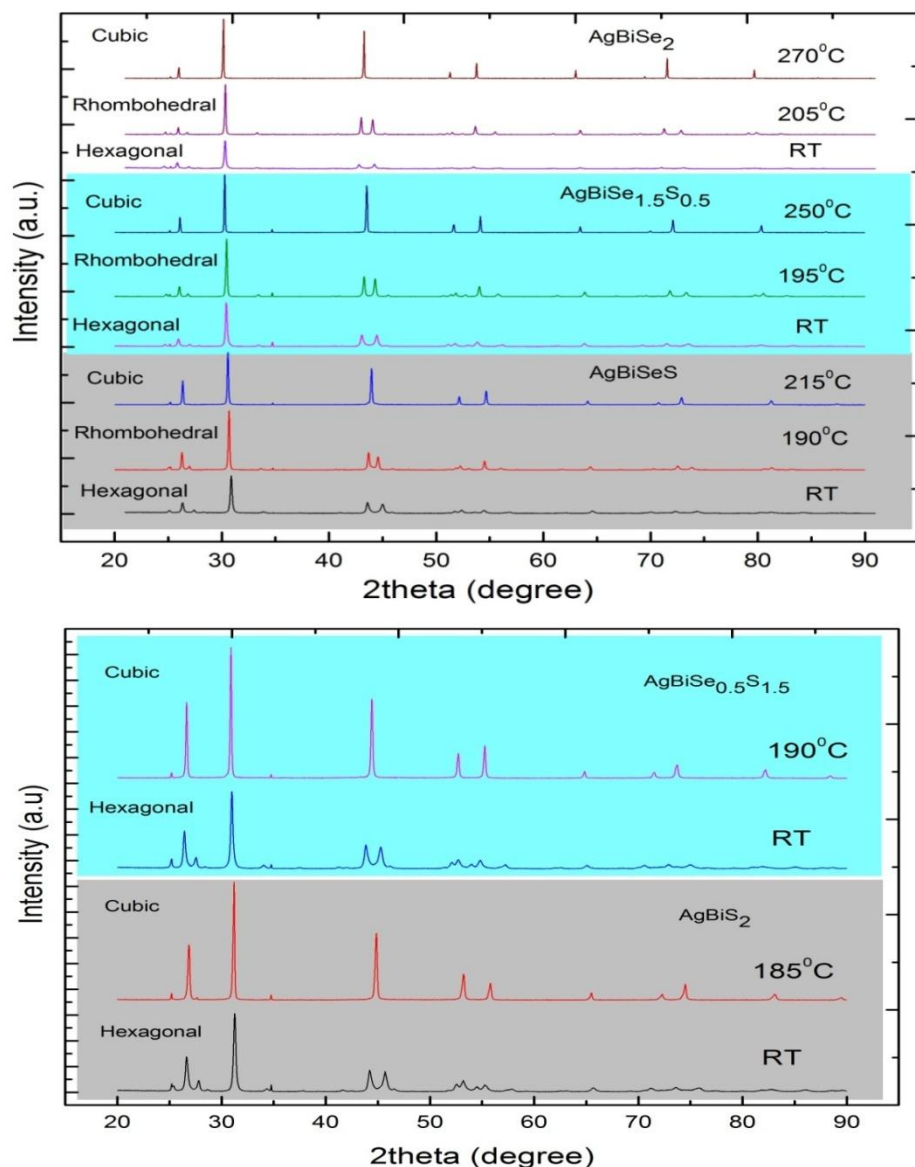


Figure 7: Diffractogrammes d'une sélection d'échantillon de la solution solide à différentes températures.

Cette étude confirme bien la présence de trois phases allotropiques pour les échantillons les plus riches en sélénium (hexagonale, rhomboédrique et cubique), et de deux phases allotropiques pour les échantillons les plus riches en soufre (hexagonale et cubique).

A partir de ces diffractogrammes, il a été possible d'obtenir la dépendance en température des paramètres de maille des différents échantillons dans leurs différentes formes allotropiques, et donc de la dépendance en température du volume par unité formulaire AgBiCh_2 . Cette dépendance en température est tracée figure 8.

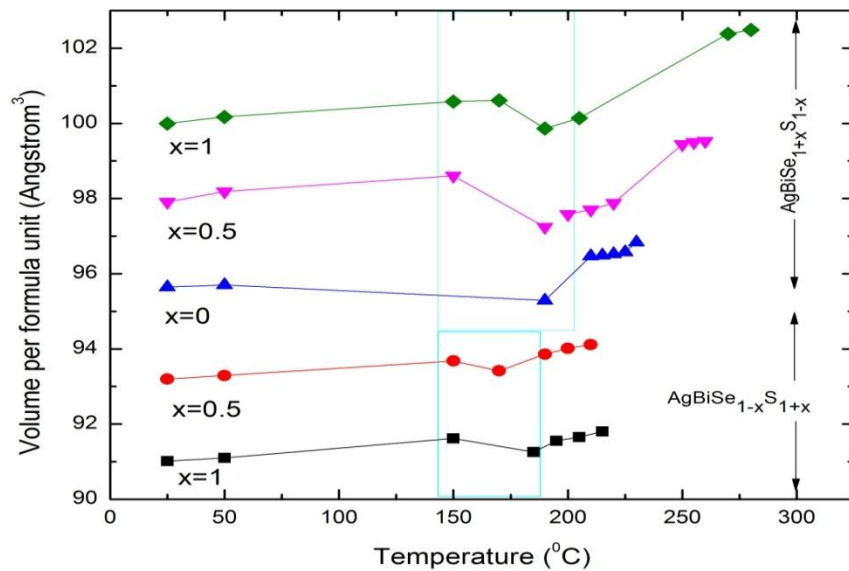


Figure 8: dépendance en température du volume par unité formulaire AgBiCh_2 .

Dans cette figure, la zone encadrée en bleu correspond à la transition structurale hexagonal→cubique pour les échantillons riches en soufre, et à la transition structurale hexagonal→rhomboédrique pour les échantillons riches en sélénium. Dans les deux cas, on observe un changement volumique notable à la transition, avec une réduction du volume par unité formulaire en passant de la forme hexagonale à la forme rhomboédrique ou cubique. En revanche, aucun changement volumique n'est observé lors du passage de la phase rhomboédrique à la phase cubique. Cette observation est cohérente avec la structure cristalline du matériau et en particulier avec la nature des polyèdres de coordination. Dans la phase hexagonale, les cations occupent un environnement cubique légèrement distordu, et dans les phases cubiques un environnement octaédrique distordu. Le passage de la phase hexagonale aux phases cubique ou rhomboédrique correspond donc à une augmentation de la compacité de la structure, et donc à une réduction du volume par unité formulaire. En revanche, la transition rhomboédrique→cubique est une transition ordre-désordre (avec une disparition concomitante de la distorsion rhomboédrique), qui n'est donc pas associée à un changement

volumique. C'est la première de ces deux transitions qui limite le potentiel de ces matériaux dans des applications de conversion thermoélectrique, puisque le changement volumique associé risque d'entraîner une fatigue et une rupture des matériaux ou des brasures matériaux/électrodes lors d'un cyclage en température.

L'un des objectifs de ce travail de thèse était d'étudier la possibilité de stabiliser la phase haute-température, dont les propriétés thermoélectriques sont prometteuses, afin de pouvoir utiliser ces matériaux dans des applications de conversion thermoélectrique dans une gamme de température 300-600°C. L'étape suivante a donc été d'étudier l'influence de la pression sur la structure cristalline de ces matériaux. La composition choisie pour cette étude, AgBiSe_2 , est celle pour laquelle les températures de transition sont les plus élevées (et donc celle pour laquelle les phases basse-température sont les plus stables. Pour ce faire, des mesures de diffraction des rayons X sous pression ont été faites sur synchrotron. Deux échantillons ont été étudiés, l'un de structure cubique et l'autre de structure hexagonale. Les diffractogrammes correspondants sont tracés figures 9 et 10.

Dans le cas de l'échantillon de structure cubique, figure 9 (le pic indiqué par une étoile correspond à un pic de Bragg du cuivre, qui sert d'étalon interne de pression), l'application d'une pression jusqu'à 18.2 GPa n'induit pas de changement structural. Un simple déplacement des pics de diffraction est observé, qui correspond à la réduction attendue du volume de la maille sous l'application de la pression isostatique.

Dans le cas de l'échantillon de structure hexagonale, figure 10 (le pic indiqué par une étoile correspond ici également à un pic de Bragg du cuivre, qui sert d'étalon interne de pression), la situation est différente. Un déplacement des pics de diffraction vers les plus grands angles est observé, qui correspond là encore à la réduction du volume de la maille sous l'effet de la pression. En revanche, on observe également une diminution du nombre de pics visibles sur le diffractogrammes. Si la transition hexagonal→rhomboédrique est difficile à observer (les diffractogrammes théoriques des deux structures sont très proches, la différence entre les diffractogrammes aux pressions les plus basses et ceux aux pressions les plus hautes ne souffre aucune ambiguïté : la structure change d'hexagonale aux pressions les plus faibles, à cubique aux pressions les plus élevées. Il semble donc qu'il soit possible d'induire la transition structurale et de stabiliser la phase cubique par l'application d'une pression de l'ordre de 15-18 GPa. Cette observation est en accord avec le fait que le volume par unité formulaire est plus petit dans la phase cubique que dans la phase hexagonale. Il devrait donc être possible de stabiliser la phase cubique, d'intérêt pour les propriétés thermoélectriques, par l'application d'une pression chimique. Ce point fera l'objet de la partie 2.

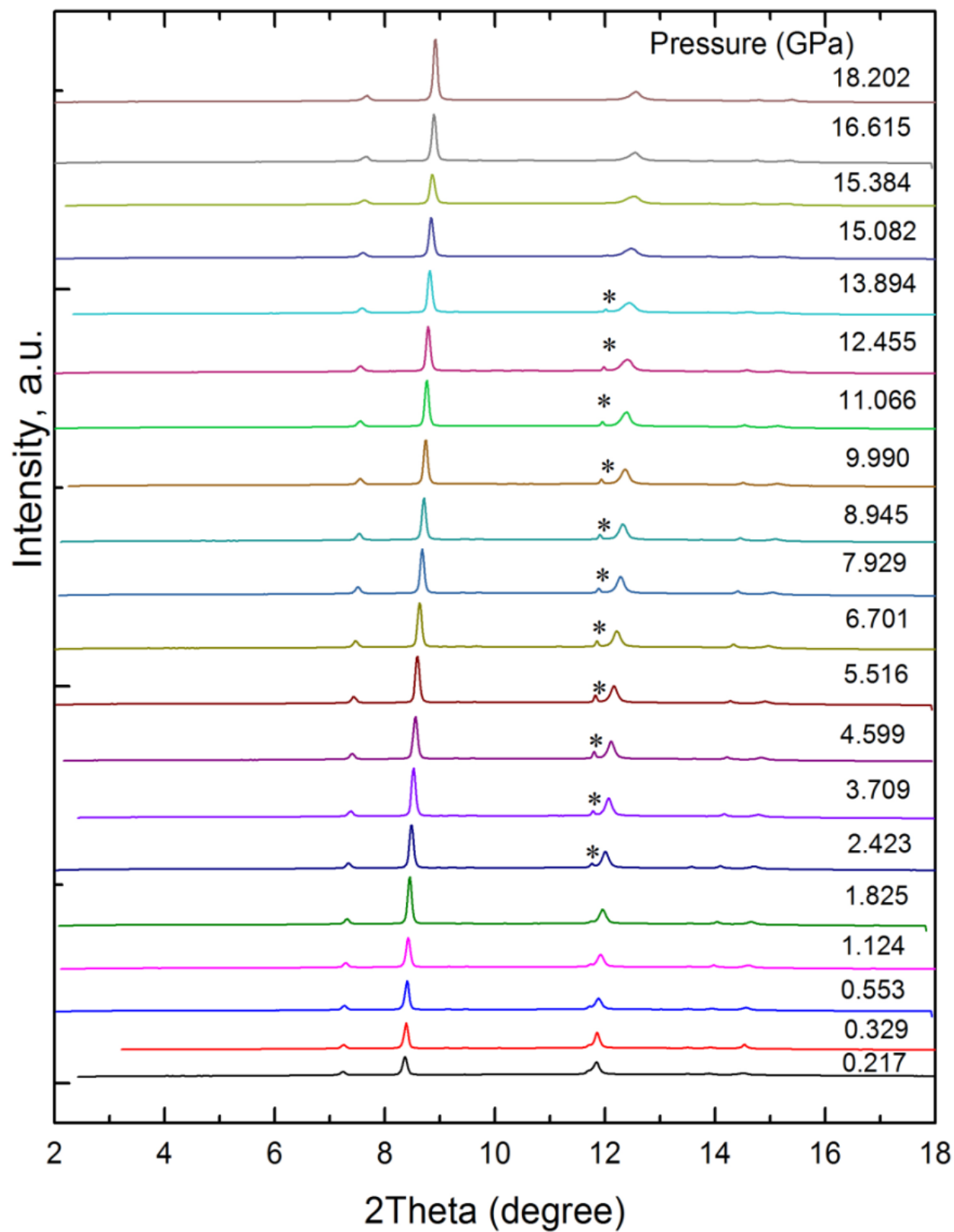


Figure 9 : Influence de la pression sur les diffractogramme de rayons X de AgBiSe₂ cubique.

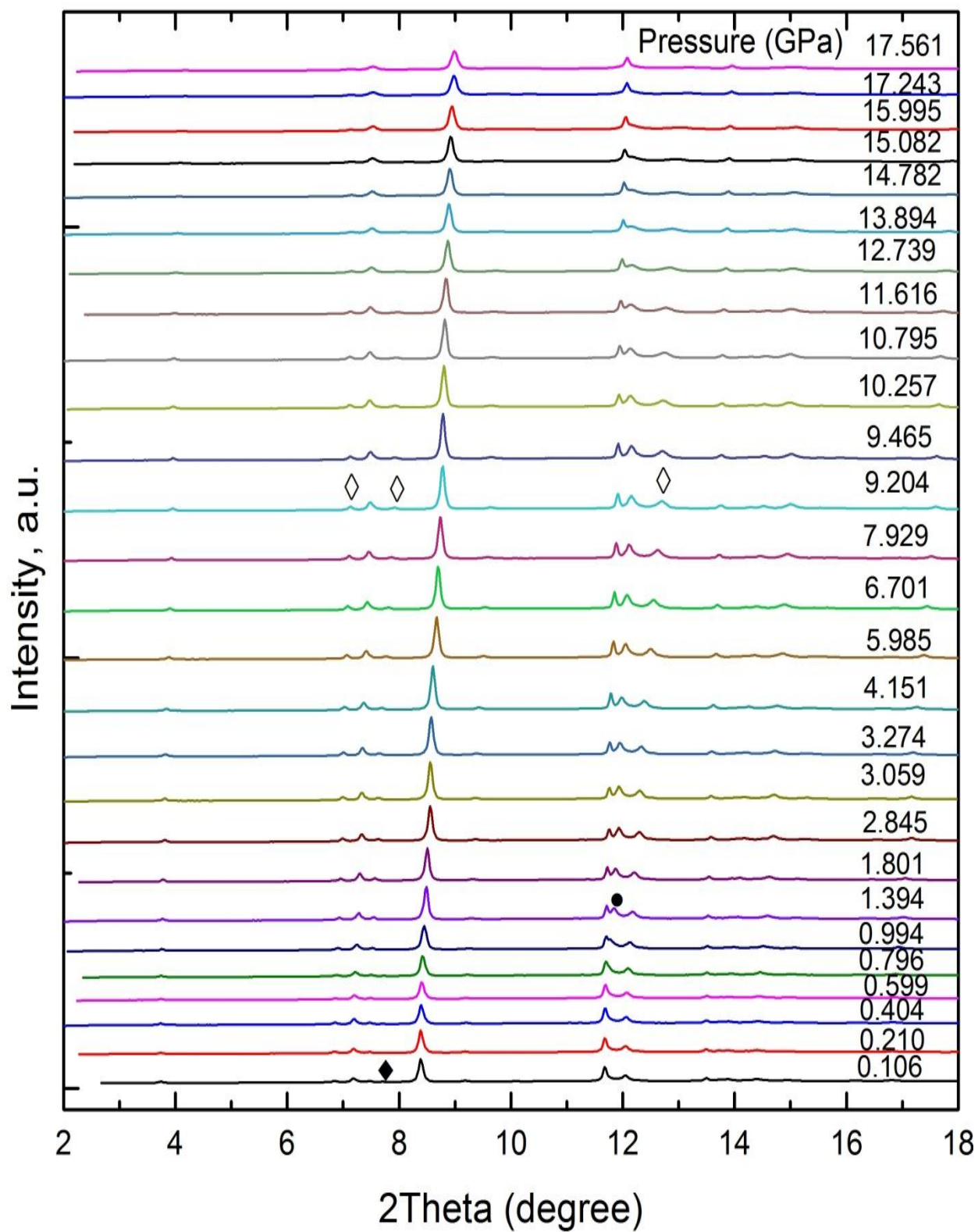


Figure 10 : Influence de la pression sur les diffractogramme de rayons X de AgBiSe₂ hexagonal.

2 Substitutions et stabilisation de la phase cubique dans la solution solide $\text{AgBiS}_{2-x}\text{Se}_x$

Nous avons vu que l'application d'une pression de 15-18 GPa permet d'obtenir la phase cubique à la température ambiante à partir de la phase hexagonale. Il est donc envisageable de stabiliser cette phase à la pression ambiante par l'application d'une pression chimique. Pour ce faire, nous avons choisi d'effectuer une substitution partielle du bismuth par de l'antimoine. En effet, ce dernier est plus petit que le bismuth, ce qui correspond bien à l'application d'une pression chimique. Par ailleurs, sa configuration électronique est similaire à celle du bismuth, il pourrait donc ne pas trop perturber la structure de bande des composés, et donc leurs propriétés de transport électrique. De plus, la différence de masse importante entre Bi et Sb pourrait conduire à une nouvelle réduction de la conductivité thermique des composés, du fait de la diffusion accrue des phonons par les fluctuations de masse. Enfin, AgSbSe_2 est connu pour cristalliser préférentiellement dans une structure cubique. Notre premier objectif a été de rechercher la fraction d'antimoine minimum permettant de stabiliser la phase cubique (nous souhaitons évidemment utiliser cette fraction la plus faible pour que les propriétés de transport soient le moins perturbées possibles par rapport à celles des composés sans antimoine). Cette première étude a été effectuée en élaborant des échantillons de composition $\text{AgBi}_{1-x}\text{Sb}_x\text{Se}_2$ par recuit à 850°C durant 48h (afin d'obtenir un mélange homogène) suivi par un refroidissement lent, de manière à permettre aux éventuelles transformations de phase de se réaliser, au moins partiellement. Les échantillons obtenus ont ensuite été analysés par diffraction des rayons X et DSC. La composition Se_2 a été choisie parce que c'est celle pour laquelle les températures de transition sont les plus élevées, et donc celle pour laquelle il devrait être le plus difficile de stabiliser la phase cubique.

Les figures 11 et 12 montrent respectivement les diffratogrammes de rayons X et les thermogrammes des échantillons de la série $\text{AgBi}_{1-x}\text{Sb}_x\text{Se}_2$. Aucune démixtion n'est observée dans les diffractogrammes, ce qui met en évidence l'existence d'une solution solide complète entre AgBiSe_2 et AgSbSe_2 (ce qui n'avait pas été montré dans la littérature au début de cette étude, et l'a été en 2016 dans le cas de nanoplaquettes élaborées par voie liquide). Par ailleurs, on constate une évolution de la structure cristalline, d'une phase hexagonale pour $x=0.1$ et $x=0.2$ (échantillons les plus riches en bismuth) vers une phase cubique lorsque la fraction d'antimoine est supérieure ou égale à 0.3. Cette observation est confirmée par les thermogrammes obtenus par DSC. Des pics endothermiques correspondant à des transitions de phase sont nettement visibles pour les échantillons $x=0$ à $x=0.2$. En revanche, aucune transition n'est observée pour les fractions d'antimoine supérieures ou égales à 0.3. (Les pics encadrés en noir correspondent aux points de fusion de phases secondaires en quantités mineures dans les échantillons. La fraction d'antimoine permettant de stabiliser la phase cubique dans la solution solide $\text{AgBi}_{1-x}\text{Sb}_x\text{Se}_2$ est donc comprise entre $x=0.2$ et $x=0.3$).

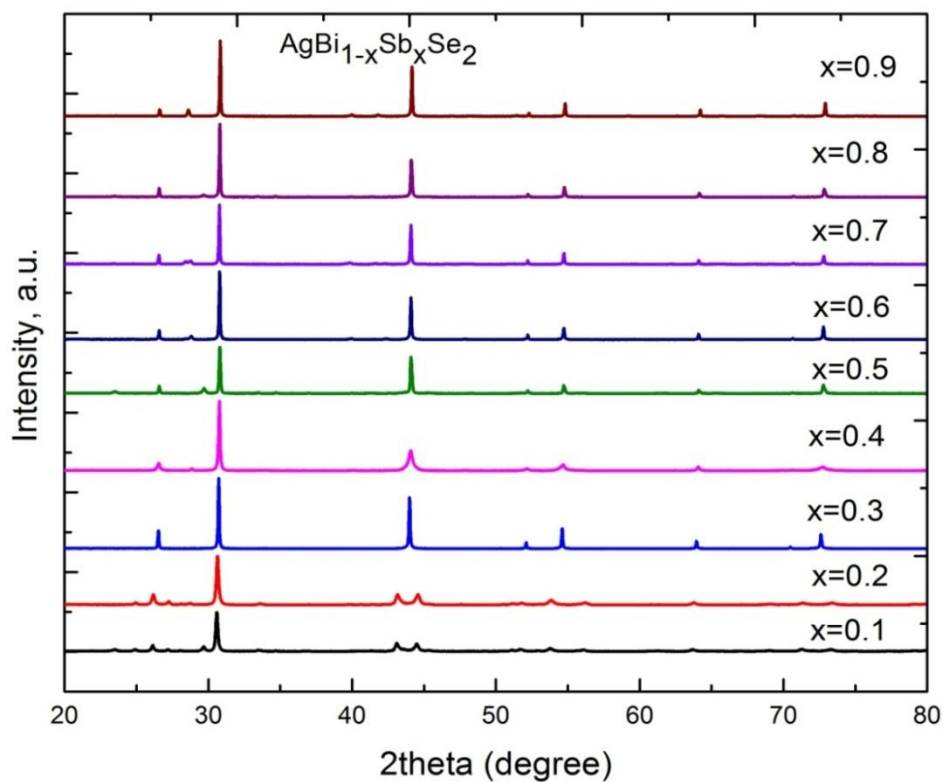


Figure 11: Diffractogrammes de rayons X des échantillons de la série $\text{AgBi}_{1-x}\text{Sb}_x\text{Se}_2$, ($0.1 \leq x \leq 0.9$).

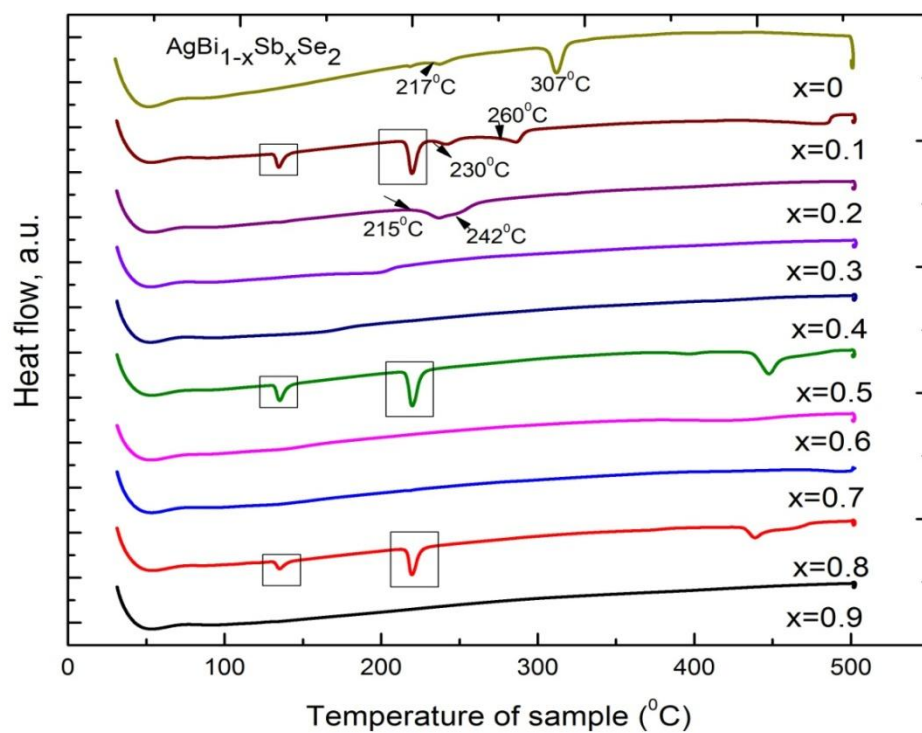


Figure 12: Thermogrammes des échantillons de la série $\text{AgBi}_{1-x}\text{Sb}_x\text{Se}_2$, ($0.1 \leq x \leq 0.9$).

L'étape suivante a été de préparer une sélection d'échantillons de la série $\text{AgBi}_{0.7}\text{Sb}_{0.3}\text{S}_{2-x}\text{Se}_x$ ($x=0$ à 2 par pas de 0.5) pour vérifier que cette fraction d'antimoine stabilise la phase cubique pour toute la solution solide. Les échantillons ont été préparés par recuit à 650°C durant 72h (afin d'homogénéiser le mélange) suivi d'un refroidissement lent, afin là encore de permettre à d'éventuelles transformations de se réaliser. Les échantillons obtenus ont alors été analysés par diffraction des rayons X et DSC. La figure 13 montre un zoom des diffractogrammes obtenus dans la gamme angulaire 20°-35°.

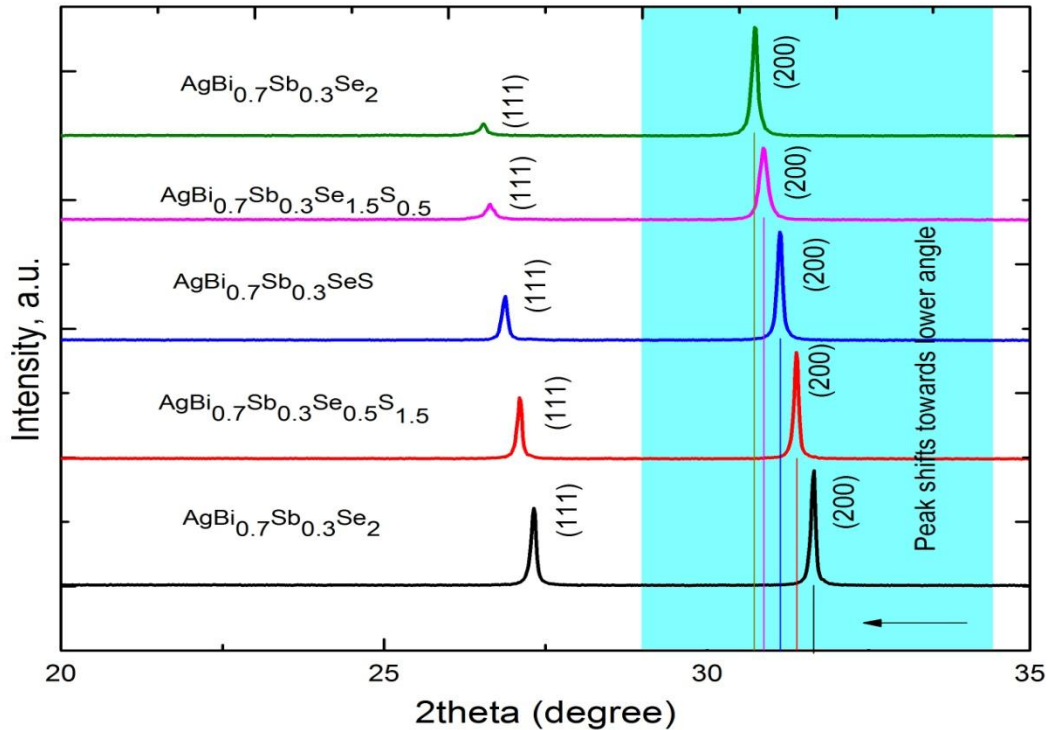


Figure 13: Diffractogrammes de rayons X des échantillons de la série $\text{AgBi}_{0.7}\text{Sb}_{0.3}\text{S}_{2-x}\text{Se}_x$.

Les seuls pics visibles dans ces diffractogrammes sont les pics (111) et (200) de la phase cubique, ce qui confirme que la fraction d'antimoine de 30% permet de stabiliser cette phase pour toutes les compositions de la solution solide. Par ailleurs, on peut également observer un déplacement des pics de diffraction vers les bas angles lorsque la fraction de sélénium augmente, correspondant à l'augmentation attendue du paramètre de maille. Un affinement de LeBail a permis de mettre en évidence une variation linéaire du paramètre de maille avec la fraction de sélénium, en accord avec une loi de Vegard.

Le premier résultat est confirmé par les analyses DSC. Contrairement aux échantillons initiaux ($\text{Sb}=0$, figure 14b) où des pics endothermiques correspondant aux transitions de phase sont nettement visibles, aucun pic endothermique n'est observé pour les échantillons de la série

$\text{AgBi}_{0.7}\text{Sb}_{0.3}\text{S}_{2-x}\text{Se}_x$ (figure 14a, les pics encadrés correspondent au point de fusion de phases secondaires en quantités mineures dans certains échantillons).

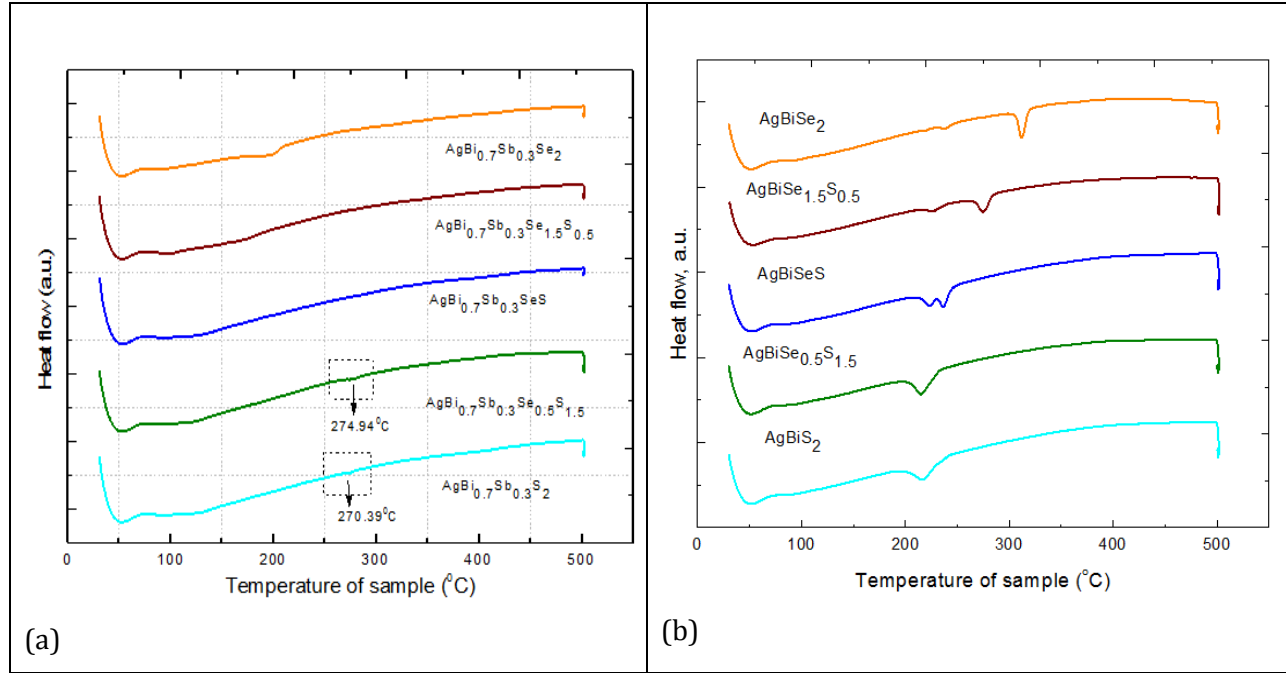


Figure 14: (a) Thermogrammes des échantillons de la série $\text{AgBi}_{0.7}\text{Sb}_{0.3}\text{S}_{2-x}\text{Se}_x$ (b) Thermogrammes des échantillons de la série $\text{AgBiS}_{2-x}\text{Se}_x$

Par application d'une pression chimique, il a donc été possible de stabiliser la phase cubique pour toutes les compositions de la solution solide.

3 études préliminaires des possibilités de dopage et des propriétés de transport

L'origine de ce projet est des études effectuées en 2012-2013 au laboratoire, dans laquelle de bonnes performances thermoélectriques ont été mises en évidence pour AgBiSe_2 et AgBiSeS . Cependant, lorsqu'ils ne sont pas dopés, les propriétés électriques (coefficient Seebeck, résistivité électrique, et facteur de puissance $S^2\sigma$) sont médiocres, et un dopage est nécessaire. Dans ces études, il avait été montré qu'un dopage de type n par la substitution partielle de l'argent par du niobium permettait d'optimiser les propriétés, avec un facteur de mérite thermoélectrique de l'ordre de l'unité pour une fraction de niobium de 4%.

Pour notre étude préliminaire du dopage de la solution solide $\text{AgBi}_{0.7}\text{Sb}_{0.3}\text{S}_{2-x}\text{Se}_x$, nous avons donc choisi de tester deux fractions de niobium, $\text{Nb}=0.02$ et $\text{Nb}=0.04$, en préparant deux séries d'échantillons de compositions $\text{Ag}_{1-y}\text{Nb}_y\text{Bi}_{0.7}\text{Sb}_{0.3}\text{S}_{2-x}\text{Se}_x$ ($y=0.02$ et 0.04 , et $x=0$ à 2 par pas de 0.5). Ces synthèses ont été effectuées par recuit à 850°C durant 48h afin d'homogénéiser les

mélange des précurseurs, suivi d'un refroidissement lent jusqu'à la température ambiante. Après caractérisations par diffraction des rayons X et DSC, les échantillons obtenus ont été broyés manuellement, et densifiés par Spark Plasma Sintering (voir plus loin).

Les diffractogrammes obtenus pour les 10 échantillons mettent en évidence une phase cubique bien cristallisée, et l'absence de phases hexagonale ou rhomboédrique (quelques exemples représentatifs sont tracés figure 15).

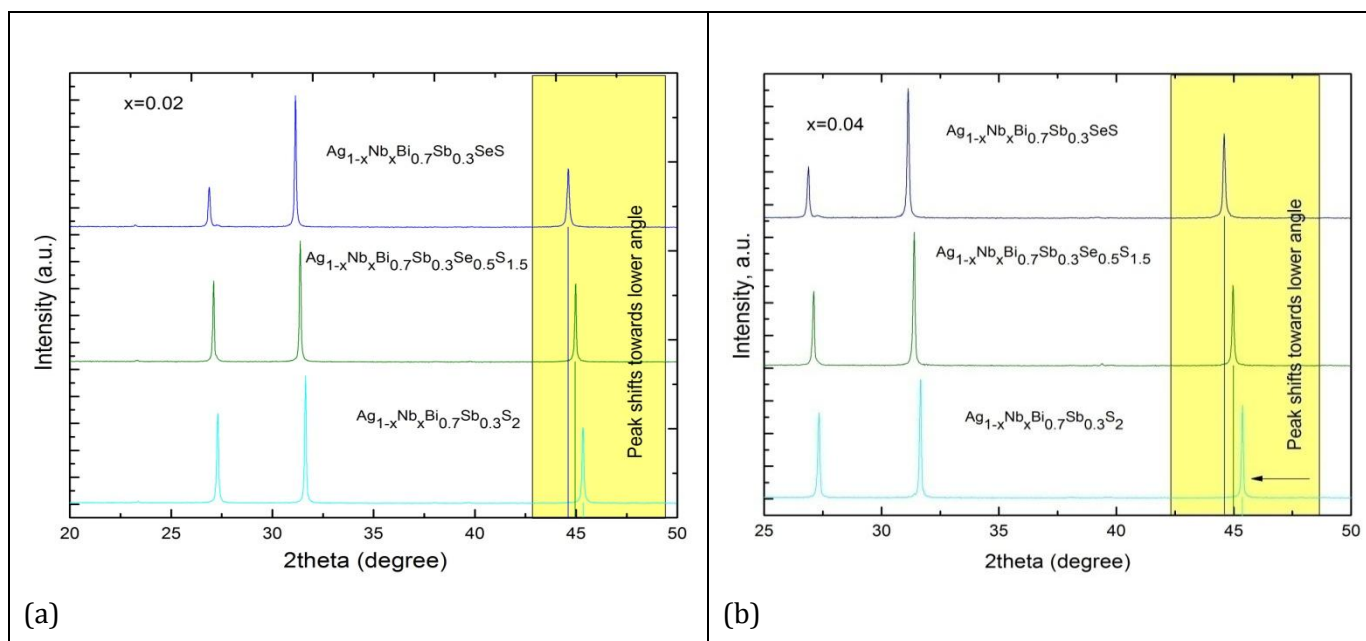


Figure 15: Diffractogrammes de rayons X d'une sélection d'échantillons des séries $\text{Ag}_{1-y}\text{Nb}_y\text{Bi}_{0.7}\text{Sb}_{0.3}\text{S}_{2-x}\text{Se}_x$.

Comme dans le cas des échantillons non dopés, les affinements par la méthode de LeBail ont permis de mettre en évidence une évolution des paramètres de maille conforme à la loi de Vegard.

Les thermogrammes obtenus pour les 10 échantillons, représentés figure 16, confirme la seule présence de la phase cubique, aucun pic endothermique correspondant à une transition structurale n'étant visible. Les pics encadrés correspondent au point de fusion du Bi, en quantité mineure dans les échantillons, et ceux indiqués par une flèche à ceux d'une phase secondaire non identifiée (elle n'est pas visible dans les diffractogrammes). De manière intéressante, ces pics « parasites » ne sont plus présents après un cyclage dans le cas de la phase non identifiée, ou dans les échantillons ayant été densifiés par SPS dans le cas également du bismuth. Il est probable que cette phase non identifiée se volatilise à plus haute température, et dans le cas du bismuth, il passe à l'état liquide et est éliminé dans la feuille de graphite de protection lors du frittage par SPS.

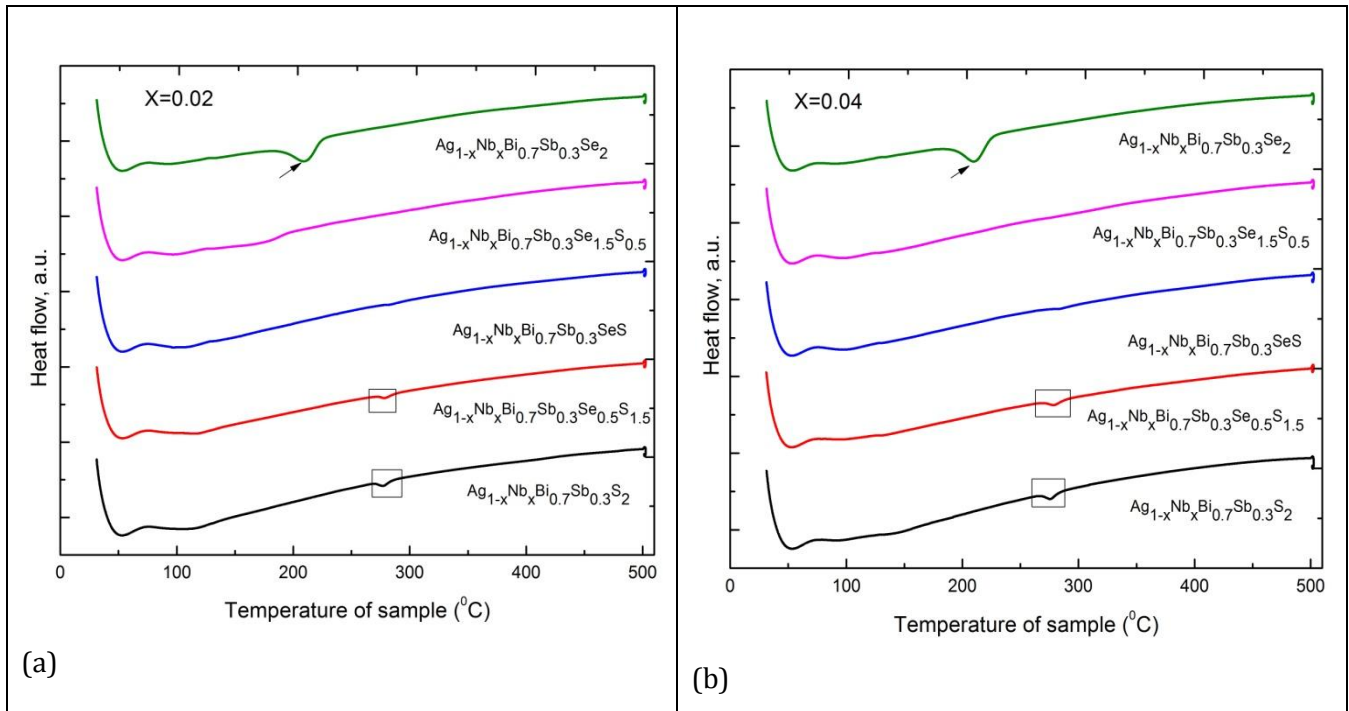


Figure 16: Thermogrammes des échantillons des séries $\text{Ag}_{1-y}\text{Nb}_y\text{Bi}_{0.7}\text{Sb}_{0.3}\text{S}_{2-x}\text{Se}_x$.

Nous avons donc obtenus des échantillons de bonne pureté et bien cristallisés pour toutes les compositions de la série $\text{Ag}_{1-y}\text{Nb}_y\text{Bi}_{0.7}\text{Sb}_{0.3}\text{S}_{2-x}\text{Se}_x$, dans tous les cas dans une structure cubique.

Après broyage manuel, les poudres obtenues ont été densifiées par SPS pour obtenir des pastilles de diamètre 15mm. Le frittage a été effectué à 400°C, sous argon, sous une pression de 75 MPa, dans des moules de graphite.

Malheureusement, la plupart des pastilles se sont révélées fissurées à l'issue du frittage, après élimination de la couche de graphite par polissage. Trois raisons principales peuvent expliquer cet échec. En premier lieu, aucune optimisation préalable de la microstructure d'avait été effectuée avant ces essais de densification, les poudres ayant été obtenues par simple broyage manuel. En second lieu, les analyses DSC ont mis en évidence la présence de bismuth résiduel en faible proportion dans certains échantillons. En fondant lors de la densification, celui-ci peut contribuer à initier des fractures dans les pastilles. Enfin, s'agissant ici d'études préliminaires, aucune optimisation du procédé de frittage (température, pression appliquée, vitesses de rampe, ...) n'a été effectuée. Ces problèmes devront être réglés afin de pouvoir étudier les propriétés de transport thermoélectrique de ces matériaux.

Néanmoins, des morceaux de taille suffisante ont pu être collectés et mis en forme, permettant d'effectuer des premières mesures du coefficient Seebeck, de la résistivité électrique et de la conductivité thermique, pour certaines des compositions. Les résultats obtenus sont représentés respectivement dans les figures 17 à 19, et les résultats à la température ambiante

sont résumés dans le tableau 1. Suite à une panne de l'un des instruments de mesure, le coefficient Seebeck et la résistivité électrique n'ont pas pu être mesurés à haute température.

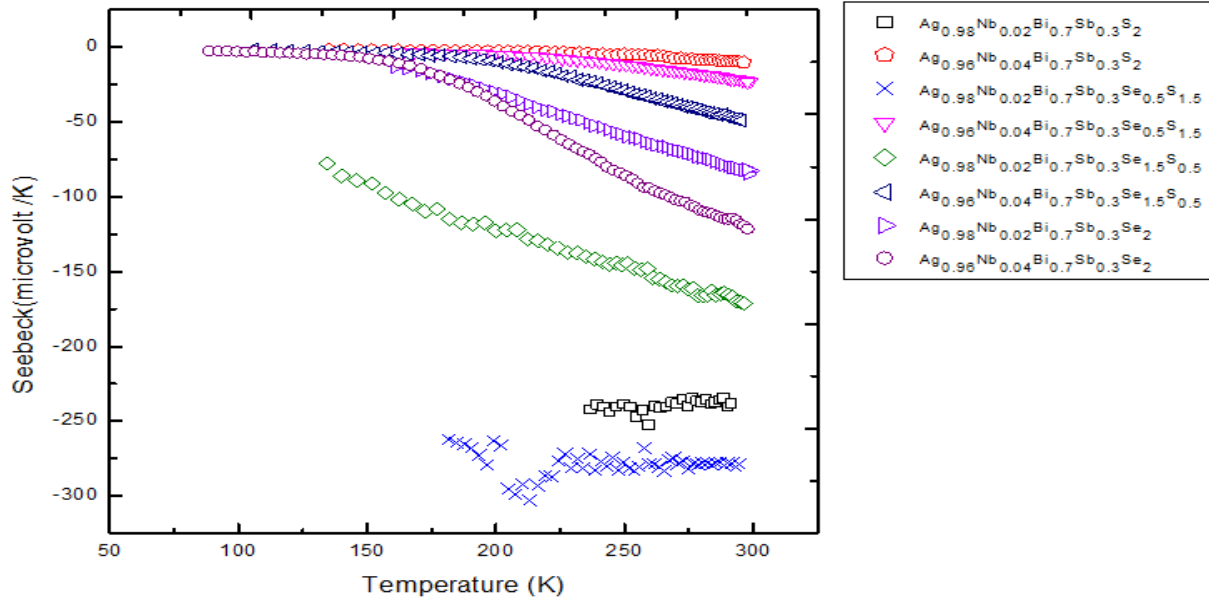


Figure 17: Coefficient Seebeck des échantillons des séries $\text{Ag}_{1-y}\text{Nb}_y\text{Bi}_{0.7}\text{Sb}_{0.3}\text{S}_{2-x}\text{Se}_x$.

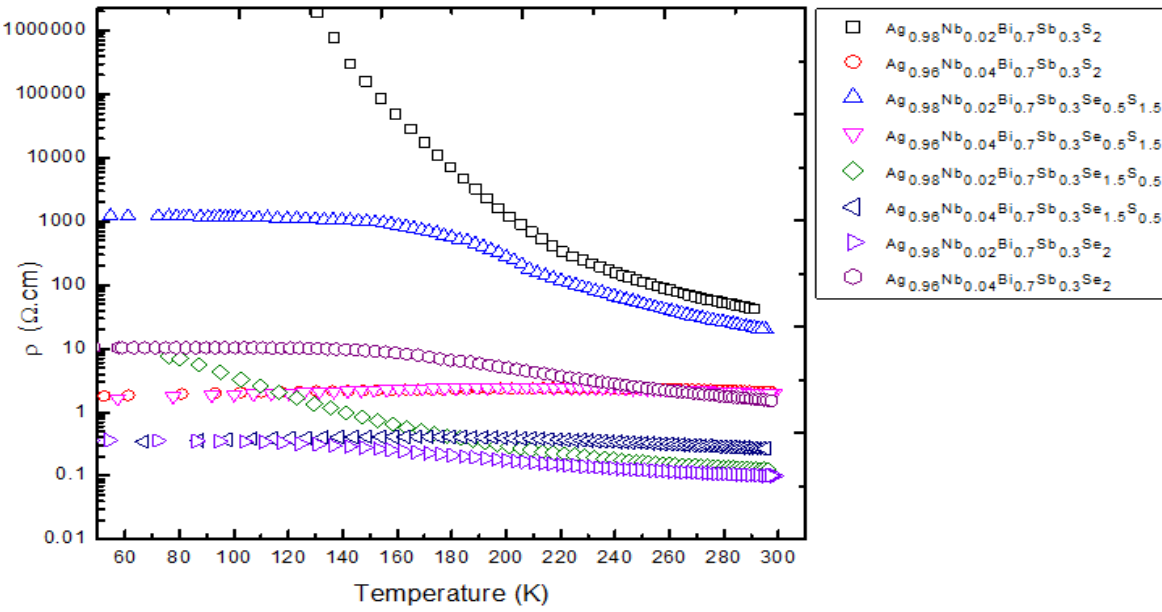


Figure 18: Résistivité électrique des échantillons des séries $\text{Ag}_{1-y}\text{Nb}_y\text{Bi}_{0.7}\text{Sb}_{0.3}\text{S}_{2-x}\text{Se}_x$.

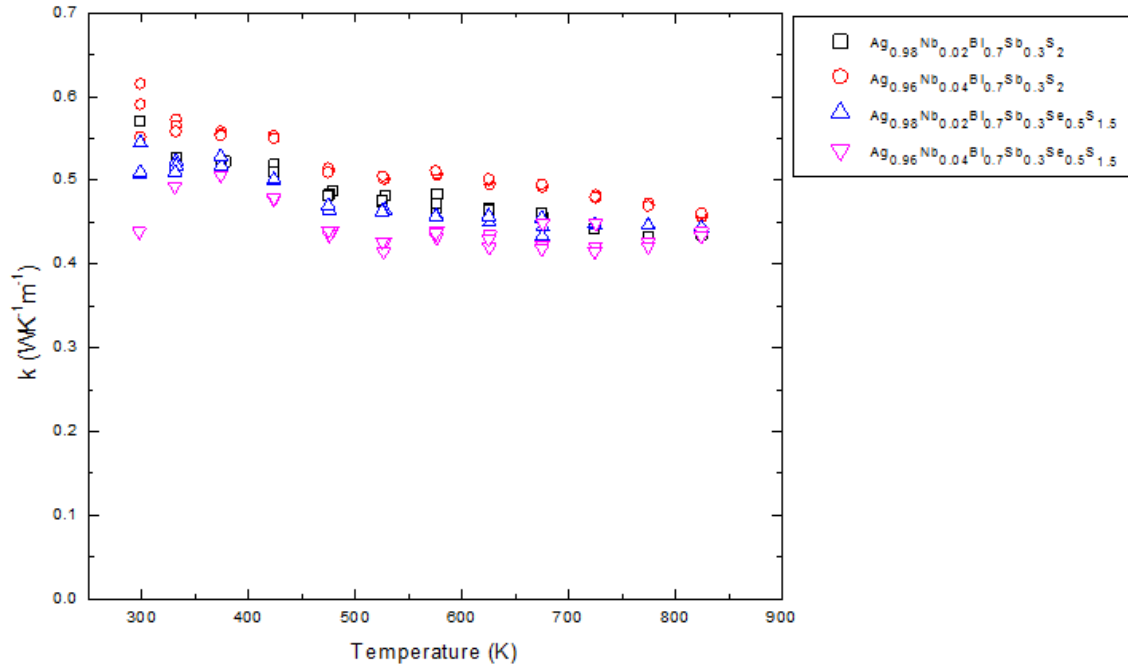


Figure 18: Conductivité thermique des échantillons des séries $\text{Ag}_{1-y}\text{Nb}_y\text{Bi}_{0.7}\text{Sb}_{0.3}\text{S}_{2-x}\text{Se}_x$.

Tableau 1: $|S|$, ρ , κ et ZT à 300K pour les échantillons des séries $\text{Ag}_{1-y}\text{Nb}_y\text{Bi}_{0.7}\text{Sb}_{0.3}\text{S}_{2-x}\text{Se}_x$.

Composition name	$ S $ ($\mu\text{V/K}$)	ρ ($\Omega\cdot\text{cm}$)	κ ($\text{WK}^{-1}\text{m}^{-1}$)	ZT
$\text{Ag}_{0.98}\text{Nb}_{0.02}\text{Bi}_{0.7}\text{Sb}_{0.3}\text{S}_2$	238	42.8	0.57	6.9×10^{-5}
$\text{Ag}_{0.96}\text{Nb}_{0.04}\text{Bi}_{0.7}\text{Sb}_{0.3}\text{S}_2$	9	2.1	0.62	1.8×10^{-6}
$\text{Ag}_{0.98}\text{Nb}_{0.02}\text{Bi}_{0.7}\text{Sb}_{0.3}\text{Se}_{0.5}\text{S}_{1.5}$	278	19.9	0.51	2.2×10^{-4}
$\text{Ag}_{0.96}\text{Nb}_{0.04}\text{Bi}_{0.7}\text{Sb}_{0.3}\text{Se}_{0.5}\text{S}_{1.5}$	23	1.9	0.44	1.8×10^{-5}
$\text{Ag}_{0.98}\text{Nb}_{0.02}\text{Bi}_{0.7}\text{Sb}_{0.3}\text{Se}_{1.5}\text{S}_{0.5}$	171	0.1	-	-
$\text{Ag}_{0.96}\text{Nb}_{0.04}\text{Bi}_{0.7}\text{Sb}_{0.3}\text{Se}_{1.5}\text{S}_{0.5}$	49	0.3	-	-
$\text{Ag}_{0.98}\text{Nb}_{0.02}\text{Bi}_{0.7}\text{Sb}_{0.3}\text{Se}_2$	81	0.1	-	-
$\text{Ag}_{0.96}\text{Nb}_{0.04}\text{Bi}_{0.7}\text{Sb}_{0.3}\text{Se}_2$	121	1.5	-	-

Les valeurs négatives du coefficient Seebeck observées pour tous les échantillons confirment que ces composés sont bien de type n. Les valeurs obtenues sont très dispersées et dépendent très fortement à la fois du taux de dopage en niobium (elles décroissent lorsque la fraction de niobium augmente de 0.02 à 0.04, ce qui correspond bien à une augmentation de porteurs de charge lors d'un dopage de type n, à une exception près qui pourrait correspondre à une inversion de deux échantillons), et de la fraction de soufre/sélénium dans la solution solide (la

tendance semble être à des valeurs absolues plus élevées pour les échantillons les plus riches en soufre).

Les valeurs observées pour la résistivité électrique se corrélient avec celles observées pour le coefficient Seebeck : plus ce dernier est faible en valeur absolu, plus la résistivité électrique est faible, ce qui indique un rôle prépondérant de la structure électronique et de la position du niveau de Fermi sur les propriétés, et secondaires de la mobilité des porteurs. Pour toutes les compositions, la résistivité électrique reste beaucoup plus élevée que celle qui avait été observée dans les échantillons de la série $\text{Ag}_{1-x}\text{Nb}_x\text{BiSe}_2$ pour les mêmes taux de dopage (les valeurs étaient comprises entre 5-15 $\Omega\cdot\text{cm}$). En revanche, elle est du même ordre de grandeur que celle qui avait été observée dans les échantillons sous-dopés au cours de cette étude. Il semble donc que la substitution partielle du bismuth par le niobium induise des changements non-négligeables dans la structure électronique des composés de la solution solide, et qu'ils conviennent d'optimiser à nouveau la concentration de porteurs de charge.

En ce qui concerne la conductivité thermique, les valeurs observées sont extrêmement faibles, voisines de 0.5 $\text{W}\cdot\text{m}^{-1}\cdot\text{K}^{-1}$ pour tous les échantillons. Ces valeurs intrinsèquement très faibles confirment l'intérêt de ces échantillons pour des applications thermoélectriques, à la condition de pouvoir améliorer les propriétés électriques pour qu'elles soient du même ordre que celles observées précédemment dans $\text{Ag}_{1-x}\text{Nb}_x\text{BiSe}_2$. Du fait du nombre réduit d'échantillons qui a pu être mesuré, il n'est pas possible d'obtenir une tendance quant à l'influence de la fraction de soufre/sélénium sur la conductivité thermique.

4 Conclusions et perspectives

Au cours de cette étude, nous avons montré qu'une solution solide complète existe entre AgBiS_2 et AgBiSe_2 . Tous les composés de cette solution solide cristallisent dans différentes phases allotropiques. Pour $x < 1$ dans $\text{AgBiS}_{2-x}\text{Se}_x$, une transition existe d'une phase hexagonale à la température vers une phase cubique à haute température. Pour $x > 1$, deux transitions sont observées, d'abord de la phase hexagonale à une phase rhomboédrique, puis de cette phase rhomboédrique à la phase cubique. Une contraction du volume par unité formulaire est associée à la transition de la phase hexagonale à la phase cubique ou rhomboédrique, ce qui limite les possibilités d'utilisation de ces matériaux dans des modules thermoélectriques en conditions réelles. Cependant, nous avons pu montrer qu'il est possible de passer de la phase hexagonale à la phase cubique sous l'application d'une pression isostatique de l'ordre de 15-18 GPa. Suite à cette observation, nous avons montré qu'il en est de même par application d'une pression chimique, qui permet de stabiliser la phase cubique à la pression et à la température ambiante. Des échantillons monophasés de structure cubique ont ainsi pu être obtenus pour

toutes les compositions de la solution solide en substituant 30% du bismuth par de l'antimoine. Notre étude préliminaire des propriétés de transport a permis de confirmer que les composés sont bien de type n malgré cette substitution. Cependant, l'influence de la substitution sur la structure électronique ne peut pas être négligée, et la résistivité électrique mesurée pour nos composés est nettement supérieure à celle qui avait été observée auparavant pour des échantillons de composition $\text{Ag}_{1-x}\text{Nb}_x\text{BiSe}_2$. En revanche, la conductivité thermique demeure intrinsèquement très faible.

Dans la suite, il conviendrait dans un premier temps d'optimiser le processus de densification par SPS, afin d'éviter la fracturation des pastilles lors du démoulage, du polissage et du découpage. On peut notamment suggérer l'utilisation du broyage mécanique préalablement à la densification, de manière à optimiser la microstructure des poudres.

Dans un second temps, il conviendrait d'optimiser la concentration de porteurs de charge pour les échantillons de la série $\text{Ag}_{1-y}\text{Nb}_y\text{Bi}_{0.7}\text{Sb}_{0.3}\text{S}_{2-x}\text{Se}_x$ afin de diminuer la résistivité électrique et donc d'augmenter le facteur de puissance et le facteur de mérite thermoélectrique de ces composés. Cette optimisation pourra se faire via l'utilisation de mesures d'effet Hall, qui n'ont pas pu être effectuée lors de cette thèse du fait de la fissuration des pastilles.

Titre : Chalcogénures de type I-V-VI₂ pour applications thermoélectriques

Mots clés : Thermoélectricité, Matériaux chalcogénures, Transition de phase, Pression chimique

Résumé : Ce travail de thèse porte sur une série d'échantillons de composition nominale AgBiSe_{2-x}S_x (avec x= 0 à 2), appartenant à la famille des chalcogénures ternaires de type I-V-VI₂. Les analyses structurales et thermiques ont mis en évidence une solution solide complète sans gap de miscibilité, et des transitions de phase pour toutes les compositions. Nous avons pu obtenir des composés monophasés à la fois des phases hexagonale et cubique, et notre étude de DRX en température a mis en évidence une phase rhomboédrique pour certaines compositions (x=1 à 2 dans AgBiSe_xS_{2-x}). Les résultats de DSC ont confirmé la présence de transitions de phase pour toutes les compositions, avec un déplacement des températures de transition en fonction de la fraction de soufre/sélénium. Notre étude de DRX sous pression de l'échantillon AgBiSe₂ a montré une transition de phase induite par la pression d'une phase hexagonale à rhomboédrique puis cubique. Suite à cette observation, l'application d'une

pression chimique, par la substitution de 30% du Bi par du Sb a été utilisée avec succès pour stabiliser la phase cubique pour toutes les compositions. Le dopage par Nb des échantillons substitués par l'antimoine l'a pas eu d'influence sur la nature des phases stables à l'ambiante en comparaison aux échantillons non dopés. Nous avons ensuite étudié l'influence du dopage sur les propriétés de transport. Les valeurs négatives de S pour toutes les compositions indiquent un comportement de semi-conducteur de type n dans la gamme (50-300K). Par ailleurs, nos mesures ont montré à la fois de très faibles valeurs de κ mais aussi une décroissance de |S| et ρ avec l'augmentation de la fraction de Nb. Ces résultats devraient permettre d'optimiser le facteur de puissance pour améliorer les valeurs de ZT. Enfin, une étude en collaboration avec une équipe chinoise a permis d'obtenir une valeur de ZT de 1.3 à 890K dans un composé AgPb_mSnSe₂.

Title: Chalcogenides of type I-V-VI₂ for the thermoelectric applications

Keywords: Thermoelectric, Chalcogenide materials, Phase transition, Chemical pressure

Abstract: Here, we report on a series of samples with nominal compositions AgBiSe_{2-x}S_x (with x= 0 to 2) belonging to the class of ternary chalcogenides of type I-V-VI₂. The structural and thermal analysis result shows a complete solid solution without miscibility gap and phase transitions for all compositions. We have succeeded in obtaining single phase compounds, of both hexagonal and cubic phase, and the high temperature XRD study showed the rhombohedral phase too for selected compositions (x=1 to 2 in AgBiSe_xS_{2-x}). The DSC results confirmed the presence of the phase transitions for all compositions, with a shift of the temperature of transition as a function of the sulfur/selenium fraction. The high pressure XRD investigation of the compound AgBiSe₂ showed a pressure induced phase transition

from hexagonal-to-rhombohedral-to-cubic phase. In this respect, chemical pressure with 30% Sb on the Bi site has been successfully applied to stabilize the cubic phase for all compositions. Nb doping in the Sb-substituted samples does not show any change in the phase behavior at RT. The influence of doping on transport properties was analyzed. The negative value of S for all compositions indicates n-type semiconducting behavior over the range (50-300K). Further, the results not only shows very low value of κ but the |S| and ρ value also decreases for each composition from Nb fraction 0.02 to 0.04. So, we can optimize the power factor in order to improve the ZT value. At last, collaborative study with Chinese team showed that ZT of 1.3 at 890 K can be achieved for AgPb_mSnSe_{2+m} (m = 50).